Modified Linear Theory Aircraft Design Tools and Sonic Boom Minimization Strategy Applied to Signature Freezing via F-function Lobe Balancing

by

Timothy Paul Jung

B.S., United States Air Force Academy, 1992

M.S., South Dakota School of Mines, 2000

M.S., Air Force Institute of Technology, 2005

A thesis submitted to the

Faculty of the Graduate School of the

University of Colorado in partial fulfillment

of the requirements for the degree of

Doctor of Philosophy

Department of Aerospace Engineering Sciences

2012

This thesis entitled:
Modified Linear Theory Aircraft Design Tools and Sonic Boom Minimization Strategy Applied to
Signature Freezing via F-function Lobe Balancing
written by Timothy Paul Jung
has been approved for the Department of Aerospace Engineering Sciences

_____

Dr. Ryan Starkey

_____

Dr. Brian Argrow

_____

Dr. Kenneth Jansen

_____

Dr. Kurt Maute

Date _____

The final copy of this thesis has been examined by the signatories, and we find that both the
content and the form meet acceptable presentation standards of scholarly work in the above
mentioned discipline.

Jung, Timothy Paul (Ph.D., Aerospace Engineering)

Modified Linear Theory Aircraft Design Tools and Sonic Boom Minimization Strategy Applied to

Signature Freezing via F-function Lobe Balancing

Thesis directed by Dr. Ryan Starkey

Commercial supersonic travel has strong business potential; however, in order for the Federal Aviation Administration to lift its ban on supersonic flight overland, designers must reduce aircraft sonic boom strength to an acceptable level. An efficient methodology and associated tools for designing aircraft for minimized sonic booms are presented. The computer-based preliminary design tool, RapidF, based on modified linear theory, enables quick assessment of an aircraft's sonic boom with run times less than 30 seconds on a desktop computer. A unique feature of RapidF is that it tracks where on the aircraft each segment of the of the sonic boom came from, enabling precise modifications, speeding the design process. Sonic booms from RapidF are compared to flight test data, showing that it is capability of predicting a sonic boom duration, overpressure, and interior shock locations. After the preliminary design is complete, scaled flight tests should be conducted to validate the low boom design. When conducting such tests, it is insufficient to just scale the length; thus, equations to scale the weight and propagation distance are derived. Using RapidF, a conceptual supersonic business jet design is presented that uses F-function lobe balancing to create a frozen sonic boom using lifting surfaces. The leading shock is reduced from 1.4 to 0.83 psf, and the trailing shock from 1.2 to 0.87 psf, 41% and 28% reductions respectfully. By changing the incidence angle of the surfaces, different sonic boom shapes can be created, and allowing the lobes to be re-balanced for new flight conditions. Computational fluid dynamics is conducted to validate the sonic boom predictions. Off-design analysis is presented that varies weight, altitude, Mach number, and propagation angle, demonstrating that lobe-balance is robust. Finally, the Perceived Level of Loudness metric is analyzed, resulting in a modified design that incorporates other boom minimization techniques to further reduce the sonic boom.

Dedication

To my family for allowing me to pursue my dreams and to my parents for instilling in me a strong work ethic and the passion for knowledge.

Acknowledgements

Contents

Chapter

Tables

Table

Figures

Figure

Nomenclature

a = speed of sound, ft/sec

A = acoustic ray tube area, ft

A_1, A_2 = wing cross sectional areas, ft^2

AoA = angle of attack, radians

AR = aspect ratio, -

b = span, ft

c = wave speed, ft/sec

c_p = specific heat at constant pressure, (ft-lbs)/(slug ^{0}R)

c_0 = horizontal component of wave speed, ft/sec

c_1 = scaling coefficient, -

$C_{l\alpha}$ = airfoil lift curve slope, 1/radians

$C_{L\alpha}$ = wing lift curve slope, 1/radians

C_L = lift coefficient, -

C_D = drag coefficient, -

C_p = pressure coefficient, -

D = drag, lbs

f = source strength, ft$^{3/2}$/sec

F = masking coefficient, -

   = Whitham F-function, $\sqrt{\text{ft}}$

h = cruise altitude, ft

h_o = height above ground of observer's ear, ft

H = Heaviside step function

$\mathcal{H}$ = atmospheric scale height, ft

i = incidence angle, radians

J = objective function, -

k = coefficient in non-linear characteristic equation, -

K_1 = Bessel function of second kind

l = distance to leading edge, ft

L = lift, lbs

L_b = band pressure level, dB

L_n = pressure level at frequency n, dB

$\mathcal{L}$ = length of aircraft, ft

M = Mach number, -

p = Heaviside's operator

= pressure, psf

$\Delta\tilde{p}$ = non-dimensional pressure, -

p_s = shock pressure rise, psf

q =dynamic pressure, psf

r = radial distance, ft

R = gas constant (ft-lbs)/(slugs ^{o}R)

= fuselage radius, ft

$\bar{R}_f$ = average fuselage radius, ft

Re = Reynolds number, -

s = phase or distance along ray, ft

S = area, ft^2

S_t = total sones

t = time, sec

T	= temperature, ^{o} Rankine
T_r	= shock rise time, sec
u	= velocity perturbation in longitudinal direction, -
u_e	= velocity at edge of boundary layer, ft/sec
U	= velocity in longitudinal direction, ft/sec
v	= velocity perturbation in radial direction,-
V	= velocity in spanwise direction, ft/sec
$\bar{V}$	= velocity vector, ft/sec
W	= aircraft weight, lbs
	= velocity in vertical direction, ft/sec
$\mathcal{W}$	= numerical weight in F-function equation, ft$^{-1/2}$
x	= longitudinal coordinate from nose of aircraft, ft
$\tilde{x}$	= non-dimensional distance, -
y	= characteristic coordinate, ft
	= distance in spanwise direction, ft
	= distance from wall in boundary layer, ft
y_t	= acoustical retard distance, ft
z	= distance below aircraft, ft
Z_x	= change in thickness with respect to x-direction, -
α	= age variable, ft/$\sqrt{\text{ft}}$
	= Walkden's wing coordinate, ft
β	= Prandtl-Glauert coefficient, $\sqrt{M^2 - 1}$, -
β_W	= Walkden's wing coordinate, ft
γ	= ratio of specific heats, -
δ	= boundary layer thickness, ft
Δ	= acoustic perturbation

ϵ	= small angle, radians
ζ	= dummy variable of integration
η	= spanwise distance, ft
θ	= angle from horizon to wavefront normal, radians
	= Whitham's coordinate angle, radians
θ_1, θ_2	= aircraft slicing angles, radians
Λ_t	= sweep of thickness, radians
μ	= Mach angle, radians
ξ	= phase, sec
ρ	= density, slug/ft^3
τ	= age variable, sec/$\sqrt{\text{ft}}$
	= Whitham's and Walkden's longitudinal distance, ft
τ_O	= oxygen's relaxation time, sec
τ_N	= nitrogen's relaxation time, sec
ϕ , ϕ_p	= perturbation velocity potential, ft^2/sec
ϕ	= propagation angle, radians
Φ	= velocity potential, ft^2/sec
χ	= dummy argument
ψ	= ground incidence angle of ray, radians

Subscripts

eq	= total equivalent area
exp	= exposed
F	= full-scale aircraft
$homo$	= homogeneous atmosphere
i	= summation index
in	= incidence

iso	= isothermal atmosphere
L	= lift
	= Lighthill
ML	= Modified Lighthill
MW	= Modified Whitham
$N2$ —¿	= nitrogen
n	= summation index
p	= pressure perturbation
$O2$	= oxygen
ref	= reference
s	= constant entropy
	= shock
S	= scaled test vehicle
t	= acoustical retard
V	= volume
W	= Whitham
x	= x-direction
z	= z-direction
∞	= freestream conditions
0	= location at the aircraft
	= ambient conditions
1	= starting position
2	= final position

Superscripts:

$'$, $''$	= first and second derivatives

Chapter 1

INTRODUCTION

1.1 Historical Context

In the last decade, the aerospace industry has revived its interest in a supersonic civilian aircraft, and subsequently, in sonic boom minimization research. As evidence, Fig. 1.1 shows the number of AIAA conference and journal articles published each year with "sonic boom" as a key word from 1960 to 2011 (no papers were published before 1960). Also shown in Fig. 1.1 are the major U.S. supersonic transport research programs [38,148]. The height of each program represents its relative annual expenditures. A summary of each program [12, 21, 22, 38, 45, 128, 168] can be found in Table 1.1. The first surge in sonic boom research began in the 1960s when the U.S. Government initiated its Supersonic Transport (SST) program [128]. This initiative was a national effort with the goal of producing a supersonic passenger aircraft similar to the Concorde. However, the American SST was to be technically more advanced than the Concorde and Tupolev TU-144 competitors. For example, the U.S. SST was to fly at Mach 2.7 compared to the Concorde and TU-144 which flew near Mach 2.0. Consequentially, the program had many technical challenges and the program was terminated in 1971 [22, 38].

Although the SST program ceased, NASA continued to fund supersonic transport research at a much smaller scale under the Supersonic Cruise Research (SCR) program for another decade. The aircraft name was changed from SST to High-Speed Civil Transport (HSCT), but the concept remained essentially the same: a 300 passenger, Mach 2.4 airliner [22]. In 1985, supersonic research saw an increase in funding through NASA's High Speed Research (HSR) program. As can be seen

in Table 1.1, NASA was still designing for the same the number of passengers and cruise conditions as they were during the SST and SCR years and technical progress was slow. NASA canceled the HSR program because the aerospace industry was unwilling to invest in an SST with no near term solutions to the technical gaps [38]. In 2000, DARPA funded the Quiet Supersonic Platform (QSP) initiative. Finally, the aviation community began to alter the requirements to a lower number of passengers and slower cruise speeds. Instead of aiming for a 300 passenger SST, the industry's near term goal is a smaller Supersonic Business Jet (SBJ) [103]. The QSP program demonstrated that it is possible to build an efficient SBJ with an acceptable sonic boom [38]. As can be seen
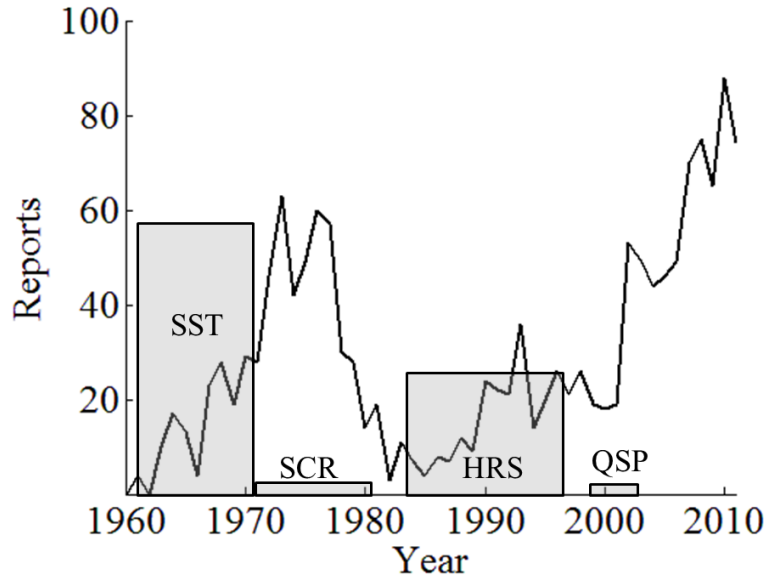
Figure 1.1: Number of AIAA "sonic boom" articles per year and U.S. government supersonic civil aircraft research programs [38, 148].

in Fig. 1.1, since the QSP program ended in 2003, there have been a high number of sonic boom papers despite limited government funding. In 2010, 88 papers were published, the highest annual rate ever, even exceeding the levels during the SST era. This suggests the combination of the easing of the design requirements and the maturing of technology have finally made a supersonic commercial aircraft practical. Currently, there are multiple companies considering producing a supersonic civilian aircraft. However, these commercial ventures are limiting their risk by flying at

Table 1.1: Summary of U.S. Supersonic Civil Transport Research Programs Compared to SBJ [12, 21, 22, 38, 45, 128, 168].

Program	Years	Cost, Billions of 2010 Dollars	Seats	Mach	Altitude, ft
SST	61-71	6.7	300	2.7	62,000
SCR	71-81	0.36	250-300	2.4+	60,000+
HSR	85-99	3.3	300	2.4	–
QSP	01-03	0.041	14	2.0 to 2.4	–
SBJ	N/A	N/A	8 to 15	1.6 to 1.8	–

Mach numbers below 2.0, greatly simplifying the technology required [38, 59, 168, 183]. Images of some designs can be seen in Fig. 1.2.

1.2 Problem Statement

Typically, a sonic boom will reach the surface of the earth as an N-wave, as shown in Fig. 1.3(a). The N-wave is not a desirable shape for a sonic boom because a human on the ground will experience two nearly instantaneous pressure increases caused by the leading and trailing shocks [165]. During the 1960s and 1970s, researchers explored ways to modify the sonic boom pressure wave to have less impact on humans and structures [161]. One approach, as shown in Fig. 1.3(b), is to minimize the overpressure by creating a "flat-top" signature. Another option is to create a maximum-rise-time sonic boom, as shown in Fig. 1.3(c). This pressure signal has a small initial shock pressure rise (ISPR) followed by a gradual increase to the peak overpressure. Although the peak overpressure may be larger than an equivalent flat-top boom, the rise time provides more time for the ear to adjust to the disturbance.

1.2.1 Need for a new design tool

The Jones-Seebass-George-Darden (JSGD) sonic boom minimization process [42] produces cross-sectional area profiles that generate either flat-top or a maximum-rise-time boom, which are essentially modified N-waves. The JSGD minimization process is shown in Fig. 1.4. The user
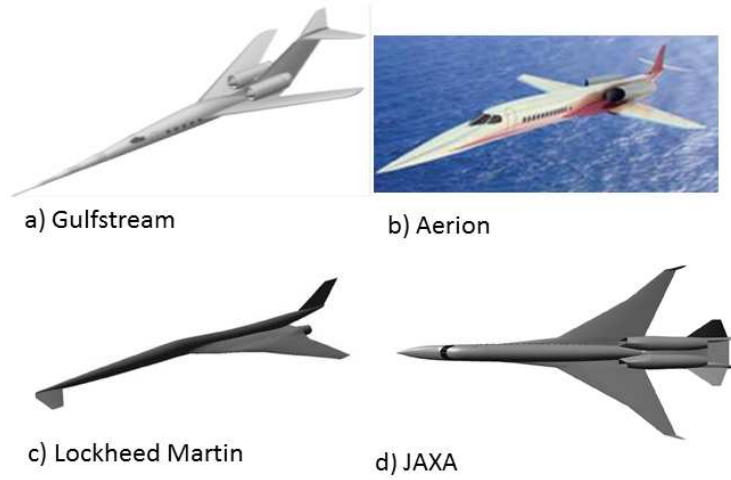
Figure 1.2: Industry SBJ designs, reproduced from Refs. [2, 41, 51, 58].

(a) N-wave

(b) Min. Overpressure

(c) Max. Rise Time

(d) Multi-shock
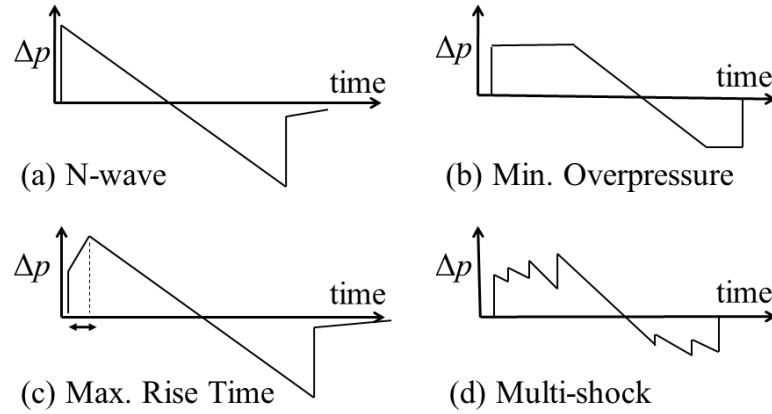
Figure 1.3: Types of sonic booms [42].

selects the altitude, weight, Mach number, nose and overall length, then the software outputs an equivalent area profile. This software is very limited:

- Key steps are left to the designer. The designer tasks are shown in blue in Fig. 1.4. The designer must divide the area into volume and lift. Then, the designer must create an aircraft that meets these area restrictions [51].

- The JSGD process is also restrictive. It assumed that the sonic boom must look like Figs. 1.3(b) or 1.3(c).

- It is a reverse process. It starts with the desired shock shape and works backwards to find an area profile that yields that shape.

- It does not incorporate other design requirements, such as performance (lift-to-drag ratio) or stability. Therefore, if the JSGD process is used in isolation, the design may not be flyable.

Therefore, designing a low-boom supersonic civil aircraft will require new design processes and tools. As further evidence, Peter Coen, NASA's principal investigator for supersonics stated [181]:

> Developing a 3D design approach and validating it both with wind tunnel experiments and, eventually, with larger scale in flight is the number one challenge to supersonic overland vehicle development.

Most current SBJs designs create a multi-shock sonic boom, as shown in Fig. 1.3(d), which prevent the sonic boom from developing into an N-wave. Instead of hearing one large pressure increase, an observer hears many smaller pressure discontinuities. The ISPR is a significant contributor to the subjective loudness rating [40, 106]. As will be demonstrated later, a multi-shock sonic boom has a weaker leading shock; thus it is more acceptable to humans. The multi-shock sonic boom greatly increases the design space and number of variables, requiring new design tools. To avoid the difficulty in adapting an aircraft to an area profile, the design tool should start with an aircraft and adapt its shape to incorporate a low boom strategy. Since the design space has been expanded this design tool should be able to analyze multiple designs quickly.

1.2.2 Need for scaled flight tests

Typically in the preliminary design stage, designers validate key aerodynamic performance parameters by conducting wind tunnel tests [23]. When designing a supersonic civil aircraft, one of the key performance parameters that will need to be validated is the sonic boom ground pressure
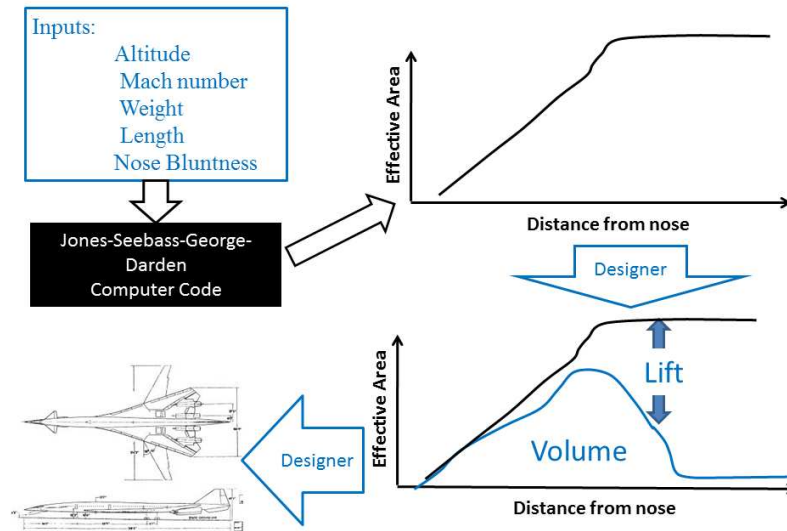
Figure 1.4: The Jones-Seebass-George-Darden process with designer actions in blue [42].

profile. However, wind tunnels are not well suited for this type of testing because the desired measurement location is hundreds of body lengths below the aircraft. Figure 1.5 shows scaled wind-tunnel models, which were made as small as practical (approximately 4/10,000 scale), so pressures could be measured many body lengths away from the model [33, 150]. At these small scales, wind tunnel testing is challenging because manufacturing a properly scaled model is difficult; the measured pressures are small; tunnel vibrations are more pronounced; and, the boundary layer thickness is significant [31, 33]. Furthermore, the test section size limits the propagation distance. For example, the farthest distance tested using the models in Fig. 1.5(a) was 50 body lengths [33], which is far short of the approximately 300 body lengths required to simulate the propagation from a cruising altitude of 60,000 ft to the ground.

In addition to these issues associated with using very small models, wind tunnels are also limited in their ability to replicate the temperature gradients, winds, and turbulence found in the atmosphere [39, 122]. These conditions, as well as molecular relaxation [100], can have significant impact on the measured sonic boom. Therefore, the only feasible solution for design validation is to conduct flight tests. However, there are very few studies that have investigate how to conduct

these scaled test.

1.2.3   Need for complete mission analysis

Most sonic boom minimizations design studies only consider the on-design case; however, in order to be a practical design, a supersonic aircraft must be able to create a quiet sonic boom for a variety of flight conditions. The following is an example taken from Ref. [143] to illustrate the importance of considering the off-design cases. An F-function created by the JSGD method [42] is presented in Fig.1.6(a) (NOTE: Software from Ref. [151] was used with permission from the author). This F-function is for a 120 ft long, 100,000 lb aircraft flying at Mach 1.6 and 60,000 ft. Two ground pressure profiles are presented in Fig. 1.6(b). The baseline case is for a standard atmosphere directly beneath the aircraft. The second case has the same conditions, except that the acoustic advance is increased 50%. This might occur off track where the sonic boom has traveled through more atmosphere than planned. The extra advance causes the sonic boom to distort more than anticipated and the boom becomes an N-wave, doubling the ISPR. This example highlights the fact that off-design flight conditions must be considered when designing a quiet sonic boom aircraft.
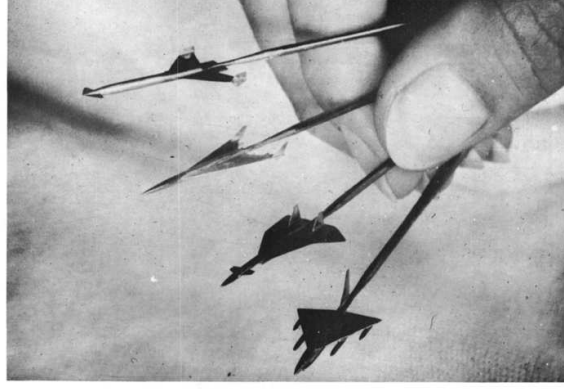
(a) SSTs, reproduced from Ref. [150].
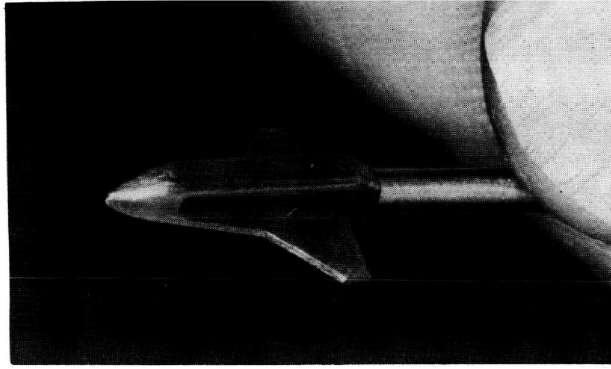
(b) Space Shuttle, reproduced from Ref. [30].

Figure 1.5: Wind tunnel models used for sonic boom testing.

1.3 Design Strategy

This study introduces a design system that fulfills these needs discussed above. The approach uses a tiered system:

- **Tier 1 RapidF:** RapidF is a low-fidelity design tool to be used in the conceptual and preliminary design phases. It outputs a first-order estimate of the sonic boom. However, it is has sufficient detail to produce a realistic sonic boom pressure signature. For example, it includes the effects of the engine plume and boundary layer growth. It is ideal for conceptual design and tradeoff studies when many configurations need to be evaluated. It is fast and simple, requiring a parametric description of the aircraft and can run on a desktop computer in seconds. RapidF is also intuitive: components can be directly linked
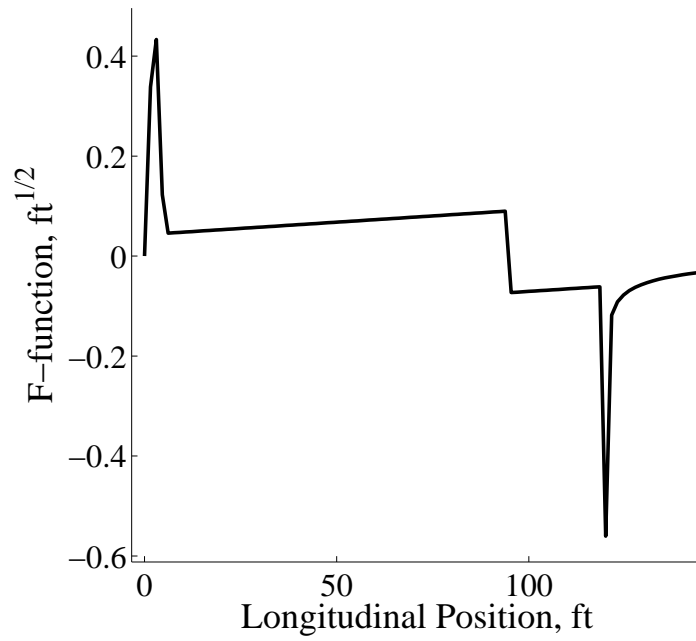
(a) F-function from JSGD method.
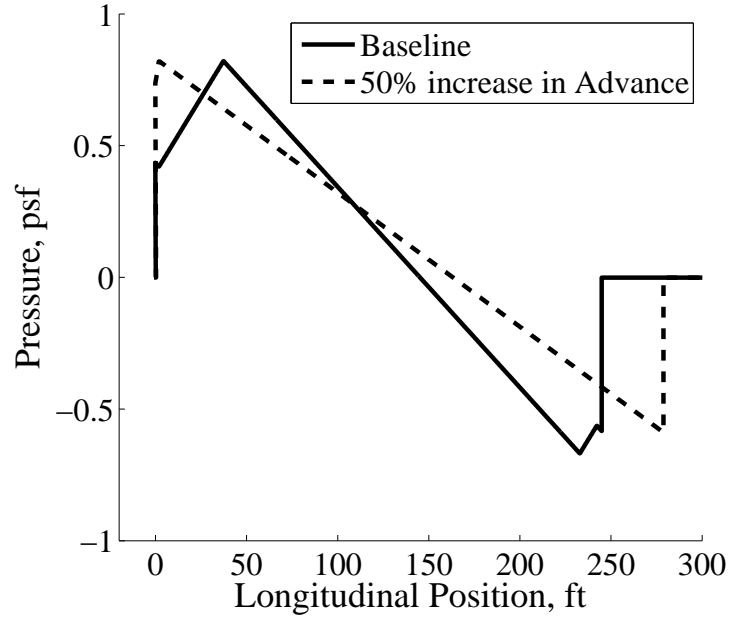
(b) Ground pressure profiles.

Figure 1.6: Off-design example for 120 ft long, 100,000 lb aircraft flying at Mach 1.6, 60,000 ft.

to segments of the sonic boom allowing effective and efficient modifications to the design. To ensure the design also meets aerodynamic and stability requirements, RapidF outputs performance metrics such as lift-to-drag ratio and static margin. Thus, the sonic boom minimization is not conducted in isolation.

- **Tier 2 CFD:** RapidF is based on axi-symmetric, linear theory. Therefore, once the designer has a conceptual design, the sonic boom estimate from RapidF should be validated using CFD. The CFD results may highlight some areas that need to be modified. However, the analysis that was conducted with RapidF should reduce the number of iteration required to tune the low boom design.

- **Tier 3 Scaled Flight Test:** As discussed earlier, it is difficult to experimentally or numerically simulate atmospheric sonic boom propagation. Thus, before entering the detailed design stage flight tests should be conducted.

The combination of RapidF, CFD and scaled flight tests will ensure the design is effective at mitigating the sonic boom and prevent costly re-designs.

1.4   Signature Freezing by F-Function Lobe Balancing

This study will demonstrate how lobe balancing can be used to lower the sonic boom. Lobe balancing is a sonic boom minimization technique that creates a frozen pressure signal by proper shaping of the F-function. The design requires equal and opposite areas of pressure to prevent the sonic boom from coalescing into an N-wave. The concept of lobe balancing has existed since the 1960s when Koegler discussed the concept [101, 102], although he attributed the idea to Whitham [177, 178]. Figure 1.7 depicts a lobe-balanced case, as presented by Koegler, where the wave is propagating to the left. The balancing line is drawn with a slope of $(k\sqrt{r})^{-1}$ which is proportional to the age variable in a homogeneous atmosphere. In principal, lobe balancing is based on the local speed of sound. For example, lobes C and D are balanced. The negative lobe C has a slightly lower speed of sound. Likewise, the positive lobe D has a slightly higher speed of

sound. Without lobe C, lobe D's high local speed of sound would cause it to advance and merge with the leading shock. However, lobe C has a low speed of sound and it will attempt to retreat. Since C and D are equal and opposite, the pair creates an intermediate shock that will remain stationary, or frozen, as long as the lobes remained balanced. Graphically, shock locations can be determined by the equal area rule. Thus, a shock will be located at the infection point between C and D as long as the shaded areas are equal. As propagation distance increases the balancing line will become more horizontal, potentially changing the size of the lobes and upsetting the balance. Koegler stated [102]:

> A question is often raised over the feasibility of keeping such loops nearly equal when the effects of variations in Mach number, level-flight lift coefficient, and trim forces for different flight speeds and altitudes are taken into account. However, an examination of the computed $F(y)$ curves for typical SST vehicles, flying at Mach numbers as far apart as 1.5 and 2.7, showed that the differences between them are less severe than anticipated. Therefore, this approach is believed to be feasible and its ultimate capability for boom reduction is worth exploring.

This study will validate Koegler's hypotheses that lobe balancing is robust, meaning that the lobe-balanced pressure profile is only minimally effected by changes in Mach number, altitude and weight changes.

1.4.0.1   Previous lobe-balancing studies

Despite Koegler's call for further investigation, the concept of lobe balancing remained dormant until 2002 when a team from the University of Colorado investigated lobe balancing's effectiveness of reducing the ISPR using optimization [8, 9, 49–51]. They applied lobe balancing to
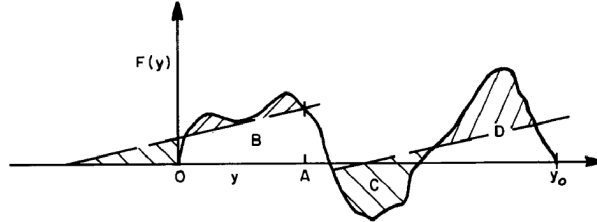
Figure 1.7: Example of a lobe-balanced F-function (reproduced from Ref. [102]).

a Lockheed Martin design by optimizing eight shape parameters while weight, length, lift, and drag were fixed. As shown in Fig. 1.8, the team was able to reduce the strength of the ISPR by 20 fold [49]; however, these results need to be qualified. The optimized pressure signature has an intermediate shock that is much larger than the leading shock. These lobe balancing studies demonstrated the ability of lobe balancing to reduce the overpressure, but also highlight that more than the ISPR needs to be considered.

The present study's implementation of lobe balancing is unique from these studies in several respects. First, the research discussed above applied lobe balancing to an existing design. In contrast, this study will implement lobe balancing at the beginning of the design process. Second, the previous designs did not create a frozen pressure signal. In Fig. 1.8, the interior shock has higher overpressure than the leading shock. Consequently, if the sonic boom were propagated further, it would coalesce with the leading shock, creating an N-wave. Finally, the previous research only minimized the leading shock. As seen in Fig. 1.8, the lobe-balanced design has a slightly higher trailing shock pressure rise (TSPR). This study will apply lobe balancing to both front and rear shocks, and will evaluate a sonic boom based on its ISPR, peak pressure, TSPR, and peak negative pressure. Furthermore, the perceived level of loudness will be compared.
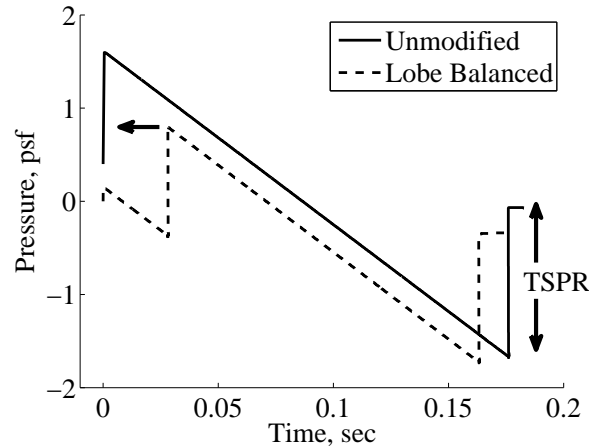
Figure 1.8: Lobe-balanced sonic boom from Ref. [9].

1.5   Assumptions

For the purpose of this study, it is assumed that the user is designing a SBJ, with the design parameters as shown in Table 1.2, based on Ref. [38, 176]. The lower and upper limits represent values that will make implementation dubious. For example, if the cruise altitude is below 49,000 ft, the SBJ will be flying at an altitude utilized by subsonic airlines making FAA deconfliction difficult. Likewise, flying above 65,000 feet will cause problems with radiation exposure and engine emissions. In all cases the researcher attempted to obtain the target quantities.

Table 1.2: Design Requirements [38, 176]

Requirement	Lower Limit	Target	Upper Limit
Mach number	1.2	1.7	2.0
Cruise weight (lbs)	50,000	120,000	200,000
Length(ft)	70	140	160
Altitude (ft)	49,000	51,000	65,000
Passengers	8	8	15
Max. overpressure (psf)	0.0	0.3	1.0
PLdB	0.0	70	75
Lift-to-Drag ratio	7.5	8.0	–

1.6   Overview

This paper shows the development of the tools required for the tiered sonic boom design system and applies them to a lobe-balanced design. Before discussing the design process, Chapter 2 and 3 provide a review of theories applied in the subsequent chapters. Topics include the speed of sound, modified linear theory and acoustic advance. Then, Chapter 4 discusses how RapidF, the Tier 1 software, works and demonstrate the reliability and sensitivity of its calculations. Chapter 5 verifies and validates RapidF by comparing its sonic booms to legacy software, wind tunnel experiments and flight test results. The development of a lobe-balanced aircraft using this software is contained Chapter 6. As stated earlier, a practical low-boom design must be quiet for a variety of flight conditions. Therefore, Chapter 7 looks at the lobe balanced design's sonic boom

with variations in Mach number, propagation angle, altitude and weight. The next two chapters investigate the Tier 3 tool, scaled sonic boom testing. Chapter 8 discusses how a scaled flight tests can be used to create a scaled sonic boom, which can be used to predict the boom from a full-scale aircraft. In order to have a properly scaled test, the user must consider acoustic advance, test vehicle weight, molecular relaxation and the limits of the data acquisition system. Another type of sonic boom flight test is to use the scaled vehicle to prove a certain type of minimization design is effective. These types of flight tests are discussed in Chapter 9. Finally, Chapter 10 looks at a variety of design strategies and proposes a road map for future works. The synergistic conclusions of these chapters is that (1) modified linear theory is very effective for designing sonic boom minimized aircraft and (2) lobe balancing, which is a linear technique, show great potential as a robust minimization strategy.

Chapter 2

BACKGROUND

2.1   The Flow Fields

As a sonic boom pressure wave propagates to the ground it goes through three fields [144], as shown in Fig. 2.1. The near-field is the portion of the flow field from the aircraft to several body length away, where the flow may have large flow deflections, is highly three dimensional and areas of subsonic flow may exist [157]. Additionally, the shocks can be strong; thus, the isentropic assumption used in the mid-field and far-field is not valid. The aircraft shape has a large influence on the pressure profile. Shocks can be attributed to components such as the wings, inlets and canopy. This is in contrast to the far-field where the sonic boom is an N-wave and the information on the aircraft shape has been lost.

Although there is no standard for the end of the near-field, typically 10 body lengths or 1,000 ft is used. At the end of the near-field and the beginning of the mid-field, the pressure profile is quasi axi-symmetric, meaning that there is no cross flow. In this region, the pressure perturbations are weak and disturbance can be analyzed as an acoustical wave. Variations in the local speed of sound, although small, continue to distort the pressure profile. Areas of high pressure have higher speeds of sound and advance toward the front of the signal. Likewise, areas of low pressure will retreat toward the rear of the signal [157]. In other words, the characteristics curve and shocks can merge. Since the shocks are weak, the flow can be assumed to be isentropic and weak shock theory can be used to determine shock locations. The far-field is the region where the sonic boom profile stops changing shape. At this point, all the interior shocks usually have coalesced with the leading
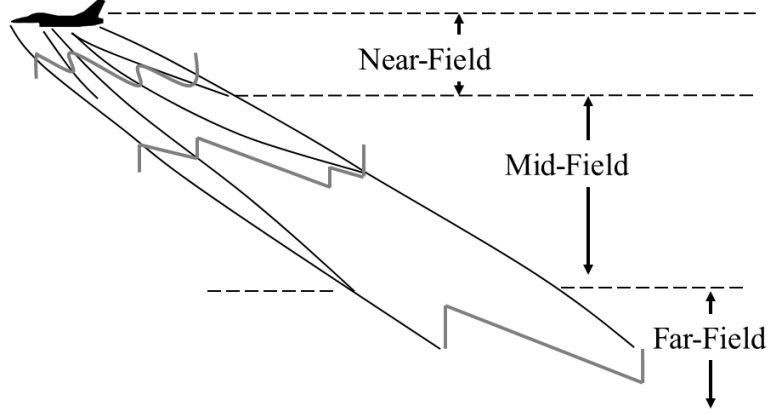
Figure 2.1: The flow fields for sonic boom propagation.

or trailing shock and the boom is an N-wave. For this study a frozen sonic boom is defined as one with stationary interior shocks and does not develop into an N-wave.

2.2   The Speed of Sound

2.2.1   Definition

The most basic equation representing the speed of sound is:

$$a = \sqrt{\rho R T} \tag{2.1}$$

In some aerodynamics text books [5, 17], the speed of sound is derived by starting with the one-dimensional, steady, and isentropic continuity and momentum equations with the velocity being the speed of sound:

$$\rho a = (\rho + d\rho)(a + da) \tag{2.2}$$

$$p + \rho a^2 = p + dp + (\rho + d\rho)(a + da)^2 \tag{2.3}$$

This system of equations is solved by only retaining first order terms resulting in:

$$a^2 = \left(\frac{\delta p}{\delta \rho} \right)_s \tag{2.4}$$

By applying the isentropic assumption and the perfect gas law, Eq. (2.4), can be simplified to Eq. (2.1). However, this development started with the assumption that the wave was propagating at the speed of sound and does not explain why pressure waves propagate at $\sqrt{\delta p/\delta \rho}$.

To understand why Eq. (2.4) defines the speed of sound, the continuity and momentum equations can be used to obtain the wave equation [20]. Before the derivation, some nomenclature is explained. In this section u is the magnitude of the acoustical velocity and is assumed to be small relative to the speed of sound. Since the development is for one dimension, it is implied that u is in the direction of propagation. Also, the subscript '0' will be used to describe quiescent conditions. Other subscripts imply differentiation with respect to the subscripted variable. Starting with the unsteady, one-dimensional continuity equation:

$$\rho_t + (\rho u)_x = 0 \tag{2.5}$$

and assuming a small density change, $\delta \rho = \rho - \rho_0$, this equation becomes:

$$\delta \rho_t + u \delta \rho_x + \rho_0 u_x + \delta \rho u_x = 0 \tag{2.6}$$

Retaining first order terms, this simplifies to:

$$\delta \rho_t + \rho_0 u_x = 0 \tag{2.7}$$

Now, using the inviscid momentum equation of the form:

$$\rho \left(u_t + u u_x \right) + p_x = 0 \tag{2.8}$$

Introducing the small pressure change, δp, associated with $\delta \rho$, this equation becomes:

$$\rho_0 u_t + \rho_0 u u_x \delta \rho u_t u u_x + \delta p_x = 0 \tag{2.9}$$

Again, only keeping the first order terms, it reduces to:

$$\rho_0 u_t + \delta p_x = 0 \tag{2.10}$$

By subtracting the time derivative of Eq. (2.7) from the spacial derivative of Eq. (2.10), yields:

$$\frac{\delta p}{\delta \rho} u_{xx} - u_{tt} = 0 \tag{2.11}$$

By inspection, one can see that this is the one-dimensional wave equation where $\sqrt{\delta p/\delta \rho}$ is the wave speed, justifying naming it as the speed of sound.

2.2.2   Local speed of sound

The previous development discarded higher order terms. As can be seen in Fig. 2.2, each segment of an acoustical wave will have a local speed of sound, based on the local slope of the pressure versus density graph. The variations in an acoustical wave are small; thus, the variations from the ambient speed of sound are also small. Under most engineering applications the difference between the local and ambient speeds of sound only has minor effects, but for a sonic boom the propagation distance is usually large (50,000+ ft) and the cumulative effect becomes significant.

The following is a derivation of the local speed of sound based on Ref. [20]. Using Eq. (2.1) and the isentropic relationships, pressure and density can be expressed as:

$$p = p_0 \left(\frac{a}{a_0} \right)^{\frac{2\gamma}{\gamma - 1}} \tag{2.12}$$

$$\rho = \rho_0 \left(\frac{a}{a_0} \right)^{\frac{2}{\gamma - 1}} \tag{2.13}$$

The one-dimensional, unsteady, and inviscid continuity and moment equations are:

$$\frac{D(\rho u)}{Dt} = 0 \tag{2.14}$$

$$\rho \frac{Du}{Dt} + \nabla p = 0 \tag{2.15}$$

Combining the above four equations to eliminate pressure and density results in:

$$a_t + u a_s + \frac{\gamma - 1}{2} u_s = 0 \tag{2.16}$$

$$u_t + u u_s + \frac{2}{\gamma - 1} a a_s = 0 \tag{2.17}$$

where s is propagation distance (in later discussions s is along the acoustical ray). The solution to this system is:

$$a_u = \pm \frac{\gamma - 1}{2} \tag{2.18}$$

Thus, the local speed of sound for a forward traveling wave is:

$$a = a_0 + \frac{\gamma - 1}{2} u \qquad (2.19)$$

However, this development has ignored higher order terms. To gain insight into the significants of the higher order terms, using the isentropic relation:

$$\frac{p}{p_0} = \left(\frac{\rho}{\rho_0}\right)^\gamma \qquad (2.20)$$

and applying a Taylor series expansion, produces:

$$a = a_0 + \frac{\gamma - 1}{2} u + \frac{\gamma - 1}{6(\gamma - 2)} u^2 + H.O.T. \qquad (2.21)$$

Since the coefficient of the quadratic term is small and u is assumed to be small in this study retaining the first two terms is sufficient.
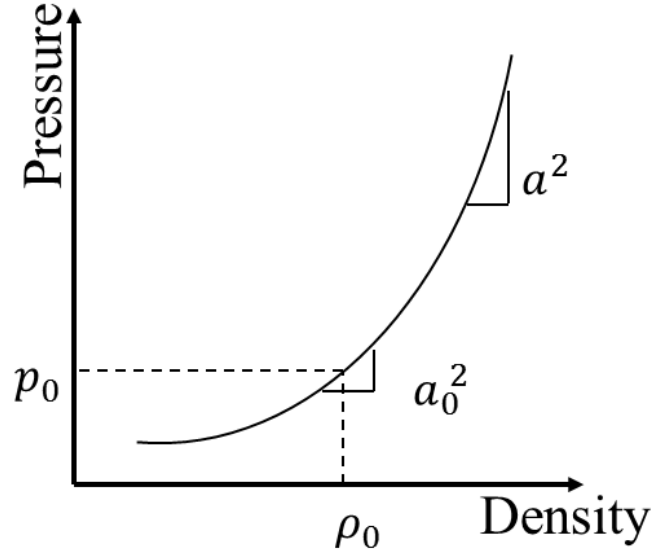
Figure 2.2: Graphical explanation of the speed of sound.

2.2.3   Equilibrium and frozen speeds of sound

In this report, the terms frozen and equilibrium speeds of sound refer to the variation in the speed of sound at difference frequencies. The dependency on frequency is caused by molecular

relaxation [100]. In the previous section the speed of sound was expressed as a function of the local acoustical velocity perturbation (see Eq. (2.19)). The acoustical velocity is proportional the acoustical pressure:

$$u = \frac{\Delta p}{\rho_0 a_0} \tag{2.22}$$

Thus, the local speed of sound can also be thought of as a function of the acoustical pressure. In accordance with the isentropic relationships, the local temperature should follow the changes in acoustical pressure. However, the local temperature will take a finite amount of time to transform the kinetic energy into internal energy. This time is referred to as the relaxation time. Initially, the vibrational mode will be excited, then exponentially decayed as the local temperature adjusts. If the phase of the pressure wave is shorter than the relaxation time, then the local temperature never reaches equilibrium and the local speed of sound is frozen. Thus, the frozen speed of sound is the speed of sound for high frequency waves. In contrast, the equilibrium sound speed is for low frequencies where the signal duration is greater than the relaxation time. For these conditions the local temperature will change with the local pressure; thus each portion of the signal is in thermodynamic equilibrium. The variation in the speed of sound from the equilibrium speed of sound at low frequencies to the frozen speed of sound at high frequencies is small, typically less than 1 ft/sec [100]. However, over long propagation distances, this variation will cause the shocks to smooth and develop into shapes with discrete rise times.

NOTES:

- In some texts the equilibrium sound speed is referred to as the adiabatic sound speed and the frozen sound speed is referred to the isothermal sound speed [20].

- The name frozen and equilibrium speeds of sound have multiple definitions. In some literature, the speed of sound for a calorically perfect gas is referred to as the frozen speed of sound. The equilibrium speed of sounds, is defined for chemically reacting flows [6]. Since this study deals with the atmosphere, which is calorically perfect, these definition of the equilibrium and frozen speeds of sound are beyond the scope of this research.

2.3   Shock Rise Times

The molecular relaxation phenomena discussed in the previous section cause a shock wave to
to have finite rise time [100], which can be estimated as:

$$T_r = \frac{16\rho}{(\gamma + 1)p_s} \left(\tau_{O2}\Delta a_{O2} + \tau_{N2}\Delta a_{N2} \right) a \tag{2.23}$$

where p_s is the shock pressure rise, τ is the relaxation time and Δa is the differences in the
equilibrium and frozen speeds of sound and the subscripts represent oxygen and nitrogen. An
example of rise time as a function of overpressure from Ref. [16] can be seen in Fig. 2.3. These
results are theoretical and for 30% humidity and 295 Kelvin. These results also include absorption
and dispersion effects in addition to molecular relaxation. The causes of shock rise times are not
fully understood and theoretical rise times have consistently under predicted rise times from flight
tests. Humidity and turbulence both strongly effect the rise time and are difficult to quantify.
However, the values used in Fig. 2.3 represent a conservative estimate. Based on this graph, since
this study deals with sonic booms with shock pressures under 1.0 psf and signal durations, in some
cases, less than 20 msec, rise times must be considered.
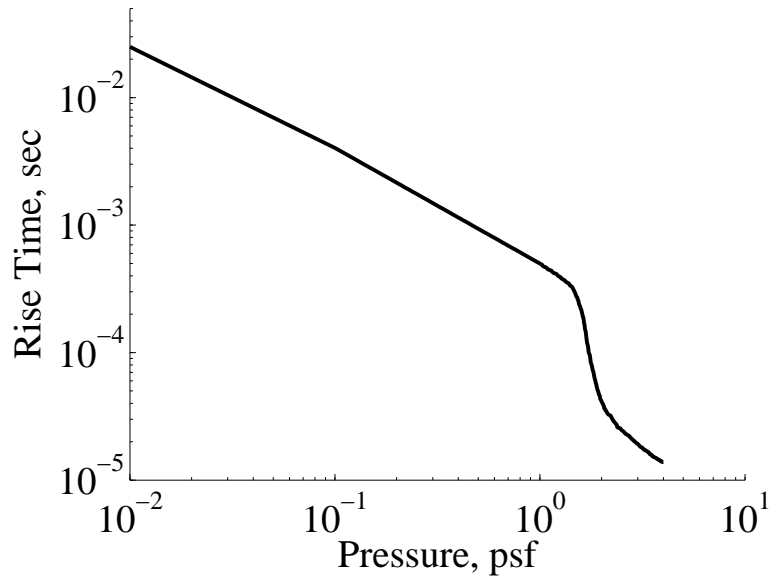
Figure 2.3: Overpressure vs. shock rise time [16].

2.4   Linear Theory

This study implements modified linear theory; therefore, this section contains a brief review of classical linear theory followed by modified linear theory, which adapts linear theory to be applicable to the mid-field and far-field. Although linear theory can be applied to a three dimensional system, since this report uses an two-dimensional axi-symmetric solution, the discussion will focus on this case.

2.4.1   Classical linear theory

An explanation of linear theory can be found in most aerodynamic text books, such as Ref. [109]. A development specific to sonic booms can be found in Ref. [157]. The following is a discussion based on these references, showing how the continuity, momentum and energy equations can be reduced to a single equation with one variable, the velocity potential.

For steady, inviscid, flow the continuity and momentum equations are:

$$\nabla \cdot \rho \bar{V} = 0 \tag{2.24}$$

$$\frac{D\bar{V}}{Dt} - \frac{1}{\rho} \nabla(p) = 0 \tag{2.25}$$

For irrotational flow, the isentropic relationship between state variables closes the system:

$$p = p_\infty \left(\frac{\rho}{\rho_\infty} \right)^\gamma \tag{2.26}$$

The assumption of irrotational or homentropic (constant entropy) flow limits the applicable velocity region to below Mach 3.0 (Since this study is investigating conditions below Mach 2.0, this assumption has limited implications). Using Eqs. (2.1) and (2.24), Eq. (2.25) can be simplified to:

$$\bar{V} \cdot \frac{D\bar{V}}{Dt} - a^2 \nabla \cdot \bar{V} = 0 \tag{2.27}$$

Using the velocity potential:

$$U = \frac{\delta \Phi}{\delta x} = \Phi_x \tag{2.28}$$

$$V = \frac{\delta \Phi}{\delta y} = \Phi_y \tag{2.29}$$

$$W = \frac{\delta \Phi}{\delta z} = \Phi_z \tag{2.30}$$

Substituting the velocity potential into Eq. (2.27) and assuming steady flow produces the velocity potential equation:

$$\left(1 - \frac{\Phi_x^2}{a^2}\right)\Phi_{xx} + \left(1 - \frac{\Phi_y^2}{a^2}\right)\Phi_{yy} + \left(1 - \frac{\Phi_z^2}{a^2}\right)\Phi_{zz} - \frac{2\Phi_x\Phi_y}{a^2}\Phi_{xy} - \frac{2\Phi_x\Phi_z}{a^2}\Phi_{xz} - \frac{2\Phi_y\Phi_z}{a^2}\Phi_{yz} = 0 \tag{2.31}$$

The speed of sound is not a constant in the above equation. Therefore, the energy equation is used to obtain an expression for the local speed of sound. The energy equation:

$$c_p T + \frac{1}{2}|\bar{V}|^2 = const. \tag{2.32}$$

can be transformed to find the local speed of sound:

$$a^2 = a_0^2 - \frac{\gamma - 1}{2}(|\bar{V}|^2) \tag{2.33}$$

or in terms of the velocity potential:

$$a^2 = a_0^2 - \frac{\gamma - 1}{2}\left(\Phi_x^2 + \Phi_y^2 + \Phi_z^2\right) \tag{2.34}$$

By substituting the above expression into Eq. (2.31), one obtains one equation for one unknown, the velocity potential. It is valid for any irrotational, steady flow.

An axi-symmetric velocity profile is introduced by using perturbations:

$$U = |\bar{V}_\infty| + |\bar{V}_\infty|u \tag{2.35}$$

$$V = |\bar{V}_\infty|r = v \tag{2.36}$$

with the associated potentials:

$$u = \phi_x \tag{2.37}$$

$$v = \phi_r \tag{2.38}$$

Notes:

- Unlike the previous section, here u is used as the velocity perturbation in the x-direction.

- u is a non-dimensional quantity. Some text books, such as Ref. [7], develop the linear equations with a dimensional perturbation.

Using these perturbation equations and Eq. (2.34), Eq. (2.27) can be expressed in cylindrical coordinates as:

$$
\begin{aligned}
\phi_{rr} + \frac{v}{r} - (M_\infty^2 - 1)\phi_{xx} =& M_\infty^2 \left((\gamma + 1)\phi_x + \frac{1}{2}(\gamma + 1)\phi_{xx} + \frac{1}{2}(\gamma - 1)\phi_r^2 \right) \phi_{xx} \\
&+ M_\infty^2 \left((\gamma - 1)\phi_x + \frac{1}{2}(\gamma - 1)\phi_x^2 + \frac{1}{2}(\gamma + 1)\phi_r^2 \right) \phi_{rr} \\
&+ M_\infty^2 \left((\gamma - 1)\phi_x + \frac{1}{2}(\gamma - 1)(\phi_x^2 + \phi_r^2) \right) \frac{\phi_r}{r} \\
&+ M_\infty^2 \left(\phi_x \phi_r + \phi_r \right) \left(\phi_{xr} + \phi_{rx} \right)
\end{aligned}
\tag{2.39}
$$

The above is the axi-symmetric perturbation velocity equation. It can be simplified by making two restrictions: 1) The perturbations are small ($u \ll 1$ and $v \ll 1$) and 2) the flow is not transonic or hypersonic. Applying these restrictions, all the right hand side terms are small compared to the left handed terms and can be ignored and Eq. (2.39) becomes:

$$
\phi_{rr} + \frac{\phi_r}{r} - \beta^2 \phi_{xx} = 0
\tag{2.40}
$$

where the Prandtl-Glauert coefficient is:

$$
\beta = \sqrt{M_\infty^2 - 1}
\tag{2.41}
$$

To summarize the assumptions taken to up to this point, linear theory is a first order solution to a steady, irrotational and isentropic flow field with small perturbations. Furthermore, in order to eliminate terms, the flow was assumed not to be transonic nor hypersonic. Linear theory is widely used to obtain first-order approximation of surface pressures and aerodynamic forces on aircraft. It has consistently compared well to experimental data [7].

2.4.2   Modified linear theory

Linear theory, as presented above, cannot predict the flow field far from a supersonic source, which is the location of concern for sonic boom minimization research, because the theory fails to

account for nonlinear effects. Modified linear theory, pioneered by Whitham [178], enabled linear theory to be used in the far-field. Now, linear theory is *modified* to by applicable to regions away from the surface. The solution to Eq. (2.40) is a source strength such that:

$$\phi = \int_0^{x-\beta r} \frac{-f(\zeta)}{\sqrt{(x-\zeta)^2 - \beta^2 r^2}} d\zeta \tag{2.42}$$

This can be shown by substituting Eq. (2.42) into Eq. (2.40). By defining the characteristics as:

$$y = x - \beta r \tag{2.43}$$

and assuming $f(0) = 0$ and that $\beta r \gg y$, the velocity perturbations can be expressed as:

$$u = \frac{-1}{\sqrt{2\beta r}} \int_0^y \frac{f'(\zeta)}{\sqrt{y-\zeta}} d\zeta \tag{2.44}$$

$$v = -\beta u \tag{2.45}$$

Using the energy equation, Eq. (2.34) and isentropic relationships, Eq. (2.12), it can be shown that a first order approximation for the pressure perturbation is:

$$\Delta p = -\gamma p_\infty M_\infty^2 u \tag{2.46}$$

Now by defining the F-function:

$$F(y) = \int_0^y \frac{f'(\zeta)}{\sqrt{y-\zeta}} d\zeta \tag{2.47}$$

The solution can be simplified to:

$$u = -\sqrt{\frac{2\beta}{r}} F(y) \tag{2.48}$$

$$v = \sqrt{\frac{\beta}{2r}} F(y) \tag{2.49}$$

$$\Delta p = \frac{\gamma p_\infty M_\infty^2}{\sqrt{2\beta r}} F(y) \tag{2.50}$$

It is important to note that because the axial distance, r, is in the denominator of these equations, they can only be applied away from the surface or near the nose ($\beta r \gg y$).

2.4.2.1   Boundary conditions

The last piece of information needed to complete the solution is the boundary conditions. Evaluating Eq. (2.45) near the surface and assuming a slender body ($R \approx 0$):

$$v|_{body} = \frac{f(x)}{r} \tag{2.51}$$

solving for f(x):

$$f(x) = R \ v|_{body} \tag{2.52}$$

Since the flow must be tangent to the body at the surface:

$$R' = \frac{v|_{body}}{1 + u|_{body}} \approx v|_{body} \tag{2.53}$$

Combining the above two equations, the source strength can be defined based off of the surface geometry:

$$f(x) = RR' \tag{2.54}$$

Using the cross sectional area associated with R:

$$S = \pi R^2 \tag{2.55}$$

and by differentiation:

$$S' = 2\pi RR' \tag{2.56}$$

Combining Eqs. (2.54) and (2.56):

$$f(x) = \frac{1}{2\pi} S' \tag{2.57}$$

Finally, by differentiation:

$$f'(x) = \frac{1}{2\pi} S''(x) \tag{2.58}$$

which can be substituted into Eq. (2.47), which provides a method for calculating the F-function:

$$F(y) = \int_0^y \frac{S''(\zeta)}{\sqrt{y - \zeta}} d\zeta \tag{2.59}$$

This last equation will be referred to as Whitham's F-function equation. Results from this equation can be used in Eqs. (2.48 – 2.50) to describe the flow field. However, it requires S' and S'' to be

continuous. In summary, the F-function was derived by assuming that the source strength is zero at the nose and the body is slender. Additionally, modified linear theory is only applicable to areas where $\beta z \gg y$.

Whitham initially limited his theory to axi-symmetric, non-lifting objects. However, later he [179] and Walkden [174] expanded the theory to include non-axisymetric and lifting surfaces, respectfully, which was experimentally validated by Carlson [31]. These advancements will be discussed in detail in the next chapter. In general, these researchers added the equivalent area due to lift to the equivalent area from volume to produce the total equivalent area:

$$S_{\text{eq}}(y) = S_L(y) + S_V(y) \tag{2.60}$$

Area due to lift, S_L, is the cumulative lift in units of area:

$$S_L(y) = \frac{\beta \cos \phi}{2q} \int_0^y L(\zeta)d\zeta \tag{2.61}$$

Area due to volume, S_V, is the physical cross-sectional area calculated at the Mach angle. The total effective area at each station is the sum of the two areas. Using this now complete modified linear theory Jones was able to calculate the lower bounds of sonic booms [91].

2.4.2.2   Characteristics

Reflecting back, the goal of modified linear theory is to enable linear theory to be applied to the far field. Whitham concluded that linear theory correctly predicts the density, pressure and velocity perturbations away from the body; however, the characteristics, $y = x - \beta r$, do not correct for acoustic distortions. Thus, a non-linear term is added to account for curvature [178]:

$$y = x - \beta r + k\sqrt{r}F(y) \tag{2.62}$$

where:

$$k = \frac{(\gamma + 1)M^4}{\sqrt{2\beta^3}} \tag{2.63}$$

The F-function has multiple applications. In Eqs. (2.48 – 2.50), it is used to describe the perturbations. Now, it also describes how the characteristics curve, as shown in Fig. 2.4. Since each

characteristic curves at its own rate related to its F-function value, characteristics can intersect. When two characteristics merge, a shock forms. The method to determine the location of these intersections and shocks is the subject of the next section.
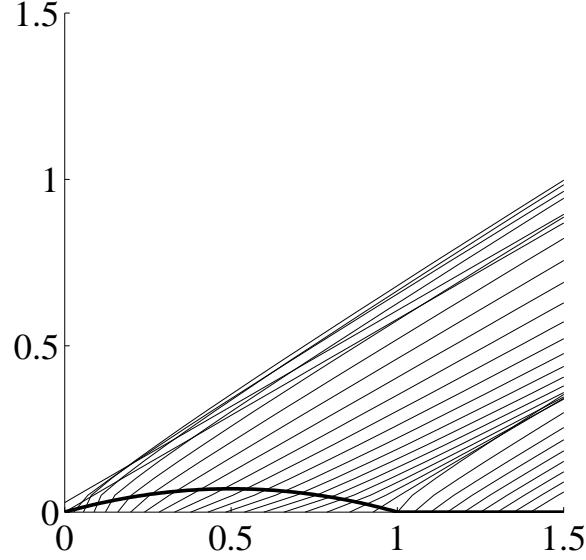
Figure 2.4: Example of characteristics from an elliptical body.

2.4.2.3   Weak shock theory

Weak shock theory provides a method to account for when characteristics merge [141]. A different perspective of the characteristics curving (Fig. 2.4) is shown in Fig. 2.5. A location with a large F-function (high pressure and acoustical velocity) has a relatively higher speed of sound, which causes it to advance faster relative to other segments of the pressure signal. After the signal has traveled down the acoustic ray, a perturbation that was at ξ_1 will be at ξ_2:

$$\xi_2 = \xi_1 - \tau F(y) \tag{2.64}$$

The amount of distortion is quantified in the age variable, τ. Using Eq. (2.62), for a homogeneous atmosphere:

$$\tau_{homo} = \frac{k\sqrt{r}}{c_0} = \frac{(\gamma+1)M^4}{c_0\sqrt{2\beta^3}}\sqrt{r} \tag{2.65}$$
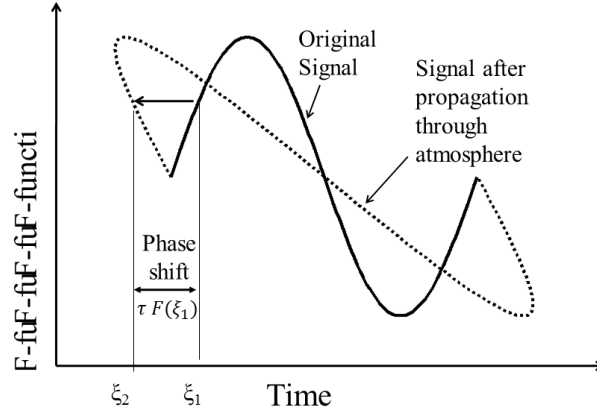
Figure 2.5: Signal distortion caused by variations in the F-function.

Without any correction, this causes one location to have multiple pressure values, which is physically impossible. The correct pressure value can be determined by weak shock theory. If two characteristics merge, a shock is formed which has a slope equal to the average of the merging slopes. In other words, when two areas of supersonic flow are in contact with each other, a shock forms with a wave speed that is the average of the two regions' wave speeds. This is analogous to the shock speed in a shock tube problem. Graphically, the shock location can be determined by the *equal area rule* as shown in Fig. 2.6 which ensures that each phase has only one pressure value. Since the age variable is a function of the radial distance, r, as the sonic boom propagates to the ground the age variable increases causing the pressure profile to stretch further to the left, which causes the location of the balancing line(s) to move. This process causes the interior shocks to move toward the leading edge and ultimately the pressure signal developing into an N-wave.

2.5   Geometric Acoustics

Modified linear theory, as presented by Whitham, did not account for atmospheric variations. Thus, researchers such as Hayes [70], George [61], McLean [127], and Seebass [159, 160], spent the 1960s adapting modified linear theory for a non-homogeneous atmosphere. By assuming the atmosphere is isothermal, they could use exponential equations for pressure and density. This assumption allowed analytical integration and enabled them to quantify the acoustic distortion due
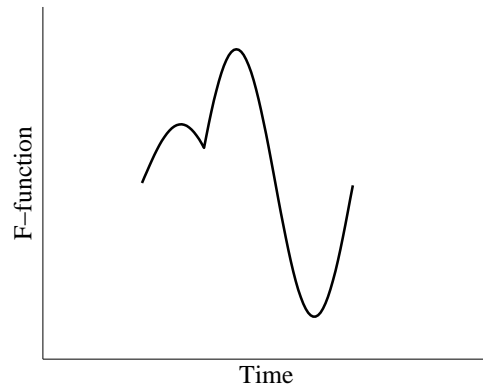
(a) Initial signal.
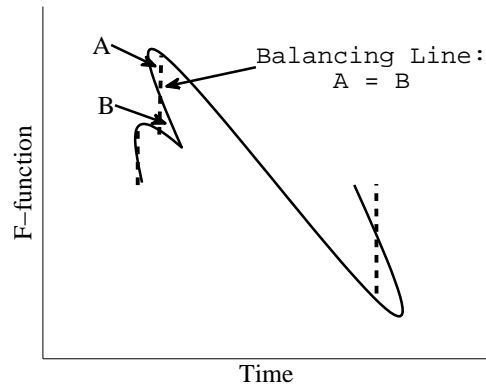
(b) Signal after propagating.
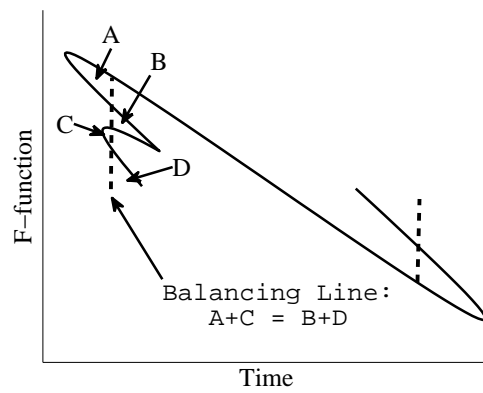
(c) Signal after further propagation.

Figure 2.6: Equal area rule.

to advance in an isothermal atmosphere.

In 1969, Hayes [72] made a major breakthrough in sonic boom research when he published his Aeronautical Research Association of Princeton (ARAP) computer code based on geometric acoustics, which applies the well-developed theory of geometric optics (diffraction, reflection, and refraction) to an acoustical problem. Hayes did not originate this concept, but his code was the first computer code to properly use geometric acoustics to model sonic boom propagation [148]. A comparison of the modified linear theory and geometric acoustic point of view can be seen in Fig. 2.7. For modified linear theory, the reference frame is fixed to the aircraft and one calculates the characteristics from the aircraft to the ground. With geometric acoustics the reference frame is fixed to the ground and one tracks the sonic boom created from one instant in time, by calculating its propagation through ray tracing [160]. Geometric acoustics can easily account for atmospheric changes. Since Hayes' code is numerical, not analytical, each numerical step in the atmosphere can have unique parameters (winds, temperature, density and pressure) [72]. Geometric acoustics is not valid in the near-field because in order for it to be valid, the wave length, the aircraft length, must be smaller than the propagation distance. Therefore, modified linear theory is still used to generate the F-function and to predict the distortion in the near-field. At the end of the near-field (approximately 10 body lengths away from the aircraft), ARAP begins geometric calculations and propagates the boom to the surface [44].

2.6   Acoustic Advance

As was shown in Fig. 2.5, areas of high pressure have a slightly higher speed of sound, which causes them to advance faster relative to other segments of the sonic boom. Whitham quantified the age variable for a homogeneous atmosphere (Eq. (2.65)). However, Hayes' age variable is much more robust because it accounts for winds, temperature and density variations [72]. The following is a development of the age variable which quantifies the cumulative effect of the nonlinear term in Eq. (2.19). The geometry used in this development can be found in Fig. 2.8. The deviation from
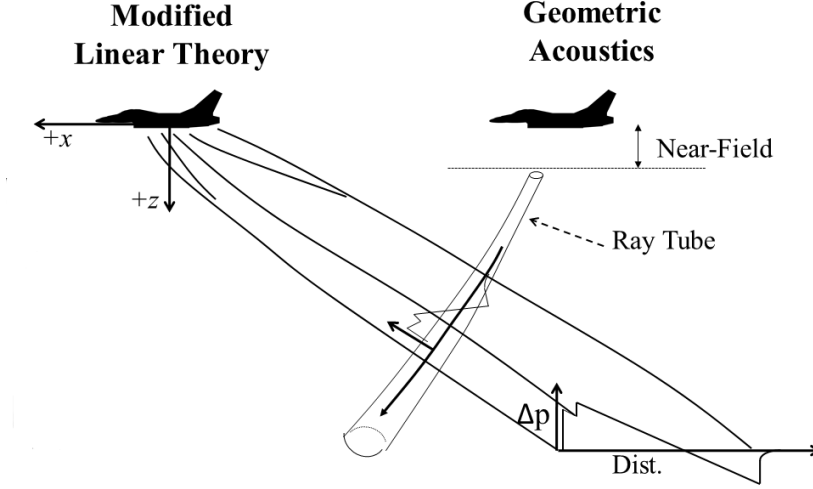
Figure 2.7: Modified linear theory and geometric acoustics frames of reference [160].

the ambient speed of sound from Eq. (2.19) is:

$$\Delta a = \frac{ds}{dt} = a - a_0 = \frac{\gamma + 1}{2}\Delta u \tag{2.66}$$

Here the "Δ" is used to emphasis it is the acoustical velocity, not the velocity perturbation in the x-direction. To convert from distance along the ray to time, the non-linear term is divided by the inverse of the ray's wave speed:

$$\frac{d\xi}{dt} = \left(\frac{ds}{dt}\right) / \left(\frac{ds}{d\xi}\right) = \frac{\gamma + 1}{2}\frac{\Delta u}{c_0 \cos\theta} \tag{2.67}$$

To convert the denominator to altitude:

$$\frac{d\xi}{dz} = \frac{d\xi}{dt}\frac{dt}{dz} = \frac{d\xi}{dt}\frac{1}{a\sin\theta} = \frac{\gamma + 1}{2}\frac{\Delta u}{ac_0 \cos\theta \sin\theta} \tag{2.68}$$

The next step is to find the perturbation velocity in terms of the F-function at the aircraft. The perturbation velocity, see Eq. (2.22), can be combined with the Blokhintsev invariant:

$$\frac{\Delta p^2 A}{\rho a} = \text{const.} \tag{2.69}$$

to obtain the velocity as a function of the pressure at the start of the acoustic ray (indicated by the subscript '1'):

$$\Delta u = \sqrt{\frac{A_1}{A\rho_1 a_1 \rho a}} \Delta p_1 \tag{2.70}$$

Using the linear theory equation for pressure, Eq. (2.50):

$$\Delta u = \sqrt{\frac{A_1}{A\rho_1 a_1 \rho a}} \frac{\gamma p_\infty M^2}{\sqrt{2\beta z_1}} F(y) \tag{2.71}$$

Substituting this back into Eq. (2.68) and integrating gives the age variable:

$$\tau = \frac{(\gamma+1)M^2}{2c_0} a_1 \cos\theta_1 \sqrt{\frac{\rho_1}{2}} \int_0^{gnd} \frac{1}{a\sqrt{(\cos\theta \sin\theta)^3 \rho A}} dz \tag{2.72}$$

If a calm and homogeneous atmosphere, this equation simplifies to Eq. (2.65). After the distortion is calculated from this equations, the location of shocks can be determined from the equal area rule discussed earlier.
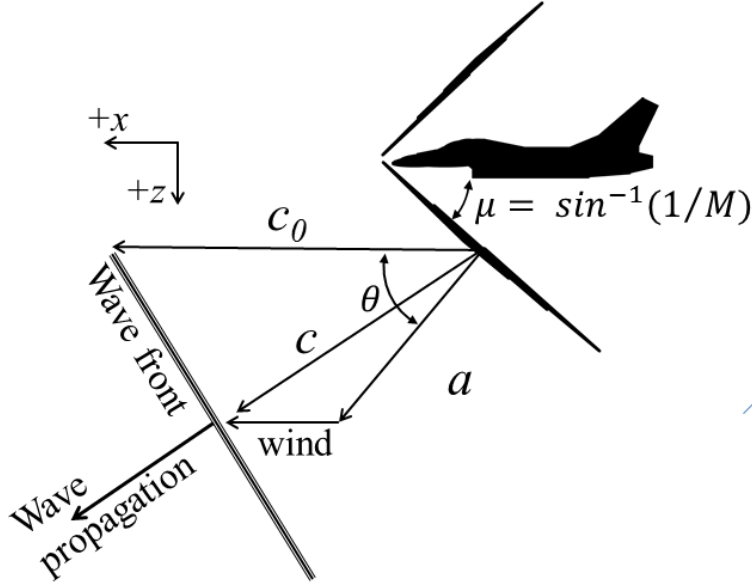
Figure 2.8: Geometry for sonic boom propagation [72].

Chapter 3

MODIFIED LINEAR THEORY APPLIED TO AN AIRCRAFT

This chapter discusses adaptations to modified linear theory in order to make it applicable to finding an *aircraft's* F-function. Two historical articles are reviewed. First, Whitham's 1956 paper which found an equivalent axi-symmsteic area for non-axi-symmetric component is introduced. Then, Walkden's 1958 paper which found an equivalent area that simulates the pressure due to lift is discussed. Based on the shortcomings of these two papers, a more straight forward approach is used to find the equivalent area and due to lift and the domain of influence. Finally, based on these topics, the method used to *slice* the aircraft used in RapidF is presented. With the slicing angles defined, the F-function for any propagation angle can be determined.

In general, an aircraft geometrical description of an aircraft can be converted into an F-function. In order to do so, the cross-sectional area needs to be converted to an equivalent axi-symmetric area. Likewise, the lift at each longitudinal location needs to be determined, and then, transformed to an equivalent area via procedures from Walkden [174] and summed with the physical area. Then, this total area distribution is converted to an F-function, by a Eq. (2.59). This chapter focuses on how to obtain the axi-symmetric, equivalent area and lift distributions.

3.1   Whitham 1956: Non-axi-symmetric Components

Whitham's 1952 paper [178] on modified linear theory was limited to axi-symmetric non-lifting projectiles. In 1956, he adapted his theory to a non-lifting wing [179] based on the geometry shown in Fig. 3.2. He concluded that the wing can be replaced by an "equivalent body of revo-

lution." This method has been widely used in sonic boom research and is used in RapidF. The geometry used can be found in Fig. 3.3 with example results in Fig. 3.4.

In order to calculate the equivalent area, Whitham defines constructions lines, such as QR in Fig. 3.1, which are *parallel to the leading edge.* He then calculates the wing's cross sectional area at each slice and projects that area onto a plane perpendicular to the streamwise direction. Referring to Fig. 3.2(a), the independent variable used to describe the leading edge is η, the distance from centerline in the y-direction and the dependent variable is $l(\eta)$, the x-coordinate. As shown in Fig. 3.2(b), Whitham says, "The wavefront is the surface generated by PM as P moves along AB." This is a significant statement since section AB is the region of the leading edge that is *supersonic.*
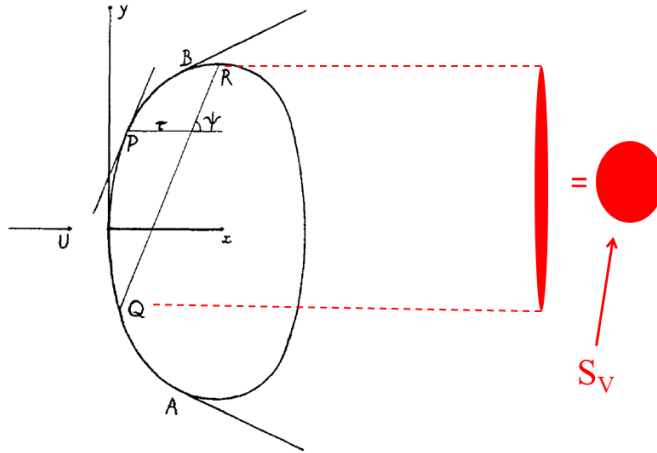
Figure 3.1: Top view of wing used by Whitham, reproduced from Ref. [179].

By assuming the aircraft is in the $z = 0$ plane, the Mach cone is defined as:

$$(x - l(\eta))^2 = \beta \left((y - \eta)^2 + z^2 \right) \tag{3.1}$$

By taking the derivative and rearranging:

$$\frac{l'(\eta)}{\beta} = \frac{\beta(y - \eta)}{(x - l(\eta))} \tag{3.2}$$

Whitham says, "The latter is the equation of a plane through $(l(\eta), \eta)$ parallel to the z axis and
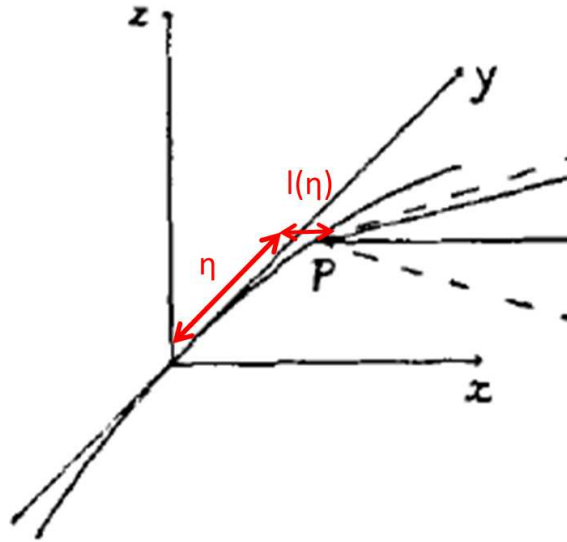
(a) Axis system.
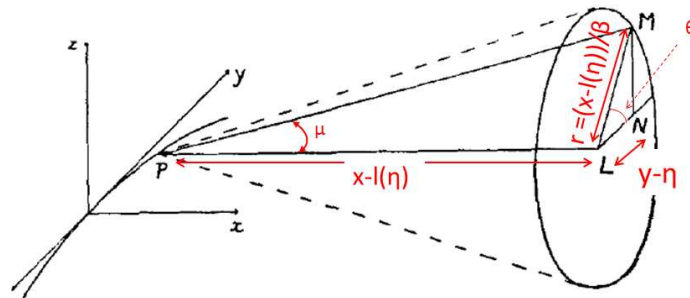
(b) Far-field geometry.

Figure 3.2: Whitham's geometry and nomenclature, reproduced from Ref. [179], red text added by author.
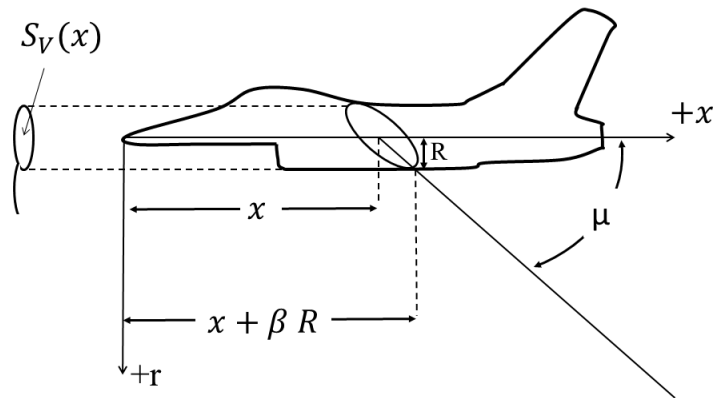
Figure 3.3: Slicing to determine equivalent area.

(a) Profile view with F-function overlayed.

(b) Cross-sectional areas.
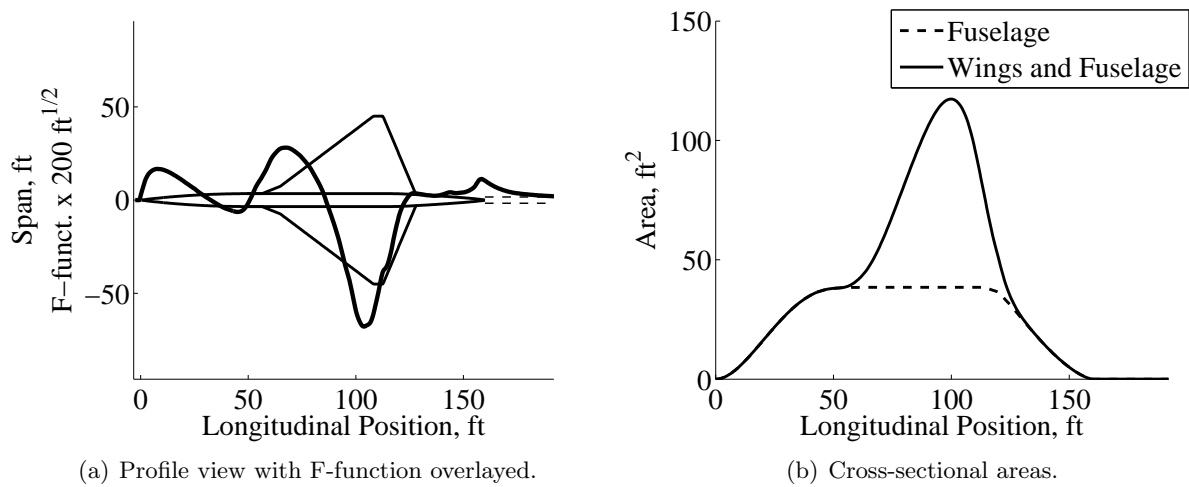
Figure 3.4: Example of wing's equivalent area.

making the angle $tan^{-1}(l'(\eta)/\beta^2)$ with the x axis. This plane is shown as PNM." See Fig. 3.2(b) for clarification. He creates a coordinate system:

$$x = x$$

$$y = \eta + r\cos\theta$$

$$z = r\sin\theta$$

$$\tau = x - l(\eta) - \beta r$$

where τ is the distance behind the leading edge as shown in Fig. 3.1. The potential from the wing is:

$$\phi_p(x, y, z) = -\frac{1}{\pi} \int \int \frac{Z_x(x_i, y_i)}{\sqrt{(x - x_i)^2 - \beta^2 \left((y - y_i)^2 + z^2\right)}} dx_i dy_i \tag{3.3}$$

- **NOTE:** In this chapter a 'p' subscript is added to emphasis the term is a potential to avoid confusion with ϕ the propagation angle.

Z_x is the change in thickness with respect to x. Although he acknowledge that the limits of integration is the intersection of the $z = 0$ plane with the upstream Mach cone from point M with coordinates (x, y, z), he uses his constructions lines parallel to the leading edge. He arrives at the F-function using a similar process as was done in Selection 2.4.2 of the previous chapter:

$$F(\tau) = \frac{1}{2\pi} \int_0^\tau \frac{S_V''(\zeta)}{\sqrt{\tau - \zeta}} d\zeta \tag{3.4}$$

Thus, any non-symmetric body can be replaced with an equivalent axi-symmetric body with equal cross-sectional area. Although, Whitham was concerned with a wing, this formula has been applied to any non-axi-symmetric component such as canopies, engine inlets, etc.

3.2   Walkden 1958: Equivalent Area due to Lift

Wings generate lift by creating a pressure differential between the top and bottom of the wing. These pressure perturbations, like the pressure change caused by a fuselage cross-sectional area change, contribute to the near-field and the far-field pressure profiles. Walkden adapted modified linear theory to account for these pressure changes caused by lift [174]. He quantified an equivalent area that would generate the same pressure profile as the lift. Using superposition this value can be added to the equivalent area due to thickness from the previous section to get the total effect of the wing as shown in Fig. 3.5:

$$S_{\text{eq}}(\zeta) = S_V(\zeta) + S_L(\zeta) \tag{3.5}$$

with the associated F-function:

$$F_{\text{aircraft}}(\tau) = \frac{1}{2\pi} \int_0^\tau \frac{S_{\text{eq}}''(\zeta)}{\sqrt{\tau - \zeta}} d\zeta \tag{3.6}$$

Walkden's geometry is shown in Fig. 3.6, which is essentially the same as Whitham's. Walkden used the flat plate potential:

$$\phi_p(x,y,z) = \frac{1}{4\pi} \int \int \frac{z(x-x_i)}{(y-y_i)^2 + z^2} \frac{c_L(x_i,y_i)}{\sqrt{(x-x_i)^2 - \beta^2\left((y-y_i)^2 + z^2\right)}} dx_i dy_i \qquad (3.7)$$

to show the wing's lift can be represented as an equivalent body of revolution:

$$S_L(t) = \frac{\beta\cos\phi}{2} \int_0^t \int_{\beta_{W1}}^{\beta_{W2}} c_L(\alpha, \beta_W) d\beta_W d\alpha \qquad (3.8)$$
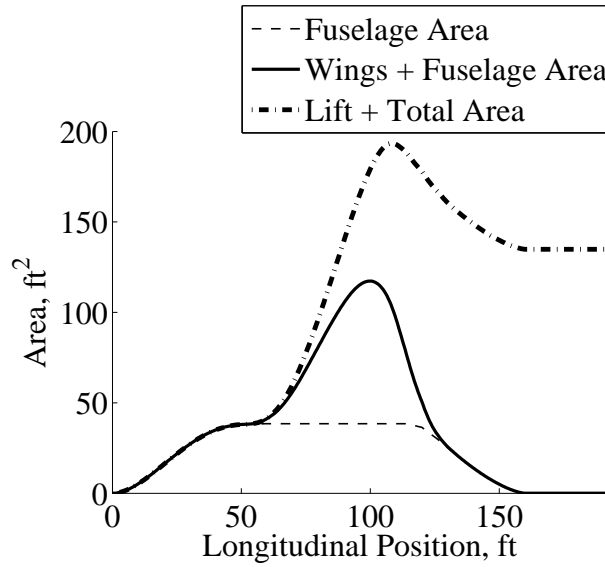
Figure 3.5: Example of lift's equivalent area [174].

- **NOTE:** Whitham and Walkden used the variable B for the Prandtl-Glauert coefficient of compressibility, $\sqrt{M^2 - 1}$ and Walkden used β for a wing coordinate. In this report β is the Prandtl-Glauert coefficient and β_W is Walkden's wing coordinate.

Like Whitham, Walkden uses construction lines parallel to the leading edge. Also consistent with Whitham, Walkden assumed a supersonic leading edge, or the domain is limited to the portion of the wing with a supersonic leading edge (see pages 173 to 174 of Ref. [174]). Walkden states that the geometry is such that: $l'(\eta) = \beta\sin\phi$. Since $\beta = 1/\tan\mu$, this can be arranged to:

$$\frac{l'(\eta)}{\beta^2} = \tan\mu\sin\phi \qquad (3.9)$$
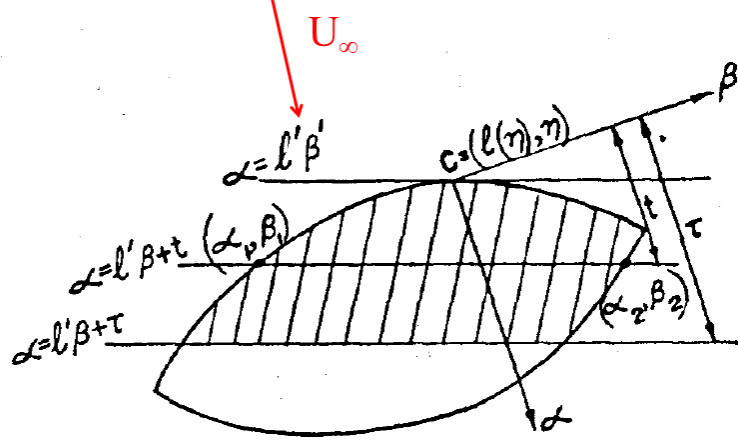
Figure 3.6: Walkden's domain of integration [174].

This is comparable to Whitham's Eq. (3.2). Both methods are dependent on the leading edge geometry. This is undesirable and motivation to find a less restrictive method. The following is a list of concerns about Whitham's and Walkden's approaches:

- **Issue #1**: Using Whitham's logic, the region of the wing outboard of A or B in Fig. 3.2 which has a subsonic leading edge does not contribute to the sonic boom. In other words, Whitham's procedures are not valid for wings with subsonic leading edges such as ones with strakes. Although a subsonic leading edge will not generate an attached shock, it will create a pressure disturbance that may develop into a shock away from the aircraft. The subsonic section of the wing does contribute to the far-field pressure profile and cannot be ignored. Also, strictly following his theory there is no process to incorporate the effects of irregular components without a leading edge, such as a canopy.

- **Issue #2**: Slicing the wing with lines parallel to the leading edge was done so that these

slices approximated the intersection of the Mach cone with the aircraft, as will be demonstrated later. However, in the modern computer age, this simplification is not longer required, but it must be replaced with a theoretically-correct procedure.

3.3 Modernization of Whitham and Walkden

3.3.1 Equivalent area due to lift

The following is a derivation of the wing's equivalent body of revolution using the potential for a wing *without* thickness. The potential is essentially the same as Wakden's [112]:

$$\phi_p(x, y, z) = \frac{1}{4\pi} \int \int \frac{z(x - x_i)}{(y - y_i)^2 + z^2} \frac{\Delta C_p(x_i, y_i)}{\sqrt{(x - x_i)^2 - \beta^2((y - y_i)^2 + z^2)}} dy_i dx_i \qquad (3.10)$$

where:

$$\Delta C_p = \frac{p_{lower} - p_{upper}}{q} \qquad (3.11)$$

and the limits of integration are defined by the area of influence, discussed in the next section. As can be seen in Fig. 3.7:

$$r^2 = (y - y_i)^2 + z^2$$

$$\frac{-z}{r} = \cos\phi$$

$$\frac{x - x_i}{r} = \frac{-z}{r \tan\theta_1} = \frac{\cos\phi}{\cos\phi \tan\mu} = \beta$$

Using these relationships, Eq. (3.10) simplifies to:

$$\phi_p(x, y, z) = -\frac{\beta}{4\pi} \cos\phi \int \int \frac{\Delta C_p(x_i, y_i)}{\sqrt{(x - x_i)^2 - \beta^2 r^2}} dy_i dx_i \qquad (3.12)$$

Since modified linear theory's definition of a potential is [178]:

$$\phi_p = \int \frac{-f(x_i)}{\sqrt{(x - x_i)^2 - \beta^2 r^2}} dx_i \qquad (3.13)$$

by comparing the two above equations:

$$f(x_i) = \frac{\beta}{4\pi} \cos\phi \int \Delta C_p(x_i, y_i) dy_i \qquad (3.14)$$

Thus, by differentiation:

$$f'(x_i) = \frac{\beta}{4\pi} \cos\phi \frac{d}{dx}\left(\int \Delta C_p(x_i, y_i) dy_i\right) \tag{3.15}$$

Substituting Eq. (3.15) into the F-function equation, Eq. (2.47):

$$F_L(x) = \frac{\beta}{4\pi} \cos\phi \int_0^x \frac{\frac{d}{dx}\left(\int \Delta C_p(x_i, y_i) dy_i\right)}{\sqrt{x - \zeta}} d\zeta \tag{3.16}$$
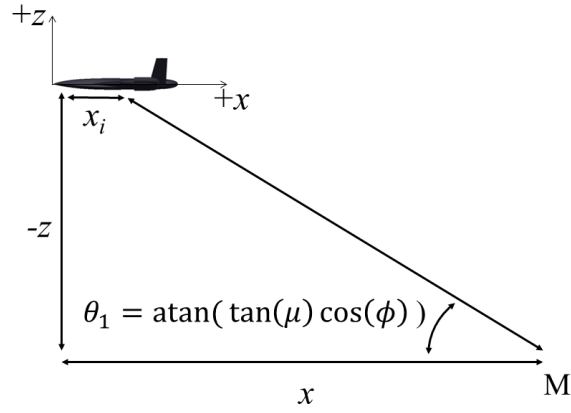
(a) Side view.
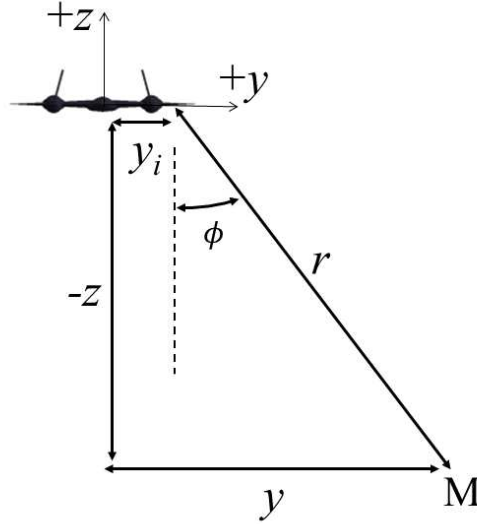
(b) Rear view.

Figure 3.7: Geometry for velocity potential.

Let:

$$S_L''(x_i) = \frac{\beta \cos \phi}{2} \frac{d}{dx} \left(\int \Delta C_p(x_i, y_i) dy_i \right) \tag{3.17}$$

Then, the F-function becomes:

$$F_L(x) = \frac{1}{2\pi} \int_0^x \frac{S_L''(\zeta)}{\sqrt{x - \zeta}} d\zeta \tag{3.18}$$

By integrating Eq. (3.17) twice:

$$S_L(x) = \frac{\beta \cos \phi}{2} \int \int \Delta C_p(x_i, y_i) dy_i dx_i \tag{3.19}$$

This equation is consistent with Walkden's Eq. (3.8). However, there is no restriction on leading edge geometry. In order to further simplify the equation, ΔC_p can be replaced by L/q:

$$S_L(x) = \frac{\beta \cos \phi}{2q} \int \int L(x_i, y_i) dy_i dx_i \tag{3.20}$$

3.3.2   Aircraft slicing

The range of integration of Eq. (3.20) needs to be specified. The domain of influence, or "zone of influence" as Hayes called it [68], is the region of the flow field that can effect the conditions at the location of interest. The limits of integration are the boundaries of the domain of influence. Thus, instead of specifying the limits, the slicing angles are found that represent the border of the domain of influence. In supersonic flow the governing equations are hyperbolic, thus the domain of influence is a forward Mach cone from the point of interest. For example, the domain for point M on a wing is shown in Fig. 3.8(a). For this case, the aircraft and the point of interest lie in the same plane and the cone can be reduced to a triangle. For sonic boom analysis, the location of interest is thousands of feet below to the aircraft. This location may be directly beneath the flight path, $\phi = 0$ as in Fig. 3.9(a), or to the side as shown in Fig. 3.9(b).

First consider the case where M is directly under the aircraft. Assuming the aircraft is in the $z = 0$ plane, the region of influence is the intersection of the Mach cone from point M with this plane, as shown in Figs. 3.8(b). The horizontal slicing angle is shown in Fig. 3.10(a). Although the intersection is a hyperbola, because the location of interest is far away, the slice can be approximated
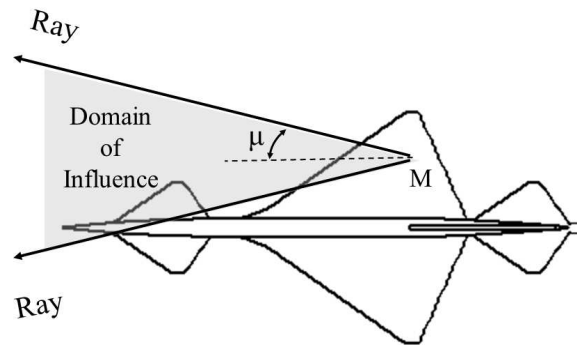
(a) For point M on the wing.
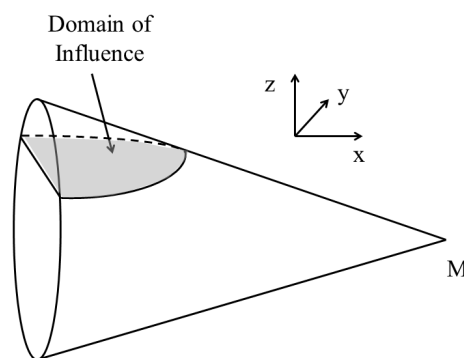
(b) When point M is beneath the aircraft.

Figure 3.8: Domain of influence for supersonic flow.

as a straight line. The hyperbola varies less than 1.0 ft over a 150 wingspan when M is 1,000 below the aircraft. As shown in Fig. 3.11, the vertical slicing angle is:

$$\theta_1 = \mu - AoA \tag{3.21}$$

Thus, in order to determine the pressure at point M beneath the aircraft, one must slice the aircraft with a plane that is defined by $\theta_1 = \mu - AoA$ and $\theta_2 = 0$ and calculate the influence of the geometry forward of the plane. To get the complete pressure profile a series of slices need to be taken as shown in Fig 3.12.

If point M is is to the side, then the geometry is as shown in Fig. 3.9(b). The vertical cutting
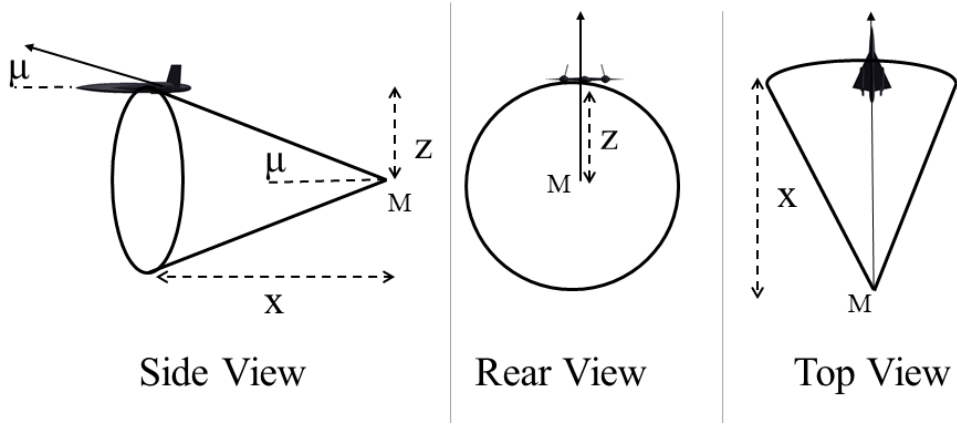
(a) Location of interest directly beneath aircraft.
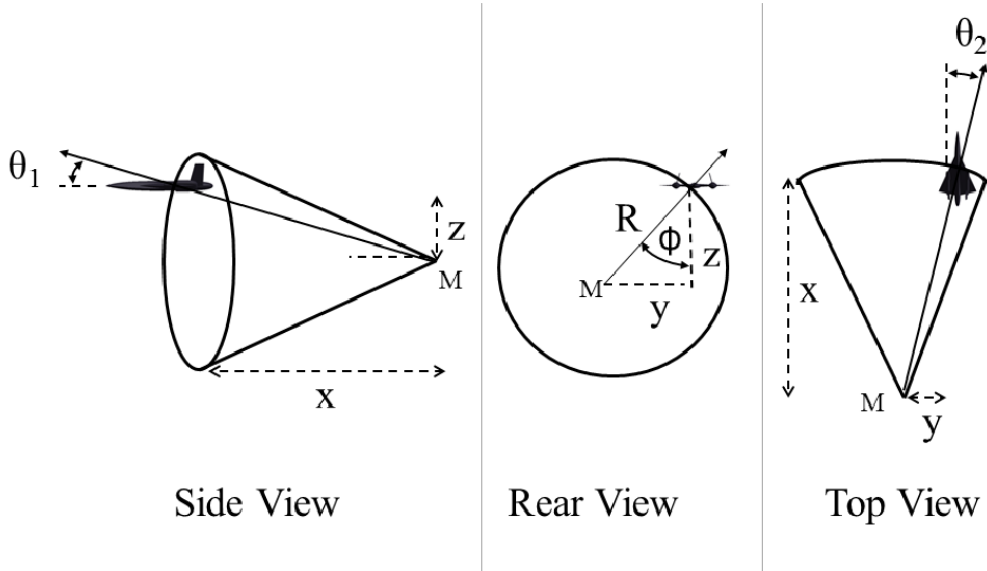
(b) Location of interest is beneath and offset to the side.

Figure 3.9: Geometry to determine domain of influence.

angle is now:

$$\theta_1 = \tan^{-1}\left(\cos\phi\tan\left(\mu - AoA\right)\right) \tag{3.22}$$

As shown in Fig. 3.10(b), the horizontal cutting angle is:

$$\theta_2 = \tan^{-1}\left(\sin\phi\tan\left(\mu\right)\right) \tag{3.23}$$

By using $\beta = 1/\tan\mu$, this angle is consistent with Whitham's angle of $tan^{-1}(l'(\eta)/\beta^2)$ from Eq. (3.2), and Walkden's Eq. (3.9), but makes no restrictions on the leading edge geometry. Thus, this process can be applied to any aircraft component and resolves Issues #1 and #2. A summary
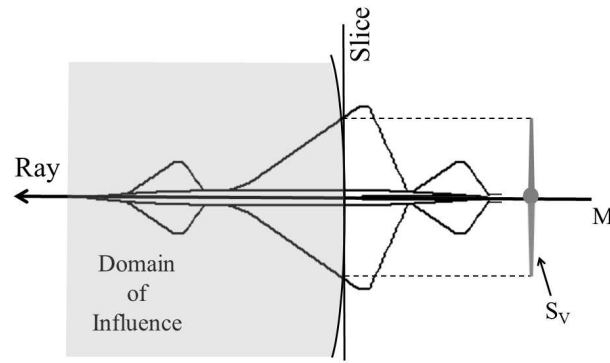
(a) Location of interest directly beneath aircraft.
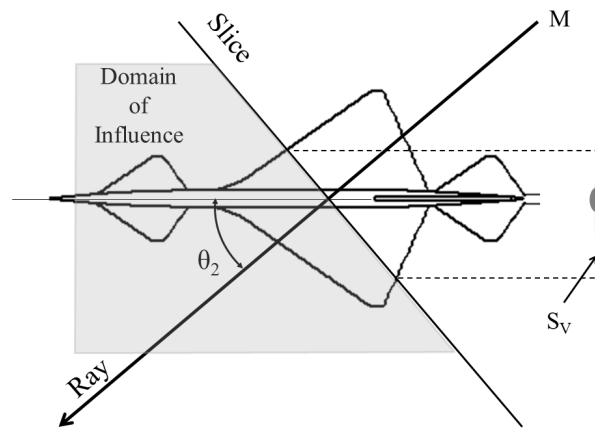
(b) Location of interest is offset to the side.

Figure 3.10: Horizontal slicing geometry.
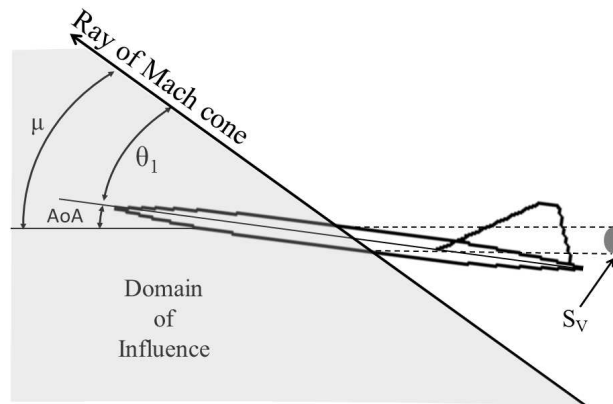
Figure 3.11: Vertical slicing geometry.
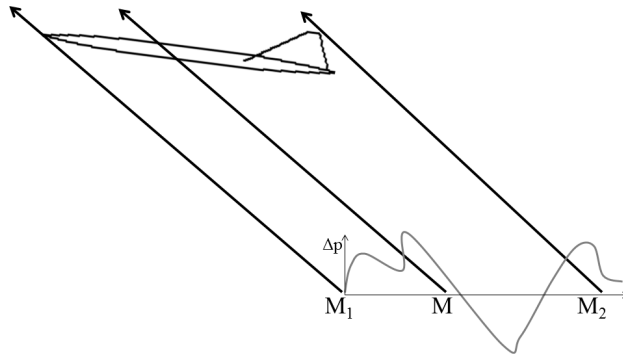
Figure 3.12: Series of slices used to obtain the far-field pressure profile.

of these angles is shown in Fig. 3.13. For example, a supersonic business jet flying at Mach 1.7 and 51,000 ft, has a Mach angle of 36.0^o. The limit of its sonic boom carpet is $\phi = 51^o$ and for this case, $\theta_1 = 22.7^o$ and $\theta_2 = 29.0^o$. RapidF accounts for the slicing angles in the following manner.
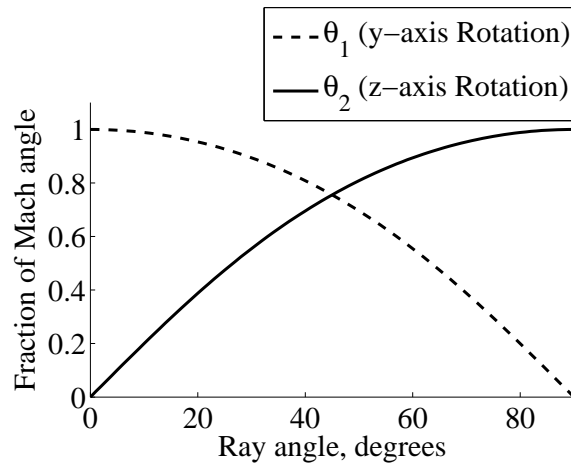
Figure 3.13: Slicing angles as functions of the propagation angle.

Since, lifting surfaces are slender, RapidF slices wings, canards and horizontal tails at θ_2. Based on the above discussion, lifting surfaces should also be sliced at θ_1 as shown in Fig. 3.14. The wing should be cut at the Mach angle to obtain A_1, then this area should be projected into the plane

perpendicular to the freestream to obtain S_V. However, airfoil thickness changes gradually with respect to the downstream direction. Therefore, the vertical displacement from the centerline, A_2 is a good approximation for S_V. Thus, to simplify computations and enable fast processing, lifting surfaces are not cut at θ_1. Likewise, vertical components are sliced at θ_1, but not θ_2. Its airfoil thickness is used to approximate its horizontal thickness. For asymmetric components, such as the fuselage, S_V is constant for all slicing angles and requires no special procedures for side propagation cases. Slicing the aircraft as describe and summing the lift along that slice is the same as the interior integration of Eq.(3.20). After this slicing, this equation simplifies back to Eq. (2.61).
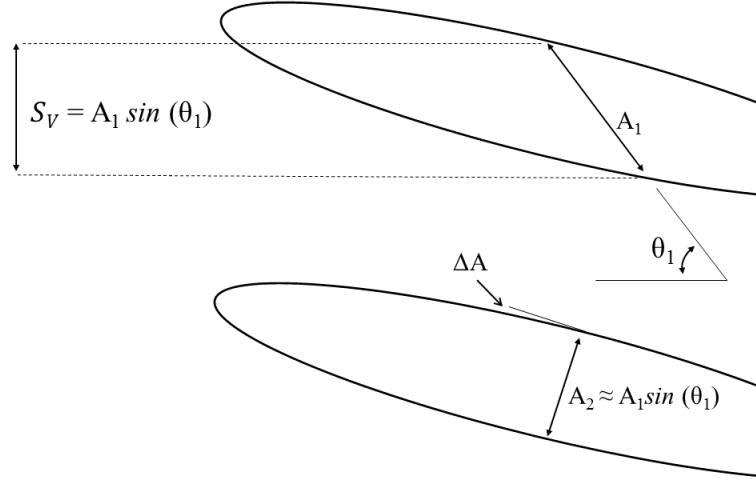
Figure 3.14: Simplification in vertical cut.

Chapter 4

RAPIDF DESIGN TOOL

4.1   RapidF Description

This chapter describe how RapidF works and demonstrate its sensitivity and grid convergence. RapidF is a conceptual and/or preliminary design tool based on modified linear theory and is used to incorporate sonic boom minimization early in the design process. Given a parametric aircraft description, RapidF predicts the design's sonic boom. It also calculates key performance metrics, such as lift-to-drag ratio and static margin, allowing the user to assess the aerodynamic efficiency and sonic boom mitigation simultaneously. Since RapidF is used as a conceptual design tool, it must be fast, and thus, low fidelity so that many designs can be compared in a short period of time. However, it must also be accurate so that the designer can properly evaluate a configuration. The focus of this chapter is to demonstrate the accuracy of its sonic boom estimate. First, how RapidF converts an aircraft description into an axi-symmetric area distribution is discussed. Then, the F-function calculation method used is presented. Finally, the accuracy and sensitivity of the numerical methods are analyzed.

RapidF is based on the assumption that the aircraft geometry can be resolved to an equivalent axi-symmetric volume and lift profile along the aircraft's longitudinal axis. The program accepts design inputs and flight parameters as shown in Table 4.1. An example input file can be found in Appendix A. Once each component has been resolved into an axi-symmetric equivalent area profiles, then the F-function can be found using methods discussed in the next section.

Table 4.1: Summary of Inputs into RapidF Program

Fuselage	Surfaces	Engine	Flight Conditions
Diameter	Location	Location	Mach number
Length	Leading edge sweeps (2)	Length	AoA
Diameter changes	Trailing edge sweeps (2)	Radius	Altitude
Nose type	Chord and span	Internal/external	Weight
Nose length	Airfoil shape	Pressure ratio	
Boat tail type	Lift curve slope	% Spillage	
Boat tail length	$AoA_{L=0}$	TSFC	
	Twist	Thrust	
	Incidence angle	Weight	

4.2   Component build-up

4.2.1   Fuselage

Given the fuselage inputs from Table 4.1, an area vs. distance profile is created. Alternatively, the fuselage shape may be read from a file. Once the fuselage is fully defined, it is sliced at θ_1 as shown in Fig. 3.11 to obtain the equivalent area, S_V. Fuselage lift is estimated by [53, 109]:

$$L = 2q_\infty \ AoA \ \pi \bar{R}_f^2 \tag{4.1}$$

The lift is distributed over the fuselage based on the local radius.

4.2.2   Lifting and non-lifting planar surfaces

Lifting and non-lifting surfaces, like the vertical tail, are evaluated using the same process. The planform shape is determined by the chord, span and sweeps. The thickness distribution is created by multiplying the airfoil shape by the local chord. The thickness of the surface that overlaps the fuselage is set to zero, for example see Fig. 4.1(a). This thickness distribution is cut by θ_2, as was shown in Fig. 3.10, to obtain the local equivalent area. Theoretically, the slicing should also take θ_1 into account. However, as was previously discussed since airfoils are slender and have gradual shape changes, the local thickness is a good approximation for S_V. If the component is oriented vertically, it is sliced vertically was shown in Fig. 3.11.

RapidF offers several methods to calculate the lift distribution. The simplest option is to determine the lift coefficient based on the wing planform and leading edge sweep [154]. If the leading edge is subsonic then the lift curve slope is:

$$c_{L\alpha} = \frac{2\pi AR}{2 + \sqrt{4 + AR^2 \left(2\pi/c_{l\alpha}\right)^2 \left(1 + \tan^2\Lambda_t/\beta^2\right)}} \frac{S_{exp}}{S_{ref}} 1.07 \left(1 + \frac{2\bar{R}_f}{b}\right)^2 \tag{4.2}$$

and if the leading edge is supersonic:

$$c_{L\alpha} = \frac{4}{\beta} \tag{4.3}$$

With the lift curve slope, the lift can be found:

$$L = c_{L\alpha}(AoA + i)q_\infty S_{ref} \tag{4.4}$$

This lift is evenly distributed over the component's exposed area. If the component has twist it is treated as a local increase in the lift coefficient. Alternatively, linear theory, singularity-distribution method can be used [32], an example of which can be seen in Fig. 4.1(b). This method was added to increase the accuracy of RapidF. However, it provided minimal improvement and dramatically increased run times. For example, distributions for both methods can be seen in Fig. 4.2 along with the resulting ground pressure signatures. Since the singularity-distribution method offers no clear advantage, the homogeneous lift distribution was used in in this thesis. However, it is fully operational and available for future studies. Regardless of how the lift distribution is calculated, it is then sliced as shown in Fig. 3.10 to resolve it to a lift distribution along the aircraft centerline.

4.2.3   Engines

Engines can have a significant effect on sonic booms. There are three major ways that engines can impact the sonic boom:

(1) Cross sectional area increase from the nacelle and plume

(2) Interference lift

(3) Shielding of shocks

(a) Thickness distribution.

(b) Lift distribution.
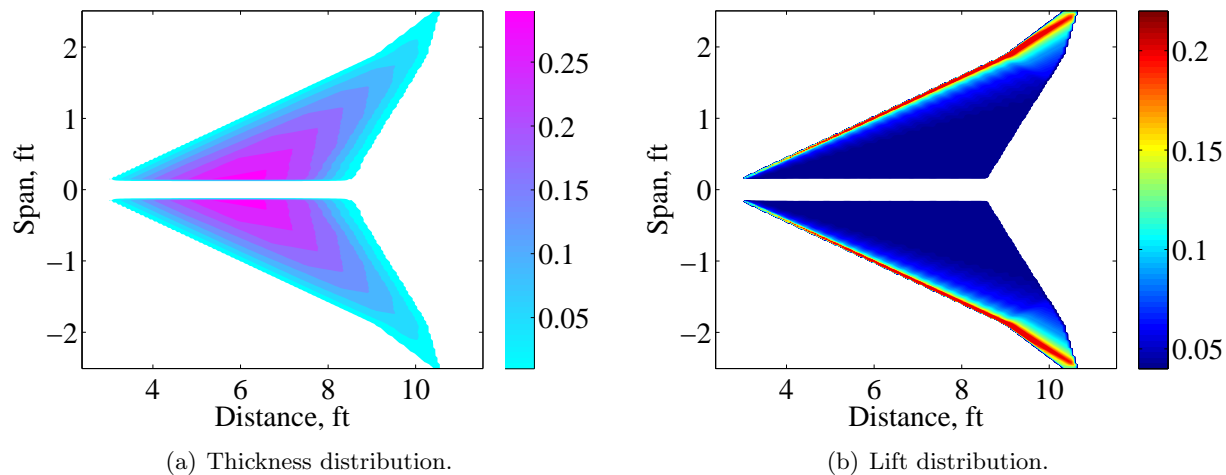
Figure 4.1: Lifting surfaces in RapidF.

(a) Homogeneous lift.

(b) Panel method lift.
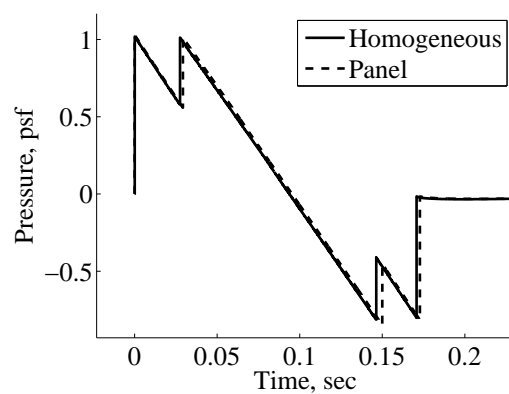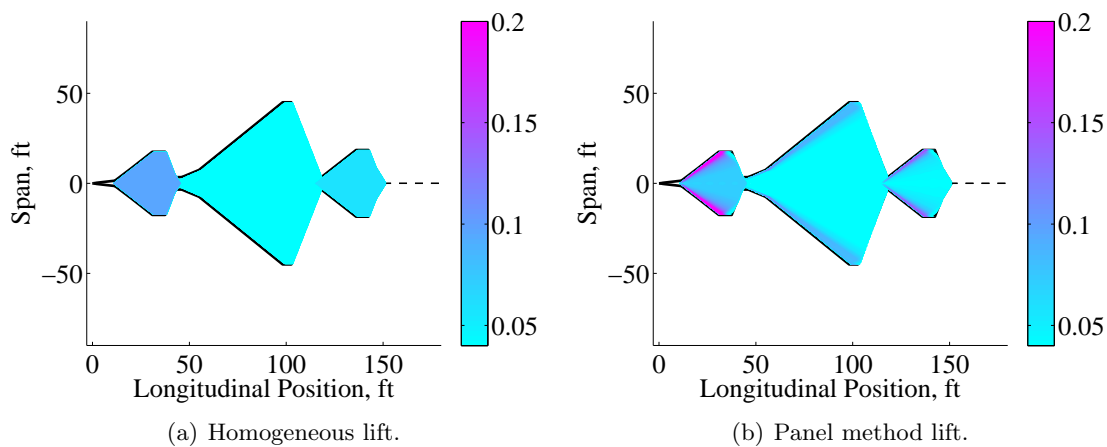
(c) Ground pressures.

Figure 4.2: Comparison of RapidF's lift calculating methods.

The first two items have been incorporated into RapidF.

The cross sectional area of the engines is handled as shown in Fig. 4.3. Engine nacelles are modeled as cylinders which are user defined by the radius and length. To model the plume, the user can select one of four nozzle pressure ratios, 3.9, 4.7, 9.7 and 25.7. The exhaust plume shape is then calculated based on data from Ref. [25]. The stream tube area that passes through the engine does not effect the area profile and is subtracted off [31, 151]. Finally, the engine area is sliced at θ_1 to obtain S_V of the engines, as shown in Fig. 4.4. If the engines are externally mounted, lift is calculated in the same manner as the fuselage.

The exhaust plume shape will vary based on the specific engine and flight conditions. Therefore, this method is a low fidelity way of capturing plume effects. Although the pressure ratios are numerical inputs, they should be thought of as: "over expanded, perfectly expanded, under expanded and very under expanded." Despite, the low fidelity model, Fig. 4.5, demonstrates that they show the same trends as CFD studies. In general, an under expanded plume forces the flow to turn a bigger angle, creating a stronger trailing shock.
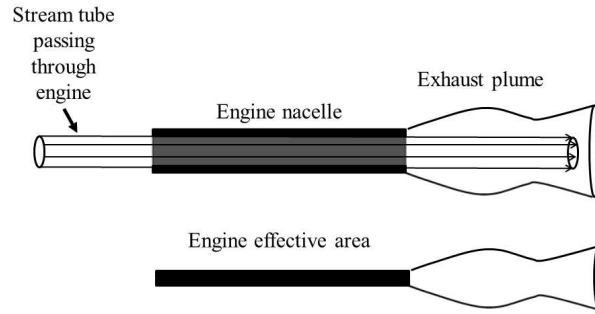
Figure 4.3: Estimating the engine equivalent area.

The interference lift created by the engines is caused by the local change in pressure from the inlet shock. If the engines are located under the wings, the areas of high pressure after the inlet has a favorable effect of creating lift. RapidF estimates this lift using a procedure from Mack [114]. This method finds the F-function from the engine nacelle and plume. Then a local increase in the
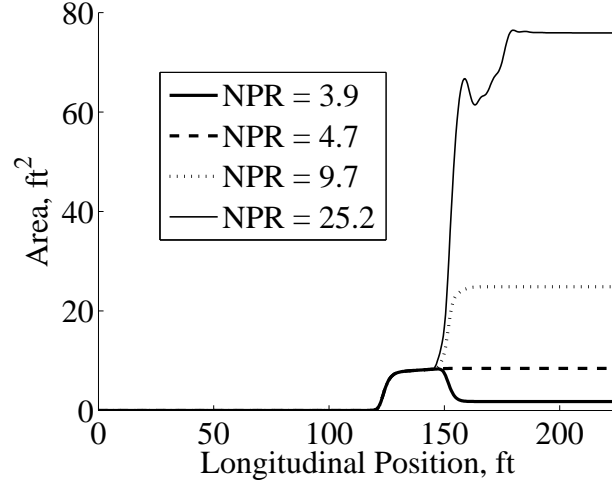
(a) Engine equivalent areas.
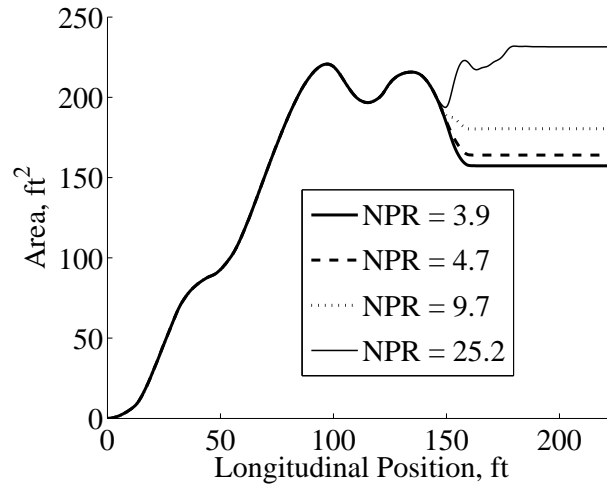
(b) Total equivalent areas.

Figure 4.4: Equivalent areas for various nozzle pressure ratios.

pressure coefficient is determined:

$$\Delta C_L(x, r) = \sqrt{\frac{8}{\beta r}} F_{engine}(x - \beta r) \tag{4.5}$$

This lift coefficient is added to the local lift coefficient determined from the wing lift subroutine. An example of the interference lift can be seen in Fig. 4.6. Clearly, the engines can have a significant impact on the lift distribution, and ultimately, the associated sonic boom.
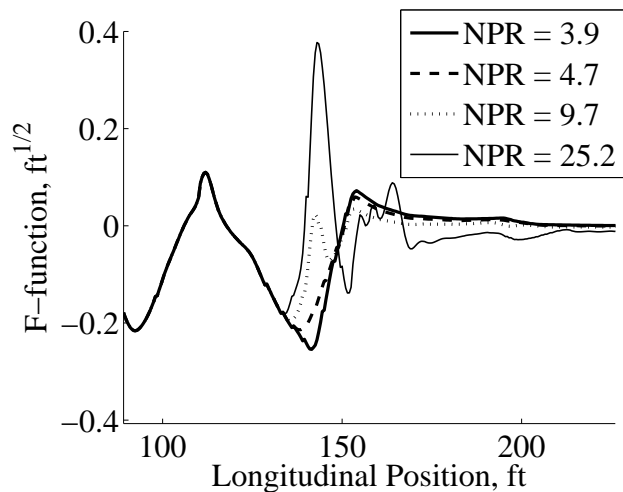
(a) F-functions.
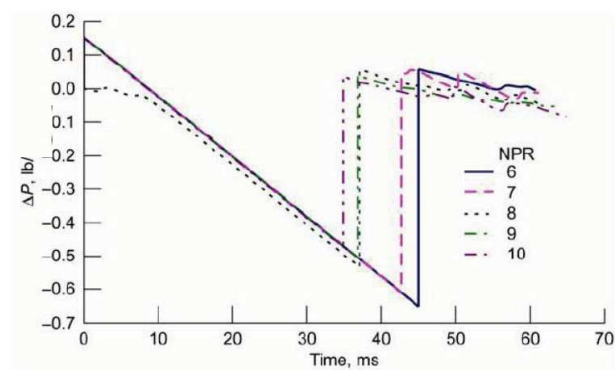
(b) Published results.
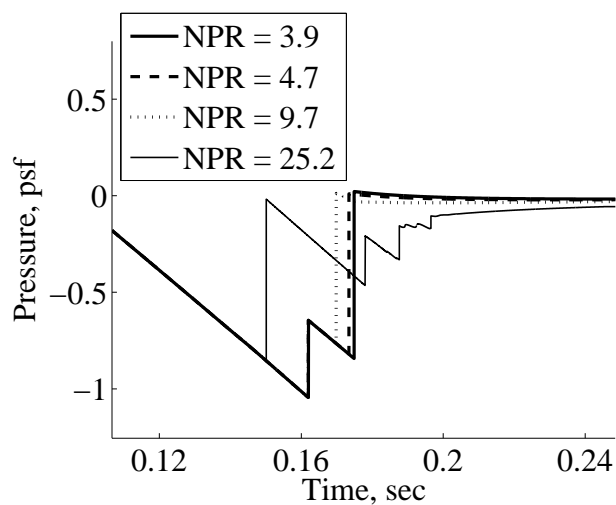
(c) RapidF results.

Figure 4.5: Effects of various nozzle pressure ratios on the ground pressure profile.
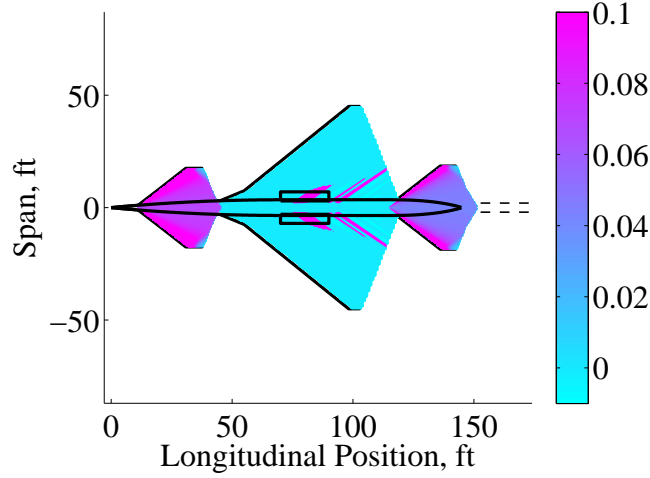
Figure 4.6: Example of RapidF interference lift calculations.

4.2.4 Boundary layers

One critique of modified linear theory is that it is an inviscid method. Therefore, RapidF was adapted to include viscous effects. RapidF calculates the boundary layer thickness, by assuming a turbulent boundary layer [18]:

$$\delta = \frac{0.3747}{Re^{0.2}} x \tag{4.6}$$

with an associated a velocity profile of:

$$u = \left(\frac{y}{\delta}\right)^{1/7} u_e \tag{4.7}$$

With these two equations the displacement thickness at each location is calculated. When the component terminates the boundary layer area turns into a wake, which is similar to Ref. [31]. An example of the results of including the wake is shown in Fig. 4.7. Although the viscous effects do contribute to the area, the impact on the F-function is minimal. This is because the F-function is proportional to the curvature of the area distribution, not its magnitude.

The cross-sectional area distributions from the fuselage, planar surfaces, engines, and boundary layer are summed to yield the total equivalent area due to volume. Likewise, the lift generated from all the components is summed and converted to units of area via Eq. (3.20) to produce the
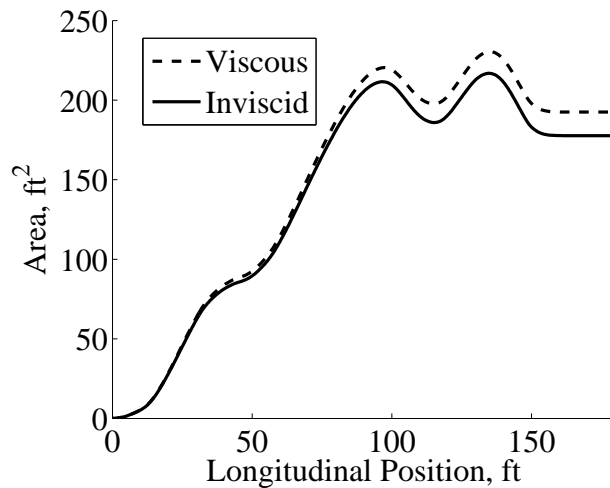
(a) Total equivalent area.
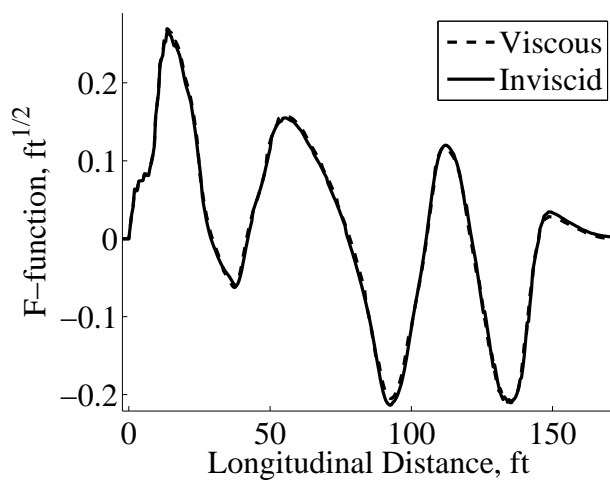
(b) F-functions.

Figure 4.7: Viscous effects on area profile and F-function.

equivalent area due to lift. These two areas are summed to produce the total equivalent area, which is used to calculate the F-function.

4.3 F-function calculations

After RapidF calculates the total equivalent area form the aircraft components as discussed in the previous section. This area profile needs to be converted to an F-function. This section discusses the F-function process used. This will be done by reviewing several historical methods as well as proposing several modifications to make them better suited to RapidF.

4.3.1 Whitham

Modified linear theory's F-function was defined as:

$$F(y) = \int_0^y \frac{f'(\zeta)}{\sqrt{y-\zeta}} d\zeta \tag{4.8}$$

in Chapter 2. Then, by assuming a slender and smooth body, the F-function can be expressed as a function of the area profile:

$$F(y) = \int_0^y \frac{S''(\zeta)}{\sqrt{y-\zeta}} d\zeta \tag{4.9}$$

Equation (4.9) is usually referred to as the *Whitham* F-function based on its introduction in 1952 [178]. It is appealing because it easy to implement and is based on physical characteristics of the aircraft. To find the F-function at location y, the second derivative at location ζ is weighted by:

$$\mathcal{W}_W(\zeta) = \frac{1}{\sqrt{y-\zeta}} \tag{4.10}$$

Based on this weighting, one can interpret Eq. (4.9) as stating that the F-function is mostly a function of the local curvature. The curvature of locations in front of the point of interest do influence the F-function; however, the influence rapidly decreases as the distance between the points increases. For example, Fig. 4.8 compares the local second derivative to the F-function. The F-function used for this section's analysis is for the lobe balanced aircraft developed in Chapter 6. A profile view and area profile are shown in Fig. 4.9. As seen in Fig. 4.8, the second derivative follows the F-functions trends and the second derivative can be used as a crude approximation of the F-function. This is consistent with supersonic linear theory where the surface pressure is only a function of the local surface inclination and that information cannot be transmitted upstream.
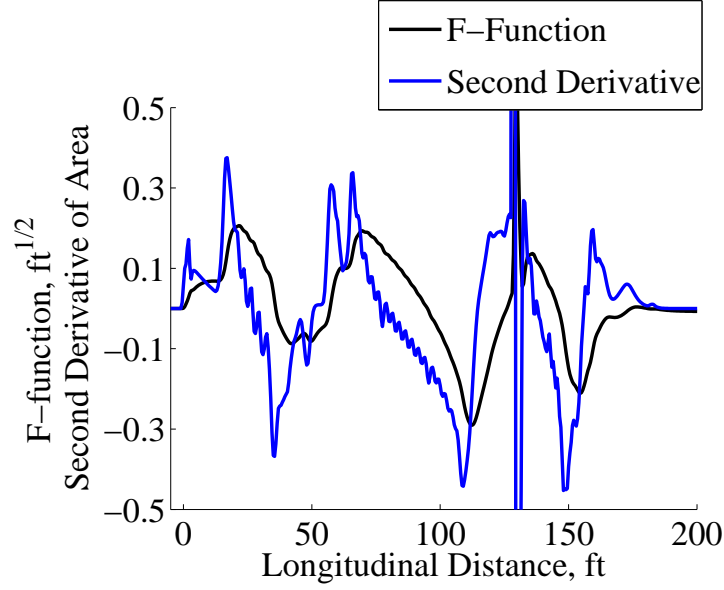
Figure 4.8: Comparison of F-function to second derivative of area.

(a) Profile view and F-function.
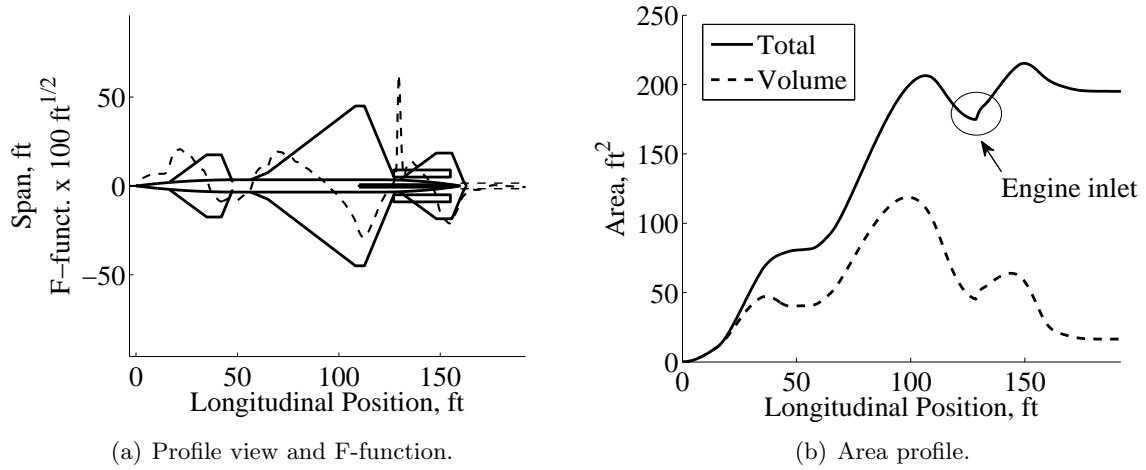
(b) Area profile.

Figure 4.9: Aircraft used for F-function analysis.

Equation (4.9) does have some limitations. To use this equation the area profile must be smooth. Although aircraft are usually smooth to minimize drag, discontinuities do exist in the cross-sectional area profile, such as the engine inlets in Fig. 4.9. Furthermore, referring to Eq. (4.10), as ζ approaches y, the weight approaches infinity. This asymptotic limit is not an issue when doing analytical integration as Whitham did in his 1952 paper, but when doing numerical integration,

the last point, just in front of point y, where $\zeta = y - \Delta x$, the weight is:

$$\mathcal{W}_W(\zeta) = \frac{1}{\sqrt{\Delta x}} \tag{4.11}$$

Thus, as the number of points used in the numerical integration increases, the weight on this last point increases, making Whitham's equation sensitive to grid density. Because of this issue, combined with the inability to account for discontinuities, a more robust equation is sought.

4.3.2 Lighthill

Lighthill also developed a method to find the F-function, but his method does not require the area profile to be smooth [110]. His F-function equation is:

$$F(y) = \int_0^\infty \sqrt{\frac{2}{\beta R(\zeta)}} \quad h\left(\frac{y - \zeta}{\beta R(\zeta)}\right) \frac{dS'(\zeta)}{2\pi} \tag{4.12}$$

where:

$$h(\chi) = \sqrt{\frac{\pi}{2p}} \frac{1}{K_1(p)} H(\chi) \tag{4.13}$$

This $h(\chi)$ function is plotted in Fig. 4.10. Based on Eq. (4.12), each point is weighted by:

$$\mathcal{W}_L(\zeta) = \sqrt{\frac{2}{\beta R(\zeta)}} h\left(\frac{y - \zeta}{\beta R(\zeta)}\right) \tag{4.14}$$

This method has not been widely implemented due to the difficulty in implementing Heaviside calculus and Bessel functions. In the 1980s, Gottlieb and Ritzel compared Whitham's and Lighthill's methods to projectiles with discontinuities [63, 157]. They found that Whitham's theory poorly predicted the F-function at discontinuities, which should have been anticipated since a discontinuity violates the smooth assumption. For example, a comparison of Whitham and Lighthill methods is shown in Fig. 4.11 for a nose cone to fuselage joint with a 3.2^o change in flow angle. Although the discontinuity is small, Whitham predicts a large expansion. This example demonstrates that even a small discontinuity can have significant effect on Whitham's F-function. Since a digitized representation of an aircraft's area profile has a finite jump at each grid point as shown in Fig. 4.12, Lighthill's method appears better suited for calculating an aircraft F-function using numerical

integration. Furthermore, Lighthill's weighting, Eq. (4.14), is finite and less sensitive to changes in grid density.

One drawback of using Lighthill's method is a higher computational cost. In order to speed processing time, Gottlieb and Ritzel proposed using a modified method where Whitham's equation is used in regions with a smooth area profile and adding a correction at discontinuities based on Lighthill's equation. Initially, this method was attempted in this study, but was difficult to implement since it requires logic to find discontinuities. Gottlieb and Ritzel were hesitant to solely use Lighthill's equation because of computation time. In the 20+ years since their papers were published, advances in computers have made this argument irrelevant. Thus, for this study a method was developed to implement Eq. (4.12) for aircraft designs.

Lighthill's method is more computationally expensive than Whitham's because Eq. (4.13) is time consuming to calculate. Previously, this cost was avoided by approximating $h(\chi)$ as $(2\chi)^{-1/2}$. However, if this approximation is used, Eq. (4.12) simplifies to Eq. (4.9) and any advantage in using Lighthill's method is lost. Thus, in order to improve accuracy and computational speed a look-up table was created for $h(\chi)$ without any approximations, as suggested by Gottlieb and Ritzel [157]. This allows Lighthill's method to be used accurately and with no speed penalty.

Lighthill's equation has never been applied to an aircraft, only to axisymmetric, non-lifting
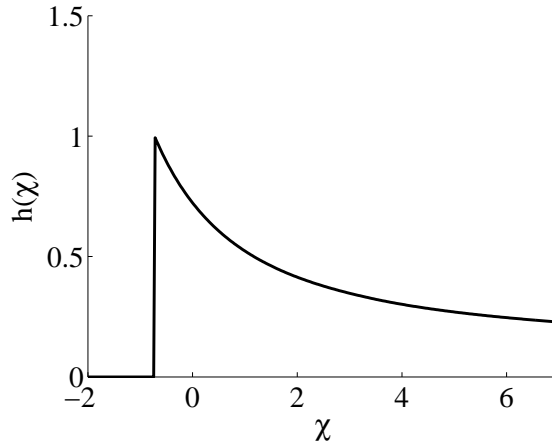
Figure 4.10: The $h(\chi)$ function.

objects and some adaptations need to be made. First, the total equivalent area is used to calculate $dS'(\zeta)$. Also, a value is needed for $R(\zeta)$. How $R(\zeta)$ is used in Lighthill's method is shown in Fig. 4.13. As seen in Eq. (4.14), the $\beta R(\zeta)$ term provides a method to non-dimensionalize $y - \zeta$. It is also important to note that the upper limit of integration in Eq. (4.12) is infinity. Since $h(\chi)$ is non-zero for $\chi > -1$, the quantity $\beta R(\zeta)$ also controls how far beyond point y, the shape contributes to the F-function at point y, as shown in Fig. 4.13(b). In fact if $R(\zeta)$ is approximated as $R(y)$, then the domain of influence is as shown in Fig. 4.13(c), which is consistent with linear
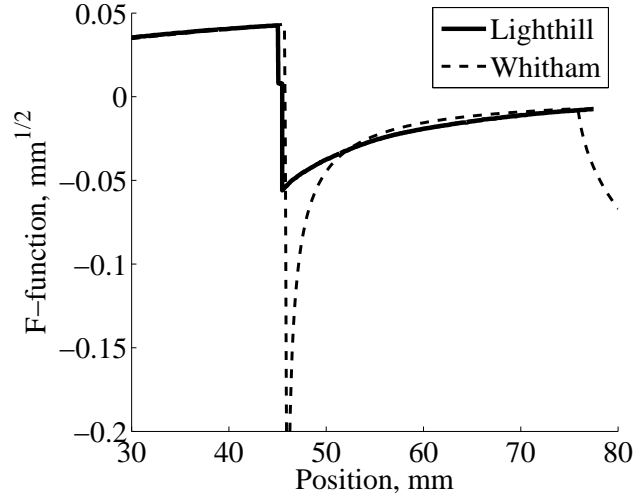
Figure 4.11: Comparison of Whitham and Lighthill F-functions at a discontinuity. [157].

(a) Smooth or continuous.
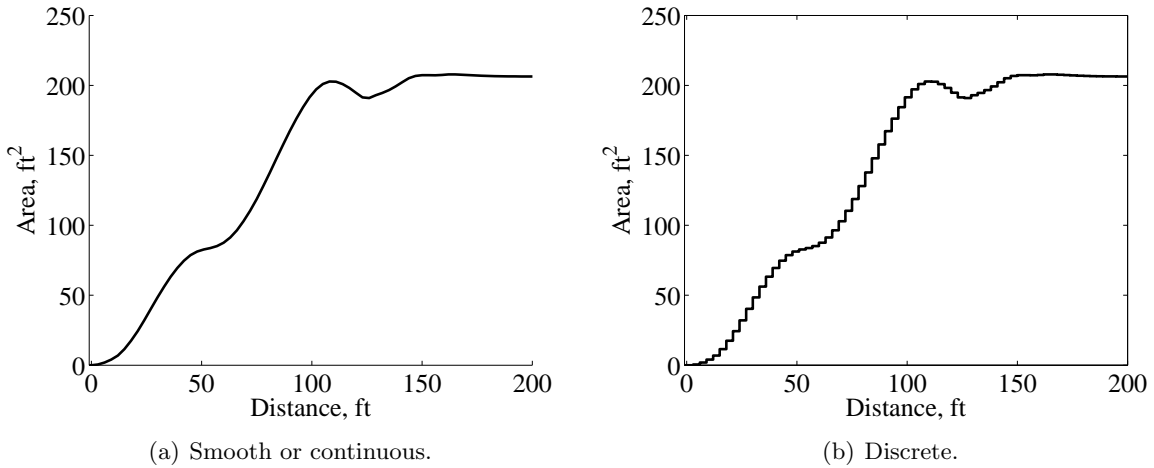
(b) Discrete.

Figure 4.12: Smooth and discrete total equivalent area profiles.

theory: a radius change at $y + \beta R(y)$ act as if it began at the centerline at y.

The effect of $R(\zeta)$ and the associated domain of influence on an aircraft F-function can be seen in Fig. 4.14 which shows the F-functions for three choices of $R(\zeta)$. The first choice of $R(\zeta)$ is the equivalent area due to volume in units of length, $\sqrt{S_V/\pi}$. The second is the fuselage radius. Refer to Fig. 4.15 for a comparison of these two radii. The final radius choice in Fig. 4.14 is a constant value of 0.5 ft. An F-function from Whitham's equation is also presented for comparison. In Fig. 4.14(b), the graph is zoomed in to show the area around the engines located at 127 ft. As supported by Eq. (4.14), the largest radius, $\sqrt{S_V/\pi}$, allows larger values of ζ before the -1 cut-off, as shown in Fig. 4.10. Therefore, the effects of the engines appear earlier than the other radius choices. This example highlights an undesirable attribute of Lighthill's method, due to the upper limit of integration, features are shifted forward in the F-function. Since the aircraft has already been sliced at the Mach angle, as shown in Fig. 3.3, the equivalent area at point x includes the effects of area changes at $x + \beta R$. This is equivalent to the shifting forward of Lighthill's method. Therefore, a way to avoid this double correction will be addressed in the Modified Lighthill section. Besides controlling the effective upper limit of integration, the $\beta R(\zeta)$ term has minimal effect on the F-function. When χ is large, $h(\chi) \approx (2\chi)^{-1/2}$, and the weight simplifies to:

$$W_L \approx \sqrt{\frac{2}{\beta R(\zeta)}} \sqrt{\frac{\beta R(\zeta)}{2(y - \zeta)}} \approx \frac{1}{\sqrt{y - \zeta}} \tag{4.15}$$

In other words: when $(y - \zeta)/(\beta R(\zeta))$ is large, the weighting is not significantly affected by $R(\zeta)$. Based on this discussion, the fuselage radius is used for $R(\zeta)$.

(a) Points in front of y.

(b) Points after y.

(c) Domain of influence assuming $R(\zeta) \approx R(y)$.
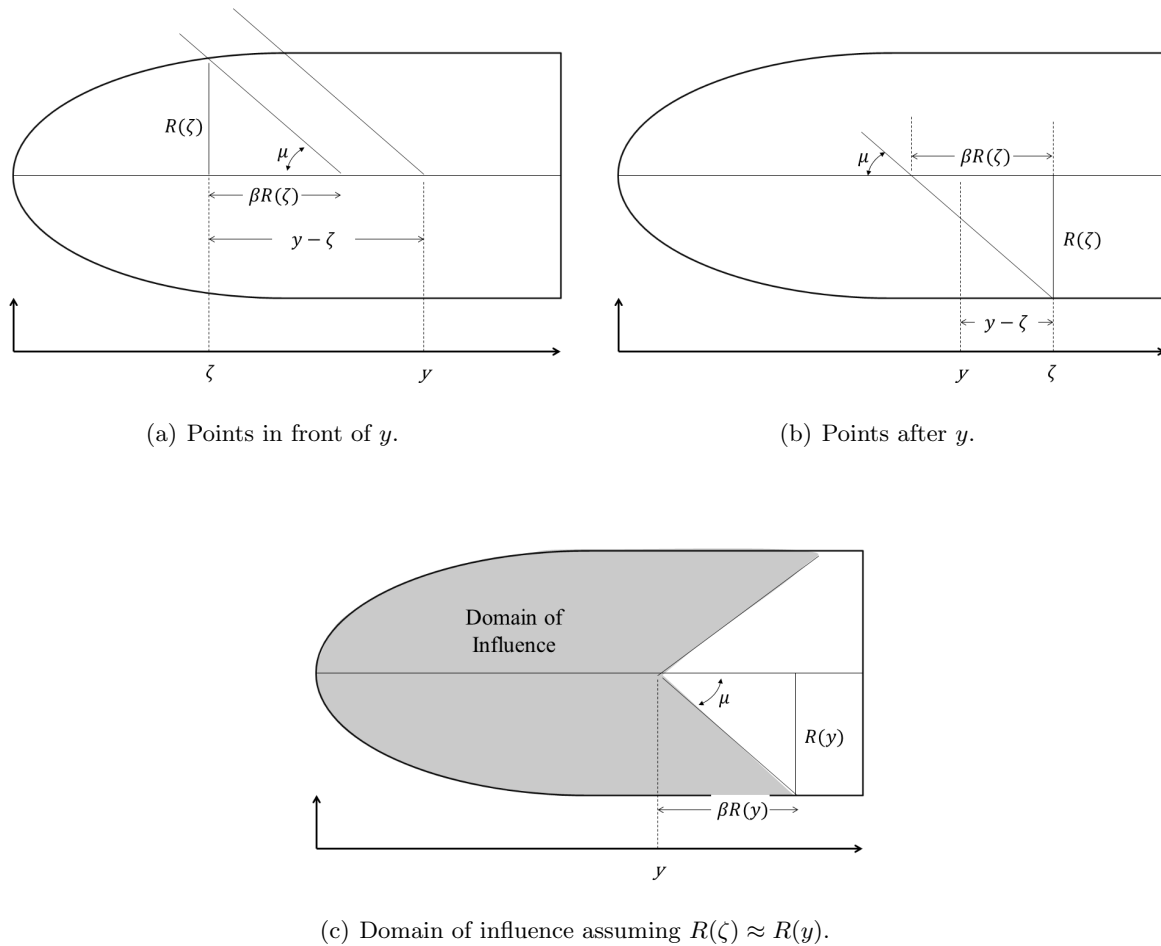
Figure 4.13: Lighthill's weighting.

(a) F-functions.

(b) Zoomed in view near engines.
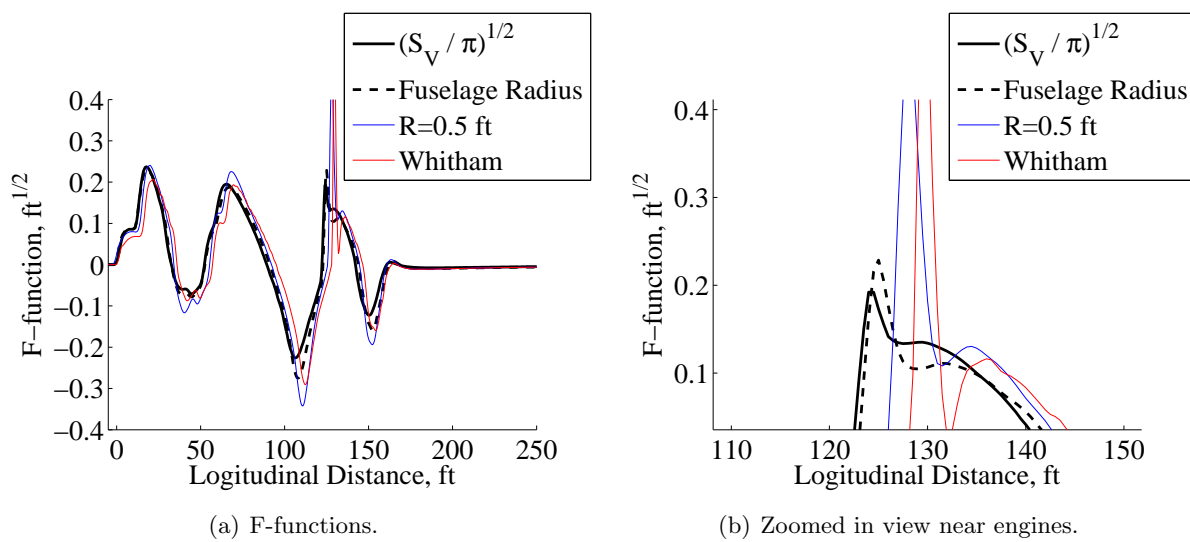
Figure 4.14: Lighthill F-functions for various radii.
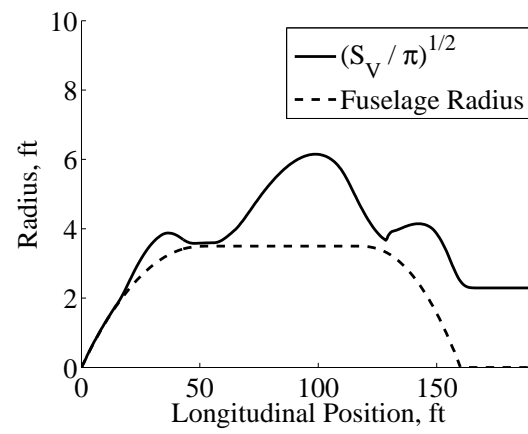
Figure 4.15: Radius based on equivalent area compared to fuselage radius.

4.3.3 Modified Lighthill

Two improvements to Lighthill's equation are proposed. The first modification is a correction of the weighting so that components do not show up early in the F-function, as discussed in the previous section:

$$\mathcal{W}_{ML}(\zeta) = \sqrt{\frac{2}{\beta R(y)}} h\left(\frac{y-\zeta}{\beta R(y)} - 1\right) \tag{4.16}$$

The effect of adding the -1 to the input to the $h(\chi)$ function can be seen in Fig. 4.16. This modification prevents a component from effecting the F-function in front of it as was seen in Fig. 4.14(b). When RapidF slices the aircraft, it slices forward and backwards was shown in Fig. 3.3; thus, it already has accounted for the domain of influence shown in Fig. 4.13(c).

The second improvement deals with when $R(\zeta)$ is very small. As seen in Eq. (4.16), since $R(\zeta)$ is in the denominator of the first term, when $R(\zeta)$ approaches zero, this term goes to infinity. Likewise, the second term approaches zero. To avoid errors associated with these very large and small numbers, if $R(\zeta)$ is less than 2% of the maximum radius, then Eq. (4.15) is used.
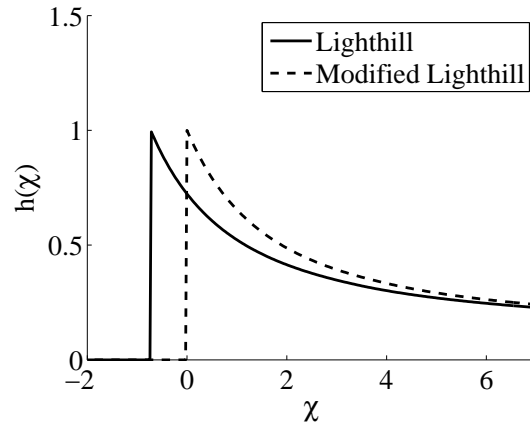
Figure 4.16: Modified weighting compared to Lighthill's weighting.

4.3.4 Stieltjes integral

As was pointed out multiple times already, Whitham's equation to calculate the F-function requires $S''(\zeta)$ to be continuous. One method to calculate an F-function with discontinuities is to

use a Stieltjes integral of the general form [47]:

$$\int P(x)dG(x) = \int P(x)G'(x)dx \tag{4.17}$$

Thus, the F-function can be calculated by [157]:

$$F(y) = \frac{1}{2\pi}\int_0^y \frac{dS'(\zeta)}{\sqrt{y-\zeta}} \tag{4.18}$$

This solution still requires a correction for where $S'(\zeta)$ is discontinuous. According to Whitham this correction is [178]:

$$\Delta F(y)_i = \frac{1}{2\pi}\sqrt{\frac{2}{\beta R_i}}\Delta S'_i \tag{4.19}$$

Ritzel and Gottlieb more precisely quantify it as [157]:

$$\Delta F(y)_i = \frac{1}{2\pi}\sqrt{\frac{2}{\beta R_i}}\Delta S'_i \, h\left(\frac{y-\zeta}{\beta R_i}\right) \tag{4.20}$$

This correction is essentially the same as Lighthill's F-function. As was discussed earlier, the above equations can be applied in the following manner: Equation (4.18) is used to calculate the F-function up to a discontinuity in $S'(\zeta)$, then Eq. (4.20) is used to calculate the F-function jump at the discontinuity. Then, Eq. (4.18) is used again until the next discontinuity. The process is repeated until reaching the end of the aircraft.

Now, Eq. (4.18) is discussed in detail. To calculate dS' at point n numerically:

$$\begin{aligned} dS'_n &= S'_{forward} - S'_{backwards} \\ &= \frac{S_{n+1}-S_n}{\Delta x} - \frac{S_n - S_{n-1}}{\Delta x} \\ &= \frac{S_{n-1}-2S_n+S_{n+1}}{\Delta x} \end{aligned}$$

Substituting this into Eq. (4.18) and discretizing:

$$F_i = \frac{1}{2\pi}\sum_{n=1}^{i}\left(\frac{S_{n-1}-2S_n+S_{n+1}}{\Delta x}\frac{1}{\sqrt{x_i - x_n}}\right) \tag{4.21}$$

The same process is now done to Whitham's equation, Eq. (4.9). The second derivative of the area can be approximated to second order as:

$$S''_n = \frac{S_{n-1}-2S_n+S_{n+1}}{(\Delta x)^2} \tag{4.22}$$

Using this to discretize Eq. (2.59):

$$F_i = \frac{1}{2\pi} \sum_{n=1}^{i} \left(\frac{S_{n-1} - 2S_n + S_{n+1}}{(\Delta x)^2} \frac{1}{\sqrt{x_i - x_n}} \right) \Delta x \tag{4.23}$$

This is numerically the same as Eq. (4.21) and there is no advantage of Eq. (4.18) compared to Eq. (4.9). For example, an F-function calculated from Eq. (4.18) is compared to one from Whitham's method in Fig. 4.17. As expected, they are identical. This observation has been previously stated by Ritzel and Gottlieb in Ref. [157]. Therefore, Eq. (4.18) is not pursued in this is study. However, this discussion does add insight into the differences between Lighthill and Whitham's equations Since Lighthill's equation, Eq. (4.12), is also a Stieltjes integral, his uses of $dS'(\zeta)$ is equivalent to Whitham's $S''(\zeta)d\zeta$. The only difference between Lighthill's and Whitham's methods is the weighting. Therefore, the large disparity in the F-functions shown in Fig. 4.11 is not caused by Whitham's use of $S''(\zeta)$, but by his weighting.
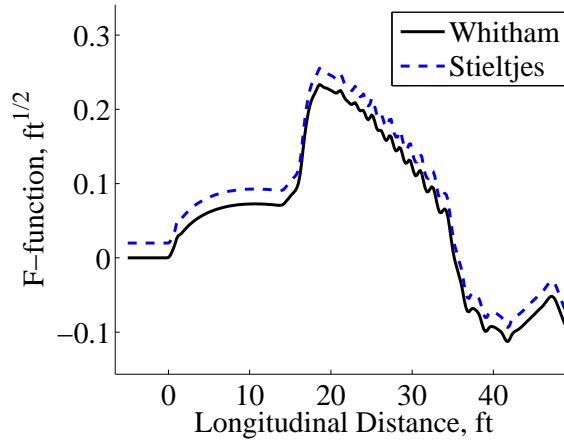
Figure 4.17: F-function from Whitham's equation and Stieltjes integral (Stieltjes integral offset 0.1 to enable comparison).

4.3.5 Modified Whitham

Gottlieb obtains another equation that should be examined. Referring to Eq. (4.13), by assuming $h(\chi)$ can be approximated as $[2(\chi + 1)]^{-1/2}$, Lighthill's equation can be simplified to:

$$F(y) = \frac{1}{2\pi} \int_0^\infty \frac{dS'(\zeta)}{\sqrt{y - \zeta + \beta R(\zeta)}} \tag{4.24}$$

with the associated weight:

$$\mathcal{W}_{MW} = \frac{1}{\sqrt{y - \zeta + \beta R(\zeta)}} \tag{4.25}$$

Equation (4.24) will be referred to as the *Modified Whitham* equation. Ritzel and Gottlieb never applied this equation; they simplified it to Eq. (4.18) and (4.20). However, it is worthy of investigation. Notice that the upper limit of integration is infinity. Thus, although the integrand will be finite at $\zeta = y$, it will be infinite at $\zeta = y + \beta R(\zeta)$ and imaginary when $\zeta > y + \beta R(\zeta)$. Thus, the integrand is summed only when it is real and finite. A comparison of all four weighting methods is shown in Fig. 4.18. The Modified Whitham method has all of the flaws of Whitham in addition to those of Lighthill. Like Whitham, the weighting approaches infinity as as $\zeta + \beta R(\zeta)$ approaches y, and like Lighthill it allows points behind the point of interest to influence the F-function. Based on these issues, the Modified Whitham F-function is not investigated further.
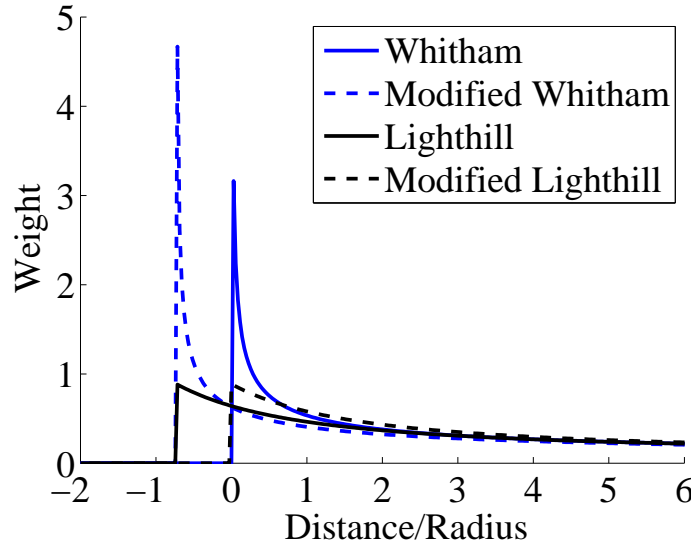
Figure 4.18: A comparison of weights for four F-function calculation methods.

4.4   F-function sensitivity

Based on the discussion from the previous section, two F-function equations will now be compared. The first is the classical Whitham method, Eq. (4.9) and the second is the Modified

Lighthill method, Eq. (4.12) and Eq. (4.16). The accuracy of any numerical simulation is effected by how coarsely the model is discretized. The primary input to the resolution of the RapidF solution is the user defined input *'options.dx'*, which is the spacing of the slices along the aircraft centerline, Δx. This analysis presents results using the number of points (aircraft length divided by Δx).

F-functions for various grid densities are shown in Fig. 4.19. The F-functions calculated using Whitham's method continue to distort as the grid is refined because the denominator in Eq. (4.9) is effected by Δx. Zoomed in F-functions near the front of the aircraft which includes the canard are shown in Fig. 4.19(c) and 4.19(d). Whitham's method shows small oscillations or "scallops." These features are caused by the grid used to calculate the canard's area and lift not being aligned with the canard's leading and trailing edges as shown in Fig. 4.20. This misalignment causes the area profile to be stepped; creating a series of positive to negative second derivatives. Although the Modified Lighthill method uses the same stepped area profile, the oscillations in the F-function are less severe because of the lighter weight given to these points. Also, Whitham's method predicts a large F-function from the engine inlet, as shown in Fig. 4.19(e). The size of this feature increases with increasing number of points. In contrast, Lighthill's method is much less sensitive to these perturbations. Figure 4.21 shows the ground pressure profiles associated with the F-function presented in Fig. 4.19. Whitham's method reasonably matches the Modified Lighthill's method despite the oscillations associated with the lifting surfaces and the engines. This is because these spikes are like delta functions and contain very little acoustical energy and quickly dissipate with distance.

The results of these tests are summarized in Fig. 4.22. Since Whitham's method does not show F-function convergence, the Modified Lighthill method is selected as the best method to be used for aircraft F-function prediction. A dashed vertical line at 320 points is drawn in the graphs of Fig. 4.22 which is the lowest number of points used in this study. This number of points allowed: (1) run times to be less than one minute, (2) the maximum F-function to be with 3.2% of the value using 1,600 points, and (3) produced essentially the same ground pressure profile as predicted using higher grid density.
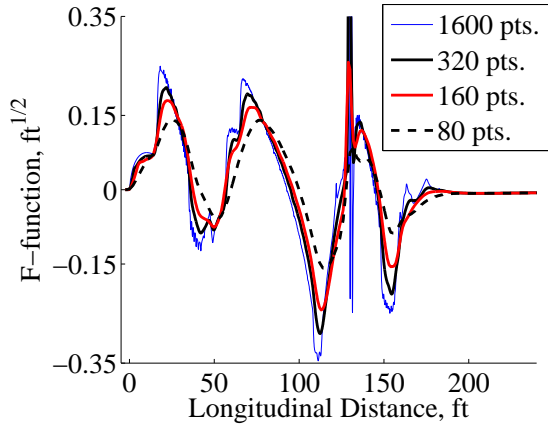
(a) Whitham's F-function.
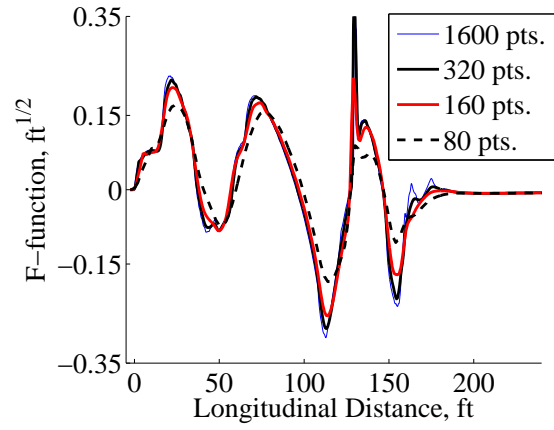
(b) Modified Lighthill's F-function.
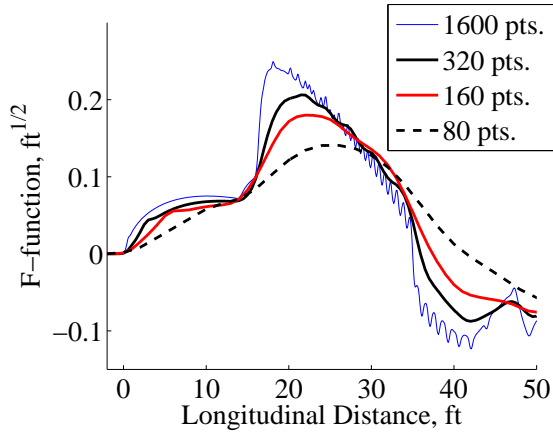
(c) Whitham's F-function near nose.
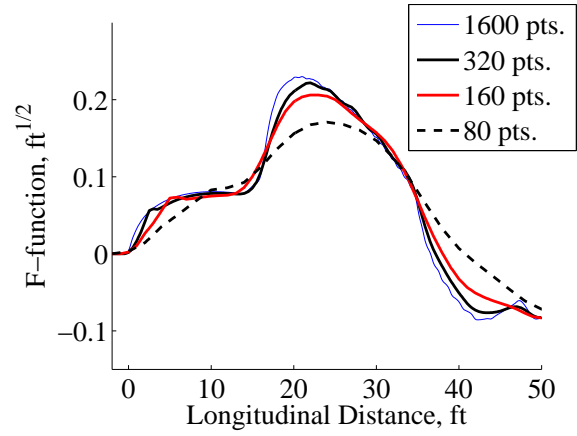
(d) Modified Lighthill's F-function near nose.
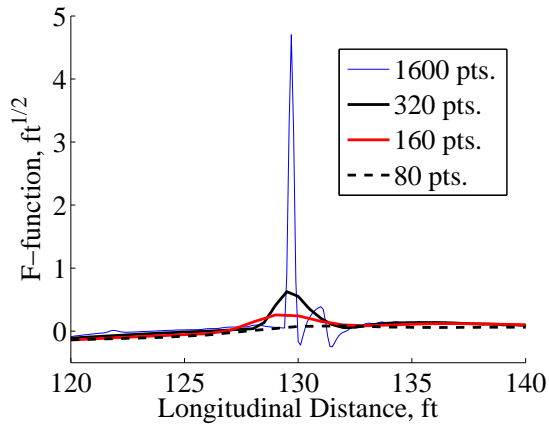
(e) Whitham's F-function at engine inlet.
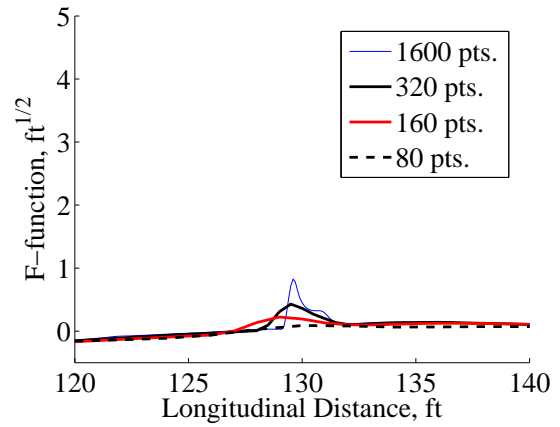
(f) Modified Lighthill's F-function at engine inlet.

Figure 4.19: F-functions for various grid densities.
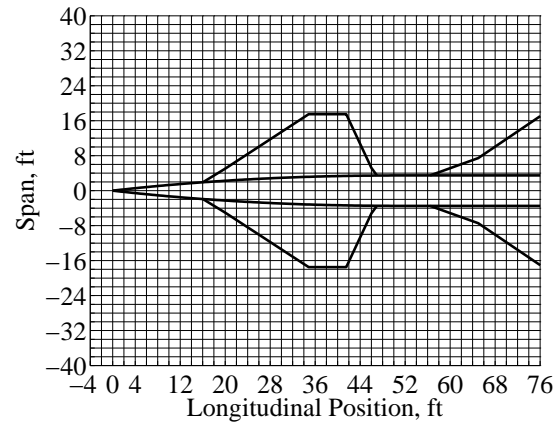
Figure 4.20: Grid used to obtain canard lift and volume distribution.

(a) Whitham's method.

(b) Modified Lighthill method.
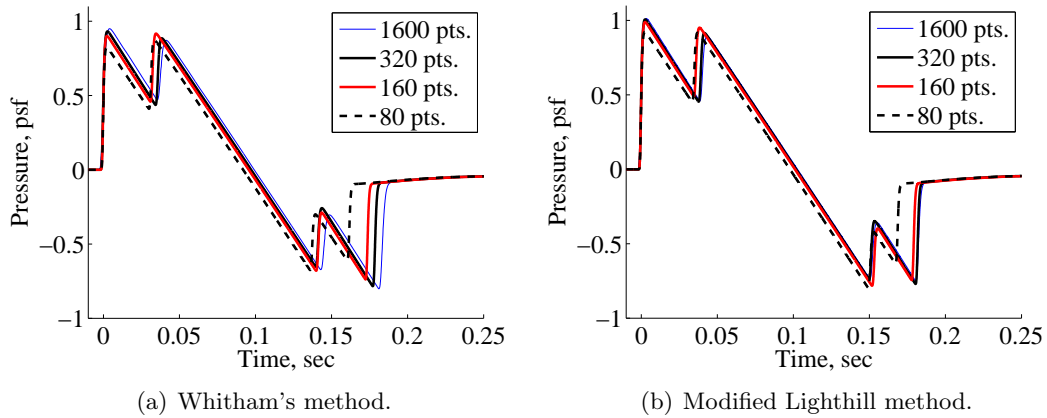
Figure 4.21: Ground pressure profiles for various grid densities.

(a) F-function.

(b) Ground pressures.

(c) Run times.
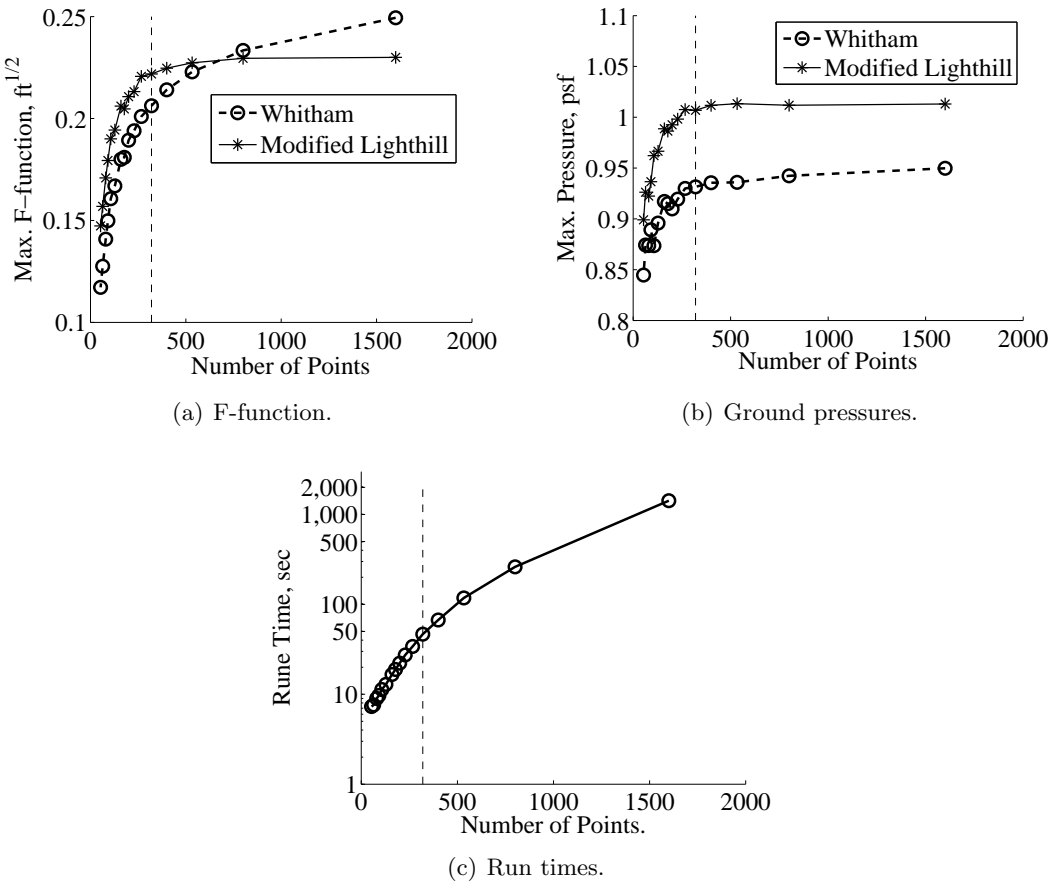
Figure 4.22: Performance metrics for various grid densities.

4.5   Acoustic propagation

The F-function from RapidF is input into a subroutine named CUBoom which is a modernization of ARAP [72]. In addition to the F-function, CUBoom also requires the following:

- Atmosphere type: Standard 1976, Homogeneous, Isothermal or Tabulated

- Winds: Altitude, direction, magnitude

- First step size

- Step size

- Aircraft heading

- Ground height

- Reflection factor

CUBoom performs ray tracing, calculates the age variable and ray area. Shock locations are determined via the algorithm based on weak shock theory [129]. There is also an option to estimate the effects of molecular relaxation. This subroutine determines the rise time based on shock strength, as was shown in Fig. 2.3. Although the shock structure and rise time are effected by many variables such as humidity and turbulence [16] and more comprehensive calculations methods are available [15,37,100], the simple look-up table used by CUBoom provides a way to get a reasonable and fast estimate of the molecular relaxation effects on the sonic boom.

4.5.1   Geometric acoustics sensitivity

The objective of geometric acoustic step is to quantify the age variable, τ, which quantifies how the F-function is stretched as shown in Fig. 4.23(a) and can be calculated by:

$$\tau = \frac{(\gamma + 1)M^2}{2c_0} a_1 \cos\theta_1 \sqrt{\frac{\rho_1}{2}} \int_0^{gnd} \frac{1}{a\sqrt{(\cos\theta\sin\theta)^3 \rho A}} dz \qquad (4.26)$$

with the associated geometry shown in Fig. 4.23(b). By assuming that pressure is consistently standard day conditions, the density is only a function of temperature. Then, the integral is only

a function of temperature, winds, and the step size used for numerical integration. The impact of these variables are summarized in Fig. 4.24.

- **Step Size:** Results for the step size are summarized in Fig. 4.24(b), where the step size was varied from 5 to 2,000 ft, which used 10,000 to 25 steps and took, 6.4 and 0.14 seconds, respectfully. Since, little variation is seen below 100 ft, this study used a 25 ft step with an approximately 1.0 second run time for the entire propagation subroutine.

- **Temperature:** This affects the density, the speed of sound, the ray tube area and the acoustical ray path. To investigate the total effect of temperature on the age variable, a hot non-standard day profile, as shown in Fig. 4.24(a), was used, where the surface temperature is 100° Fahrenheit. The age variable is also shown in Fig. 4.24(b), which is almost identical to the standard day results. This is because although the surface temperature is 41° hotter than standard day, this correlates to only a 4% increase in the speed of sound. Therefore, temperature has little effect on ground pressure profile.

- **Winds:** For an example of the effects of winds, the age variable is calculated in an atmosphere that is calm above 25,000 ft and a 25 kts headwind below this altitude, which causes higher acoustic advance as shown in Fig. 4.24(b), because the ray is refracted by the change in the winds. However, the change in the age variable is only 1.9%.

The impact of step size and winds on the ground pressure profile are shown in Fig. 4.24(c), which are minimal. The effects are not significant because the overall change in the age variable is small as can be confirmed by examining the vertical scale of Fig. 4.24(b). Therefore, it is concluded that the age variable is relative insensitive to atmospheric conditions and the numerical step size, as long as less than 100 ft.

4.5.2   Shock location sensitivity

After the age variable is calculated the F-function is distorted as shown Fig. 4.25. The unmodified F-function is shown in Fig. 4.25(a). Then after the F-function has propagated through

(a) Acoustic advance example.

(b) Geometry used to calculate advance.

Figure 4.23: Acoustic advance.

(a) Temperature profiles.

(b) Age variable.

(c) Pressure profiles.

Figure 4.24: Impact of step size and real atmosphere on advance and ground pressures.

the atmosphere, the age variable will distort it so that it looks like Fig. 4.25(b). The horizontal axis is now actually the retarded distance, y_t. The next step is to find shock locations as discussed

in the "Weak shock theory" section of Chapter 2. This is a challenging task requiring precise computations. For example, the F-function in Fig. 4.25(b) is stretched over 1,000 ft and an expanded view in Fig. 4.25(c) shows that features are nearly on top of each other. The most significant variable is the number of points used to search for shock locations. CUBoom's default value is 10,000 points. Thus, if the F-function is stretched over 1,000 ft as in Fig. 4.25, CUBoom will look for a shock location every 0.1 ft. In order to find the shocks the F-function from Fig. 4.25(b) is divided into "right running segments," where $y_{tn} > y_{tn-1}$. Then a matrix is made of:

$$\int_0^{y_t} F(\zeta_t)d\zeta_t \tag{4.27}$$

for each segment at all 10,000 points for each right running segment. If two segments have the same value for Eq. (4.27), then this is a possible shock location. If the smallest right running segment is shorter than the search step, then the number of points is increased up to 25,000 points to ensure no intersections are missed. If this upper limit is reached, then the user is warned that some fidelity in the shock structure may be lost. The details of algorithm used can be found in Ref. [129].

The results of applying this logic to the F-function in Fig. 4.25(b) can be seen in Fig. 4.26. In Fig. 4.26(a), the pressure profiles are shown for various number of points. NOTE: The logic which increases the grid density was disabled for these tests. The first interior shock location is plotted in Fig. 4.26(b) with error bars showing the search step size. These graphs demonstrate that as the number of grid points is increased the shock location converges to its proper location. As stated earlier, the uncertainty using 10,000 points is approximately 0.1 ft which is less than 0.1 msec which is more than sufficient for preliminary design estimates. However, it is important to know that if the shock search logic misses a shock, then sonic boom beyond that point will be erroneous. This is because the logic is like a decision tree and if it gets on the wrong branch, the results will be totally incorrect. However, CUBoom has multiple safety features to avoid these errors.

(a) Before distortion.

(b) After distortion.

(c) After distortion, zoomed in.
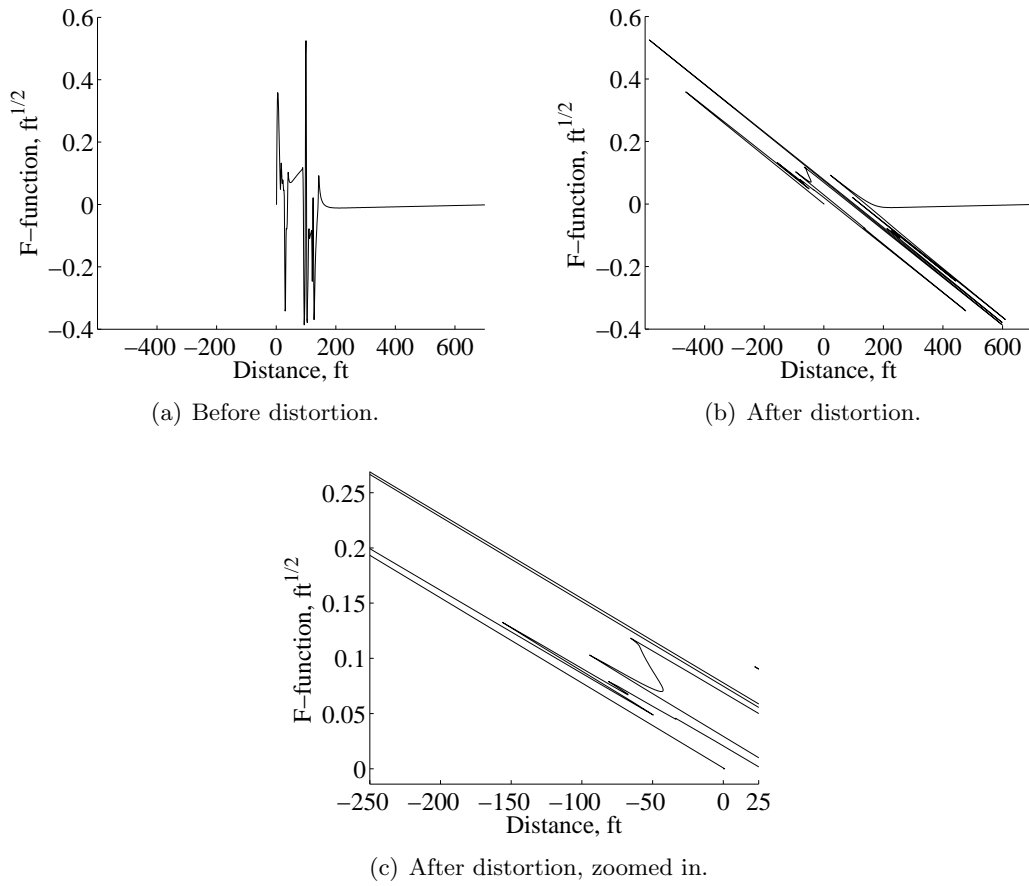
Figure 4.25: Example of acoustic advance effect on the F-function.

(a) Pressure profiles.
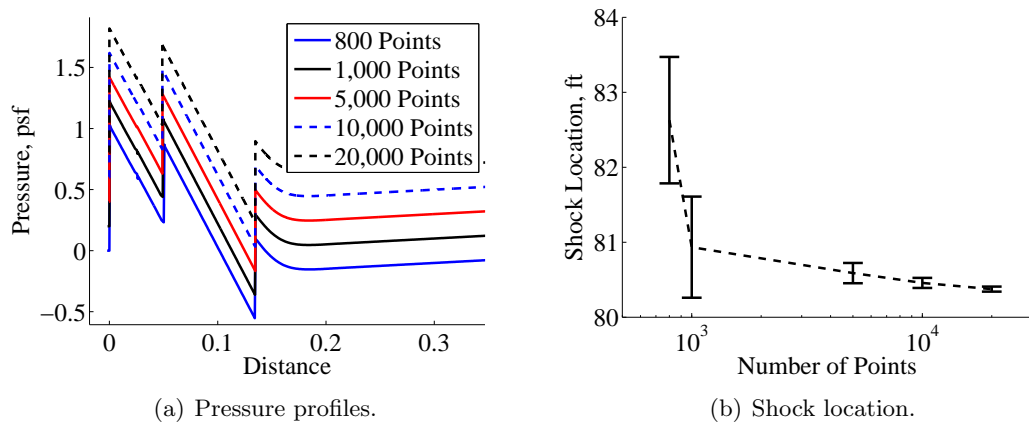
(b) Shock location.

Figure 4.26: Effects of number of points on pressure profile and shock location.

Chapter 5

RAPIDF VERIFICATION AND VALIDATION

In this chapter, sonic booms from RapidF are compared historical results including legacy software based on modified linear theory, wind tunnel experiments, and flight test results. Since RapidF is based on a first order theory, it was known prior to this research that it is not the most accurate software available. The purpose of this chapter is to show that RapidF is *accurate enough*, but what is this quantitatively? For this study, within 10% of experimental results will be used as the desired accuracy level. More specifically RapidF's sonic booms should have:

(1) The proper shape, meaning that the RapidF's sonic boom should have the correct number of shocks and the shocks should be at the correct location, within 10% of the signal length.

(2) Peak minimum and maximum overpressures within 10% of the experimental results.

(3) Signal length should be within 10% of the experimental signal length.

This chapter will show that, although it is low fidelity, based on first order theory, RapidF is able to accurately replicate sonic booms. Although RapidF occasionally does not meet the above criteria; overall, it consistently creates the correct shaped sonic boom and can be trusted to predict the sonic boom of conceptual designs.

5.1   Comparison of RapidF to Wind Tunnel Results

For an initial demonstration of RapidF's capabilities, pressure profiles are compared to wind tunnel experiments. Unlike sonic booms from flight tests, wind tunnel studies take place in a more

controlled environment, mitigating the effects of atmospheric variables such as humility, winds, and turbulence; thus, making results more repeatable. NASA TM X-1236 [31], authored by Carlson, McLean and Shrout in 1966, was selected for this purpose. Despite its age, the report has many desirable traits. First of all, it presents a complete geometric description of the wind tunnel model, allowing implementation in RapidF with minimal assumptions. Second, it presents results for a variety of test conditions:

- Configurations: with and without nacelles, and two fuselage shapes
- $M = 1.41$ and 2.0
- $C_L = 0.0$, 0.1, and 0.2
- $\phi = 0$, 45, 90 and 180°
- Pressure profiles at 2.5, 5.0 and 10.0 body lengths away

Furthermore, it provided both experimental and theoretical results, allowing verification by comparing RapidF's output to the the theoretical data and validation by comparing to the experimental results.

A drawing of the model used in the NASA TM X-1236 wind tunnel test can be seen in Fig 5.1, with dimension in centimeters. The model's engines were solid bodies of revolution with radii determined by subtracting the inlet capture area from the engine nacelle geometry. RapidF's model is depicted in Fig. 5.2. There are some minor differences compared to the model used in the the wind tunnel tests. First, at the time of the study, RapidF only accepted one vertical tail and as can be seen in Fig 5.1, the wind tunnel model had two vertical tails, or wing fences, located at the wing inflection point. RapidF's model used a single vertical tail on the centerline with the airfoil thickness doubled. This will give the correct area distribution when estimating the sonic boom directly beneath the model, but may lead to errors in the area profile when investigating sonic booms to the side as shown in Fig. 5.3. This simplification will also cause minor errors in the skin friction and wave drag, but aircraft performance is not the focus of this chapter. The engines were handled in a similar manor as the vertical tails: RapidF used one engine on the centerline

with the same area profile of all four of the wind tunnel's engines. Finally, the fillet where the wing trailing edge meets the fuselage is not modeled in RapidF.

Like RapidF, the NASA TM X-1236's theoretical pressure distribution was calculated using linear theory. The area profile was calculated by slicing the aircraft at the Mach angle, corrected for angle of attack as shown in Fig. 3.11, by adapting a code designed for wave drag calculations [67]. This code divided components into a maximum of 30 slices, then estimated the area at each location to include the boundary layer displacement thickness. The lift distribution was calculated to include the nacelle to wing interference effects. The lift profile was converted to an equivalent area via Eq. (2.61). Then, using the total area distribution, the F-function was calculated from Eq. (2.59). The pressure profile was found from the F-function as specified in NASA TN D-3082 [129], the same process as RapidF. In the following discussion and figures, the solutions from this process is referred to as the "theoretical" results.

In Fig. 5.4(a), the results are are shown for the model with $C_L = 0$ at 10 body lengths. The pressure and distance are non-dimensionalized as:

$$\Delta \tilde{p} = \frac{\Delta p}{p_\infty} \left(\frac{h}{\mathcal{L}} \right)^{3/4}$$

$$\tilde{x} = \frac{x}{\mathcal{L}} \left(\frac{h}{\mathcal{L}} \right)^{-1/4}$$

In general RapidF agrees very well with both NASA TM X-1236's experimental and theoretical results. In fact RapidF does a better job capturing the small disturbance at $\tilde{x} = 0.1$ and the wing's overpressure from $\tilde{x} = 0.2$ to 0.4. Both NASA's theoretical approximation and RapidF have some errors associated with the nacelles from $\tilde{x} = 0.4$ to 0.6. Carlson et al. were concerned about this disagreement and noted that a correction needed to be added to account for the soldering around the engines. However, this adjustment did not fully account for the difference.

Pressure profiles are presented for $C_L = 0.1$ with and without engine nacelles in Figs. 5.4(b) and 5.4(c), respectfully. In both graphs, RapidF properly captures the wing's overpressure, demonstrating that RapidF properly accounts for lift. The inlet shocks are a good indicator on how well the software predicts the effects from smaller components. As can be seen in Fig. 5.1, the outboard
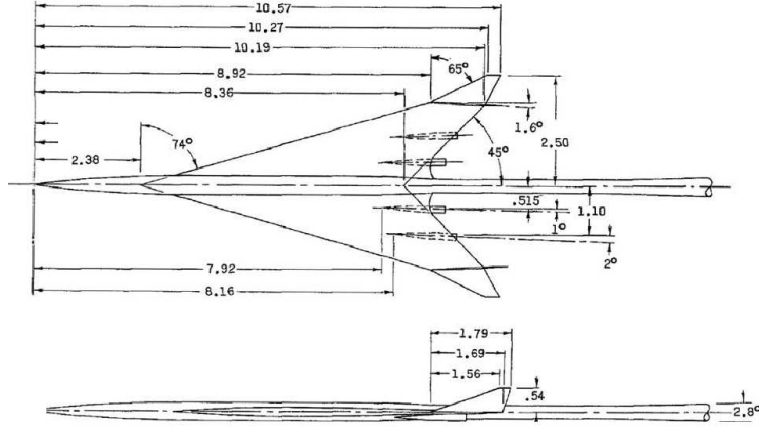
Figure 5.1: Drawing of wind tunnel model (reproduced from NASA TM X-1236 [31]).

(a) Planform.

(b) Side view.
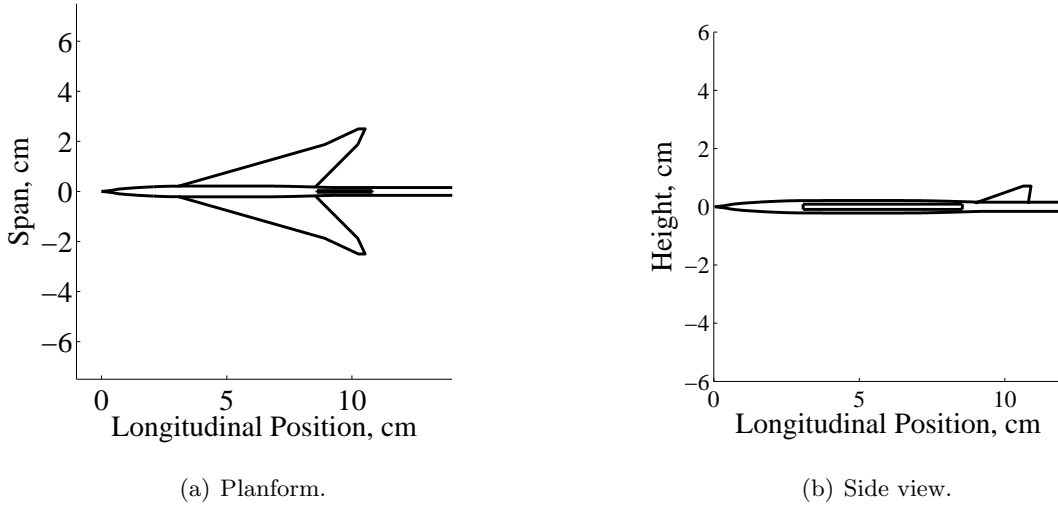
Figure 5.2: RapidF's representation of wind tunnel model used in NASA TM X-1236 [31].

engines are displaced 0.24 cm behind the inboard engines. Thus, the RapidF profile in Fig. 5.4(b) shows several shocks caused by the nacelles and the interference lift from $\tilde{x} = 0.36$ to 0.40. The experimental results do not show this complex shock system. However, since data was taken in approximately 0.02 increments of $\tilde{x}$, there is insufficient data to determine if this system existed or if viscous forces damped it out. The difference between RapidF and the experimental results

is minor compared to Carlson's theoretical pressure profile. Carlson performed the tests without nacelles because he speculated that the nacelles were causing problems. However, as can be seen in Fig. 5.4(c), even without the engine nacelles, Carlson's theoretical results poorly predict the pressure profile at the rear of the signature. RapidF does a better job, despite the exclusion of the wing-fuselage fillet.
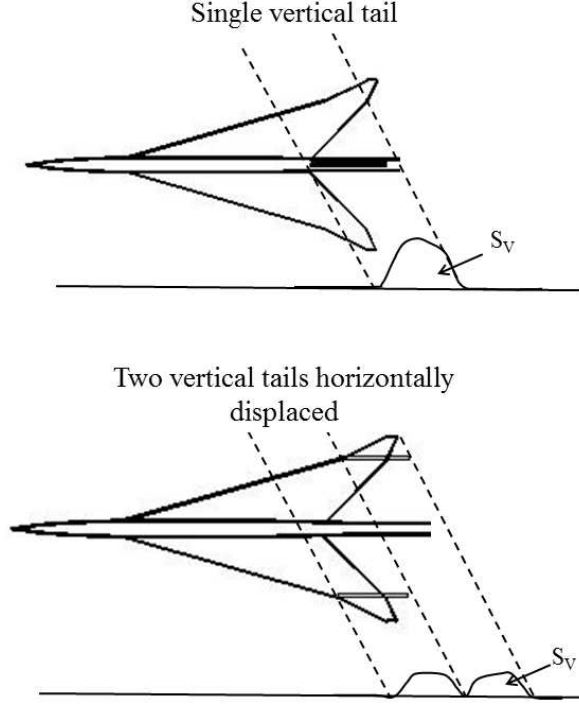
Figure 5.3: Area distribution of vertical tail on centerline compared to twin horizontally displaced tails.

Results for propagation angles of 45° and 180° can be seen in Figs. 5.4(d) and 5.4(e). For 45°, the agreement is very good despite the fact that RapidF models the verticals tails as one tail on the centerline. Examining the pressures for 180° in Fig. 5.4(e), RapidF under-predicts the wing's contribution from $\tilde{x} = 0.2$ to 0.3. The cause of this disagreement is not known and is unexpected because for all the cases thus far, RapidF has done an equal or better job matching the experimental results than Carlson's theoretical predictions. Therefore, an error in RapidF's lift or area calculations is ruled out. Furthermore, the results for 45° show proper application of

the trigonometry for cases where $\phi \neq 0$. Carlson discussed some model distortions that occurred when attaching the nacelles to the wings, and the wings to the fuselage. These issues of working with small wind tunnel models may account for disagreement for this case. He may have used a correction to get his theoretical estimate to match the wind tunnel data, but did not provided the details in the report.

The final test case is for Mach 2.0 which should assess how well RapidF accounts for Mach number changes. The results can be seen in Fig. 5.4(f). Compared to Carlson's theoretical method, RapidF more accurately predicts the shock locations from the nacelles. RapidF also does a better job at predicting the signal duration.

A summary of the metrics used to assess to accuracy of RapidF are summarized in Table 5.1 for RapidF compared to the theoretical solution from the NASA report. Despite the qualitative good agreement demonstrated in the figures, 16 of the 36 data points exceed the 10% threshold. To investigate this disagreement, the differences compared to the experimental results is presented in Tables 5.2 and 5.3. Both methods have about the same number of points outside of the 10% tolerance, nine for NASA TM X-1236 and seven for RapidF. While better agreement was desired, these results should be put in perspective. The wind tunnel model was small, 10.54 cm in length and the engine nacelles were 0.142 cm in diameter. NASA TM X-1236, was inspired by previous tests with a 2.5 cm long model (similar to Fig. 1.5(a)). NASA TX X-1236's test were scaled up from these tests in an attempt to mitigate the issues with manufacturing, measuring forces, vibrations and quantifying the boundary layer effects. Although the 10.45 cm model was better, some of these issues still exist. For example, lift was estimated by setting the angle of attack, because the model was too small for a force balance. The angle of attack was set based on the theoretical lift curve slope including an estimation of model deformation under test conditions with 10 psi of dynamic pressure. In fact, Carlson et al. concluded, "In view of the difficulty of constructing accurate small-scale models and the difficulty of evaluating boundary-layer effects for the models, there remains some doubt whether extrapolation of wind-tunnel results (based on theory) offers any increase in accuracy of flight overpressure estimates compared with estimates based on theory alone." [31]

Since only 35 data points were measured along the sonic boom, resolution is limited and the the shock locations had to be interpolated to obtain the data presented in Tables 5.2 and 5.3. Finally, NASA TM X-1236 only tested to 10 body lengths away. Modified linear theory is better suited for far field predictions. Thus, at this close distance, errors are magnified. If tests were conducted at farther distances, the differences would be less dramatic. As for disagreement between RapidF and the theoretical results, despite the fact that RapidF uses 550 points along the fuselage, the fuselage description in the NASA report only had 21 points. Therefore, RapidF had to interpolate between the data provided, and minimum improvements in results should be expected from the increased grid density. The bottom line is that RapidF is capable using a geometric description to predict the pressure profile of a wind tunnel model with various configurations, lift, Mach number and propagation angles.

(a) $C_L = 0$

(b) $C_L = 0.1$, with nacelles.

(c) $C_L = 0.1$, without nacelles.

(d) $\phi = 45^o$.

(e) $\phi = 180^o$.

(f) Pressure profiles for $M = 2.0$
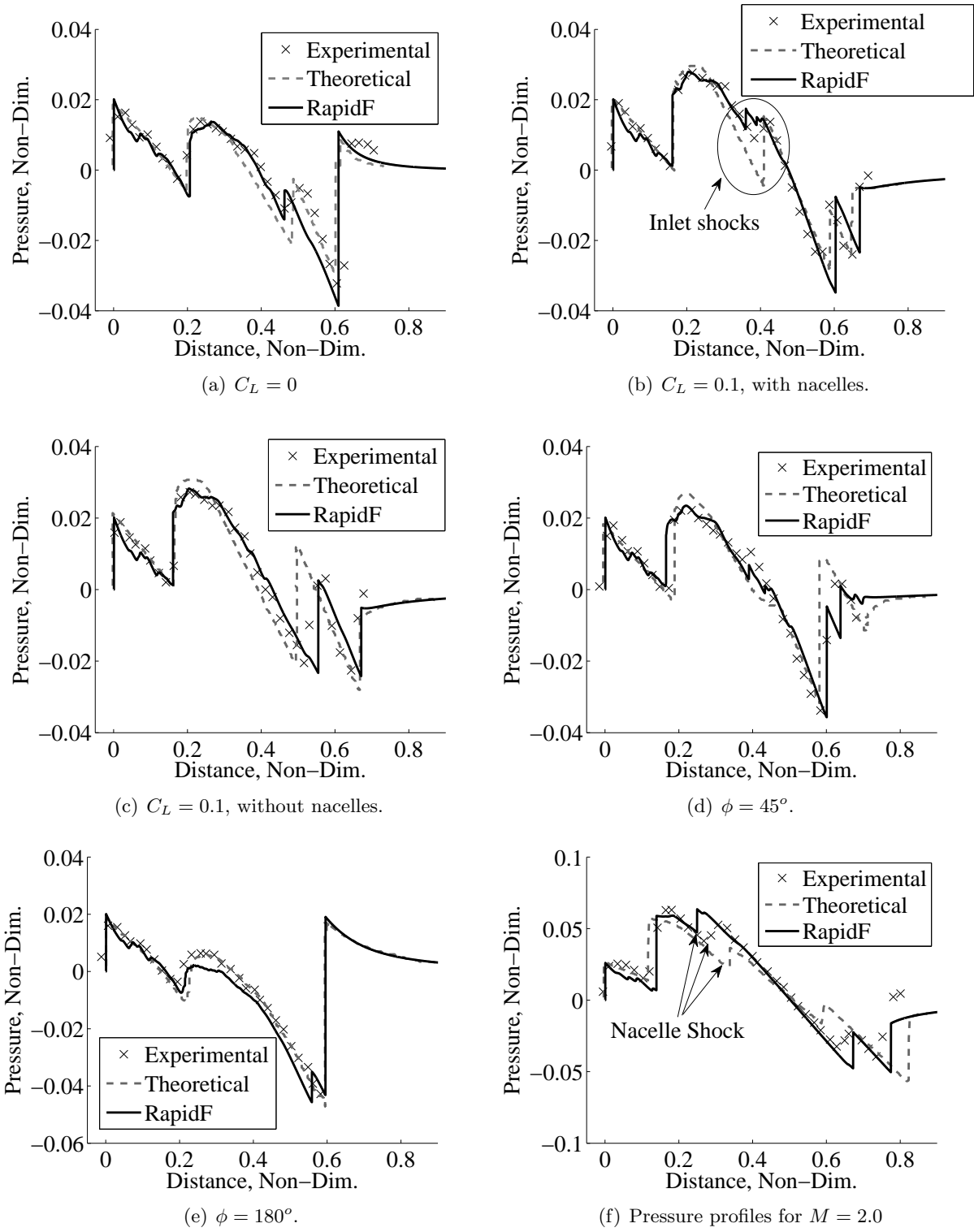
Figure 5.4: Pressure profiles of NASA TM X-1236 [31].

Table 5.1: RapidF Percent Difference from NASA TM X-1236 Theoretical [31]

Case	Location 1	Location 2	Location 3	p_{max}	p_{min}	Duration
$C_L = 0$	4.1	-4.3	N/A	**15**	**33**	1.4
$C_L = 0.1$	-1.2	**-12**	2.6	-5.7	**25**	3.1
No engines	-1.8	**12**	N/A	-8.1	**-14**	0.58
$\phi = 45^o$	**-12**	**-18**	3.4	**-17**	**14**	N/A
$\phi = 180^o$	1.7	N/A	N/A	**11**	2.6	0.17
$M = 2.0$	**19**	**-36**	**13**	**12**	**-11**	-5.5

Table 5.2: NASA TM X-1236 Theoretical Solution Percent Difference from Experimental [31]

Case	Location 1	Location 2	Location 3	p_{max}	p_{min}	Duration
$C_L = 0$	0	0.46	N/A	14	**-13**	-0.64
$C_L = 0.1$	-0.97	2.4	-0.34	6.8	**20**	-1.7
No engines	0.68	-6.3	N/A	13	**24**	0.88
$\phi = 45^o$	4.8	**20**	-3.3	**20**	-7.7	N/A
$\phi = 180^o$	-6.7	N/A	N/A	**13**	4.0	2.1
$M = 2.0$	-6.9	**35**	-8.3	**-15**	**42**	6.5

Table 5.3: RapidF Percent Difference from Experimental Data [31]

Case	Location 1	Location 2	Location 3	p_{max}	p_{min}	Duration
$C_L = 0$	4.1	-3.9	N/A	**31**	**16**	0.76
$C_L = 0.1$	-2.1	-9.9	2.3	0.72	**50**	1.4
No engines	-1.2	4.6	N/A	3.7	7.0	1.5
$\phi = 45^o$	-8.1	-1.3	0.0	-1.0	5.6	N/A
$\phi = 180^o$	-5.2	N/A	N/A	**26**	6.7	2.3
$M = 2.0$	**11**	**-13**	3.9	-4.1	**27**	0.65

5.2   Flight Test Comparisons

5.2.1   Lockheed F-104 Starfighter

Having demonstrated the ability of RapidF to predict sonic booms in the controlled wind tunnel environment, a demonstration of its ability to replicate sonic booms from flight tests is now appropriate. In addition to the more complex flow field with winds, turbulence and humidity; replicating sonic booms from flight test is also more challenging because the test aircraft is much more complex than a wind tunnel model. An aircraft has many minor protuberances such as lights, antennas, sensors, trim tabs, etc.. Thus, in order to properly predict its sonic boom, RapidF must account for the dominate features to obtain correct area distribution and F-function.

An example of the accuracy of RapidF's cross-sectional area estimate is can be seen in Fig. 5.5, where the cross sectional area of an F-104 from RapidF is compared to published data [87]. It is important to note that this is the actual cross-sectional area, sliced perpendicular to the longitudinal axis, not at the Mach angle. Although there is slight differences, RapidF's area profile has the correct shape and magnitude. Thus, RapidF has enough fidelity to capture the dominant features of an aircraft.
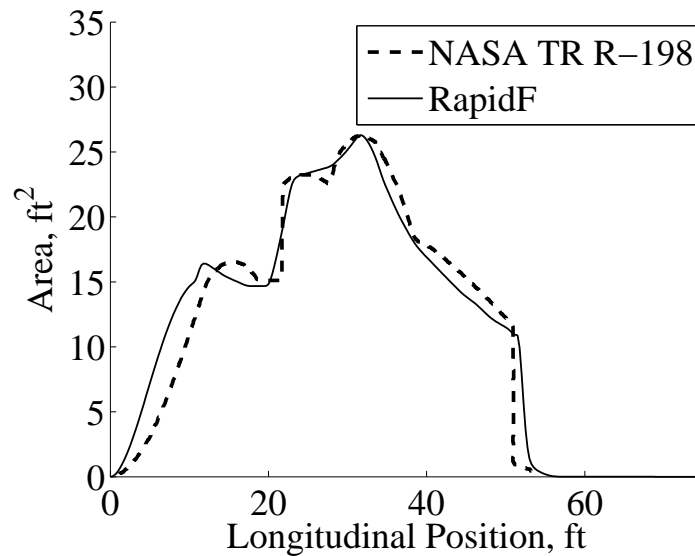
Figure 5.5: F-104 cross sectional area distributions from RapidF compared to NASA TR R-198 [87].

Figure 5.6 compares RapidF's F-function for a 15,000 lb F-104 flying at 20,000 ft at Mach 1.4 to that published by Hayes in 1968 [71]. In order to get the lobes to line up, Hayes's F-function had to be shifted 5 ft to the left. By doing this adjustment, one can see that both F-functions have the same general shape for the first 40 ft, but the magnitudes differ. In order to investigate these discrepancies, the F-function as presented in Eq. (2.59) can be inverted to find the area distribution [42]:

$$S_{\text{eq}}(y) = 4 \int_0^y F(\zeta)\sqrt{(y - \zeta)}\, d\zeta \tag{5.1}$$

The area determined from the above equation for Hayes's F-function is compared to that used by RapidF in Fig. 5.7. These results differ from the cross sectional area distribution shown in Fig. 5.5 in that they include lift, boundary layer growth and engine effects. They also differ in that the aircraft is cut at the Mach angle corrected for angle of attack. Both area profiles have the same shape except that Hayes's area is spread over a larger distance. The effective length of the aircraft was calculated to determine which area distribution is correct. The component that is farthest aft on the F-104 is the horizontal tail, which terminates at 54.8 ft [57] as shown in Fig. 5.8. Since the horizontal tail is 7.2 ft above the centerline, its influence will affect the area distribution until 61.9 ft. Thus, the effective length of the F-104 is 61.9 ft and after this location the area should remain constant. A vertical line is drawn at this location in Fig. 5.7. Since Hayes's area distribution continues to change past this location, it is concluded that there must be an error in his area profile. As another check, using the same process, the canopy's influence should be a maximum at 13.7 ft, yet Hayes's area distribution shows it at 20 ft. Therefore, it is concluded that our F-104 F-function is more accurate than Hayes's F-function.

Next, CUBoom's ability to properly predict how a sonic boom propagates through the atmosphere is accessed. The accuracy was checked by running multiple cases through ARAP [72] and CUBoom. For brevity, only one case is presented here. The F-104 F-function from NASA SP-180 presented in Fig. 5.6 was inputted into ARAP and CUBoom. Although this F-function is less accurate than RapidF's results were published in NASA SP-180, allowing comparison to historical
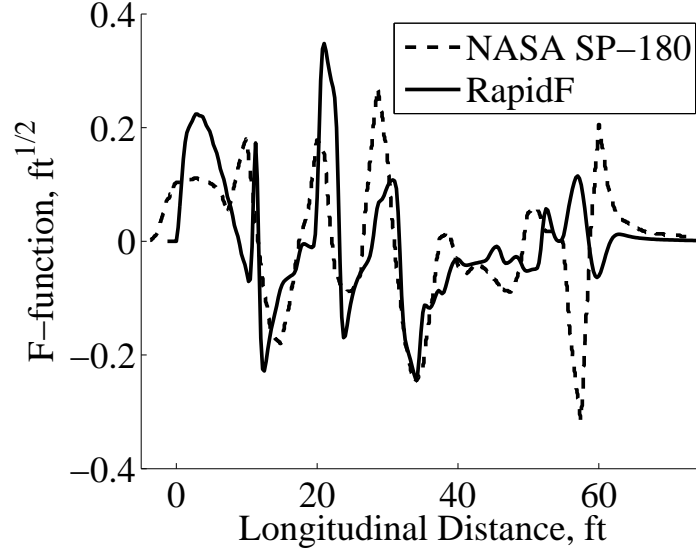
Figure 5.6: F-functions from RapidF and NASA SP-180 for a 15,000 lb F-104 cruising at Mach 1.4 and 20,000 ft [71].
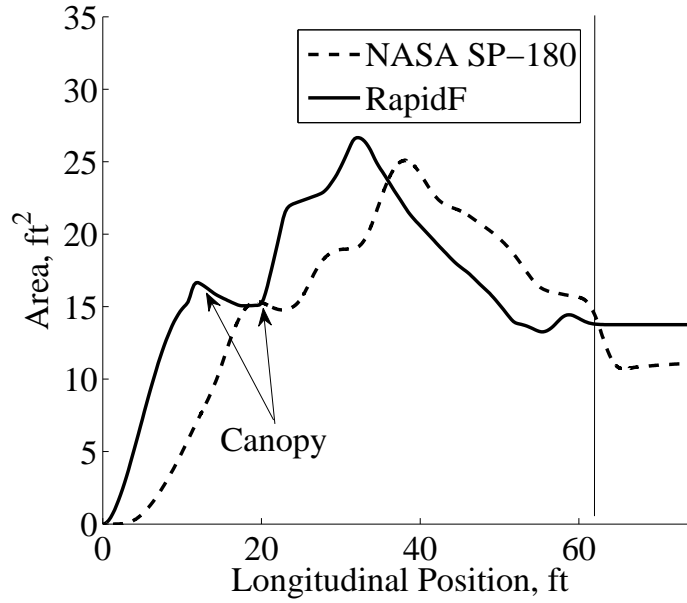
Figure 5.7: F-104 equivalent area distributions from RapidF and NASA SP-180 for same case as Fig. 5.6 [71].

data. The results for this case are summarized in Table 5.4 and Fig. 5.9. Since all values differ by less than 6% and the interior shock is in the correct location, it is concluded that CUBoom is
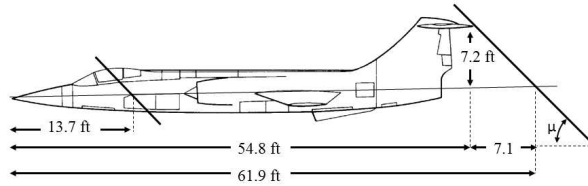
Figure 5.8: Side view of F-104 showing influence of canopy and horizontal tail [57, 71].

sufficient replacement to ARAP.

As a check of the entire RapidF system, Fig. 5.10(b) shows the sonic boom for an F-104 flying at Mach 1.5 and 28,000 ft compared to flight test data [77]. Since only surface weather was published, RapidF used standard day conditions and no winds. Despite the limited information, RapidF properly predicts that the sonic boom is a multi-shock, saw-toothed signature. The shocks for the flight test data are considerably more smoothed out by molecular relaxation, than predicted by RapidF. However, in general, RapidF captures all the key features of the signature. A unique feature of RapidF is demonstrated in Fig. 5.10, each portion of the sonic boom is shaded coded to allow the user to determine what part of the F-function and the aircraft creates that portion of the boom. Based on this information, it can be concluded that the interior shocks are caused by the inlet and wings, respectfully. The summary RapidF predicts the interior shock locations within 0.55% and 10%, respectfully and the duration with 0.52% difference than the flight test results. However, RapidF over-predicts the peak pressures by 14% and 13%, which is attributed to an underestimate of the molecular relaxation impact on rise times.

Table 5.4: Comparison of CUBoom to ARAP [71]

	ARAP	CUBoom	% Difference
Horz. Dist. (ft)	194,300	193,500	**-0.41**
Ray Area (ft)	19,040	18,960	**-0.42**
Age (ft/$\sqrt{\text{ft}}$)	703.5	717.7	**2.0**
Δp_{max} (psf)	2.17	2.21	**1.8**
Δp_{min} (psf)	-2.37	-2.23	**-5.9**
Duration (sec)	0.080	0.078	**-2.5**
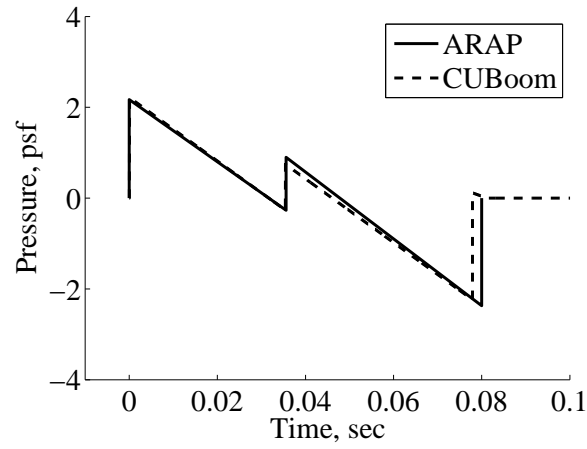
Figure 5.9: Sonic booms from ARAP and CUBoom using NASA SP-180 F-function in Fig. 5.6 [71].

(a) Profile.
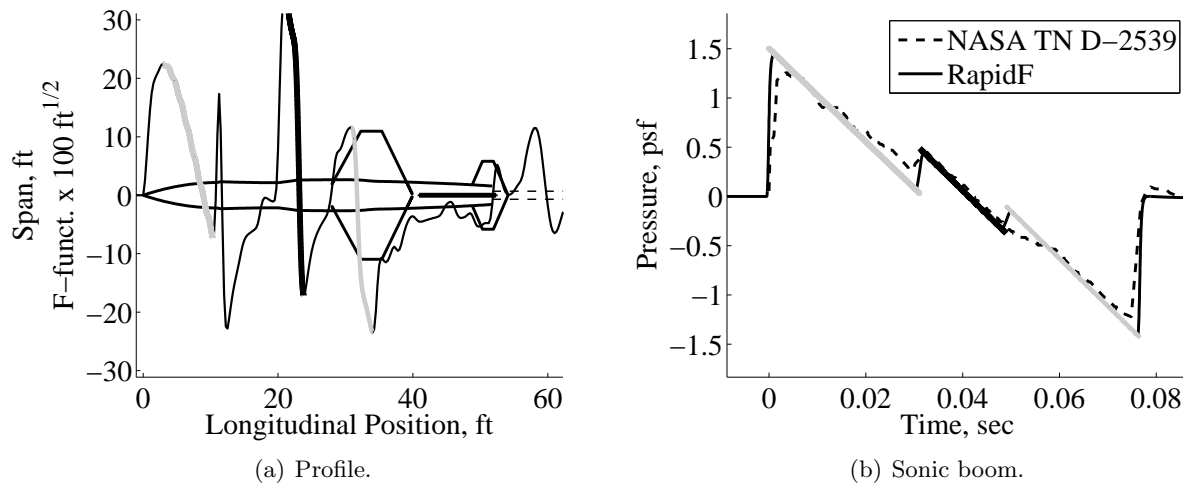
(b) Sonic boom.

Figure 5.10: Sonic boom from RapidF of a F-104 flying at Mach 1.5 and 28,000 ft compared to flight test results [77].

5.2.2   Shaped Sonic Boom Demonstrator

A second example of RapidFs sonic boom prediction capability is shown in Fig. 5.11 for the Shaped Sonic Boom Demonstrator (SSBD) flying at Mach 1.4 and 32,700 ft [99, 131]. For this case atmospheric data was available and entered into RapidF. The CFD solution presented was accomplished prior to flight by Lockheed-Martin using SPLITFLOW3D using an inviscid solver with 5.5 million cells. The CFD solution was propagated to the ground using PCBoom [147]. As summarized in Table 5.5, RapidF is just as accurate as the CFD. However, the CFD predicts a weak shock at 0.022 seconds that does not exist in RapidF or the flight test data. RapidF's solution properly predicts all other metrics within 10% of the flight test results. Considering the speed of RapidF, 20 seconds on a PC, and the fact that it requires no mesh generation, the slight decrease in accuracy of RapidF is good are off for the time savings.
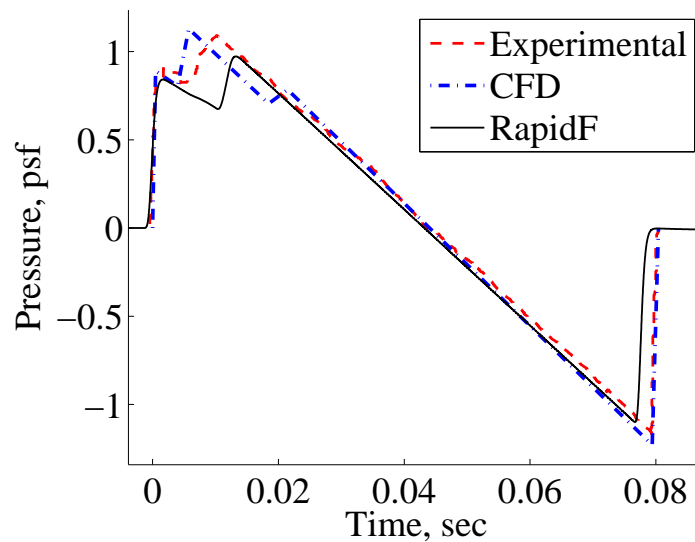
Figure 5.11: SSBD sonic boom from RapidF compared to experimental results for Mach 1.41 and 32,700 ft [99].

Table 5.5: RapidF and CFD Percent Error Compared to SSBD Flight Test [99, 131]

	ISPR	Shock Location	p_{max}	p_{min}	Duration
RapidF	-4.8	3.6	-10	-4.1	-1.9
CFD	0.0	-5.7	4.3	7.3	0.0

5.2.3   North American XB-70 Valkyrie

Newly refined XB-70 sonic boom data was published by Maglieri, Henderson and Tinetti in 2011 [117]. Although the testing was conducting in 1966 the data was never fully reduced to a usable form. Maglieri recognized that the data was valuable for code verification because the sonic booms were recorded in the upper atmosphere, free from the majority of the distortions created by the earth's boundary layer; thus the data was "clean." Also, the sonic booms had multiple shocks and were not simple N-waves. Furthermore, there were multiple data runs at different ranges and angles, thus allowing many comparisons. For these tests the XB-70's weight ranged from 340,000 to 350,000 lbs, the Mach number from 1.47 to 1.50 and altitude from 37,584 to 37,917 ft. Although the specific flight conditions were inputted into RapidF, they can be interpreted as nominally the same: 345,000 lbs, Mach 1.5 at 37,500 ft. The 1966 in-flight data was obtained by flying a F-104 through the sonic boom with a specially designed pressure probe. Due to the difficulty in transforming the sonic boom data to a static frame of reference, in flight sonic booms are presented with respect to a non-dimensional distance (distance / signal length).

Images of the XB-70 can be seen in Fig. 5.12. RapidF's XB-70 model was made from geometric description from NASA CR-2011-217078 [172] and NASA TP 1516 [11] and can be seen in in Fig. 5.13. The aircraft had several features that made inputing into RapidF difficult. First, it has twin vertical tails, but RapidF only accepts one (Later, RapidF was modified to accept two vertical tails). As was done for the NASA TM X-1236 model, this was handled by inputting one vertical tail and doubling the airfoil thickness. Second, the XB-70 has a hinged wing allowing the outer portion to deflect down during flight, as shown in Fig. 5.14. This was accounted for by projecting the wing tip onto the wing horizontal plane, which appears as a wing sweep change in

(a) Planform.

(b) Side view.
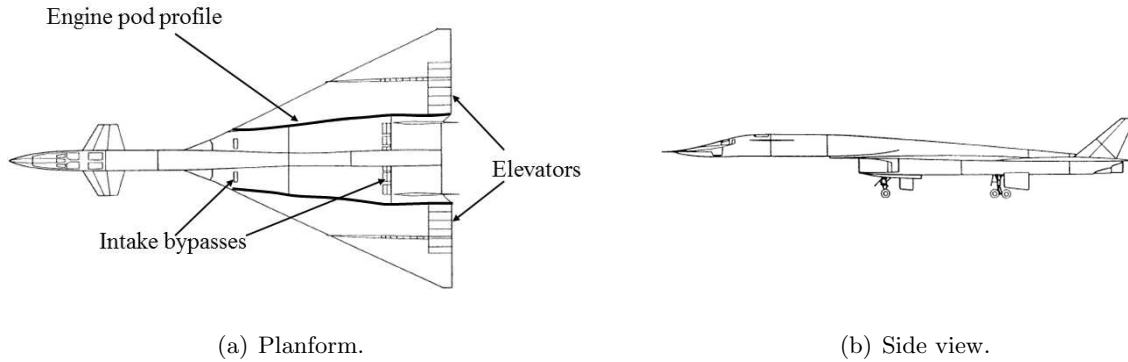
Figure 5.12: XB-70 drawings [117].

Fig. 5.13(a). The vertical projection was modeled as a single ventral fin, as seen in Fig. 5.13(b). Like the vertical tail, the thickness was doubled since RapidF does not accept two ventral fins. The canard deflection was published for each data set and accounted for in RapidF, but the elevator deflections were not modeled. Although, the XB-70 has two inlets which distribute airflow to six engines, the engines were modeled as two large engines. The inlet capture area is published, as well as, the percent of spillage. This allowed the authors to quantify the effective area of the engine inlets. The exhaust pressure ratio was set assumed to be 4.7. RapidF models engines as cylinders, but the XB-70's engine pod has a significant area increase as shown in Fig. 5.12(a). This was accounted for by adding area to the fuselage at the correct longitudinal distance (area increase can be seen in Fig. 5.13(a) from 120 to 170 ft). The ducts have a system of bypasses to bleed off excessive airflow through the inlet, see Fig. 5.12(a). Although this bleed does contribute the the effective cross sectional area, it was not modeled. As a check of the quality of RapidF's XB-70 model its performance was compared to published data [11, 172] as shown in Table 5.6. Besides the coefficient of drag, all other metrics match reasonable well.

Sonic booms for 26 body lengths are shown Fig. 5.15. RapidF's solution is missing one interior shock. This can be fixed by increasing the percent spillage from the published 38% to 100%, as shown on Fig. 5.16. Although this is an artificial fix, it demonstrates that RapidF's simple cylindrical nacelle model lacks the fidelity required to capture actual flight conditions. The ground

(a) Planform.

(b) Side view.
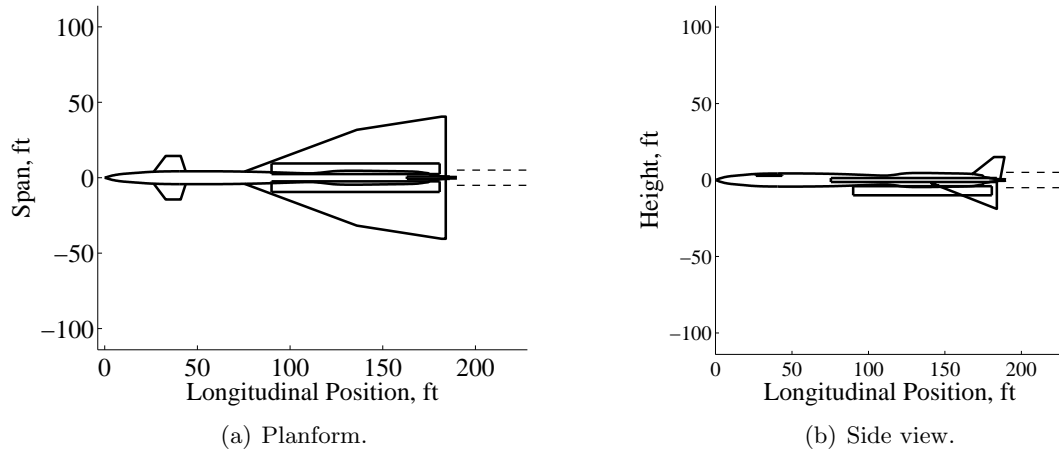
Figure 5.13: RapidF XB-70 model.

Projection onto
wing's plane

Wing tip in
65°position

Projection
onto vertical
plane
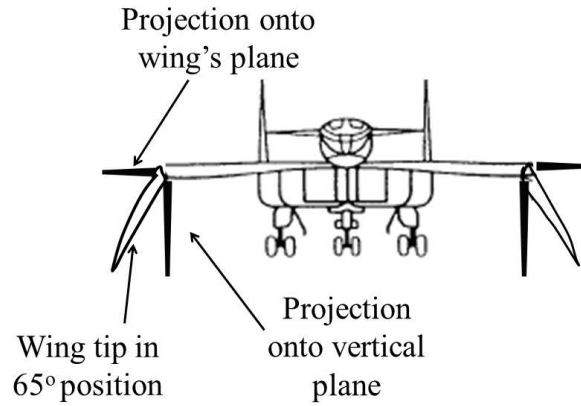
Figure 5.14: RapidF XB-70 wingtip projections.

Table 5.6: Comparison of XB-70 Performance for Mach = 1.67, AoA =3.5^o [11, 172]

	Planform (ft^2)	MAC location (ft)	Empty Weight (lbs)	C_L	C_D
Published	6,298	78.53	270,000	0.10	0.019
RapidF	6,291	78.53	252,700	0.11	0.024

(a) Planform and F-function.
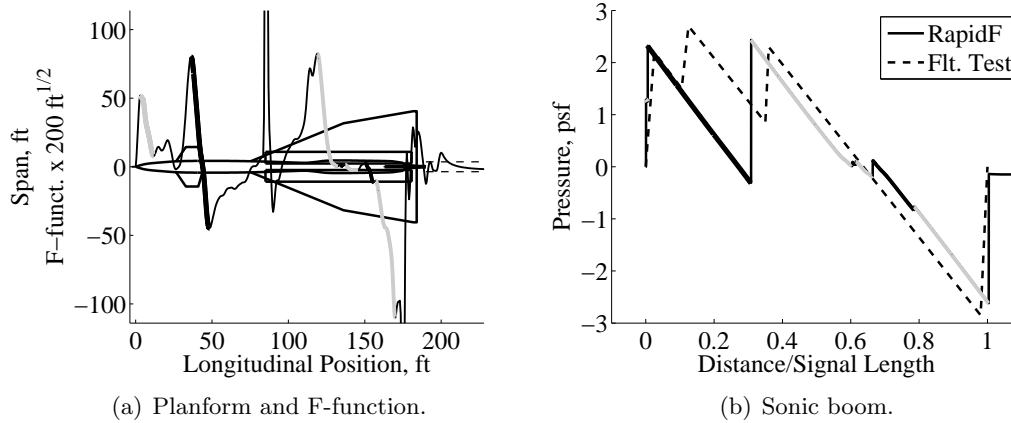
(b) Sonic boom.

Figure 5.15: Sonic booms for XB-70 at 26 body lengths [117].

sonic booms are shown in Figs. 5.17 and 5.18 for the un-modified and modified cases, respectfully. Since the ground measurements did not have the issues with a moving reference frame, they are presented with a dimensional horizontal axis of seconds. The experimental results are the average of six microphones at discrete locations: leading shock, interior shock, and trailing shock. Thus, the results do not show any effects of turbulence or molecular relaxation. The results are summarized in Table 5.7. In general, RapidF does has difficulty in replicating the XB-70 sonic boom. Without knowing what the boom looked like, the problem of the missing interior shock would not have been known. Furthermore, without modification, the peak ground pressure is under predicted by 28%. Therefore it is concluded that RapidF has limited ability in predicting sonic booms of aircraft with complex geometry.

(a) Planform and F-function.
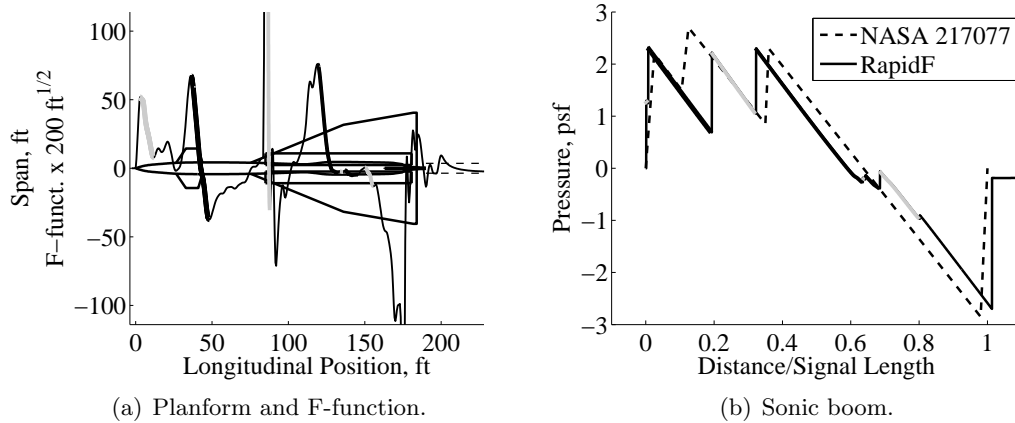
(b) Sonic boom.

Figure 5.16: Sonic booms for XB-70 at 26 body lengths with modifications [117].

(a) Planform and F-function.
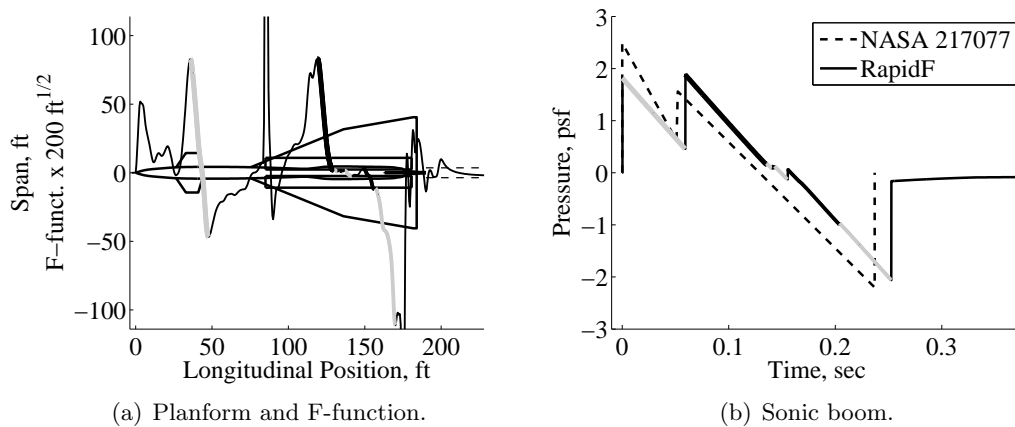
(b) Sonic boom.

Figure 5.17: Sonic booms for XB-70 at the ground [117].

(a) Planform and F-function.
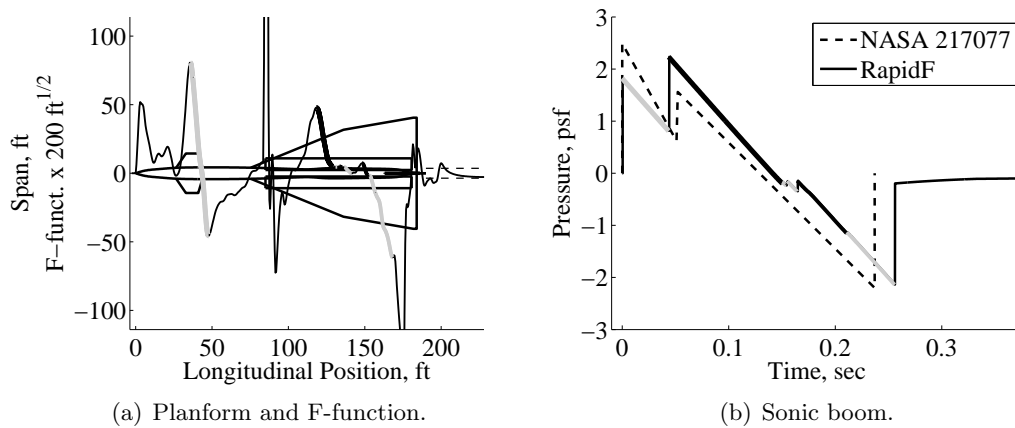
(b) Sonic boom.

Figure 5.18: Sonic booms for XB-70 at the ground with modifications [117].

Table 5.7: Percent Error of RapidF Compared to XB-70 Flight Test [117]

	Location 1	Location 2	p_{max}	p_{min}	Duration
26 Body lengths	**N/A**	**-14**	-10	- 8.1	N/A
26 Body lengths, modified	**55**	- 10	**-15**	-6.0	N/A
Ground	**17**	N/A	**-28**	-6.4	6.5
Ground, modified	**-15**	N/A	**-12**	-2.7	7.9

5.3   Conclusions about RapidF

The intent of this chapter was to demonstrate the accuracy of RapidF to replicate historical sonic booms, so that the user can trust the software to predict the sonic boom of his design. The comparison of RapidF to NASA TM X-1236 showed that RapidF is capable of replicating changes of Mach number, lift, configuration and propagation angle. The flight test comparisons show that RapidF captures the dominate characteristics of an aircraft's lift and area profile enabling it to properly predict the far field sonic boom. The final test explored the limits of the modified linear code. The XB-70's complicated geometry, unique nacelle design and the bleed air made it difficult to predict its sonic boom. Despite these challenges, it was able to predict the correct shape and duration of the sonic boom on the ground. Based on these results several modifications were made to RapidF, such as adding the ability to have twin vertical tails.

Chapter 6

SONIC BOOM FREEZING AND LOBE-BALANCED DESIGN

In Chapter 1, several shaped N-waves were presented that should reduced the human reaction to a sonic boom. However, there is another option to reduce the annoyance of the sonic boom on humans, a multi-shock signature, as shown in Fig. 1.3(d). The most significant part of a sonic boom that contributes to the subjective loudness rating is the leading pressure rise [40, 106]. As will be demonstrated later, a multi-shock sonic boom has a weaker leading shock and a lower PLdB value; thus it is more acceptable to humans. In order for an aircraft to create this type of sonic boom, the interior shocks must be stationary, thus *frozen* in the mid-field. The purpose of this chapter is to explore how to design a supersonic aircraft that produces a multi-shock sonic boom in order to minimize the annoyance to humans.

The goal of this chapter is to use modified linear theory and/or weak shock theory to freeze a multi-shock sonic boom pressure signal in order to reduce its impact on humans. Metrics are needed to quantify the anticipated human response to a sonic boom. ISPR has been used for decades and many studies have shown good correlation of ISPR to human subjective ratings [106]. Therefore, it will be used as the primary quantity to evaluate sonic booms. However, there is no standard definition of what is "quiet" enough. In recent studies, the goal of getting the ISPR below 0.3 psf has been used, based on DARPA's Quiet Supersonic Platform program requirements [51]. However, other studies have suggested below 1.0 psf would be acceptable [38]. This study will use 1.0 psf as a benchmark. In addition to ISPR, perceived level of loudness (PLdB) will also be used as a metric. PLdB is a variation of the decibel used in acoustics, where each third octave frequency

band is weighted based on the sensitivity of the human ear [167]. NASA has set a target of 70 PLdB for supersonic flight over land without restrictions [176]. PLdB will be discussed in dept in Chapter 10.

Examining Eq. (2.64), one will note that there are two factors that affect the acoustical distortion that cause pressure signals to develop into N-waves: the age variable and the F-function, either one can freeze a pressure signal. The first part of this chapter investigates whether the atmosphere can freeze a pressure signal by causing τ to approach a limit as the sonic boom propagates to the ground. The second part examines how a *lobe-balanced* F-function can freeze the pressure signal. Then, an example SBJ design is presented that creates a frozen sonic boom using lobe balancing.

6.1   Atmospheric Signature Freezing

Atmospheric freezing can be explained by a quote from Hayes [72]:

> If τ gets very large, the signal shape approaches that of an N-wave. ... The presence of the factor $1/\sqrt{\rho}$ in the integral of [Eq. (2.72)] indicates that for downward propagating rays in a real atmosphere the integral will be convergent; thus τ approaches a limiting value $\tau_{\lim}$ as z approaches $-\infty$. Thus the signal shape "freezes" and does not become the ever-thickening N-wave of common far-field theory.

This quote is often used to justify the existence of atmospheric freezing [10,51,122,138,151,162,163]. Hayes refers to his 1968 paper [70], which gives credit for this idea to Busemann [28]. However, neither of these references provides more clarification. The following discussion explores how Hayes came to this conclusion.

In order to simplify Eq. (2.72), an analytical equation for the ray area, A is required (Hayes uses numerical integration). So, for this analysis George and Plotkin's formula is used [146]:

$$A = \frac{A_1}{z_1} M_1 \sqrt{1 - \frac{1}{M_2^2}} \int_{z_1}^{z_2} \frac{dz}{\sqrt{M^2 - 1}} \tag{6.1}$$

which in homogeneous and isothermal atmospheres reduces to:

$$A = \frac{A_1}{z_1} z_2 \tag{6.2}$$

This is also a reasonable approximation for the real atmosphere, since the variations of the speed of sound with altitude are small (13% variation from sea level to the stratosphere [135]). By substituting the above equation into Eq. (2.72) for a quiescent atmosphere, where $\cos\theta \sin\theta = \beta/M^2$, and using the definition of an isothermal atmosphere, $\rho = \rho_1 \exp\left((z - z_1)/\mathcal{H}\right)$:

$$\tau_{\text{iso}} = \frac{1}{2c_0} \frac{(\gamma + 1)M^4}{\sqrt{2\beta^3}} \int_{z_1}^{z_2} \frac{1}{\sqrt{z \, \exp\left((z - z_1)/\mathcal{H}\right)}} dz \tag{6.3}$$

Again this is a good estimate for the age variable for the real atmosphere ($\tau \approx \tau_{\text{iso}}$). For a homogeneous atmosphere:

$$\tau_{\text{homo}} = \frac{1}{2c_0} \frac{(\gamma + 1)M^4}{\sqrt{2\beta^3}} \int_{z_1}^{z_2} \frac{1}{\sqrt{z}} dz \tag{6.4}$$

Hayes arrives at the above conclusion by setting $z_2 = \infty$ and $z_1 = 0$. Then, Eq. (6.3) becomes:

$$\tau = \frac{1}{2c_0} \frac{(\gamma + 1)M^4}{\sqrt{2\beta^3}} \sqrt{2\pi\mathcal{H}} \tag{6.5}$$

By setting $z_1 = 0$, Eq. (6.4) simplifies to:

$$\tau_{\text{homo}} = \frac{1}{c_0} \frac{(\gamma + 1)M^4}{\sqrt{2\beta^3}} \sqrt{z_2} \tag{6.6}$$

which is consistent with Eq. (2.65). By setting the right hand sides of the equations above equal to each other, he concludes that the advance approaches a limiting asymptotic value equal to that of the advance in a homogeneous atmosphere at $z = \pi\mathcal{H}/2$.

The impact of setting $z_2 = \infty$ is depicted in Fig. 6.1, which shows the age variable for an aircraft flying at Mach 1.7. The age variables presented in this figure are obtained by numerical integration of Eq. (2.72) in a standard/homogeneous atmosphere without any simplifying assumptions. Figure 6.1(a) is for an aircraft cruising at 160,000 ft. Although this is not a realistic altitude for a near term supersonic civil aircraft, this altitude was chosen to maximize the chance of the age variable approaching a limiting value. As predicted by Hayes, the age variable for the standard atmosphere does approach a limit (0.47 sec/$\sqrt{\text{ft}}$) and reasonably matches the age variable (0.48 sec/$\sqrt{\text{ft}}$) for $\pi/2$ scale heights below the aircraft in a homogeneous atmosphere, indicated by cross hairs. The modest difference is attributed to the differences in isothermal and standard

atmospheres. However, this case has limited application since civil supersonic aircraft will probably cruise under 100,000 ft.

Figure 6.1(b) presents the age variable for a more realistic cruise altitude of 51,000 ft. For this case the standard atmosphere age variable has not reached the asymptotic limit, nor does the value at the surface match the homogeneous atmosphere for $\pi/2$ scale heights. If the age variable were used for the homogeneous atmosphere at $\pi/2$ scale heights, this would cause an over prediction in the age variable by 24%. In general, the growth of the age variable slows as the pressure signal approaches the earth. However, for realistic cruise altitudes, it is not appropriate to use the asymptotic limit. Both Cleveland [36] and Plotkin [143] also demonstrated this fact. Plotkin noted that most of the distortion occurs in the first couple thousand feet and although the sonic boom does not freeze, it does "chill." However, designers cannot rely on the atmosphere to prevent a pressure signal from developing into an N-wave.

6.2   Signature Freezing by F-Function Lobe Balancing

Lobe balancing was briefly introduced in Chapter 1. In order further explain the concept, two examples are presented to show the benefits and limitations of the technique. The first example is shown in Fig. 6.2. The F-function starts with a small positive lobe followed by three small balanced lobe pairs. A balanced lobe pair refers to a negative lobe followed by a positive lobe with equal areas. The small lobe pairs are followed by two large balanced lobe pairs. As shown in Fig. 6.2(b), the pressure signature after 51,000 ft of propagation has not coalesced into an N-wave because the balanced pairs generate stationary or frozen shocks. Even when the F-function is propagated from 100,000 ft, as in Fig. 6.2(c), the sonic boom retains its shape; thus, this pressure signal is truly frozen.

Each portion of the pressure signal and the F-function in Fig. 6.2 are shaded to allow the reader to determine where parts of the sonic boom came from. Despite the fact that the leading lobe has the same magnitude in the F-function as the small balanced pairs, after propagation, its overpressure is significantly higher than the stationary shocks (0.84 to 0.094 psf for the 51,000 ft
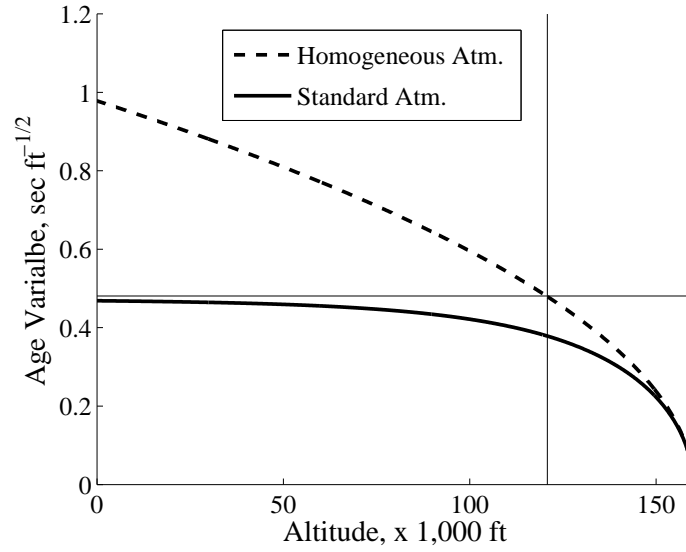
(a) Cruise altitude = 160,000 ft.
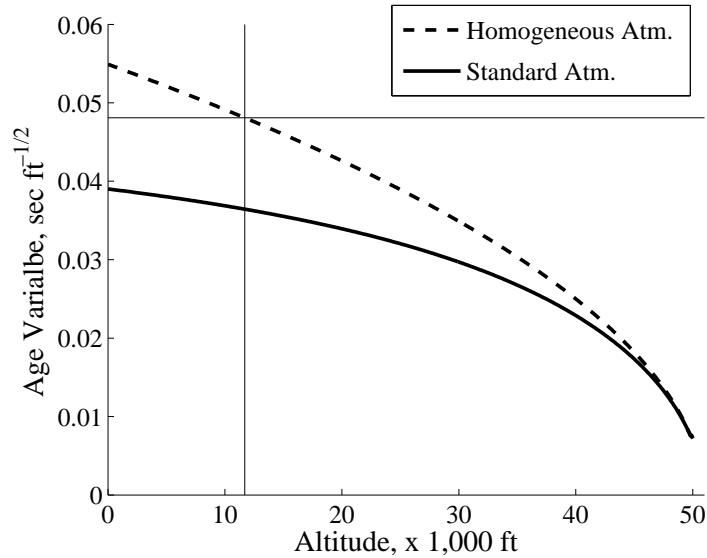
(b) Cruise altitude = 51,000 ft.

Figure 6.1: Age variable for homogeneous and standard atmospheres for aircraft flying at Mach 1.7.

case). Based on this observation, a casual reader may wonder why a designer does not balance this lobe by starting with a negative lobe. However, this would require the nose of the aircraft to have relatively low static pressure, when in fact this area must have high pressure since it is a stagnation point. It can be concluded that lobe balancing is unable to influence the leading positive lobe.

(a) F-function.

(b) Sonic boom from 51,000 ft.

(c) Sonic boom from 100,000 ft.
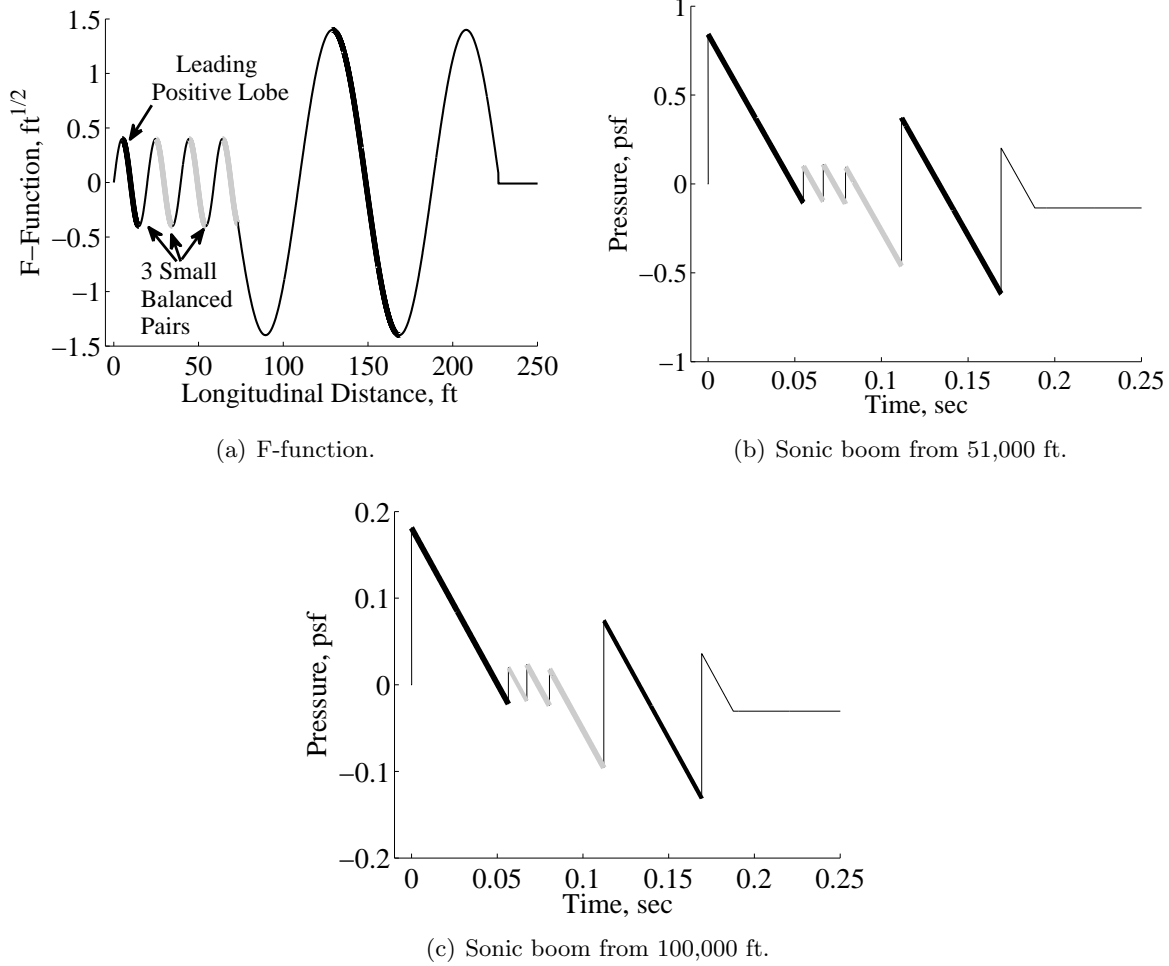
Figure 6.2: Example of a lobe-balanced F-function and corresponding ground pressure profiles.

Thus, the overpressure created by the leading lobe represents the lower limit for lobe balancing.

The second example, as seen in Fig. 6.3, highlights another limitation of lobe balancing. The F-function is identical to that used in Fig. 6.2 except the two large lobe pairs are inverted, creating a positive to negative pair. With no preceding negative lobe, the large positive lobe advances and the coalesces with the series of small shocks created by the three small balanced lobes and the leading shock, resulting in a large increase in the initial overpressure, from 0.84 to 3.0 psf, and a significant increase in duration and impulse (NOTE: different scales are used in Fig. 6.2(b) and Fig. 6.3(b)). Likewise, the trailing negative lobe lacks a balancing positive lobe, causing a large increase in magnitude of the trailing shock. This example demonstrates two important facts about

lobe balancing. First, the order of the lobes is critical. There must be a negative lobe followed by a positive lobe. Second, in order to use lobe balancing to freeze a sonic boom, the entire aircraft's F-function should be considered.

(a) F-function.

(b) Sonic boom from 51,000 ft.
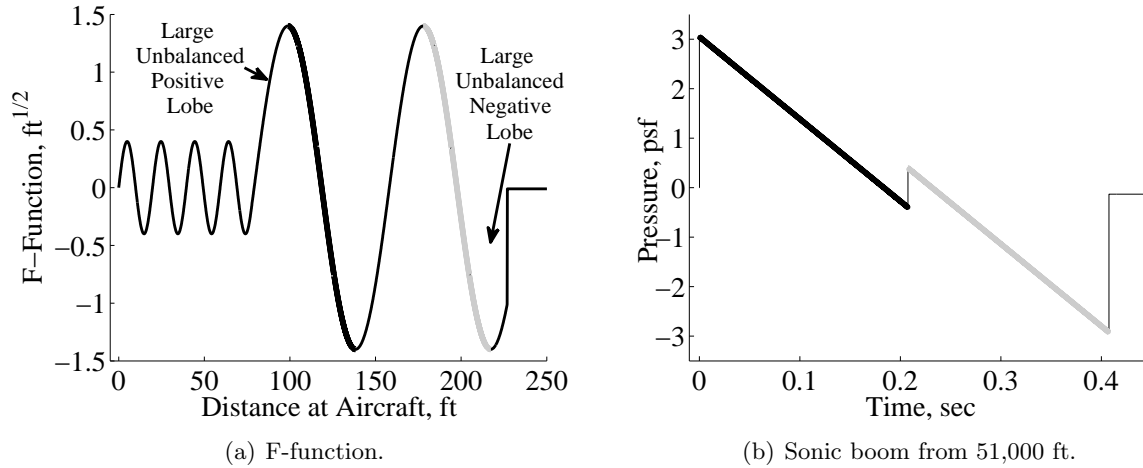
Figure 6.3: Example of incorrect lobe balancing and corresponding ground pressure profile.

6.3   Aircraft Design using Lobe Balancing

6.3.1   Component analysis

In order to apply lobe balancing to an aircraft design, the ability of components to create positive or negative lobes must be known. Figure 6.4 shows each aircraft component's impact on the F-function superimposed on a planform view of the aircraft. In this figure components are not positioned in their traditional locations, but positioned in the middle of the fuselage so that their effect on the F-function is not obscured by the nose cone or boat tail.

- **Fuselage**: As shown in Fig. 6.4(a), the fuselage is 160 ft long, 7 ft wide and has a 50-ft ogive nose and 40-ft ogive boat tail. Its F-function has a weak overpressure at the nose followed by a modest expansion as the nose merges to the fuselage. As shown in Fig. 6.5, the ogive nose was selected over conical and power noses because this expansion can be used to balance the overpressure from the wing as will be shown later.

- **Engines**: This study uses two externally mounted F-100 engines. The nacelles are estimated to be 6 ft in diameter by 28 ft in length which includes the inlet. Although RapidF can account for various nozzle pressure ratios, this study assumes the exhaust is perfectly expanded. As seen in Fig. 6.4(b), the nacelles have a leading weak overpressure caused by the cowl shock and a minor expansion at the engine termination.

- **Vertical tail**: The vertical tail, as seen in Fig.6.4(c), has a limited effect on the F-function. The vertical tail's displacement from centerline distributes the area over a wider range of longitudinal distances, reducing the F-function magnitude.

- **Radius change**: Figure 6.4(d) shows the impact of a 1.3 ft positive and negative fuselage radius changes distributed over 10 ft, which make corresponding positive and negative lobes.

- **Canard**: The canard has 50° and -30° leading and trailing edge sweeps, and a 35 ft chord. In Fig. 6.4(e), the F-function is shown for two incidence angles. Since the airfoil used in this study, NACA 65A003, is symmetric, the F-function at 0.0^o of incidence is only from the canard's cross sectional area. At 4.0^o of incidence, lift creates a large overpressure and reduces the expansion at the trailing edge.

- **Wing**: The wing has 49° and -20° leading and trailing edges and a 90 ft span. Small 65° strakes are used to enhance low speed lift. As seen in Fig. 6.4(f), the wing creates a similar F-function as the canard, but larger in scale. The wing planform shape was selected because it creates distinct lobes which can be balanced. An example of a more conventional supersonic wing shape is shown in Fig. 6.6. This wing has subsonic leading and trailing edges which should decrease drag, but leaves no room before and after to add other components.

In comparison to other components, the wing creates the largest pressure changes and its lobes will need to be balanced using the other components. Since the theory being used is a linear theory,

(a) Fuselage.

(b) Engine nacelles.

(c) Vertical Tail.

(d) Radius Change.

(e) Canard.

(f) Wing.
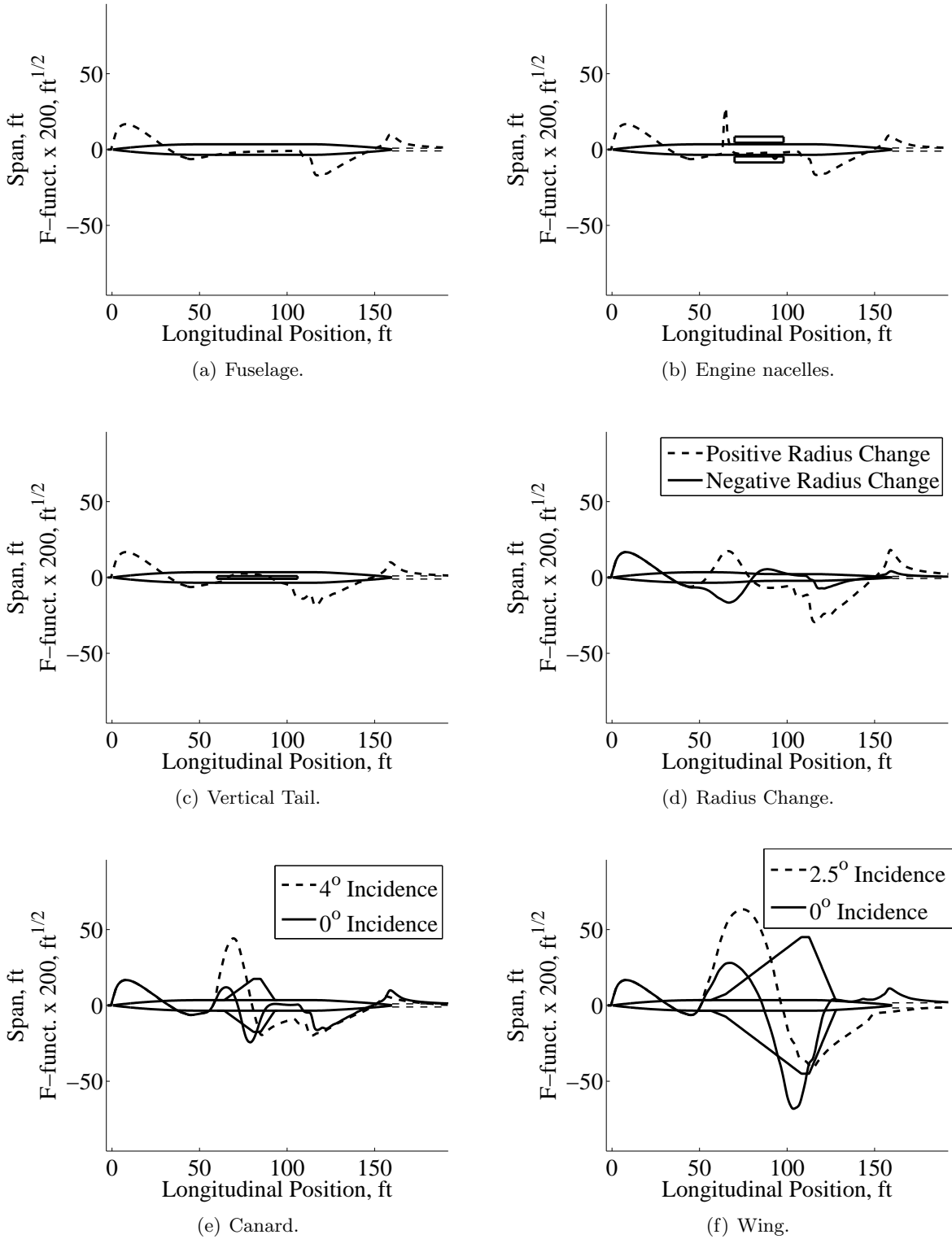
Figure 6.4: F-functions of individual components.
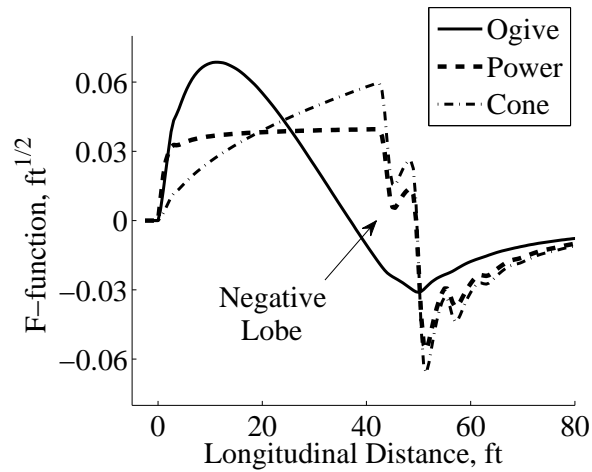
Figure 6.5: F-functions of various noses.
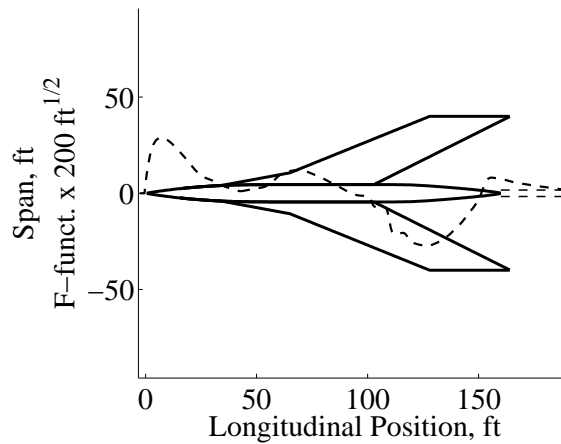
Figure 6.6: Planform view and F-function of design with highly swept wings.

superposition can be used to assemble an aircraft. However, there are limitations. For example, the F-function from a canard and a radius increase will not be exactly the sum of the two because the radius change will reduce the exposed area of the canard, reducing its lift.

6.3.2   Design build-up

As a sample of how lobe balancing can be used, it is now applied to a 120,000-lb SBJ, which is assumed to be cruising at Mach 1.7 at 51,000 ft. The fuselage effects are shown in Fig. 6.7. The leading shock and the trailing shock have pressure rises of 0.55 and 0.50 psf, respectfully, which are

the minimum pressures that can be obtained after adding the other components. Next, the wing, engine nacelles and vertical tail are added, as shown in Fig. 6.8(a). This will be referred to as the baseline configuration. The aircraft is at 0.62^o angle of attack and the wing is at 0.84^o of incidence, producing 118,300 lbs of lift (The remaining lift is produced by the fuselage.), with $L/D = 7.4$. As shown in Fig. 6.8(b), the wing's overpressure has merged with the leading shock, increasing the ISPR to 1.4 psf. Likewise, the wing's trailing edge expansion has merged with the rear shock, increasing the TSPR to 1.2 psf.

(a) Profile view.
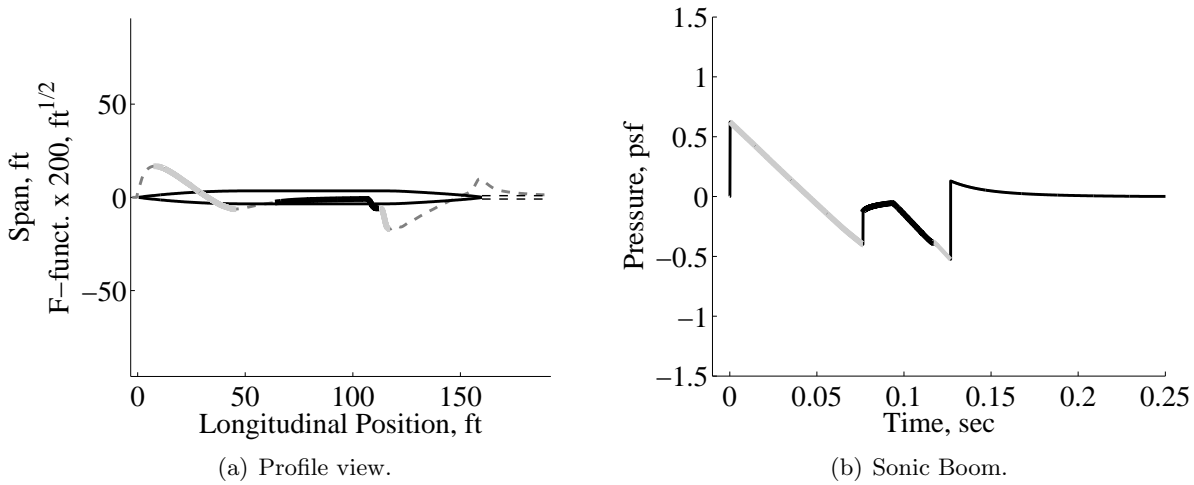
(b) Sonic Boom.

Figure 6.7: Profile view and sonic boom of fuselage.

The objective is to add other components to reduce the leading and trailing shocks by lobe balancing. A balancing line is drawn in Fig. 6.8(a), to show the negative lobe from the nose-to-fuselage intersection is too small to balance the wings overpressure. A canard is added such that its trailing edge increases this area of low pressure from the fuselage. This canard can be used to create two pressure signatures. As shown in Fig. 6.9, the canard is deflected just enough to prevent the wing's overpressure from coalescing with the leading shock, producing an ISPR of 0.84 psf, as shown in Fig. 6.9(a). This will be referred to as the PR_{min} trim condition. This configuration is similar to lobe balancing from Ref. [9] shown in Fig. 1.8. In the second case, the canard is deflected further to produce 34,000 lbs of lift. This allows the incidence angle of the wing to be reduced which decreases the strength of its overpressure, helping to bring the two lobes into balance. The

shock from this case is shown in Fig. 6.10(b). The ISPR is 1.0 psf, which is sightly higher than the PR_{min} trim condition, but since the interior and the leading shocks have the same magnitude, the pressure signal is completely frozen and will retain its shape even if propagated further. This will be hereafter referred to as the *Frozen* trim condition.

Next the rear shock is modified. In order to prevent the wing's negative lobe from retreating (see Fig. 6.10(a)), a positive lobe needs to be created behind the wing. Since the nacelles and vertical tail have very minor impact on the F-function, other components are used. One option is

(a) Profile view.
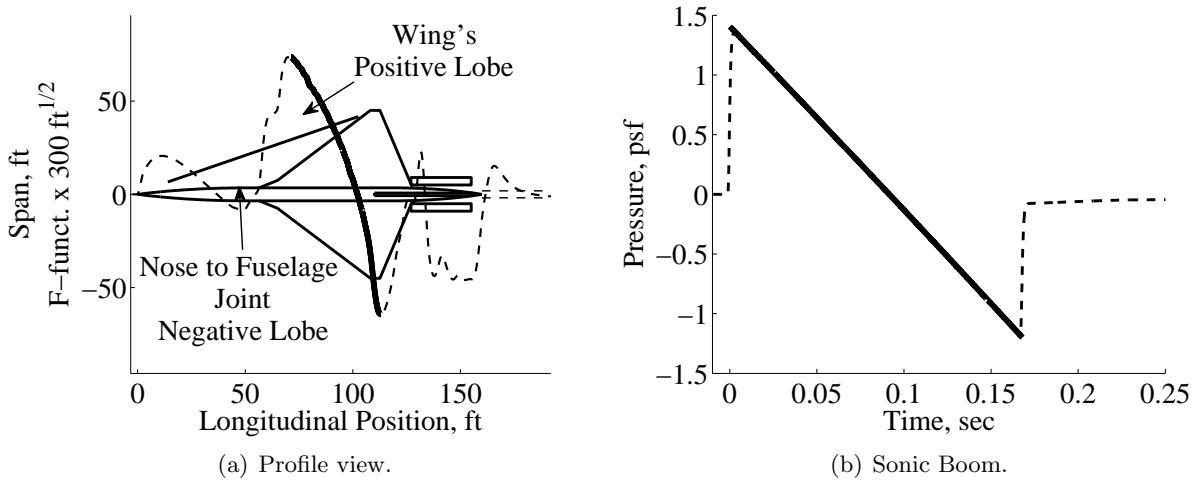
(b) Sonic Boom.

Figure 6.8: Profile view and sonic boom from fuselage, wing, engine nacelles and vertical tail.

(a) Profile view.
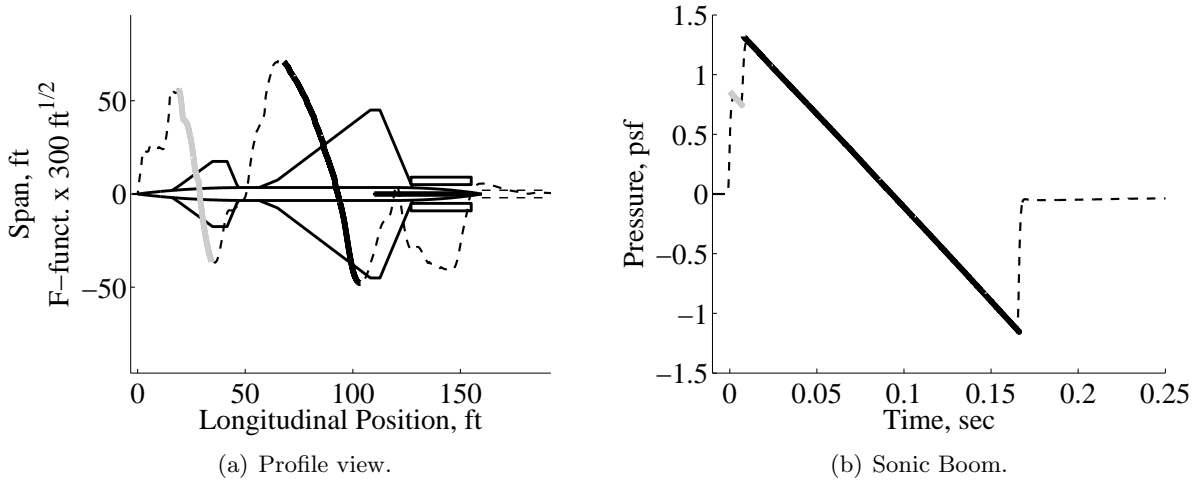
(b) Sonic Boom.

Figure 6.9: Profile view and sonic boom with the addition of the canard trimmed for PR_{min}.

to add a radius increase after the wing to create a large positive lobe, as seen in Fig. 6.11(a). The radius change is 0.4 ft and can be seen as a fuselage area increase between the engine nacelles. This area change was selected to create a frozen rear shock system as shown in Fig. 6.11(b). The trailing shock is now a multi-shock boom and TSPR is 0.93 psf, a 23% reduction from the original value of 1.2 psf. This radius change also has the benefit of 12% increase in fuselage volume. Alternatively, the radius change could have been selected to create a PR_{min} trim condition. However, since this radius change will be a permanent part of the structure, it will be only valid for one weight and trim condition. Therefore, a more efficient method is sought to balance the wing's trailing edge expansion.

A horizontal tail is added with the same dimensions as the canard. This is the final configuration and Fig. 6.12 shows an isometric view of this design. Like the canard, the horizontal tail can be trimmed for PR_{min} or the Frozen condition. The results for these cases are shown in Figs. 6.13 and 6.14. A summary of all cases is presented in Table 6.1. The best value for each metric is in bold font. When the aircraft is flown in the PR_{min} condition, it has the lowest ISPR, but when flown in the Frozen condition it has the smallest minimum and maximum overpressures, TSPR, and PLdB. However, none of the configurations meet NASA's 70 PLdB goal.

(a) Profile view.
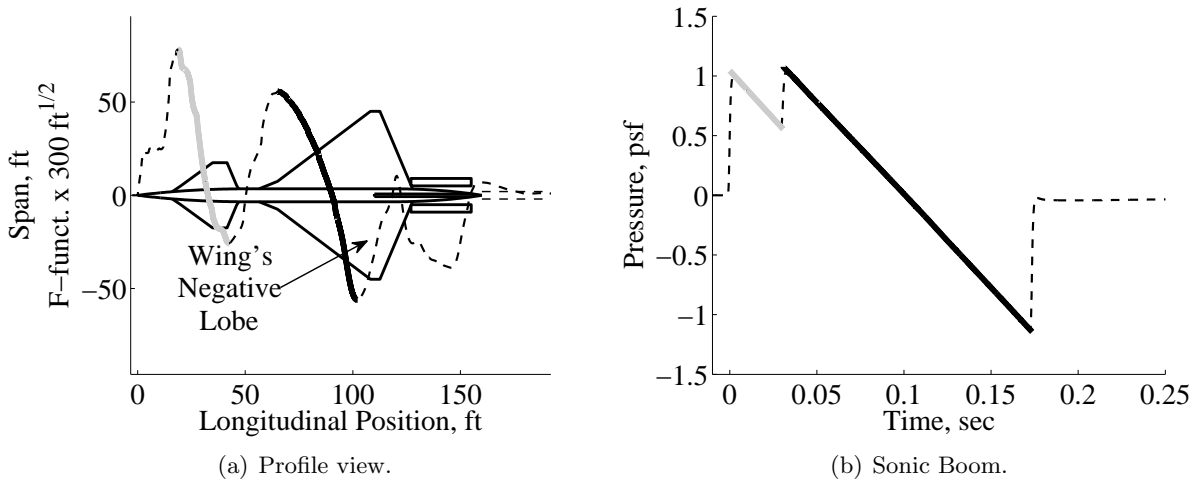
(b) Sonic Boom.

Figure 6.10: Profile view and sonic boom for canard in Frozen condition.

(a) Profile View.
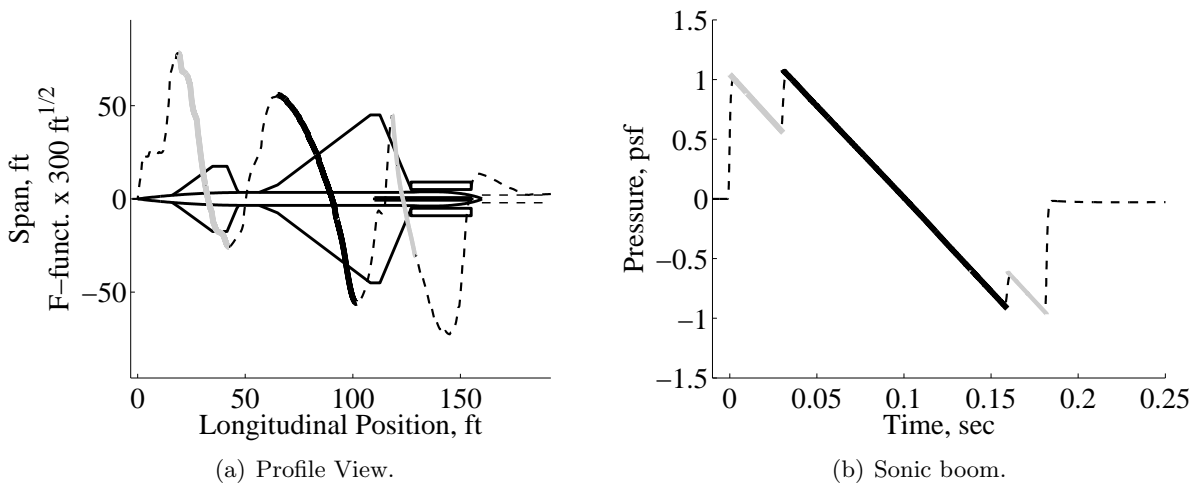
(b) Sonic boom.

Figure 6.11: Radius change to balance rear shock.
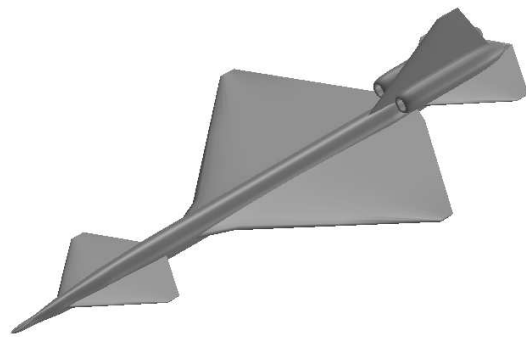
Figure 6.12: Isometric view of final lobe-balanced design.

(a) Profile View.
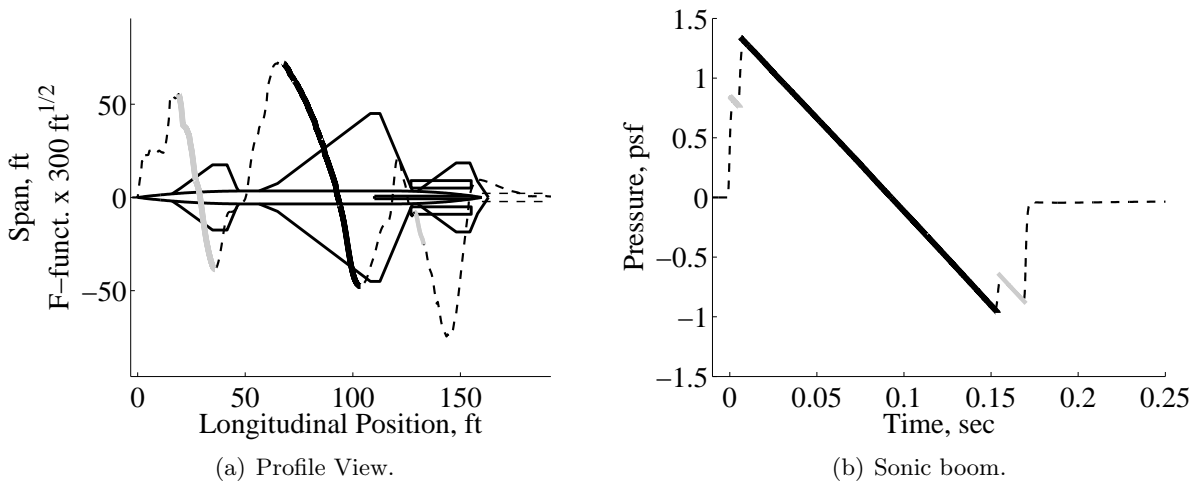
(b) Sonic boom.

Figure 6.13: Horizontal tail trimmed for PR_{min}.

(a) Profile View.
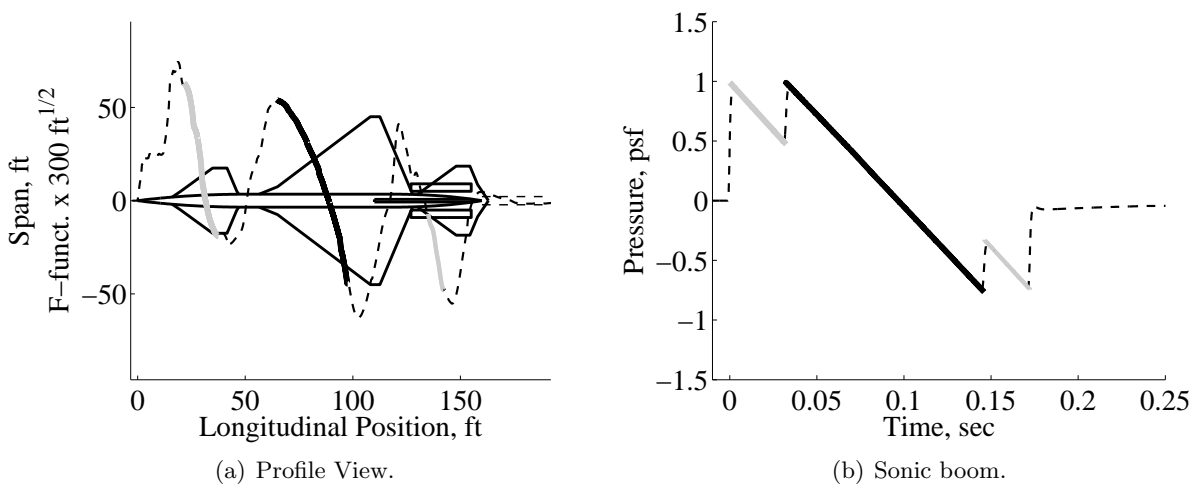
(b) Sonic boom.

Figure 6.14: Horizontal tail trimmed for Frozen sonic boom.

Table 6.1: Lobe-Balanced Design Sonic Boom Summary

Design	ISPR (psf)	$p_{\max}$ (psf)	TSPR (psf)	$p_{\min}$ (psf)	PLdB
Baseline	1.4	1.4	1.2	-1.2	99
Canard, $PR_{\min}$	0.84	1.3	1.2	-1.2	97
Canard, Frozen	1.0	1.0	1.2	-1.2	96
Radius Change, Frozen	1.0	1.0	0.93	-0.93	**92**
Hor. tail, $PR_{\min}$	**0.84**	1.3	0.91	-0.96	95
Hor. tail, Frozen	0.95	**0.95**	**0.78**	**-0.78**	**92**

6.3.3 Performance and stability

Creating a lobe-balanced aircraft does impact performance as summarized in Table 6.2. The $PR_{\min}$ and Frozen conditions have comparable L/Ds of 5.8 and 6.1, which are significantly smaller than the 7.4 of the baseline aircraft. Since all designs produce the same 120,000 lb of lift, the change is entirely due to increased drag. Table 6.3 breaks down the drag for the baseline and Frozen configurations to help explain the cause of the drag increase. As seen in Table 6.3, the Frozen case has higher skin friction drag caused by the increased surface area. The wave drag increase is due to the fact that by adding a canard near the front and the horizontal tail to the rear, the cross sectional area profile is further deviated from a Sears-Haack distribution, as shown in Fig. 6.15.

The aircraft is trimmed such that the pitching moment is zero. Since the canard and horizontal tail incidence angles were set to create balanced lobes, the center of gravity is moved to balance the pitching moment. Table 6.2 shows that using this technique produces a moderately positive static margin (SM); thus the aircraft is longitudinally stable.

Table 6.2: Lobe-Balanced Design Performance Summary

Design	L/D	SM	Canard Lift (lb)	Wing Lift (lb)	Tail Lift (lb)
Baseline	7.4	0.030	0	118,000	0
Canard, PR_{min}	7.0	-0.050	7,900	110,000	0
Canard, Frozen	6.9	0.17	34,000	85,000	0
Radius Change, Frozen	6.0	0.17	34,000	85,000	0
Hor. tail, PR_{min}	5.8	0.10	6,400	110,000	200
Hor. tail, Frozen	6.1	0.14	29,000	66,000	28,000

Table 6.3: Contributions to Total Drag for Lobe-Balanced Design

Design	Induced (lb)	Skin Friction (lb)	Wave (lb)	Other (lb)
Baseline	1,600	8,000	4,900	1,100
Hor. tail, Frozen	1,400	10,000	7,400	1,200
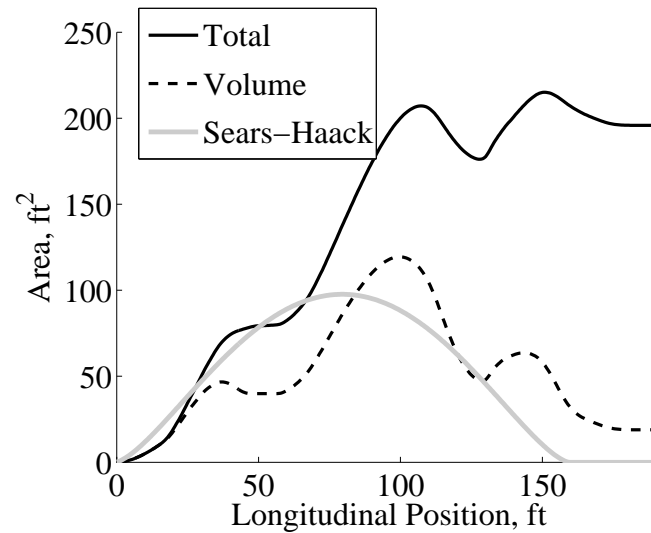
Figure 6.15: Area profile for lobe-balanced aircraft in Frozen trim condition.

6.4 Numerical Simulation

After the conceptual design was completed using RapidF, near-field pressure signatures from RapidF were compared to CFD simulations in order to validate the lobe-balanced design. The intent was to demonstrate the quality of the design created by RapidF, not to complete the CFD

Tier of the design strategy referred to in the Background section of this report. The geometry used for the CFD analysis in shown Fig. 6.16. The only modification from the design shown in Fig. 6.12 is the removal of the engines to decrease modeling complexity and eliminate them as sources of error.

6.4.1 CART3D overview

The design shown in Fig. 6.16 was transcribed into a Vehicle Sketch Pad (VSP) model (www.openvsp.org), which is an open-source parametric design tool developed by NASA [54]. VSP was used to create a water-tight surface triangulated file (*.tri) with approximately 300,000 triangles. The surface geometry from VSP was input into the CART3D CFD code to obtain pressure profiles. CART3D was selected because it has been widely used for sonic boom research and has shown good agreement compared to experimental results [34, 182]. According the *Getting Started Guide to CART3D*, it is a: "multilevel, linearly-exact upwind solver which uses on-the-fly domain-decomposition to achieve excellent scalability on modern multi-core computers [46]." CART3D uses a a multi-stage Runge-Kutta method for temporal discretization and a second-order finite volume model for spatial discretization. The flow is represented by the the Euler equations and
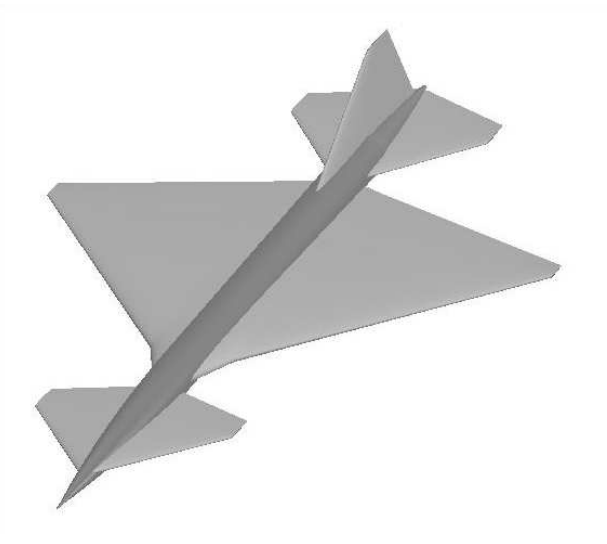
Figure 6.16: Simplified geometry used for CFD analysis.

the ideal gas law; thus it is an inviscid code. Additional, it uses multilevel grid solutions to speed convergence [3], with an advertised capability of solving 2 million hexes per hour per core [46]. For this study, CART3D was used on a workstation at the U.S. Air Force Academy Modeling and Simulation Center. The work station has 12 AMD 2.40 GHz Opteron$^{\text{TM}}$ processors and 48 GB of memory. This workstation limited the maximum grid size to approximately 15 million hexes. This restricted the distance that the pressure sensor could be located to a maximum of 3 body lengths. Farther locations required more hexes and did not converge in a reasonable time.

6.4.2   Adjoint mesh refinement

CART3D's adjoint mesh refinement routine was used to increase resolution in the vicinity of the sonic boom. Based on previous sonic boom studies [34, 182], the objective function:

$$J = \int \left(\frac{\Delta p}{p_\infty} \right)^2 ds \tag{6.7}$$

was used to drive the mesh refinement. The integral is taken along a sensor line at the location of interest, for this study 3 body lengths below the aircraft. Each cell's contribution to the objective function's error is estimated. If it is above a threshold then it is subdivided in the next cycle. The adjoint solver keeps cycling until an exit criteria is met, which might be:

- The error tolerance of the objective function is met

- The maximum number of hexes is reached

- The number of adjoint cycles exceeds a user-defined limit

A sample of the adjoint trends can be seen in Fig. 6.17. The corrected functional is the estimated value of the functional based on the adjoint prediction method and should approximate the functional on the next step. When the simulation has converged the functional should reach a horizontal asymptotic limit and the estimated error, shown in Fig.6.17(b), should be below the user specified tolerance.

(a) Objective Function.

(b) Error.
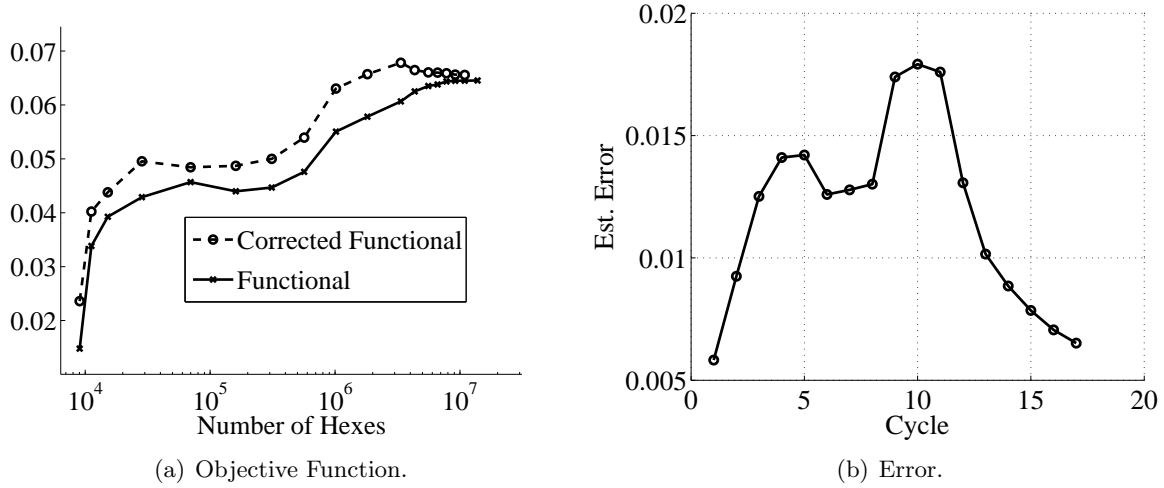
Figure 6.17: Adjoint objective function trends.

6.4.3   Test case

In order to ensure CART3D was being implemented properly, CFD was performed on Model 4 from NASA TN D-7160, which provided experimental results for comparison [88]. This case has been used by many previous sonic boom studies as a verification tool [34, 182]. The VSP model used can be seen in Fig. 6.18(a), which consists of:

- 17.52 cm fuselage (distance includes a 7.06 cm parabolic nose)

- 69° swept wing

- 5% thick diamond airfoil

Since the model was mounted on a sting in the wind tunnel, the fuselage in our study was extended to 30 cm so that the terminating shock would not affect the shocks from the nose and wing. The pressure profiles at 3.6 body lengths away for Mach 1.68 and $C_L = 0.08$ are shown in Fig. 6.18(b). Although the main purpose of this graph is to demonstrate the accuracy of CART3D by comparing it to experimental results, RapidF's solution is also shown.
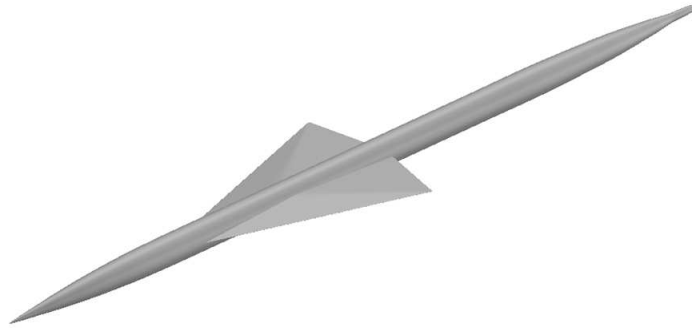
(a) VSP model.
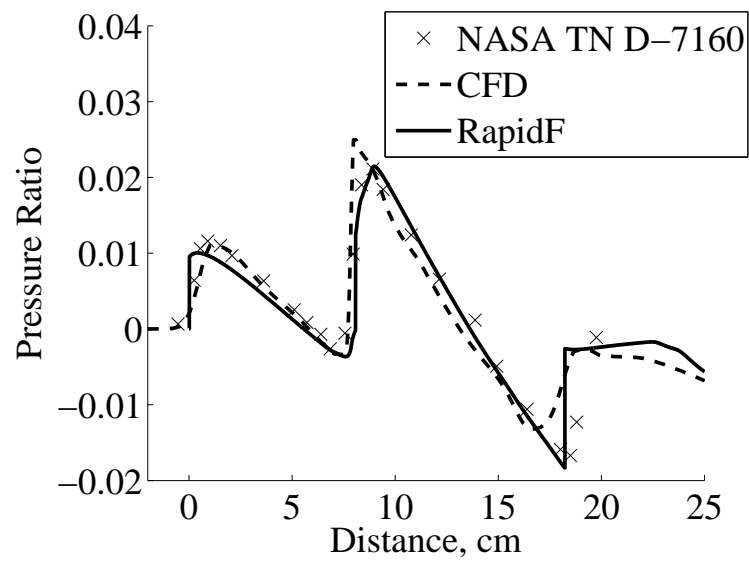
(b) Results.

Figure 6.18: NASA TN-D 7160 test case for CFD analysis [88].

6.4.4   Implementation

The initial mesh used on the lobe balanced aircraft can be seen in Fig. 6.19, which was rotated by an angle:

$$\theta_{rot} = -(\mu - AoA + \epsilon) \tag{6.8}$$

to align the cubes with the shock structures. The small angle ϵ (1° to 3°), is added to avoid the "Mach glitch" problem [170]. Various aspect ratio hexes were test, ultimately a 4 x 2 x 1 aspect ratio provided the fastest convergence. The aspect ratio maximizes the resolution in the longitudinal direction where strong pressure gradients will exist due to the shocks [182]. The initial mesh had 5,000 to 20,000 hexes, depending on run. The final mesh and pressure profile can be seen in Figs. 6.20 and 6.21, respectfully.
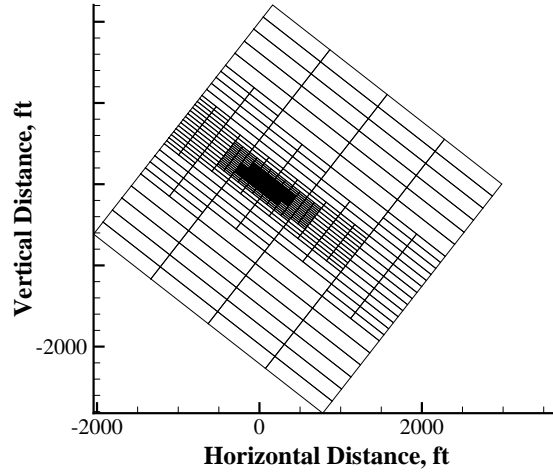
Figure 6.19: Initial CFD mesh.

6.4.5   Comparison to RapidF

The pressure profile from CART3D is compared to that from RapidF in Fig. 6.22. Despite the fact that RapidF is based on modified linear theory, which is a not intended to be used in the near field, the shape of the signatures are very similar. However, RapidF does not show the
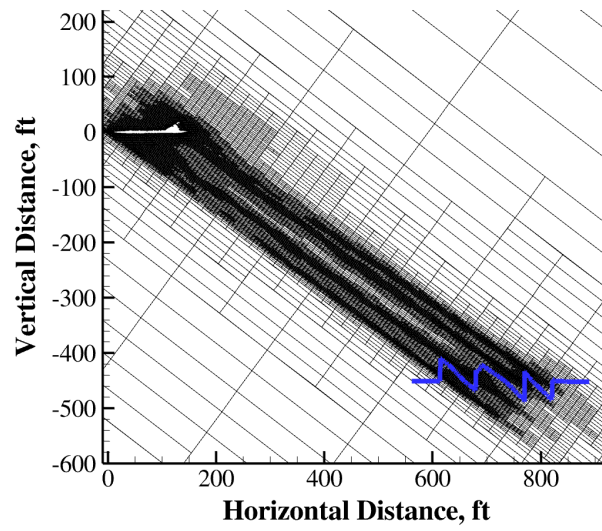
Figure 6.20: Final CFD mesh.
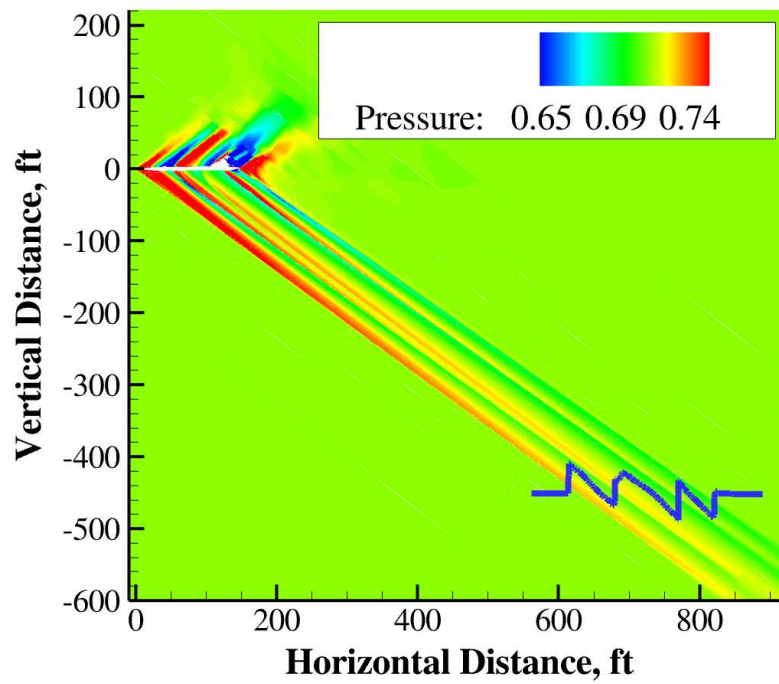
Figure 6.21: Side view of CFD simulation.

same shape for the wing shock as the CART3D solution. The double shock from the wing was determined to be a near-field phenomena caused by interference from the canard and does not exist in the far field.
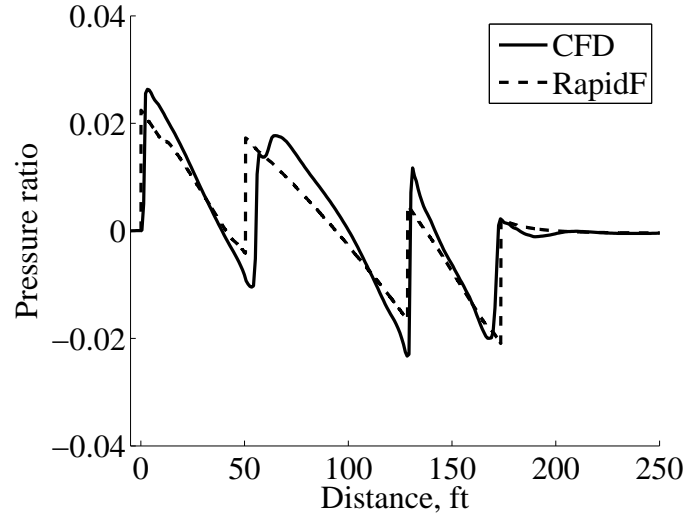
Figure 6.22: Pressure distribution at 3.0 body lengths.

The near-field pressure signature from CART3D was propagated to the ground using CU-Boom and the results are compared to RapidF in Fig. 6.23(a). CART3D also produces a frozen signature as predicted by RapidF. However, the rear shock system is not balanced. In order to re-balance the rear shock system, the horizontal incidence angle was increased from 0.45^o to 3.0^0, and the results are shown in Fig. 6.23(b). The lobes are now balanced; thus, CART3D has demonstrated that RapidF is capable of being used for preliminary design. Although, some modifications will need to be made in the CFD Tier of the design process, RapidF produces a good first-order approximation of the sonic boom. It is also helpful to compare run times. The RapidF solution took 31 sec compared to the CFD solution took 6.25 hours. This does not account for the time spent tuning all the adjoint settings which took 47 runs. Additionally, CART3D has validated that a lobe-balanced aircraft is capable of producing a multi-shock, frozen sonic boom at the surface.
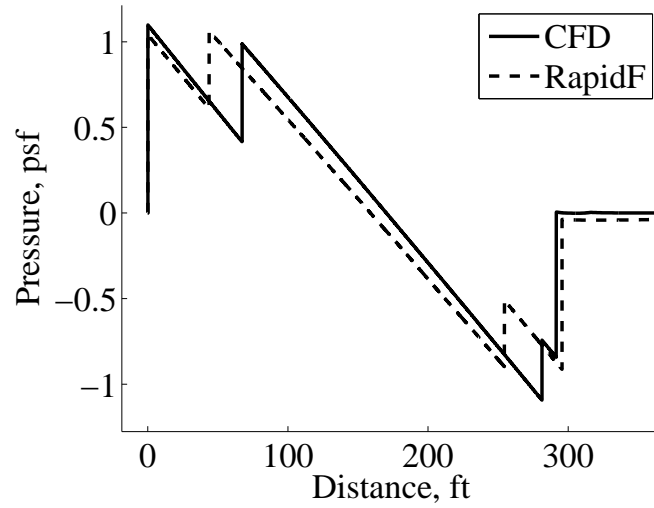
(a) Un-modified.
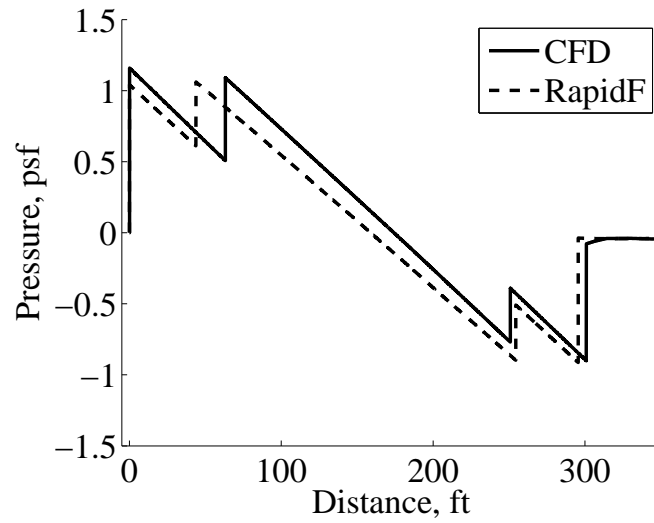
(b) Modified.

Figure 6.23: Pressure profiles on ground.

6.5   Chapter Conclusions

Although the atmosphere cannot freeze a sonic boom pressure signal, a lobe-balanced aircraft can create a frozen signal. Lobes can be created using area/volume changes. However, since these features are permanent structures they are only effective at one design condition. Therefore, the design in this study creates lobes using lift. The aircraft has three lifting surfaces which enable

it to be flown in various trim conditions. In the PR_{min} condition it creates balanced lobes which lowers the ISPR from 1.4 to 0.83 psf and the TSPR from 1.2 to 0.78 psf. The aircraft can be flown in the Frozen trim condition, creating a frozen sonic boom pressure signal which has the lowest PLdB of 90. This study has demonstrated that lobe balancing is a viable sonic boom minimization technique. The purpose of the design case presented was to demonstrate how lobe balancing can be used, but it did not explore the lower bounds of its capabilities. Additionally, this study has demonstrated that RapidF, based on modified linear theory, is an effective design tool and its capabilities have been validated by comparison to CFD. Thus, demonstrating its effectiveness for the design of low-boom aircraft.

Chapter 7

OFF-DESIGN ANALYSIS

Koegler's concern about lobe balancing that was presented in the Chapter 1 is restated here [102]:

> A question is often raised over the feasibility of keeping such loops nearly equal when the effects of variations in Mach number, level-flight lift coefficient, and trim forces for different flight speeds and altitudes are taken into account. However, an examination of the computed $F(y)$ curves for typical SST vehicles, flying at Mach numbers as far apart as 1.5 and 2.7, showed that the differences between them are less severe than anticipated. Therefore, this approach is believed to be feasible and its ultimate capability for boom reduction is worth exploring.

This chapter investigates *"...the feasibility of keeping such loops nearly equal..."* and validates Koegler's statements that *"...the differences between them is less severe..."* This chapter will use the design from Chapter 6 to show what happens to a lobe-balanced sonic boom when the flight conditions are varied or the canard and vertical tail are used as control surfaces. Lastly, the entire sonic booms carpet is explored, by looking at the sonic booms propagated to the side. The totality of all of these off-design scenarios shows that Koegler was correct: it is not as hard as one might think to keep the lobes in balance and lobe-balancing is very robust.

7.1   Flight Conditions

In the following discussion, flight conditions are varies to the limits of the expected flight profile. When a parameter is varied, the aircraft is re-trimmed to freeze the sonic boom, meaning

to obtain the shape of Fig. 6.14(b), although the duration and overpressures will change. For brevity, only the Frozen trim condition is presented.

7.1.1 Mach number

The effects of varying the Mach number from 1.2 to 2.2 on the areas, F-function, and sonic boom are summarized in Fig. 7.1. Since Mach number is not explicit in Eq. (2.59), the F-function appears to be invariant with Mach number. However, it effects both equivalent area due to lift and volume. As shown in Fig. 3.11, the aircraft is sliced at the Mach angle. Thus, in Fig. 7.1(a), the area is spread out over a larger distance for Mach 2.2. The component most effected by the Mach number is the vertical tail since it is displaced from centerline, resulting in the largest differences near the rear of the aircraft. Mach number has much more effect on the equivalent area due to lift as shown in Fig. 7.1(b), which can be explained by Eq. (3.20). Since Mach number appears in the numerator ($\beta = \sqrt{M^2 - 1}$) and denominator ($q = 1/2\gamma p M^2$), a change in Mach number has a small effect on the equivalent area due to lift. Consequently, the F-function is changed slightly as shown in Fig. 7.1(c), with the most dramatic changes near the rear where the vertical tail is located. As shown in Fig. 7.1(d), a Mach number increase does decrease the sonic boom duration and increases PLdB. The decrease in duration with an increase in Mach number is due to the higher ground speed. The baseline case from Fig. 6.14(b) is also shown in blue for comparison.

7.1.2 Altitude

The impact on changing altitude from 41,000 to 61,000 ft can be seen in Fig. 7.2. The area due to volume is essentially un-effected. The minor differences are due to the change in the boundary layer. In contrast, the impact on equivalent area due to lift is significant as shown in Fig. 7.2(b). Unlike a Mach number change, which effects both the numerator and denominator of Eq. (3.20), an altitude change only effects the denominator; thus, as altitude increases, the equivalent area due to lift increases proportionally to the static pressure decrease. Fortunately, the impact on the F-function is less significant as shown in Fig. 7.2(c). The minimal change in the F-function is

(a) Equivalent area due to volume.

(b) Equivalent area due to lift.

(c) F-functions.

(d) Ground pressure profiles.
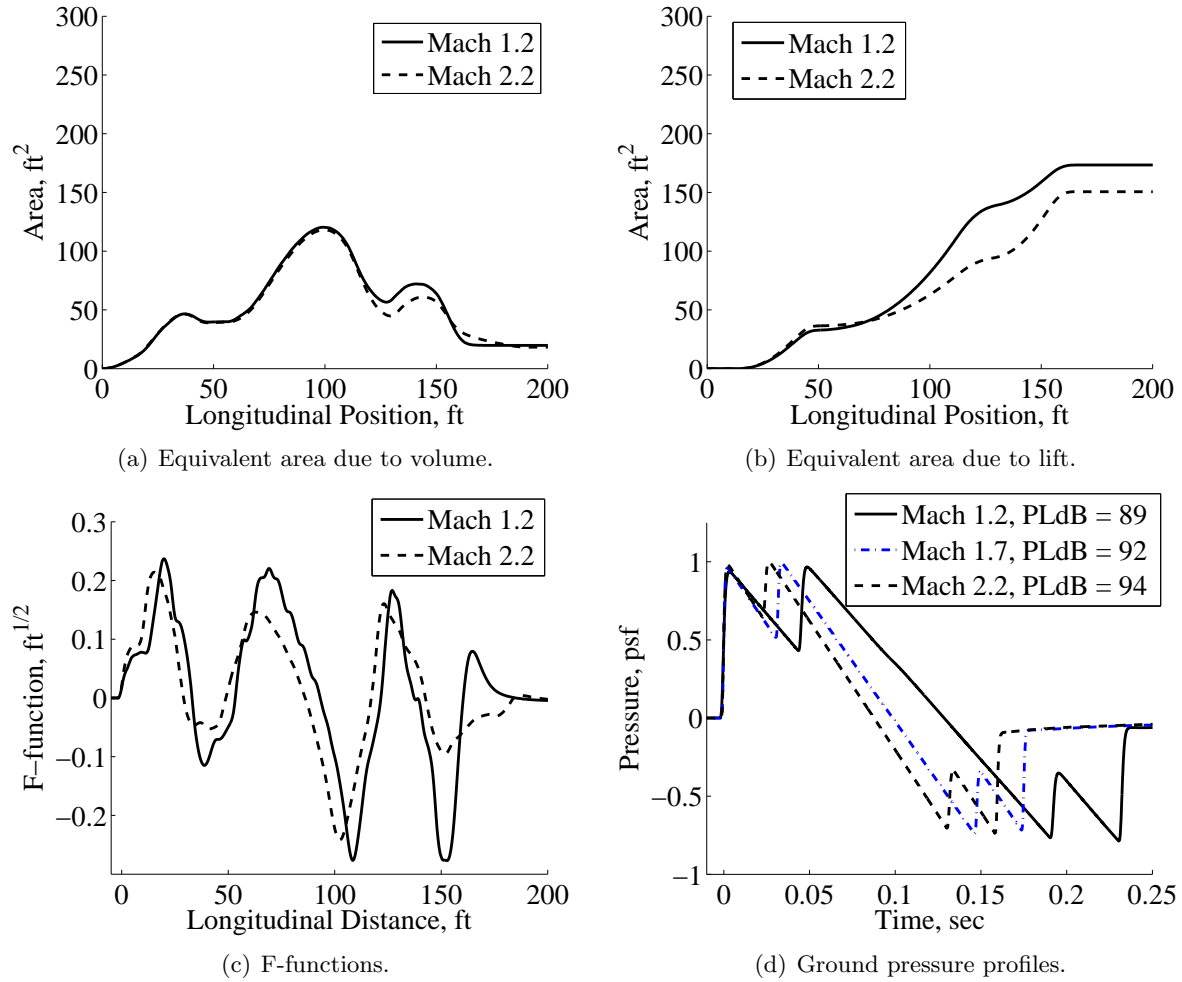
Figure 7.1: Mach number effects.

because the F-function is related to the area's curvature, not magnitude. The changes in the sonic boom are shown in Fig. 7.2(d). Increasing the cruise altitude decreases the peak overpressure and increases sonic boom duration, resulting from the longer propagation distance.

7.1.3 Weight

Weight effects are presented in Fig. 7.3. As expected, weight does not effect the area due to volume. However, the area due to lift must increase proportionally to a weight increase, to be in straight and level, unaccellerted flight. Thus, as shown in Fig. 7.3(b), lift's equivalent area increases proportionally to a weight change. Like the altitude increase, the change is mostly in magnitude,

(a) Equivalent area due to volume..

(b) Equivalent area due to lift.

(c) F-functions.

(d) Ground pressure profiles.
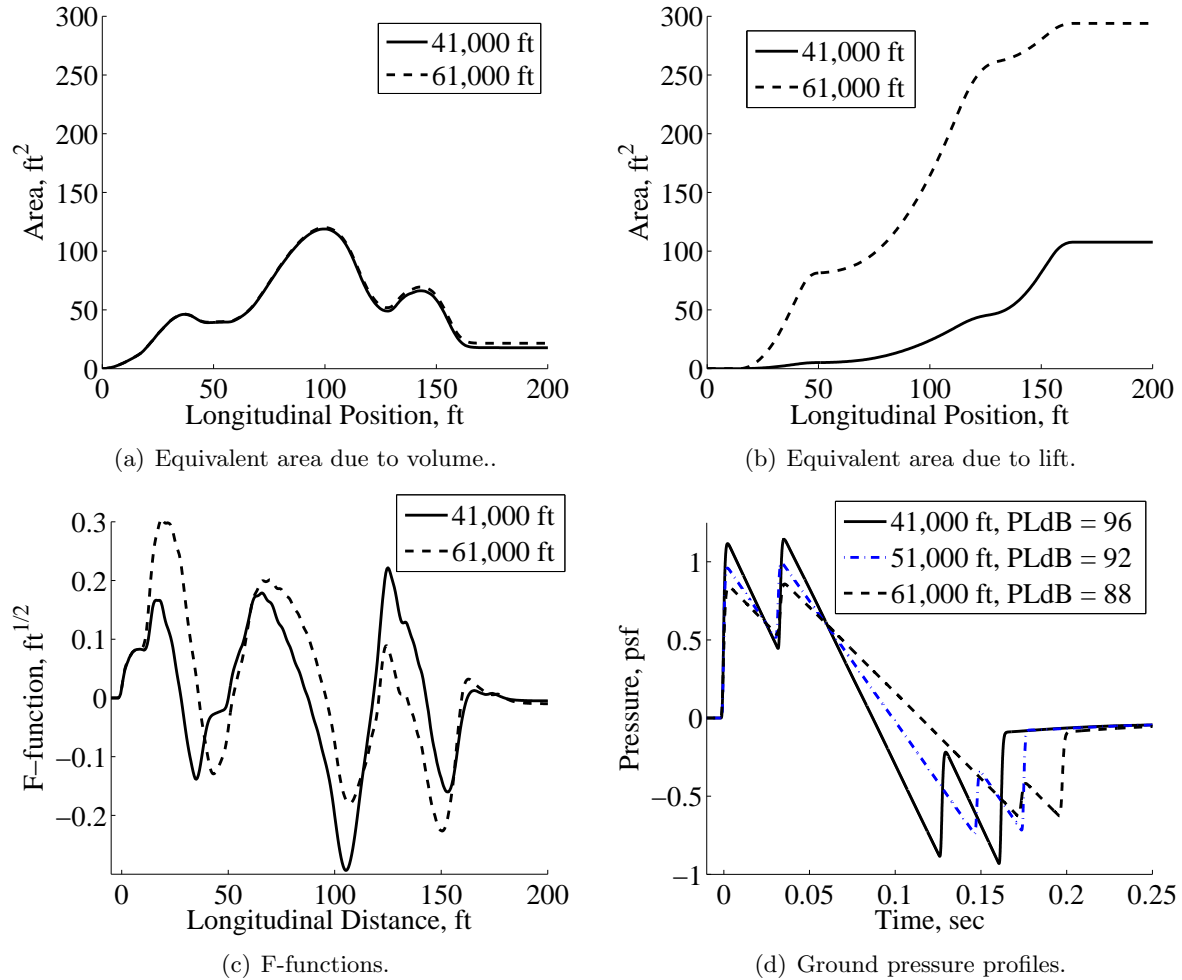
Figure 7.2: Altitude effects.

not curvature. Thus, the F-function changes moderately. Weight's impact on the sonic boom is shown in Fig. 7.3(d). A weight increase from 90,000 lbs to 150,000 lbs (67% increase) results in an increase in the peak overpressure from 0.82 psf to 1.05 psf (28%).

7.2 Mission Profile

A notional supersonic flight profile for the SBJ is presented in Fig. 7.4. The aircraft is assumed to climb to 41,000 ft performing a subsonic maximum rate climb. Then, perform a level acceleration to Mach 1.7. The first data point along this maneuver is for Mach 1.2 and 130,000 lbs (modified linear theory cannot be used in transonic region, so this is the slowest valid speed). At

(a) Equivalent area due to volume.

(b) Frozen condition, no lift correction.

(c) F-functions.

(d) Ground pressure profiles.
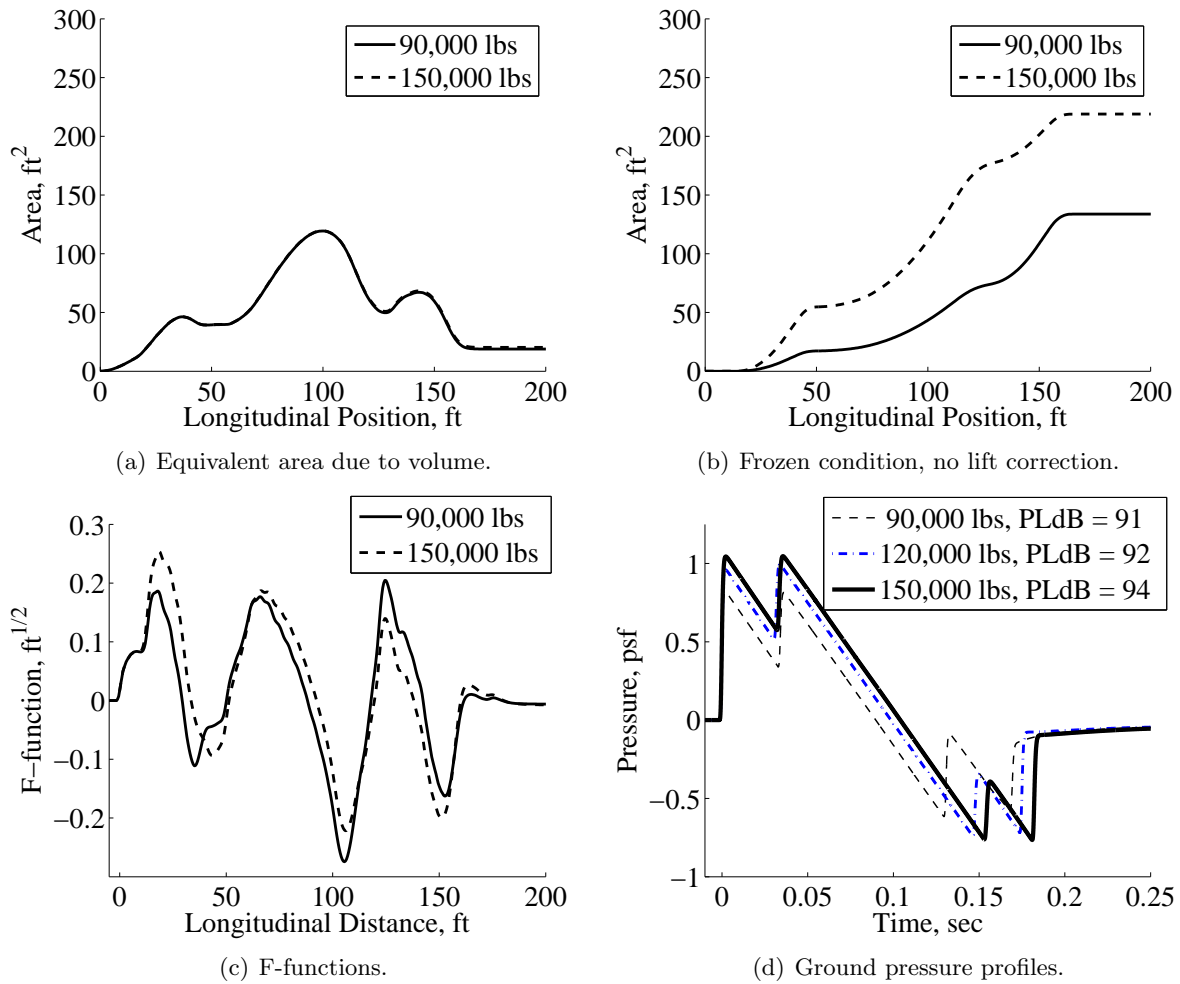
Figure 7.3: Weight effects.

this point the sonic boom will be 93 PLdB. At the end of the acceleration, the aircraft is assumed to weight 125,000 lbs. Figure. 7.2(d) shows a Frozen sonic boom for these conditions with 96 PLdB. However, the aircraft cannot be trimmed to level flight. The canard and horizontal tail are deflected to balance the lobes. Transferring fuel is used to zero the pitching moment. However, for this case, there is not enough fuel available to counter the pitch-down moment created by the horizontal tail's lift. Therefore, the aircraft must be flown in the PR_{min} condition increasing the PLdB to 98. After reaching Mach 1.7 the aircraft climbs to 51,000 ft and cruises at Mach 1.7. At the beginning of this mission segment the aircraft weighs 120,000 lbs, representing the *on-design* point used in Chapter 6. At the end of the cruise segment, the aircraft weighs 90,000 lbs. Again, the aircraft does not have enough fuel to zero the pitching moment and must be flown in the PR_{min} condition. The aircraft then descends to 41,000 ft and decelerates to subsonic conditions. Unlike the acceleration at the beginning of the mission, during the deceleration phase, the aircraft can be trimmed for the Frozen condition, despite having less fuel to use as ballast. The aircraft is easier to trim at the lower weight, because the wing has to create less lift; thus creating smaller lobes. Consequently the horizontal tail has to be deflected less, making a smaller pitch down moment.

7.3   Control Surfaces Deflections

As stated earlier, the aircraft is trimmed by setting the canard and horizontal incidence angle to balance the lobes in the F-function. However, the canard and horizontal tail may also serve as control surfaces. Figure 7.5 shows the impact of deflecting the surfaces to create a pitching moment. In order to create a pitch up, the canard incidence is increased and the horizontal tail incidence is decreased. For the case in Fig. 7.5, they are deflected 0.5^o to create a $C_M = 0.11$ which should be sufficient to recover from a gust. Although the pressure profiles are effected and no longer frozen, the changes are small and do not change the PLdB value. This example demonstrates that the control surfaces are being used for two tasks: lobe-balancing and control. Therefore, it is recommended to use another control system during supersonic cruise, such as thrust vectoring, so that the canard and horizontal tail can be dedicated to lobe balancing.

Mach 1.7
51,000 ft
120,000 lbs
92 PLdB

Mach 1.7
51,000 ft
90,000 lbs
94 PLdB
PR$_{min}$

Acceleration

Deceleration

Mach 1.2
Alt = 41,000 ft
130,000 lbs
93 PLdB

Mach 1.7
41,000 ft
125,000 lbs
98 PLdB
PR$_{min}$

Mach 1.7
41,000 ft
87,000 lbs
95 PLdB

Mach 1.2
41,000 ft
80,000 lbs
93 PLdB
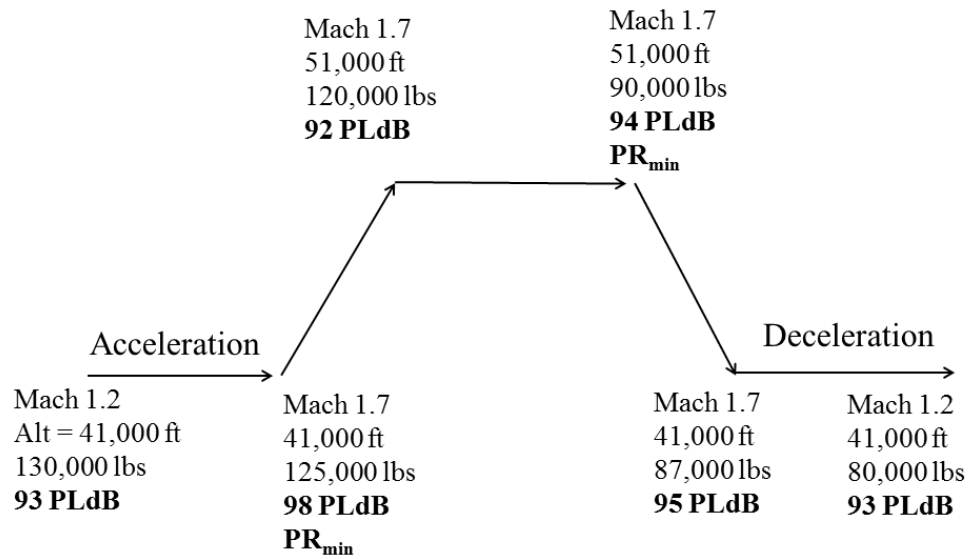
Figure 7.4: PLdB for each mission segment.
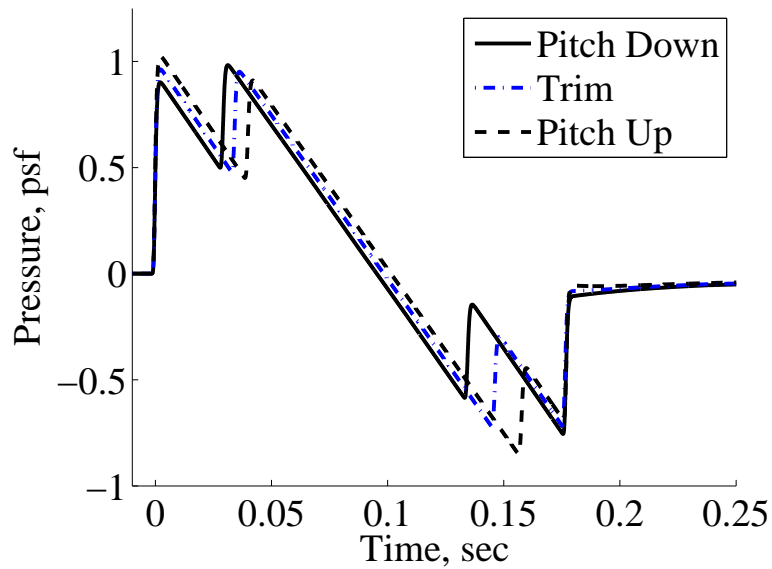
Figure 7.5: Sonic booms when aircraft is pitching up or down.

7.4   Propagation Angle

The above analysis assumed the area of interest was directly below the aircraft. However, a viable SBJ must also produce a quiet sonic boom over its entire footprint. As shown in Fig. 7.6, as

an acoustic ray propagates toward the ground it will refract toward areas of lower speed of sound, thus will bend upward. For mach 1.7 and 51,000 ft, the ray that leaves the aircraft at $\phi = 51^o$, impacts the ground 25 miles to the side and represents the limit of the sonic boom footprint. Rays greater than 51° will not reach the ground and are not relevant. Fig. 7.7 shows sonic booms for $\phi = 51^o$. In Fig. 7.7(a), the sonic boom is from the Frozen F-function in Fig. 6.14 (120,000 lbs, Mach 1.7, 51,000 ft). As expected, the sonic boom retained its shape. Unfortunately, this is not the correct F-function. As shown in Eq. (2.61), the area due to lift is proportional to the cosine of the azimuth angle. Furthermore, the slicing plane is rotated by the ray angle (see Fig. 3.10 and Eq. (3.23)). This causes the vertical tail to have a more significant impact on the aft part of the F-function, as shown in Fig. 7.8. The sonic boom with this corrected F-function is shown in Fig. 7.7(b). The front shock structure is still a multi-shock system, but it is not frozen because the first two shocks do not have the same peak pressure. Although the rear lobes are not balanced at this propagation angle, the pressures are weak enough to produce a multi-shock trailing system. Likewise, for the PR_{min} case, as shown in Fig. 7.7(c), retains the front shock-system shape, but the rear shock system is reduced to a series of weak shocks. The off-axis sonic boom metrics are shown in Table 7.1. Both shocks have the same PLdB and neither trim condition has a distinct advantage over the other. These off-track examples, highlight that lobe balancing for one ray angle does not guarantee that the F-function for other angles will also be balanced.

7.5   Chapter Conclusions

In comparison to the off-design example presented in Fig 1.6, the lobe-balanced design is less subtable to developing into an undesirable-shaped sonic boom. However, the design in Chapter 6 only balanced the lobes in one plane; future work should consider all planes that impact the surface. Also, the mission analysis revealed two cases where the aircraft is not capable of creating a frozen sonic boom and zeroing the pitching moment. Therefore, an in depth stability and control study is warranted. All of these shortcomings are minor and should not prevent lobe-balancing from being used on future quiet sonic boom aircraft.
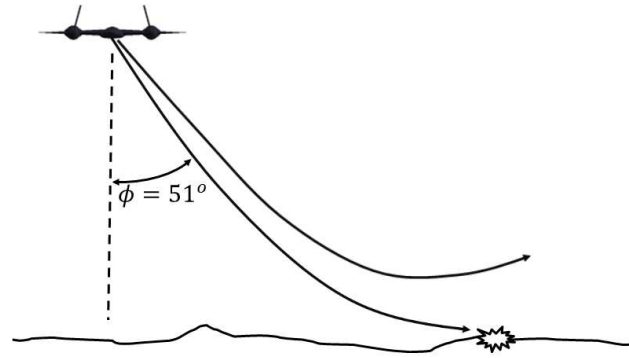
Figure 7.6: Rear view of aircraft showing azimuth angle.
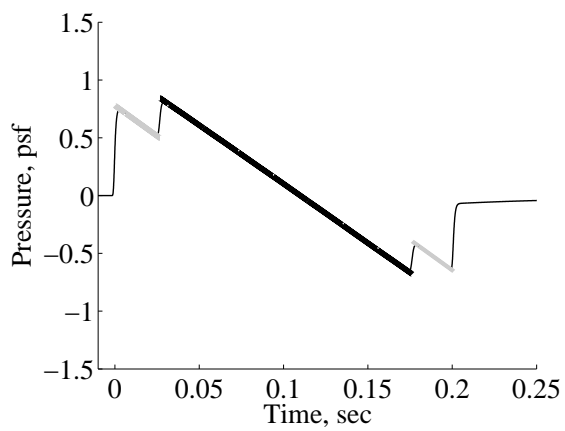
(a) Frozen condition, no lift correction.
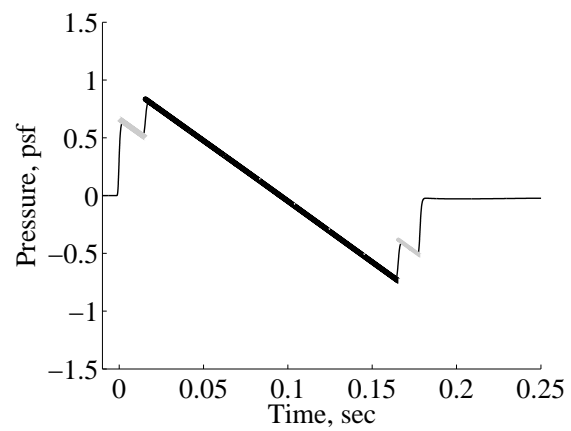
(b) Frozen condition with lift correction.
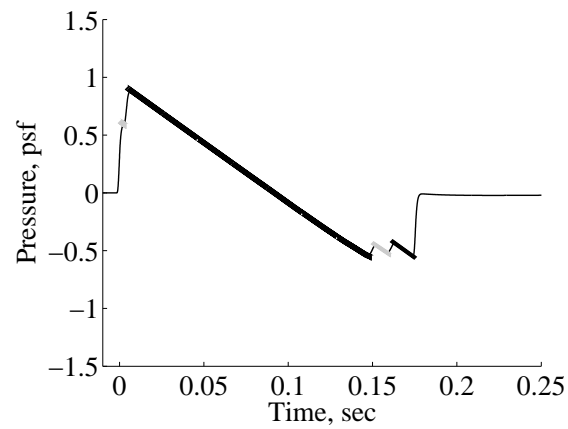
(c) PR$_{\mathrm{min}}$ condition.

Figure 7.7: Sonic booms for $\phi = 51^o$.
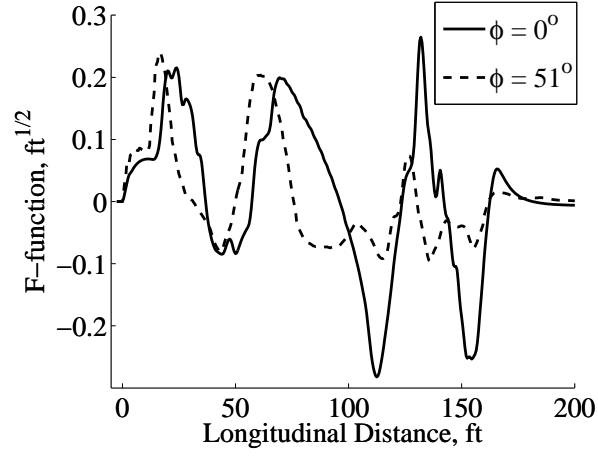
Figure 7.8: F-functions of Frozen case for different azimuth angles.

Table 7.1: Off-Axis Sonic Boom Summary

Design	ISPR (psf)	p_{max} (psf)	TSPR (psf)	p_{min} (psf)	PLdB
PR_{min}	0.63	**0.81**	**0.49**	0.70	85
Frozen	**0.60**	0.91	0.60	**0.61**	85

Chapter 8

SCALED SONIC BOOM FLIGHT TESTING

The objective of this chapter is to establish a method for using a scale model flown in the atmosphere to validate a conceptual design's sonic boom estimate. This methodology specifies the appropriate scale, flight conditions, weight and data acquisition procedures for the tests. First, previous scaled sonic boom tests and studies is reviewed. Then, the logic used to determined the proposed test Mach number, weight and altitude is discussed. Ultimately, two procedures are recommended. The first sets the scaled vehicle's cruise altitude to the same altitude as the full-scale aircraft and data is acquired at an intermediate altitude with a chase ship. Alternatively, the scaled vehicle can fly at a lower altitude; however, it will need to do a pull-up maneuver to produced the correct amount of lift. The lower limit in scale is explored and the author recommends that the lower limit in scale is 10% due to the long rise times associated with the weak shocks.

8.1   Previous Sonic Boom Scaling Studies

8.1.1   Firebee

Using a scale model flown in the atmosphere for sonic boom testing has been proposed in the past. In 1993, Maglieri et al. [122] wanted to demonstrate that an aircraft with a correctly designed fuselage could create a sonic boom that would not develop into an N-wave. Wind tunnel testing had validated that the flat-top boom existed at 30 body lengths away. However, they needed to prove that the sonic boom would not coalesce into an N-wave as it propagated over the hundreds of body lengths to the ground through varying atmospheric conditions. Other test options were

explored, such as sled tracks, wind tunnels with heat plates and jets, nose probes on full-scale aircraft, etc. However, they determined that conducting flight test with a modified aircraft was the best alternative.

Maglieri's team considered using fighter aircraft, missiles, and drones. They desired a platform that could fly at Mach 1.2 to 2.0 at 5,000 to 10,000 ft. The team ruled out the possibility of using missiles, which are not capable of flying at a constant Mach and altitude profile desired for sonic boom testing. Furthermore, a rocket motor creates a different plume than a jet engine. The cheapest platform they investigated was the Bendix Vandal at $250,000, which is equivalent to $392,000 in 2011 dollars. However, they concluded the best platform was the 29-ft long BQM-34E Firebee drone.

To compensate for the size disparity between the Firebee and a supersonic civil aircraft, the drone was to be flown at a lower altitude to match the ratio of height above ground to the length of the vehicle. An example of this scaling is shown in Fig. 8.1. A sonic boom from a 200-ft long aircraft flying at 60,000 ft would travel 300 body lengths to the ground. Thus, to scale the propagation, they concluded the 29-ft long drone should fly at 8,700 ft to have the same scaled propagation distance. Based on this scaling formula, they suggested the lower bounds of the test aircraft should be 13 ft, 6.5% of the full-scale aircraft, to allow the scale model to fly above the earth's boundary layer, which they estimated to extend up to 3,000 ft. Despite this restriction, the earth's boundary layer will still be a higher percentage of the propagation distance for the scaled aircraft. They recommended conducting tests in the morning to mitigate these effects. However, even in the absence of the boundary layer, the sonic boom from the smaller drone would still see different temperature and humidity gradients than the full-scale aircraft.

The BQM-34E can be either catapult or air launched. Maglieri recommended the air launch option because it required less logistical support, simplified test coordination and maximized time on range, making multiple passes possible. After the air launch, the drone was to dive to 8,700 ft (300 body lengths) at Mach 1.3, the maximum speed of the Firebee. It would then fly over an instrumented range which would record the sonic boom. Multiple passes would be conducted if
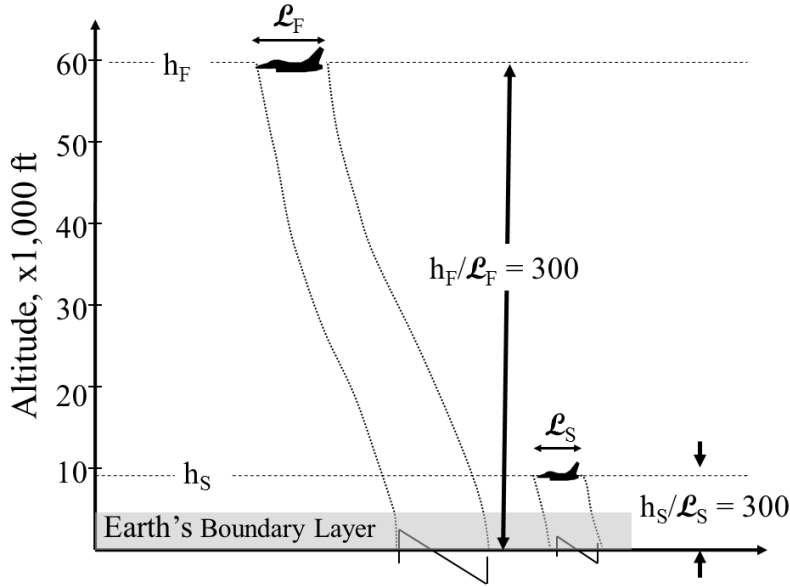
Figure 8.1: Scaling technique of Maglieri [122].

enough fuel remained. The Firebee would then be recovered via a parachute to reduce cost. This type of testing, where the pressure data is acquired on the ground, is one testing option explored in our study and will be referred to as the *low-altitude option*.

8.1.2   Shaped Sonic Boom Demonstrator

In 2000, DARPA was planning to implement Maglieri's proposal of adapting a Firebee for boom testing as part of the Quiet Supersonic Platform program. Numerous wind tunnel tests and CFD simulations were conducted [138]. However, the BQM-34E proved too difficult to modify and the program appeared to be headed for termination. Fortunately, DARPA found a suitable alternative: the F-5, resulting in the SSBD. The F-5's fuselage was modified and the 2003 flight tests validated that a shaped sonic boom still existed even after traveling thousands of feet through the real atmosphere. Although the SSBD was a technology demonstrator, not a scaled test, to put its size in perspective, it is 50 ft long; approximately 36% of a 140-ft SBJ. The SSBD flight tests were conducted above 30,000 ft; thus, the scaling proposed by Maglieri was not used.

In addition to ground measurements, in flight "probing" pressure profiles were also obtained by flying an F-15B fighter aircraft through the sonic boom at distances ranging from 60 to 720 ft from the SSBD to obtain the near-field signature [65]. In this chapter, this type of airborne testing is explored as an alternative to the ground based data acquisition system and will be referred to as the *high-altitude option.* The SSBD is an example of how a small-scale technology demonstrator can be used for sonic boom testing, and the troubles of adapting the BQM-34E highlights the need for a specially designed scale model as proposed in this study.

8.1.3   Quiet Spike [TM]

Another example of the use of flight tests to demonstrate sonic boom minimization technology is the test of Gulfstream's Quiet Spike[TM] on an F-15B aircraft [41, 82]. The Quiet Spike[TM] is a telescopic nose, which creates a series of shocks instead of the instantaneous pressure rise of an N-wave. The Quiet Spike[TM] is designed for a SBJ, but Gulfstream manufactured a 25% scale model for testing on the F-15B. The objectives of these tests were to obtain structural data, demonstrate the extension and retraction functionality and to measure the near-field sonic boom. The near-field pressure profiles were obtained using a probing aircraft similar to the SSBD tests [83]. No far-field, ground measurements were planned because the strong shocks from the F-15B fuselage and canopy would coalesce with the weaker shocks from the Quiet Spike[TM] nose. Thus, the sonic boom would be an N-wave when it reached the ground. The inability of this program to validate a low-boom far-field signature re-enforces the need for an inexpensive test platform specially designed for sonic boom testing.

8.1.4   Acoustic scaling

Howe and Henne [81] explored how to use a sub-scale aircraft to replicate the sonic boom from a full-size aircraft. Their objective was not the same as this study. Howe and Henne desired to use a sub-scale aircraft to create a sonic boom with the same duration and overpressure as a full-scale aircraft. In contrast, we propose to use a sub-scale aircraft to create a *scaled* sonic boom,

which can be used to predict the full-scale sonic boom. Howe and Henne showed that a scale model can match the duration by flying slower, but the lower Mach number has the undesired effect of also lowering the peak overpressure. They corrected for this by lowering the altitude. Howe and Henne created plots that demonstrate the correct combination of speed and altitude to accommodate for the smaller scale of the test platform. Their approach could easily match the maximum pressure and rise time, but there are physical limitations to duration. For example, if one needed to replicate a sonic boom of a Mach 3.0 aircraft, a half-scale model flying at Mach 1.5 could be used to get the correct duration. Using this logic, a quarter-scale model should fly at Mach 0.75, but obviously would not create a sonic boom. Howe and Henne recognized these limitations and did not explore below 25% scale. As will be shown later, since our objective is different, a model below the 25% scale can be used for the goals of this study.

8.2   Test Case Description

This chapter uses a generic SBJ design as the full-scale aircraft whose sonic boom needs to be validated by the scaled aircraft. Based on Refs. [1,38,59,168,183], it is assumed that this SBJ is 140 ft long, weighs 120,000 lbs, and is flying at Mach 1.7 at 50,000 ft. A planform view of the design can be seen in Fig. 8.2. The SBJ's non-dimensional area profile, used in calculating the F-function, can be seen in Fig. 8.3 and its sonic boom ground pressure profile can be seen in Fig. 8.4. The aircraft was designed with low wing loading, which creates a weak pressure perturbation. As can be seen in Fig. 8.4, this prevents the sonic boom from coalescing into an N-wave and there are intermediate shocks from the wings and engine inlets. Although one test case is presented in this report, the methodology is universal and not restricted to this design.

This study investigates how a scaled test aircraft flown in the atmosphere can be used to replicate the sonic boom of the full-scale SBJ shown in Fig. 8.4. Multiple scales are investigated, but results from 5% to 25% scales, which weigh 300 lbs to 7,500 lbs, respectively, are discussed in detail, because they represent the scales used in recent flight tests. For example, the Japanese Aerospace Exploration Agency (JAXA) has conducted tests with a 11% scale Unmanned Aircraft

System (UAS) [186] and the Quiet Spike [TM] flight tests discussed earlier used a 25% scale [82]. Based on these small scales, it is assumed that the test aircraft will be an UAS; however, whether the test aircraft is manned or unmanned does not impact the methodology.
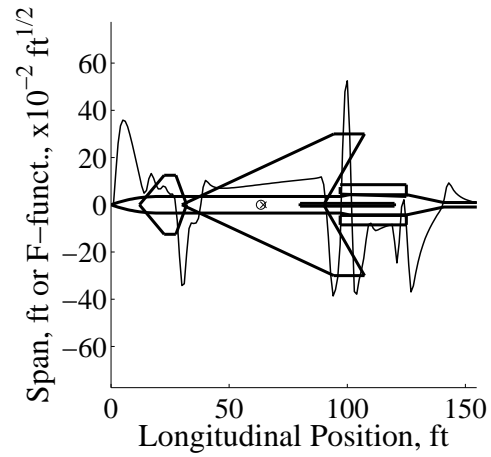
Figure 8.2: Planform view of the SBJ used for evaluating various scales.
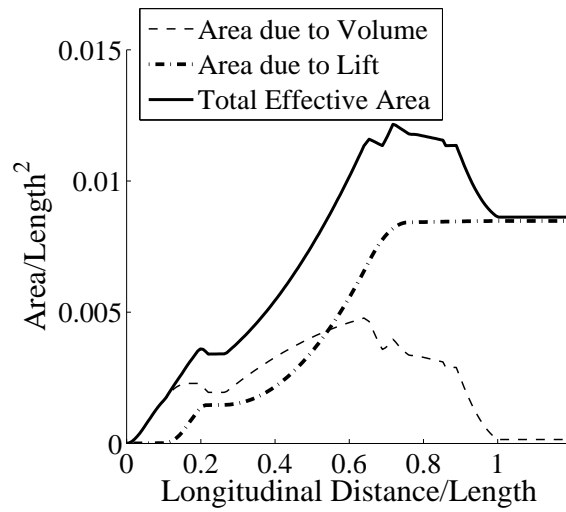
Figure 8.3: Area profiles for SBJ.
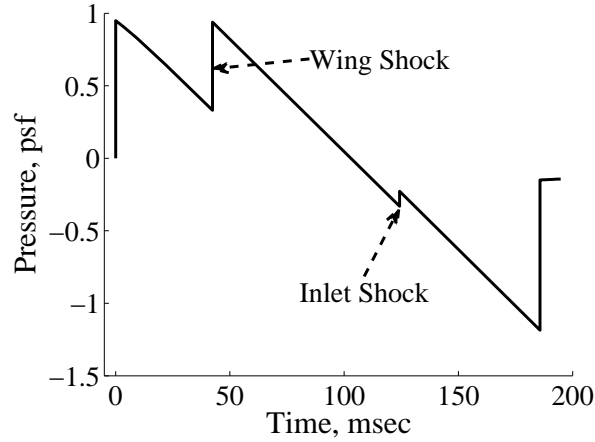
Figure 8.4: Pressure profile on ground from SBJ flying at Mach 1.7 and 50,000 ft.

8.3   Sonic Boom Scaling Discussion

8.3.1   Test Mach number

An accurate simulation requires the model to start with the correct initial conditions: the F-function. As can be seen in Eq. (2.61), if the Mach number is changed, it will affect both the area due to lift, by affecting β and q. Although much less significant, a variation in the Mach number will also impact the cross-sectional area due to volume by changing the slicing angle, refer to Eq. (3.22). Furthermore, variations in the Mach number will affect the acoustic propagation [72] as shown in Fig. 2.8. Thus, the Mach number of the scale model is set equal to the SBJ Mach number to ensures that the F-function is properly represented and the scaled boom travels down the same acoustic ray as the full-scale aircraft.

8.3.2   Test weight

Considerable effort was made in order for the scaled test aircraft to replicate key performance parameters of the SBJ. Ballast was added to keep the static margin constant, which enabled the model to fly at the same angle of attack, 3.5º, and canard incidence angle, 2º, as the SBJ. Test weight was set equal to lift produced at these flight conditions. Fuel weight was determined by

subtracting the empty aircraft weight from the test weight. The F-functions for the SBJ and the 10% scale aircraft with the same flight conditions are compared in Fig. 8.5. As expected from Eq. (2.59), the model's F-function is equal to the full-scale aircraft's F-function multiplied by the square root of the scaling ratio ($\sqrt{0.1} = 0.3162$), thus:

$$F_S = F_F \sqrt{\frac{\mathcal{L}_S}{\mathcal{L}_F}} \tag{8.1}$$

The scaled test vehicle does not necessarily need to fly at the same altitude as the SBJ. However, if the altitude is changed and weight is held constant, as can be seen in Eq. (2.61), the area due to lift will be affected by the dynamic pressure. An example of this effect can be seen in Fig. 8.6. The change in equivalent area is significant and must be accounted for. In order to compensate for the change in dynamic pressure:

$$\frac{\beta W}{2q\mathcal{L}^2} = \text{const.} \tag{8.2}$$

Solving for the scale model's desired weight:

$$W_S = \frac{p_S \mathcal{L}_S^2}{p_F \mathcal{L}_F^2} W_F \tag{8.3}$$

where the pressures are freestream conditions. The required weight to keep the area due to lift constant for the 10% scale vehicle can be seen in Fig. 8.7. Lowering the test altitude has the undesirable requirement of a higher test weight. This will require stronger structures and more thrust. Therefore, flying at the same altitude as the SBJ has the advantage of modeling a properly shaped F-function at a reasonable weight.

The ground pressure profiles of the scale models and the SBJ flying at Mach 1.7 and 50,000 ft can be seen in Fig. 8.8. As expected, the scale models have much smaller initial pressure rise and duration compared to the SBJ. For this study, the objective is to match the non-dimensional pressure profile. Time is non-dimensionalized by the signal duration and pressure by the peak overpressure. If the scaling is done properly, these profiles should be representative of the SBJ; however, they are not, as can be observed in Fig. 8.9. All three scale models incorrectly predict
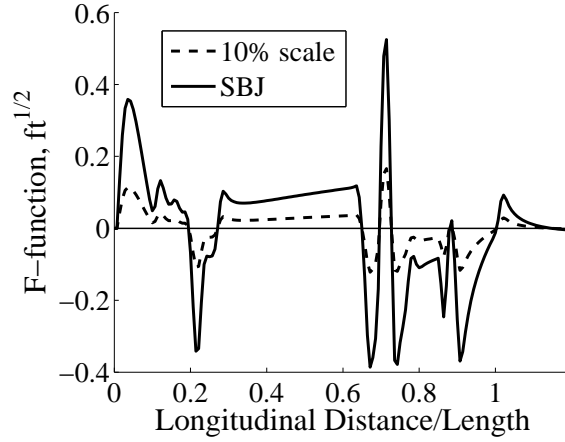
Figure 8.5: F-functions for the 10% scale model and the SBJ.
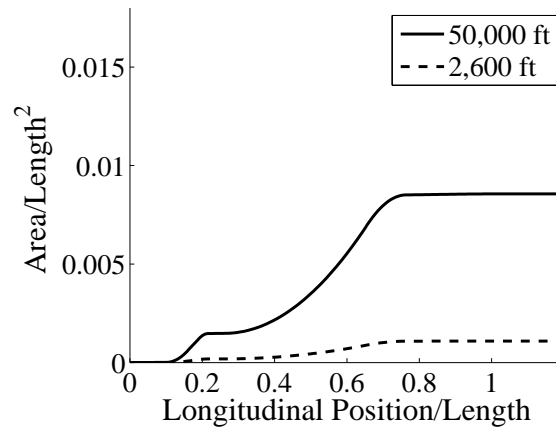
Figure 8.6: Altitude effects on area due to lift.

the location of the first interior shock. This "error" highlights the fact that, at this point, the F-functions have been matched, but the propagation has not been properly scaled.

8.3.3 Test altitude

When comparing the pressure profiles in Fig. 8.9, it can be seen that the interior shock occurs earlier for the scaled test aircraft than for the SBJ. Although the F-functions were scaled, they were not scaled proportionally. For example, the magnitude of the 10% scale aircraft's F-function was
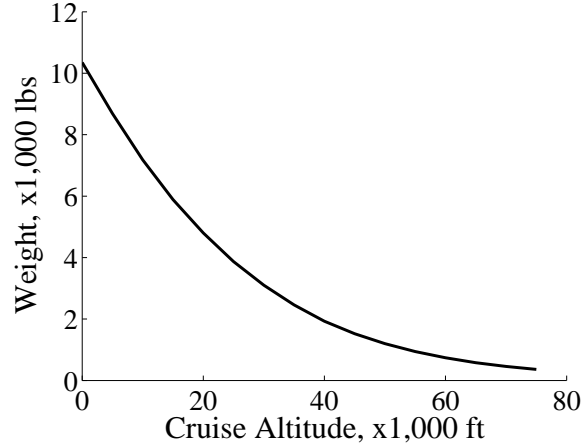
Figure 8.7: Required weight for 10% scale model to generate the same area due to lift.
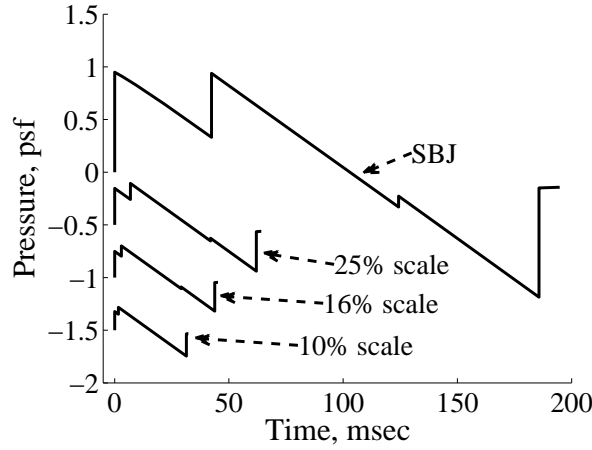
Figure 8.8: Ground pressure signatures for the scale models and SBJ, all flying at Mach 1.7 and 50,000 ft (Profiles are displaced vertically to improve readability).

31.62% of the SBJ. Due to this difference in the length scale to F-function scale, acoustic advance is not properly modeled. Acoustic advance is the nonlinear propagation due to changes in the local speed of sound [72]:

$$\Delta a = \frac{\gamma - 1}{2} \Delta v = \left(\frac{\gamma - 1}{2}\right) \frac{\Delta p}{\rho a} = \left(\frac{\gamma - 1}{2}\right) \frac{\gamma M^2 p_\infty}{\rho a \sqrt{2\beta z}} F(y) \tag{8.4}$$

For a given non-dimensional location, $y/\mathcal{L}$, on the 10% scale aircraft flying at 50,000 ft and Mach 1.7, the pressure perturbation will be 31.62% of the full-scale aircraft; thus as can be seen in

(a) 10% scale.

(b) 16% scale.

(c) 25% scale.
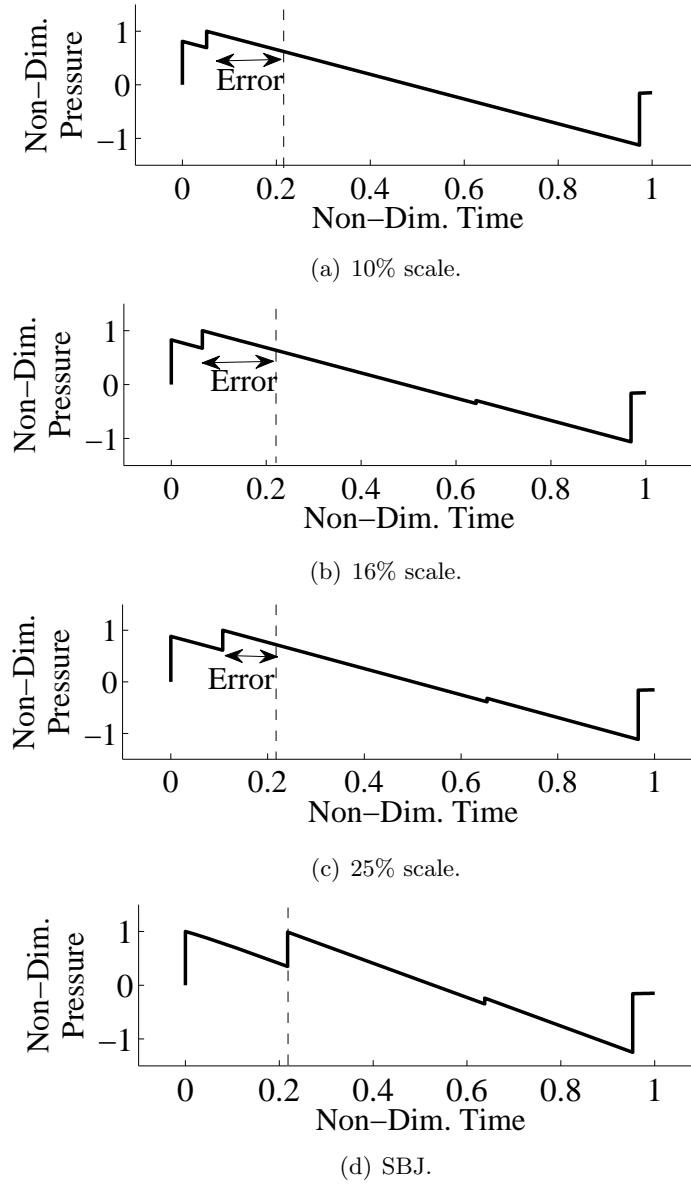
(d) SBJ.

Figure 8.9: Non-dimensional pressure profiles for scale models and SBJ flying at Mach 1.7 and 50,000 ft .

Eq. (8.4), this perturbation will advance at a rate 31.62% slower than for the SBJ, but in order to have a correctly shaped signature on the ground, the perturbation should advance at rate 10% slower. Maglieri [122] suggested this can be corrected by changing the flight altitude. As stated earlier, he proposed to keep the ratio of cruise altitude to aircraft length constant. While, this is a good approach, there is a more precise way to scale the propagation.

Hayes [72] quantifies acoustic advance by calculating an age variable, τ (see Eq. 2.72)), which is the change in phase in units of time caused by a change in the F-Function. The new phase location in units of time can be found by:

$$\xi_2 = \xi_1 - \tau F \tag{8.5}$$

Since this study uses length for scaling, both sides are multiplied by the component of the wave speed in the horizontal direction (refer to Fig. 2.8), to convert the advance to length units:

$$\xi_2 c_0 = \xi_1 c_0 - \tau c_0 \tag{8.6}$$

The left hand side and the first term on the right hand side are now phase in units of length. The last term on the right hand side can be re-organized to $\alpha F(y)$, where α is the advance in distance per unit F-function. Thus, Eq. (8.6) becomes:

$$s_2 = s_1 - \alpha F \tag{8.7}$$

To ensure areas advance in the correct proportion:

$$\frac{\alpha F}{\mathcal{L}} = \text{const.} \tag{8.8}$$

Combining this relationship with Eq. (8.1) simplifies to:

$$\alpha_S = \alpha_F \sqrt{\frac{\mathcal{L}_S}{\mathcal{L}_F}} \tag{8.9}$$

Figure 8.10 depicts advance for the SBJ flying at 50,000 ft at Mach 1.7. At the ground, the sonic boom is distorted 1381 ft/$\sqrt{\text{ft}}$ (units are feet per unit F-Function). For the 10% scale model, in order to get the correct boom shape, it needs 31.62% of this advance or 437 ft/$\sqrt{\text{ft}}$. This is depicted in Fig. 8.10 as a dashed horizontal line. Two techniques to get this advance are investigated. First, the aircraft altitude can be changed. Second, data can be measured at an intermediate altitude.

8.3.3.1   Low-altitude option

For the first case, the cruise altitude is lowered and data is acquired on the ground; thus it is the low-altitude option. This type of testing might be preferred over the high-altitude testing
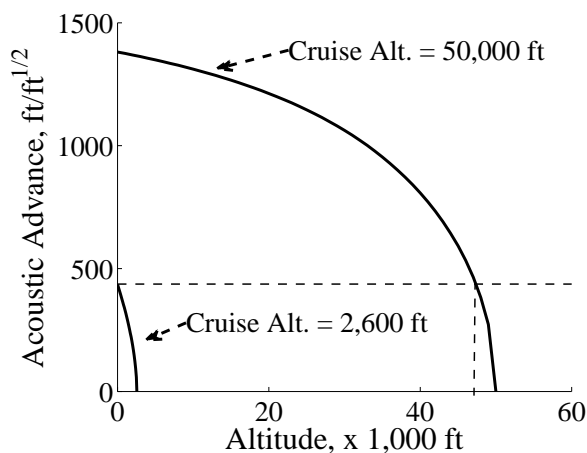
Figure 8.10: Acoustic advance vs. altitude.

because it avoids the need for a probing aircraft. This method of scaling is similar to Maglieri's solution: matching the ratio of cruise altitude to aircraft length, which is 357 for the SBJ. Using his procedure, the 10% scale test aircraft should cruise at 5,000 ft. However, the sonic boom would be distorted 610 ft/$\sqrt{\text{ft}}$ at the surface, which is larger than the 437 ft/$\sqrt{\text{ft}}$ desired. As can be seen in Fig. 8.10, the 10% scale model should fly at 2,600 ft in order to have the proper advance at the ground.

Modifying the cruise altitude has some significant consequences. As discussed earlier, if the altitude is reduced, weight must be increased in order to generate the proper F-function. As can be seen in Fig. 8.7, this would require the 10% scale aircraft to weigh 9,500 lbs, which would require a wing loading of 434 lb/ft^2 and cannot be achieved even if made from solid steel. Earlier the Mach number was restricted to that of the SBJ. If this requirement was lifted, the Mach number could be varied to balance Eq. (8.2). However, this would suggest a Mach number of 3.3, which is not seen as a practical option for a low-cost test platform due to thrust limitations and thermal heating.

Instead of trying to increase the Mach number or make a 10% scale model weigh 9,500 lbs, the aircraft can temporarily generate 9,500 lbs of lift by performing a pull-up maneuver. For the 10% scale model a 7.9 g pull-up will create the required wing loading. This can be accomplished

by performing the maneuvers shown in Fig. 8.11. The scale model starts at high altitude and dives toward the ground. This push-over maneuver will generate a caustic. The dive is held until clear of the caustic, then a pull-up is initiated at the predetermined load factor. The bottom of the pull-up should be at the low-altitude test option altitude, 2,600 ft for this case. During the pull-up the rays will diverge and will not create a caustic allowing for the recording of a simple sonic boom signal on the ground [149]. Although these maneuvers solve the weight issue, the altitude of 2,600 ft is below the 3,000 ft limit set by Maglieri in order to prevent cruising in the earth's boundary layer [122].
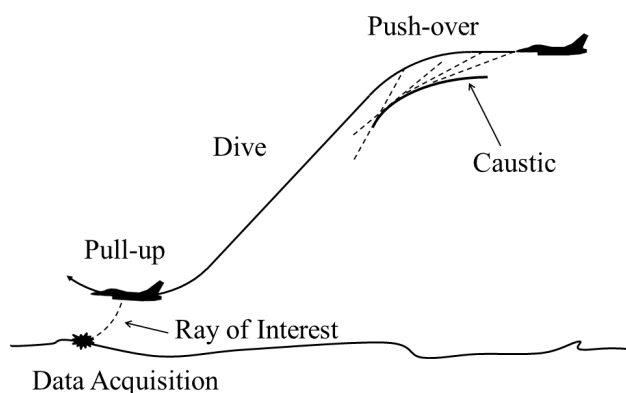
Figure 8.11: Pull-up maneuver to generate correct wing loading for low-altitude testing.

To find an alternative for the pull-up maneuver, the minimum scale for a straight and level pass is investigated. A summary is presented in Fig. 8.12 for all scales. The cruise altitude in order to satisfy Eq. (8.9) is shown in Fig. 8.12(a) and the wing loading required to satisfy Eq. (8.3) is shown in Fig. 8.12(b). To find a practical low altitude test scale, one must determine the practical limit in wing loading. Wing loading is an indication of aircraft overall performance. The upper limit of wing loading is usually determined by a takeoff distance [155] or a ceiling requirement [111]. Therefore, wing load for SBJ designs are typically below 100 lb/ft^2 [116] and fighters historically have wing loadings below 150 lb/ft^2 [111]. However, if the scale model is catapult launched or air dropped, the wing loading could be increased above these limits. For example, a cruise missile can
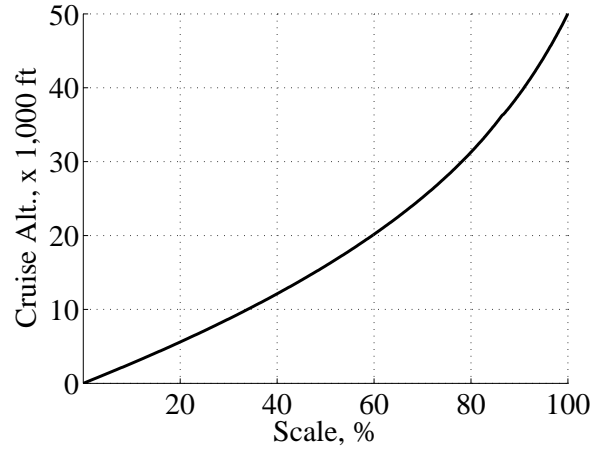
(a) Model cruise altitude.
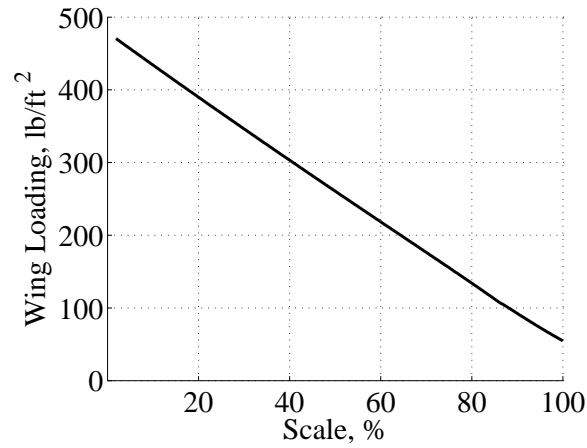
(b) Wing loading.

Figure 8.12: Low altitude test parameters.

have a wing loading as high as 300 lb/ft^2 [169]. If 300 lb/ft^2 is accepted as the upper limit in wing loading for the scale model, then as can be seen in Fig. 8.12(b), the smallest model that has a wing loading under this limit is 41% scale. However, this scale aircraft will be difficult to launch from a catapult or under a wing of a mother ship. Furthermore, if cost is assumed to be proportional to scale, the 41% scale model will cost significant more than the models below 25%. Thus, the 41% scale aircraft meets the sonic boom scaling method of this study, but it may not be practical from an operational perspective. Therefore, the pull-up maneuver is selected as the best technique for low altitude testing.

8.3.3.2   High-altitude option

The alternative to testing at low altitude, is the high-altitude test option, where the scale model flies at the SBJ's cruising altitude, 50,000 ft, and pressure measurements are taken at some distance below the model. Pressure data would be acquired using a probing aircraft similar to those conducted with the SSBD [65] and Quiet Spike [TM] [83]. As depicted in Fig. 8.10, for the 10% scale model, data should be recorded at 47,300 ft. The data acquisition altitude for all scales can be found in Fig. 8.13. These high altitude test have the advantage of avoiding the earth's boundary layer, allowing for cleaner signals to be recorded. A comparison of the ground pressure profiles for all the test options for the 10% scale test vehicle can be seen in Fig. 8.14. Both the low-altitude test, Fig. 8.14(d), and high-altitude test, with data taken at an intermediate altitude, Fig. 8.14(b), correctly predict the location of the wing shock. However, since the high-altitude test option does not require an increase in wing loading and avoids the atmospheric boundary layer, it is selected as the best test scenario. A summary of the testing options for four scales can be found in Table 8.1.
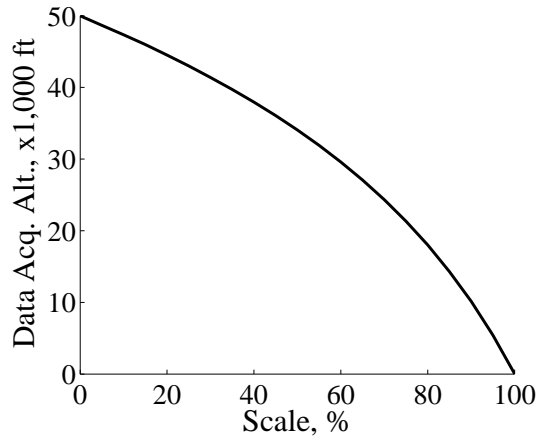
Figure 8.13: Data acquisition altitude to match acoustic advance of full-scale aircraft.
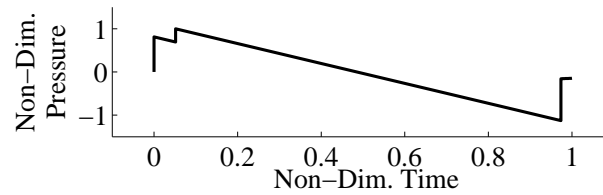
(a) 10% scale, weighing 1,200 lbs, at 50k ft, data acquisition at surface.
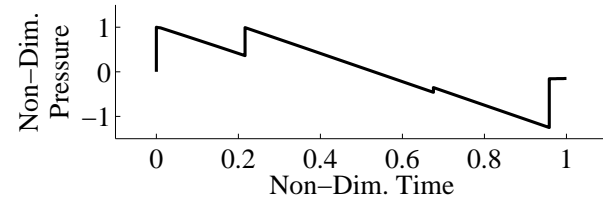
(b) 10% scale, weighing 1,200 lbs, at 50k ft, data acquisition at 47.3k ft.
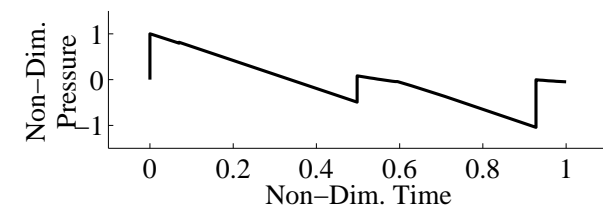
(c) 10% scale, weighing 1,200 lbs, at 2.6k ft, data acquisition at surface.
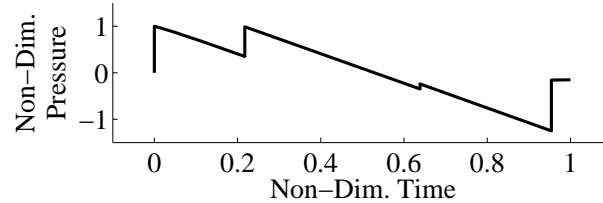
(d) 10% scale, weighing 9,500 lbs, at 2.6k ft, data acquisition at surface.
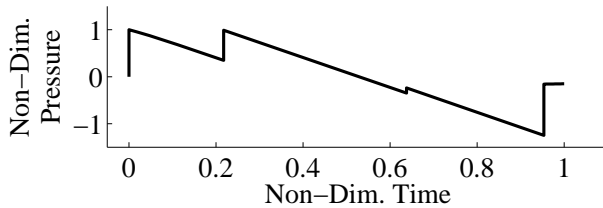
(e) SBJ, weighing 120,000 lbs, at 50k ft, data acquisition at surface.

Figure 8.14: Comparison of pressure profiles of 10% scale model and SBJ for various test conditions.

Table 8.1: Scaled Test Options

Case No.	Scale, %	Altitude, ft	Weight, lbs	Data Acq. Altitude, ft
5 High	5	50,000	300	48,600
5 Low	5	1,300	2,500	0
10 High	10	50,000	1,200	47,300
10 Low	10	2,600	9,500	0
16 High	16	50,000	3,000	45,300
16 Low	16	4,200	23,000	0
25 High	25	50,000	7,500	43,000
25 Low	25	6,900	50,600	0
SBJ	100	50,000	120,000	0

8.3.4   Post processing

Figure 8.15 presents a summary of the scaling, which depicts the percent overpressure and duration for the high-altitude test option. The duration is purely linear, while the pressure is quadratic:

$$\frac{\Delta p_S}{\Delta p_F} = 4x10^{-5}(scale)^2 + 7x10^{-4}(scale) + 0.5271 \tag{8.10}$$

These scaling relations can be used to scale up a model's pressure signature to estimate the SBJ's pressure profile.
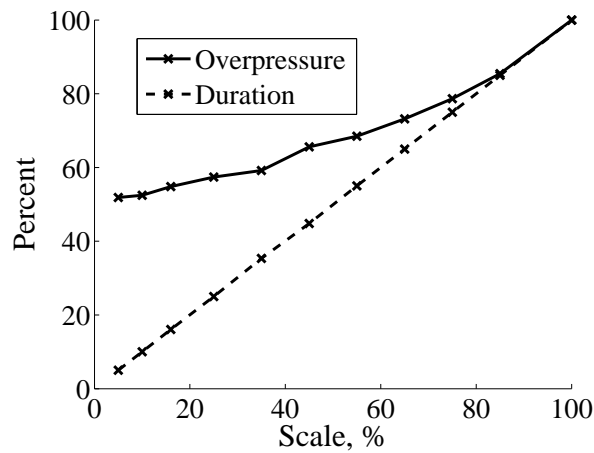
Figure 8.15: Percent of SBJ's overpressure and duration versus scale.

8.4 Lower Limit of Scale

8.4.1 Manufacturing

As can be seen in Fig. 1.5, as the wind-tunnel model scale decreases, it becomes more difficult to manufacture details. This issue is also true when testing with a scale UAS. This problem is compounded by the fact that as the scale is reduced, the boundary layer effect on the area profile becomes more significant, as shown in Fig. 8.16. For example, the 5% scale model has a boundary layer momentum thickness which is 5% of the maximum area, compared to 2.7% for the SBJ. In order to mitigate this issue, the volume of the 5% scale UAS should be decreased proportionally. In comparison, if a SBJ wind tunnel model were built at the same scale as the models in Fig. 1.5, the wing would need to be built 0.0022 inch thick, just to match the geometry and would need to be reduced to 0.0016 inches to compensate for the boundary layer. The boundary layer is less significant when conducting sonic boom testing in the atmosphere. For the smallest scale considered in this study, 5%, the wings are still a practical thickness, 1.05 inches (including the reduced area for boundary layer compensation), which is sufficient thickness to provide structural support for the 300 lbs of aircraft weight. Another challenge when building such a small supersonic UAS is finding an appropriate engine. There are several 25-lb thrust non-afterburning jet engines currently on the market [13]. If a pair of these engines were modified with a variable geometry nozzle, they would provide enough thrust to overcome the estimated 37 lb of drag predicted for the 5% UAS at test conditions. Therefore, there are no known manufacturing limitations that would prevent a scaled test aircraft from being built.

8.4.2 Molecular relaxation

All of the shocks in Fig. 8.14 are modeled as discontinuities; however, since the sonic booms are traveling thousands of feet, molecular relaxation will have a measurable effect, and the shocks will have discreet rise times. For now the discussion is limited to the the high-altitude test option. For this study, rise times are based on theoretical results from Ref. [16], which are for 30% relative
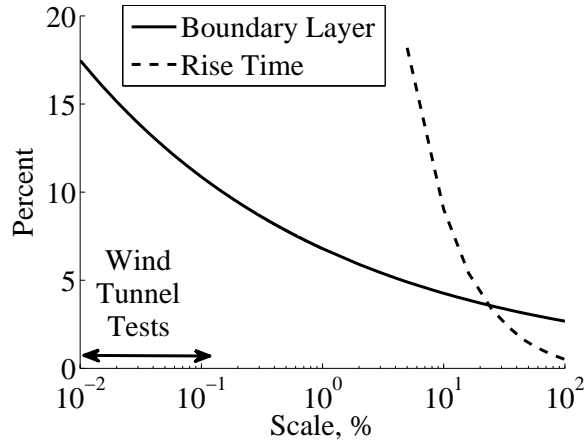
Figure 8.16: Shock rise time as a percent of signal duration and boundary layer as a percent of area profile.

humidity and include absorption and dispersion effects, shown in Fig. 2.3. Although in the past theoretical methods have under-predicted rise times compared to experimental results, using these theoretical results is justified for the following reasons:

- The propagation distances are shorter than the distance for the shock structure to reach steady state. For example, the data acquisition altitude for the 25% scale aircraft is 7,000 feet below the aircraft, while the distance to reach steady state is greater than 13,000 feet [16].

- The sonic booms will be measured in the stratosphere, where the humidity should be relatively constant and near 30% [100].

- Measuring the sonic booms in the stratosphere will also avoid the higher turbulence levels in the lower atmosphere, which increases rise times.

Therefore, the theoretical rise time is a reasonable and conservative estimate for the high-altitude case. The rise times for the low-altitude test option will be longer. Figure 8.16 shows the rise time of the initial shock as a percent of signal duration. Figure 8.17 shows sonic booms accounting for these effects. Since the 5% scale has weaker shocks than the 10% scale and full-scale aircrafts,

its shocks are affected more by molecular relaxation. For example, the inlet shock at 6 msec in Fig. 8.17(a) is washed out, but is discernible for the 10% scale model at 13 msec in Fig. 8.17(b). Based on this rise time analysis, the 10% scale is the smallest practical size recommended for this test case. In general, researchers must assess the rise time of the weakest shock they desire to measure in in order to determine the smallest practical scale.

(a) 5% scale model.

(b) 10% scale model.

(c) Full-scale aircraft.
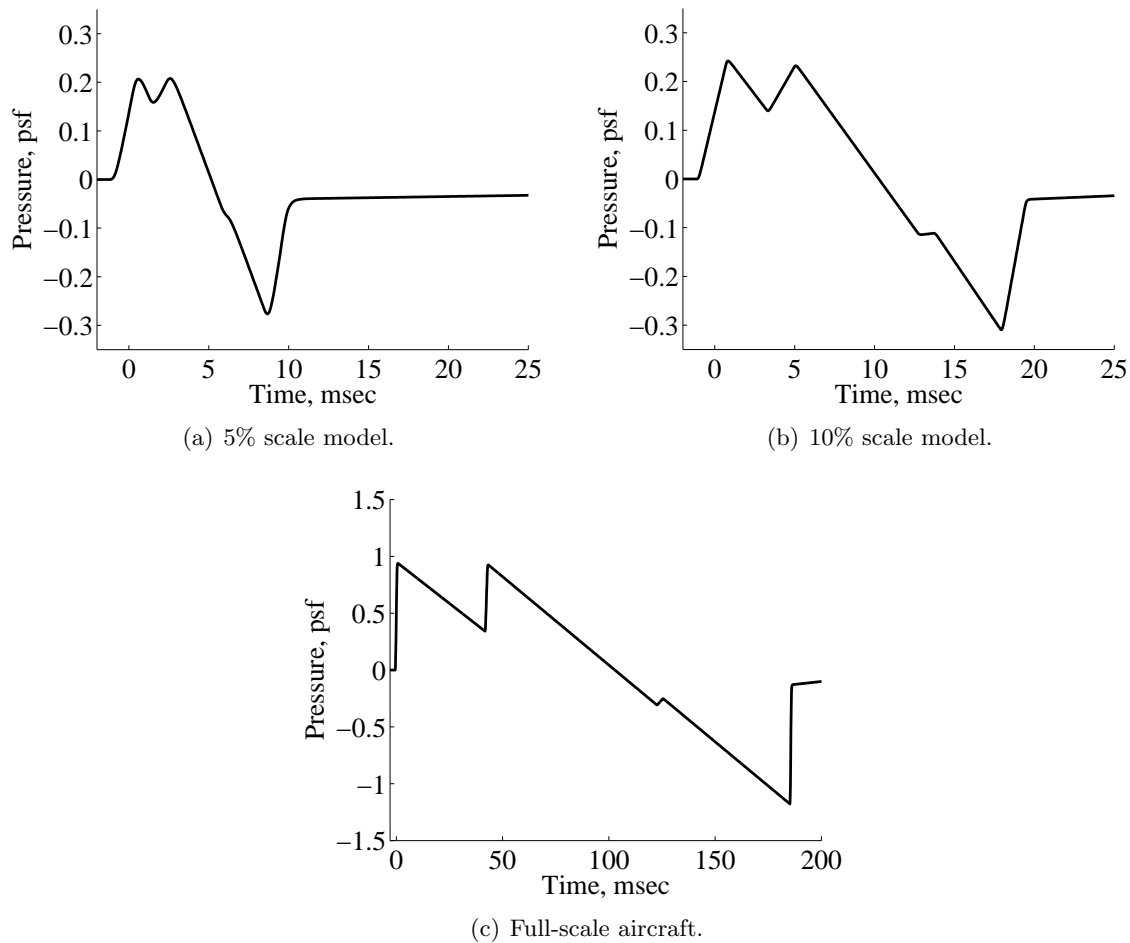
Figure 8.17: Pressure profiles accounting for molecular relaxation.

8.4.3   Data acquisition

As the scale decreases, the duration of the sonic boom decreases proportionally, making precise positioning of the probing aircraft more critical. The 5% scale sonic boom shown in Fig. 8.17(a) is approximately 16 ft long. The distance between the first two shocks is 2.4 ft. Assuming that the probing aircraft is using differential GPS to maintain position with the same accuracy of ± 2 ft as Ref. [65], the distance between the shocks for the 5% is nearly the same as the positioning system accuracy, making results unreliable. The distance between these shocks for the 10% scale test aircraft is 7.1 ft, thus the data acquisition system should be able to discern the two shocks and is the smallest scale recommended. The elimination of the 5% scale vehicle based on the above criteria is unique to our test case; however, it highlights the fact that the data acquisition system must be considered when conducting scaled flight tests. Differential GPS potentially can be used with position accuracies of less than 2 inches [180]. If such technology was applied to the probing aircraft, smaller scales would be practical. The bottom line is that researchers will need to consider the data acquisition system when selecting the test scale.

8.5   Chapter Conclusion

In summary, a scaled test aircraft flown in the atmosphere is capable of producing a scaled sonic boom that can be used to predict the ground pressure profile of the full-scale vehicle. The model must generate a scaled F-function, which requires it to fly at the same Mach number, angle of attack and canard incidence angle. When the scale model is flown at the same altitude as the SBJ, propagation is scaled by selecting the data acquisition altitude to ensure the scaled sonic boom has the correct amount of acoustic advance. In a similar manner, the cruise altitude could be modified to get the correct acoustic advance at the ground. However, this option requires a pull-up maneuver to generate the proper amount of lift. Either option will yield a properly scaled sonic boom, but both have technical challenges. The low-altitude test will require the model to do a series of high-g maneuvers and most of the propagation will occur in the earth's boundary

layer. On the other hand, the high altitude tests will require a probing aircraft. Theoretically any scale can be used, but in reality, manufacturing, data acquisition capabilities and shock rise times will constrain the lower bounds. Ultimately, for this test case the lower limit was determined to be 10% scale based on molecular relaxation's effect on rise times and data acquisition limitations. The 10% scale model will be flown at the same altitude and Mach number as the SBJ and data will be recorded via a chase aircraft at 47,300 ft. Then, its sonic boom amplitude and duration can be scaled to predict the boom for the full-scale aircraft.

Chapter 9

TECHNOLOGY DEMONSTRATION FLIGHT TESTING

This chapter will explore how a scaled vehicle can be used to demonstrate the viability of lobe-balancing. The last chapter's objective was to create a sonic boom that could be used to predict the full-scale aircraft sonic boom. This chapter's objective is to create a technology demonstrator similar to the SSBD. Since there is no full-scale aircraft to match parameters, the design space is much larger, allowing the use of any weight, Mach number and altitude. However, to minimize cost, it is assumed that the technology demonstrator will be small and un-manned. First the feasibility of using GoJett is assesses; then, a new UAS is proposed.

9.1   GoJett Suitability

The University of Colorado is perusing building a supersonic UAS named GoJett [175]. For logistical and financial reasons it would advantageous to use this platform as the technology demonstrator. As can be seen in Fig. 9.1, GoJett has a pitot inlet and internal engine. To reduced drag, GoJett will use thrust vectoring for directional control, eliminating the need for a vertical tail. Gojett is 5.9 ft long with a span of 3.6 ft and weighs 110 lb. GoJett is being designed for a world record speed run, so its on design condition is Mach 1.2 at 6,500 ft. Thus, it would be helpful if it flew at these design conditions for the technology demonstrations as well, implying that sonic boom data would be taken on the surface.

Figure 9.2 shows GoJett's non-dimensional area distributions compared to that of the lobe-balanced aircraft from Chapter 6. Due to its small size and low altitude, the equivalent area due

lift is very small. This is concerning because the lobe balancing in Chapter 6 was accomplished by adding lift to balance the lobes. Since GoJett's lift distribution is so small, it will be challenging to use the same strategy on GoJett. A planform view and F-function are shown in Fig. 9.3 for Mach 1.4 and 6,5000 ft. The F-function is dominated by the inlet, which creates a large bow shock, which cause high F-function values near the nose. As can be seen in in Fig. 9.2(b), GoJett was designed to have a perfect Sears-Haack area distribution. This causes $S''(y)$ to be negative for all locations accept the nose. Thus, as seen in Fig. 9.3, the F-function is shaped like an N-wave. Since lobe-balancing is designed to prevent a signal from developing into an N-wave, major modifications will need to be done to change the initial pressure signal to something other than an N-wave.

Figure 9.1: GoJett supersonic UAS, reproduced from Ref. [175].

With GoJett's small scale, signal distortions caused by the ground reflections will be significant. When a pressure wave from a SBJ reaches the surface, it is reflected, essentially doubling the amplitude. The doubling is a result of the long signal duration. The distance from the ground to a human ear is approximately 5 ft. So if the sonic boom is coming from directly above, the ear will be listening to two portions of the signal separated by 10 ft, the incoming signal and the one reflected from the surface. Since a sonic boom from a SBJ aircraft is approximately 250 ft long at the surface, the 10 ft difference is not significant and, in general, the incoming and reflected signal

(a) Lobe-balanced SBJ.
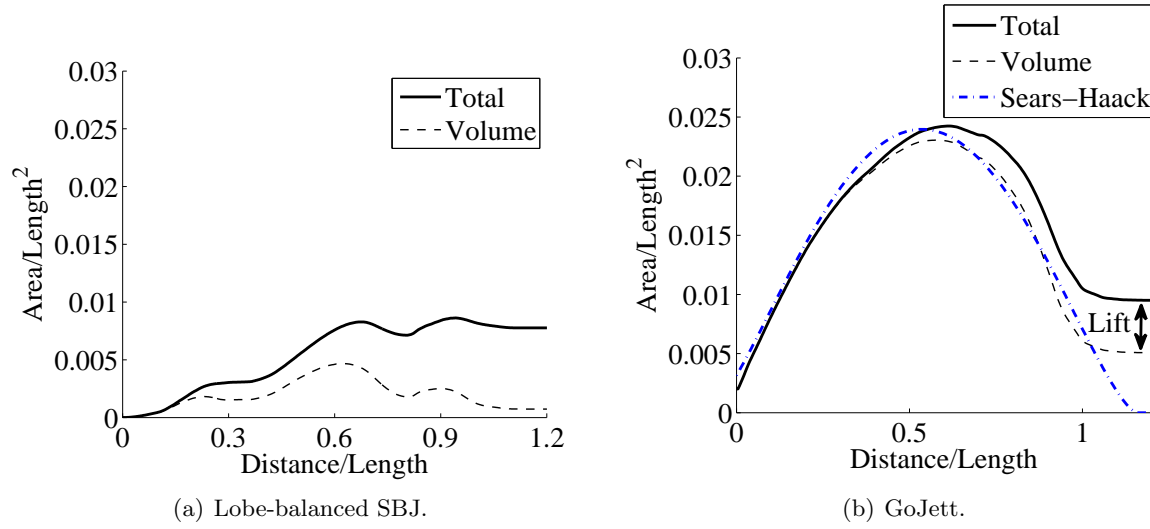
(b) GoJett.

Figure 9.2: SBJ and GoJett non-dimensional area profiles.
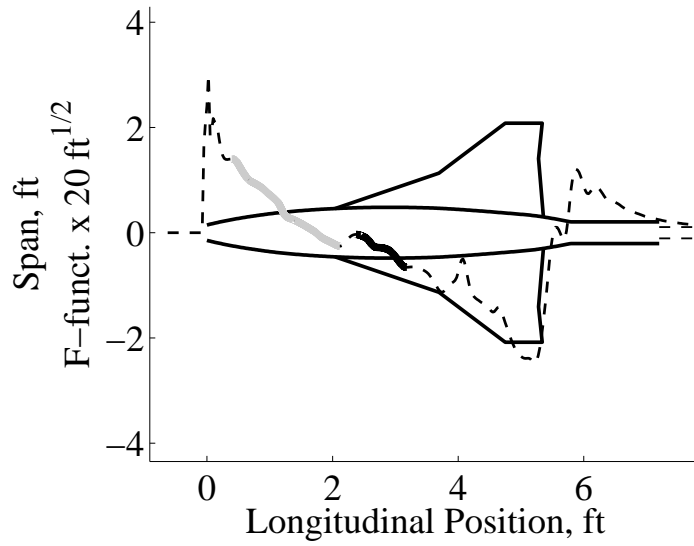
Figure 9.3: GoJett planform view and F-function.

are in phase, doubling the amplitude. The exact delay time can be calculated by [89]:

$$delay = \frac{2h_o \cos \psi}{c} \qquad (9.1)$$

where h_o is is the distance above ground to the ear, approximately 5 ft. The associated pressure heard by the human observer is:

$$\Delta p(t) = \Delta p_{in}(t) + \Delta p_{in}(t + delay) \qquad (9.2)$$

The only variable in Eq. (9.1) is ψ, the acoustical ray incidence angle. For the lobe-balanced aircraft flying at Mach 1.7 and 51,000 ft, the incidence angle is 43°, resulting in 6.6 msec delay. The delay on the lobe balanced pressure wave with a 173 msec duration is minimal, as shown in Fig. 9.4. In Fig. 9.4(a), the sonic boom is shown before reflection. In Fig. 9.4(b), shows the pressure signal heard by the observer, calculated by Eq. (9.2). This pressure signal is comparable to doubling the incident wave, which is shown in Fig. 9.4(c). Thus, it is common to multiply the incident wave by a reflection factor ranging from 1.8 to 2.0. Values slightly less than 2.0 are to account for the minimal absorption from the ground.

(a) Before reflection.

(b) After reflection.

(c) Perfect reflection.
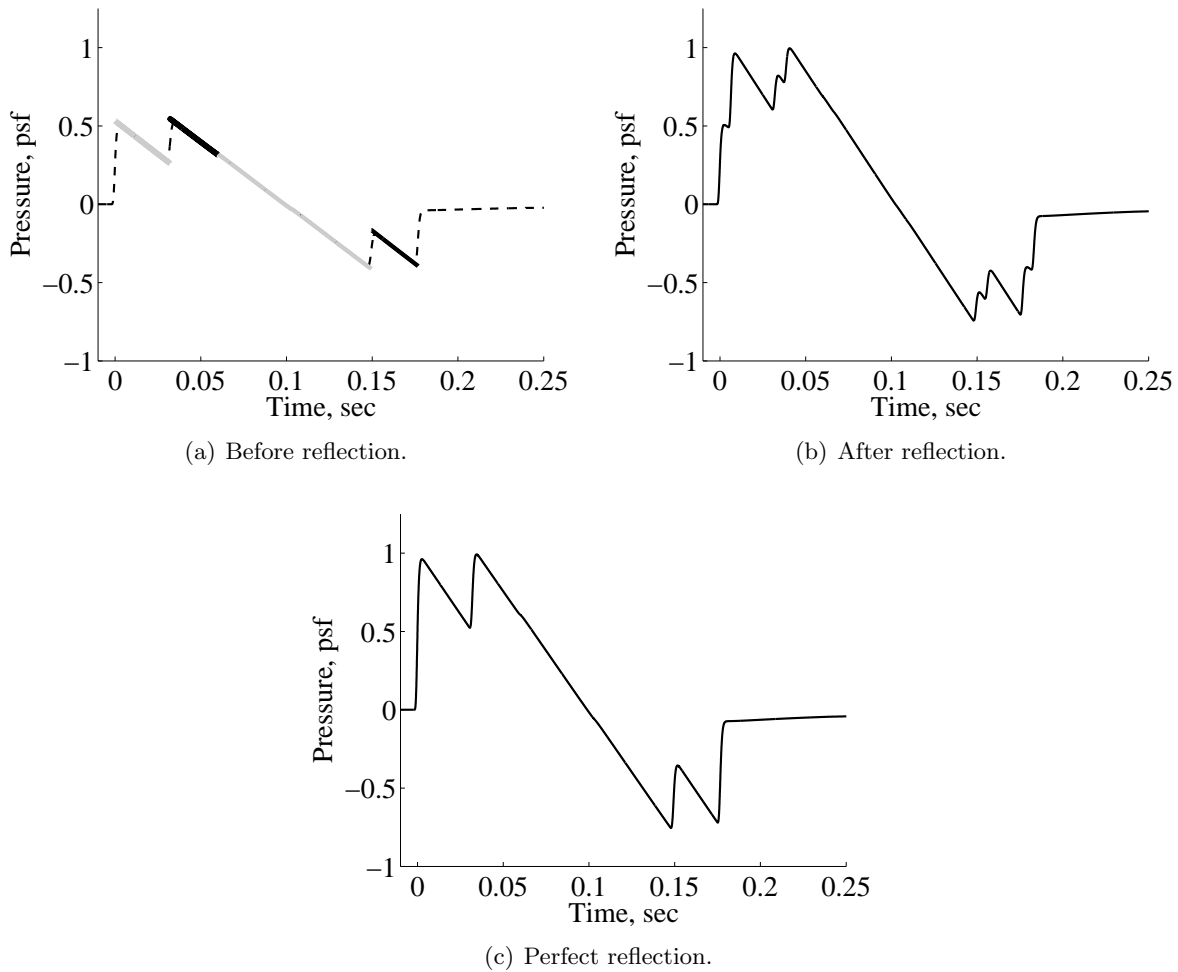
Figure 9.4: Lobe-balanced aircraft ground pressure profiles.

For GoJett flying at Mach 1.4 at 6,500 ft, the incidence angle is 43° resulting in a 6.1 msec delay, which is comparable to the lobe-balanced aircraft. However, since its sonic boom duration is 13 msec, the effect on the signal is dramatic, as seen in Fig. 9.5(b). Thus, it is recommended that data be recorded from a tower at an elevation higher than the signal length, 10 ft, to record one clean signal before the reflected signal reaches the pressure recorder.

(a) Before reflection.

(b) After reflection.

(c) Perfect reflection.
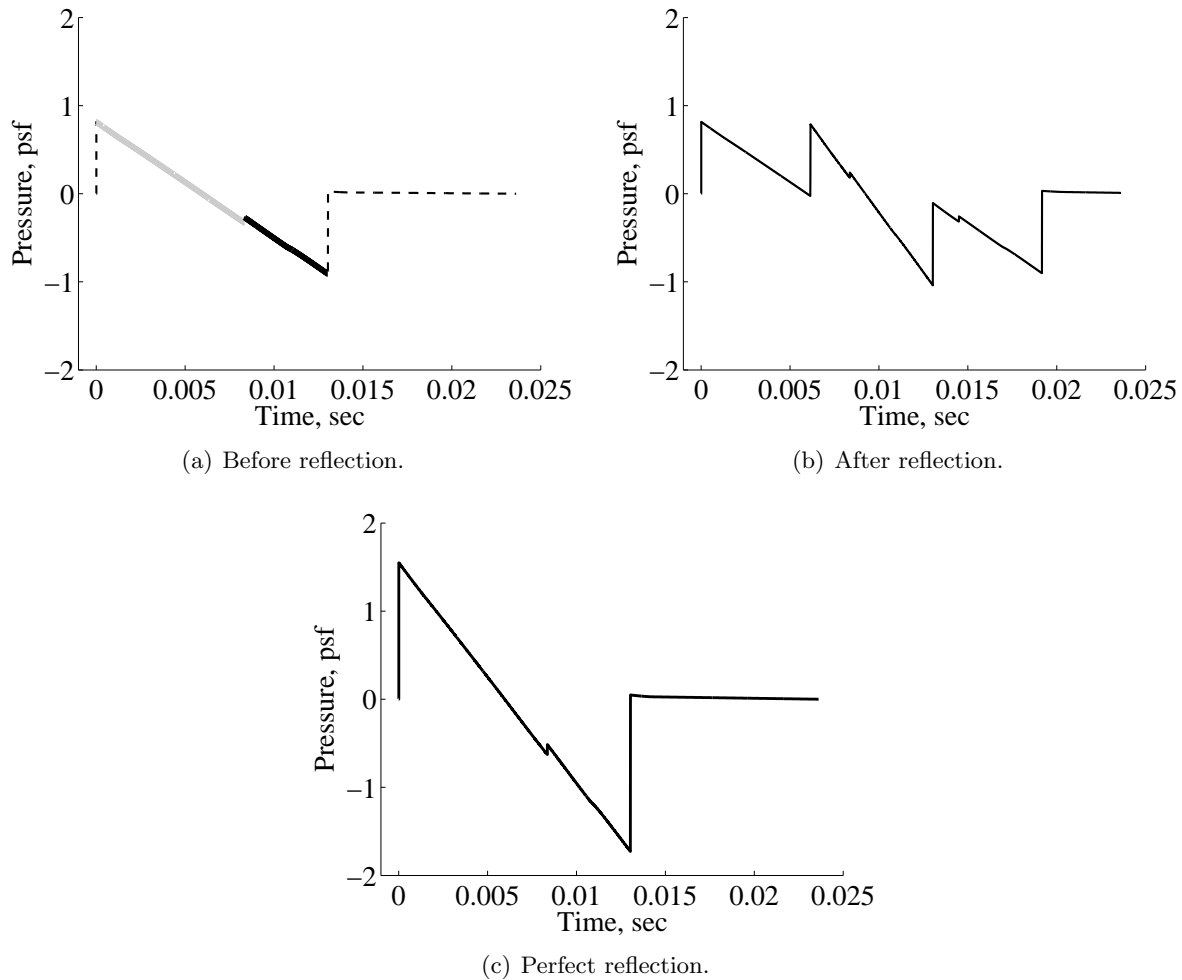
Figure 9.5: GoJett ground pressure profiles.

9.2   Lobe-Balanced Technology Demonstrator

Based on the above analysis it is concluded that GoJett in its current form is a poor platform to use as a lobe-balancing test bed. Therefore, a new design has been developed with the desire

to use as much as GoJett's hardware as practical. Since GoJett's engine is the most complicated component, the new platform named Lobe Balancing Technology Demonstrator (LBTD) was created using the engine inlet as the scale (LBTD's engine inlet has the same diamter as GoJett), as shown in Fig. 9.6(a). LBTD is 13 ft long and weighs 500 lbs and uses two GoJett engines. It was assumed LBTD would be have the same flight conditions as GoJett: 6,500 ft and at Mach 1.4. Based on the reflected shock discussion above, data will be acquired by an elevated microphone (reflection factor =1.0). The sonic boom for these conditions is shown in Fig. 9.6(b). Although it is a frozen boom, the aircraft must produce 6,200 lbs of lift, which is possible if it is performing a 12 g pull-up as shown in Fig. 8.11. However, a straight and level profile is desired. Trimming

(a) Planform view. (b) Sonic boom.
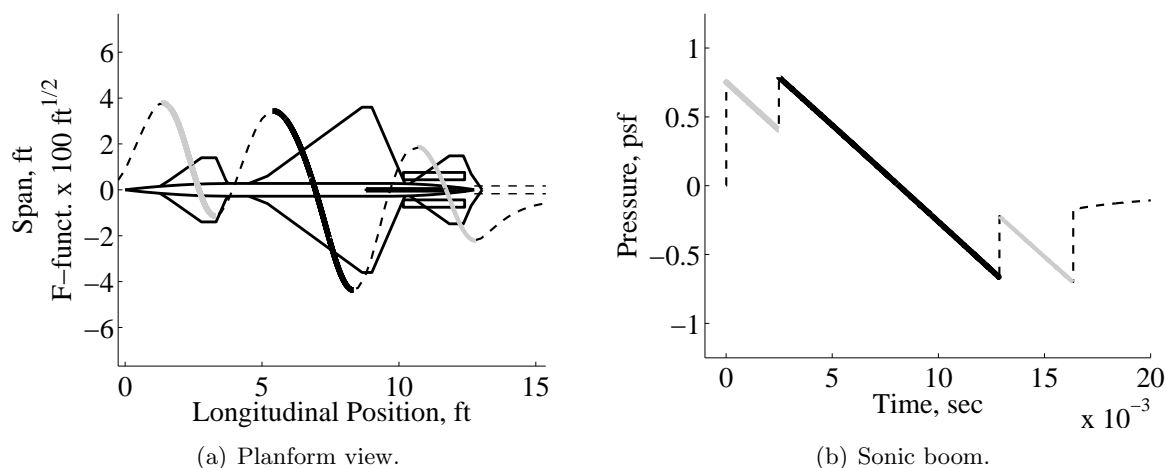
Figure 9.6: The initial design of LBTD.

the aircraft to level flight, the area profile and sonic boom are shown in Fig. 9.7. The sonic boom is not frozen. Like GoJett, LBTD's equivalent area due to lift is much smaller than is volume. Therefore, it will be difficult to balance the lobes using lift. For example, the front shocks can be frozen by making the canard produce 1,000 lbs of lift; thus, volume changes will be used instead. The front canard thickness was increased from 3% to 5%. The horizontal and vertical tail thickness was increased from 3% to 6%. Furthermore, the fuselage radius was increased by 0.14 ft near the engines. Although GoJett will be capable of flying without a vertical tail, it was retained because volume was needed to balance the wing's expansion (If the vertical tail is removed, the magnitude

of the fuselage radius change would need to be bigger.). The result of these volume increases is a frozen sonic boom as can be seen in Fig. 9.8.

9.3   Chapter Conclusions

In summary, GoJett was determined to be a poor platform for a sonic boom minimization technology demonstrator. A new UAS is proposed which will use two GoJett engines. It is essentially a scaled model of the lobe-balanced aircraft from Chapter 6. However, some volume changes need to be made to balance the lobes, because at this small scale and altitude, lift changes are not effective. LBTD should fly at Mach 1.4 and 6,500 ft over a range with elevated pressure traducers to avoid the compilations of reflected shocks. In doing so LBTD will demonstrate that lobe balancing is a viable sonic boom minimization strategy.

(a) Planform view.
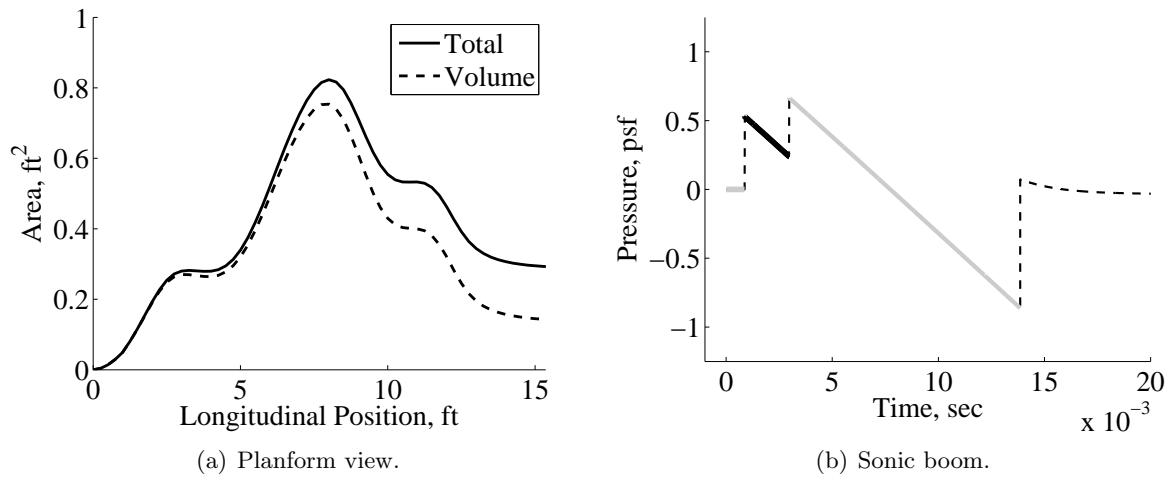
(b) Sonic boom.

Figure 9.7: LBTD trimmed for level flight.

(a) Planform view.
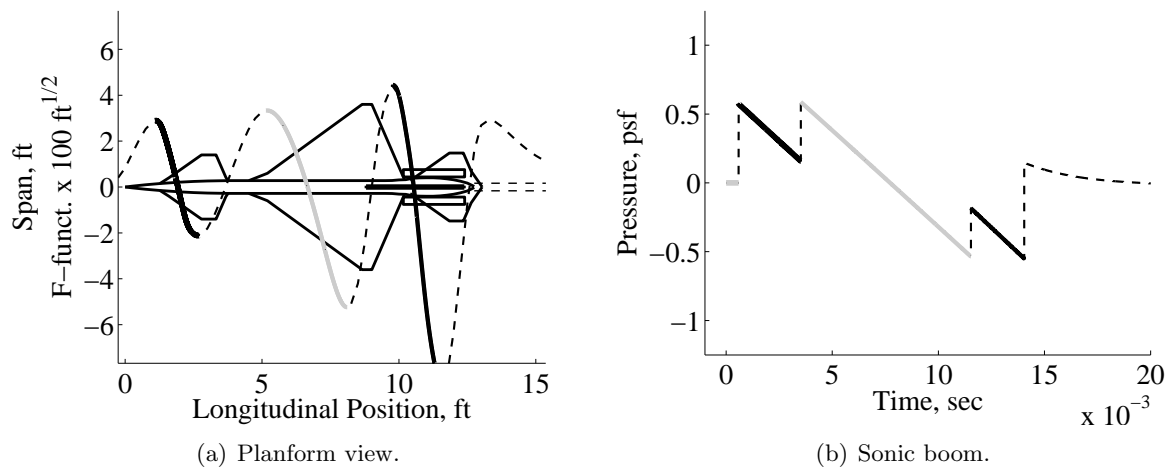
(b) Sonic boom.

Figure 9.8: LBTD modified to create frozen sonic boom in level flight.

Chapter 10

PERCEIVED LEVEL OF LOUDNESS ANALYSIS

This chapter breaks the paradigm that reducing the ISPR is the most efficient way of reducing the human annoyance to sonic booms. PLdB has shown to be the best metric for predicting human response to a sonic boom [106]; yet, researchers often emphasis ISPR. For the lobe-balanced aircraft in Chapter 6, the Frozen trim condition reduced the ISPR from 1.4 to 0.95 psf, a 32% reduction, which is significant. However, the PLdB was only reduced from 98 to 92, a more modest 7% reduction. Furthermore, the 92 PLdB is far above the 70 PLdB goal. Reflecting on the methodology in that chapter, the author changed the design in order to lower ISPR, which reduce the PLdB. However, this is not the most efficient way to lower the PLdB. For example, cutting an N-wave's overpressure in half equates to a 7 dB reduction in PLdB [164]. Thus, if this ratio was applied to the lobe-balanced aircraft with 92 PLdB and 0.95 psf overpressure, a reduction of 7 x 3 PLdB will bring the aircraft near the 70 PLdB goal, but will require a ISPR of 0.125 psf, which will be challenging. Therefore, a more targeted approach must be used to reduce PLdB.

Before discussing how to lower the PLdB, the theory behind it and its calculation methods are presented, so that the rational for proposed reduction strategies are understood. Then, various options are presented to reduce the PLdB. These options are based on the pressure profile and may not have an associated design that is capable of producing the signature. The intent is to explore multiple pressure signatures to find the best profile to set as a goal to drive the design.

10.1   Human Response to Frozen Sonic Booms

The sonic boom from the Frozen trim condition, as presented in Fig. 10.1(a), differs from sonic booms of historical literature is several respects. The two shocks in the positive portion of the boom are separated by 30 msec, as are the two shocks in the negative portion. There is limited information on how a human will react to shocks so closely spaced. As shown in Fig. 10.1(a), it is anticipated that a human will react as if there are two signals: one from the associated N-wave of the leading and trailing shocks, shown in black, and a second from the two interior shocks, shown in gray. This perspective is based on NASA TP-3134 [164]. Since the interior shock pressure rises are weak, 0.43 and 0.36 psf, the human response to the interior N-wave should be minimal. It is also significant to note that the overall duration of the Frozen sonic boom, 173 msec, is less than the integration time of the human ear, 200 msec. In the past, when considering SST aircraft, similar in size to the Concorde, the sonic boom duration exceeded 200 msec. Thus, most of the human response studies assumed the duration exceeded the integration time. These long sonic booms have the advantage that the leading and trailing shocks will be heard as two distinct events, effectively cutting the power level in half [164]. Therefore, the short duration sonic boom of the lobe-balanced aircraft may be more annoying to humans. Fortunately, PLdB is still a good metric in quantifying the human response.

10.2   Perceived Level of Loudness

Loudness is defined as "the perceived intensity of sound," while noisiness is the "attributes of a sound which make it unwanted, unacceptable, disturbing, objectionable, or annoying" [84]. In general, contours of noisiness and loudness have similar shapes. The term "annoyance" has also been used to quantify the subjective response of a pressure signal [105]. PLdB (also referred to as Mark VII) is an excellent metric to quantifying the human response to sonic booms. It captures loudness, noisiness and annoyance [106]. PLdB was developed by Stevens with the intention of being used on sonic booms [167] and is considered the best metric for predicting the human response. In

(a) Pressure profile.

(b) Power spectrum.

(c) Sones.
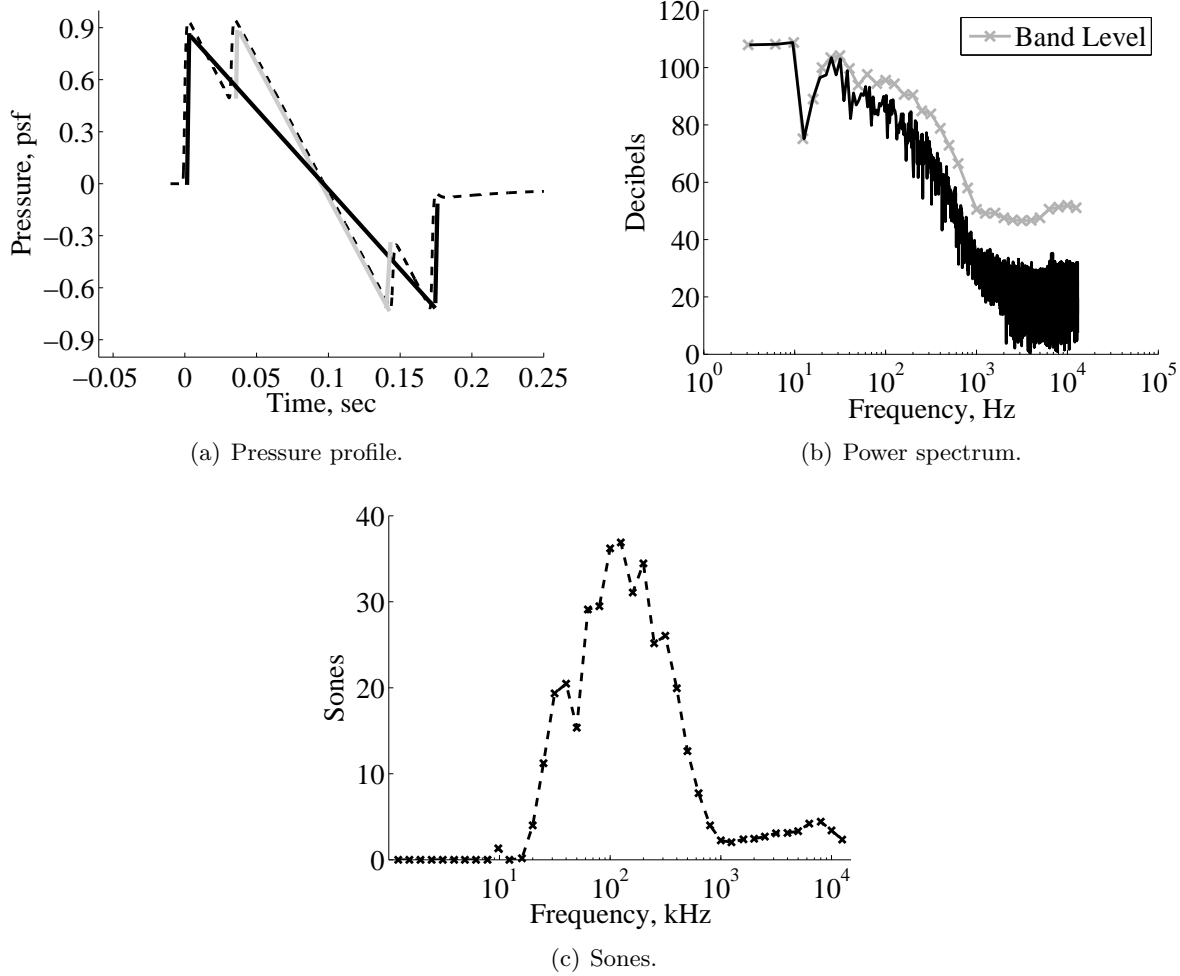
Figure 10.1: Lobe-balanced aircraft PLdB summary.

fact, when NASA developed its road map for future supersonic civil aircraft, it set a requirement that the sonic boom must be below 70 PLdB without specifying an overpressure requirement [176]. Since PLdB has shown to be such a good predictor for many sonic boom variations: indoors, outdoors, reflected sonic booms, atmospheric distortions, etc. [106], it should also be a good metric for the sonic booms from the lobe-balanced aircraft, despite their unusual shapes.

10.2.1   PLdB calculations

The first step in calculating PLdB is finding the band pressure level for each 1/3 octave (also referred to as a "band"), which is calculated by summing the pressure levels for each frequency in

the 1/3 octave [141]:

$$L_b = 10 \log_{10} \left(\sum 10^{L_n/10} \right) \tag{10.1}$$

Then, the band pressures are converted to units of *sones* which captures the ear's sensitivity to frequency as depicted in Fig. 10.2. The 1/3-octave pressure levels for an example signal are drawn with a line. The intersection of the "o" markers with the contours represents the equivalent sones for that band pressure level. The shape of the sone curves accounts for the sensitivity of the human ear. Since it is most responsive to frequencies from 3,150 to 8,000 Hz, the bands in this region are given higher weighting. For example, 50 dB band pressure level at 100 Hz equates to 0.481 sones. In contrast, 50 dB pressure level at 3,150 Hz is equal to 4.0 sones. The total loudness in sones is calculated by:

$$S_t = S_{max} + F \left(\sum S - S_{max} \right) \tag{10.2}$$

where F is a masking factor. Masking occurs because the 1/3-octave band with the highest sones dominates the human response and inhibits the response from other bands. The amount of masking is a function of S_{max}, with a typical values of F being around 0.20. Finally, S_t is converted to decibels by:

$$PLdB = 32 + 9 \log_2 S_t \tag{10.3}$$

The use of $\log_2$ differs from most acoustical signal processing which uses $\log_{10}$; thus, a doubling of S_t yields a 9 dB increase in PLdB.

10.2.2   PLdB issues

The procedures presented by Stevens do not account for all situations. Therefore, the PLdB calculations in this study are based on the algorithm provided in Ref. [139]. The following are some
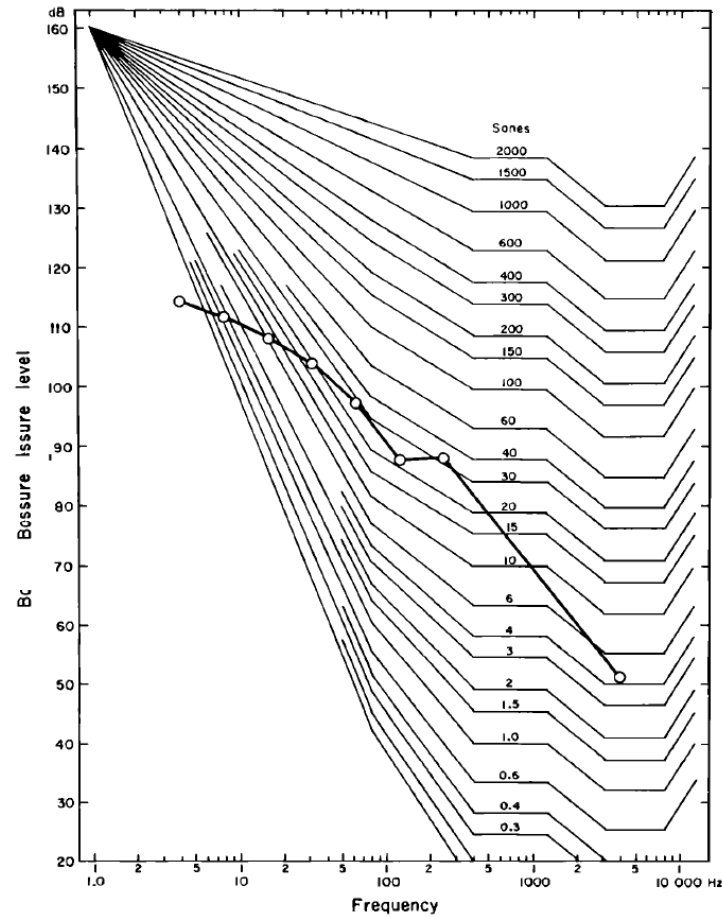
Figure 10.2: Sones as a function of frequency and band pressure level, reproduced from Ref. [167].

issues that may be handled differently by various PLdB calculating subroutines:

- **Low Frequencies:** Only the frequency content in the human audible range affects PLdB. This range is normally said to be from 20 to 20,000 Hz [84]. However, one of the major improvements of Stevens' method was extending the range of frequencies down to 1 Hz. Previous methods did not consider frequencies below 50 Hz, such as Ref. [89]. However, Stevens only tabulated the sones curves down to 50 Hz. Therefore, some algorithms for calculating PLdB may omit the range from 1 to 50 Hz. Since the lower frequencies usually have high acoustical power, they were included in the PLdB subroutine used in this report by using the contours shown in Fig. 10.2 to extend Stevens' tabulated data down to 1 Hz.

- **High Frequencies:** Stevens is not clear on how to process frequencies above 12,500 Hz. Stevens assumes that the signal has been sampled fast enough to obtain dB values for all bands up to 12,500 Hz. If a signal were sampled below 25,000 Hz (Nyquist frequency of 12,500 Hz), the highest bands would have no valid dB value. In order to ensure the FFT included frequencies up to 12,500 Hz, all signals in this study were sampled at 26,000 Hz to meet the Nyquist criteria. Although this can cause some aliasing, it was considered necessary, otherwise the upper bands would have zero sones, causing an artificially low PLdB estimate. The signal could have been sampled at a higher frequency to allow sone levels to be calculated at bands above 12,500 Hz. However, since power levels usually decay with increasing frequency, in addition to the high threshold in the lowest sone contour, the bands from 12,500 to 20,000 Hz have little effect on the PLdB level; justifying the 12,500 upper limit.

- **Low Band Levels:** As can be seen in Fig. 10.2, the sones contours do not account for all possible values of band levels, such as the lowest frequency of the example in Fig. 10.2, which falls below the lowest sones contour. For these low dB cases, the software sets the sones to zero. Regardless if the sones is set to zero or set to a very small value, it will not effect the PLdB value significantly.

- **High Band Levels:** Since sone data is only available for up to 160 dB, if the band pressure were to exceed this level, the sone level is not clearly defined. If this were to occur, the subroutine used in this study would set the sones to that for 160 dB and send a warning to the user. Another option to would be to extrapolate. Whether the sones is set to that of 160 dB or extrapolated will have significant impact on the PLdB estimate. Fortunately, this never occurred in this study.

All of the exceptions listed above demonstrate that there may be variations in PLdB calculation from study to study.

10.3   Perceived Level of Loudness Reduction Techniques

The following is analysis of six different techniques to lower the PLdB. Since the fundamental quantity in the PLdB is the sones, graphs of sones per frequency band will be used to assess the effectiveness of the technique.

10.3.1   Scaling the signal

First, the status quo solution is accomplished: reducing the entire pressures signal, including the ISPR. This is accomplished by multiplying the pressure signal by a constant, c_1. Two pressure signals for $c_1 = 0.5$ and 0.3 are presented in Fig. 10.3. Figure 10.3(b) shows the sones for $c_1 = 0.5$, compared to the original sone values. In general, reducing the amplitude reduces the sones for all bands. The PLdB for $c_1 = 0.5$ and 0.3 are for 81 and 74 PLdB, respectfully, which are still above 70 PLdB goal. These signatures have the advantage of also reducing the ISPR and impulse. However, significant design improvements will be needed to obtain even the $c_1 = 0.5$ level and the $c_1 = 0.3$ is considered un-attainable. Therefore, a more efficient method is desired.


(a) Pressure profiles.   (b) Sones.
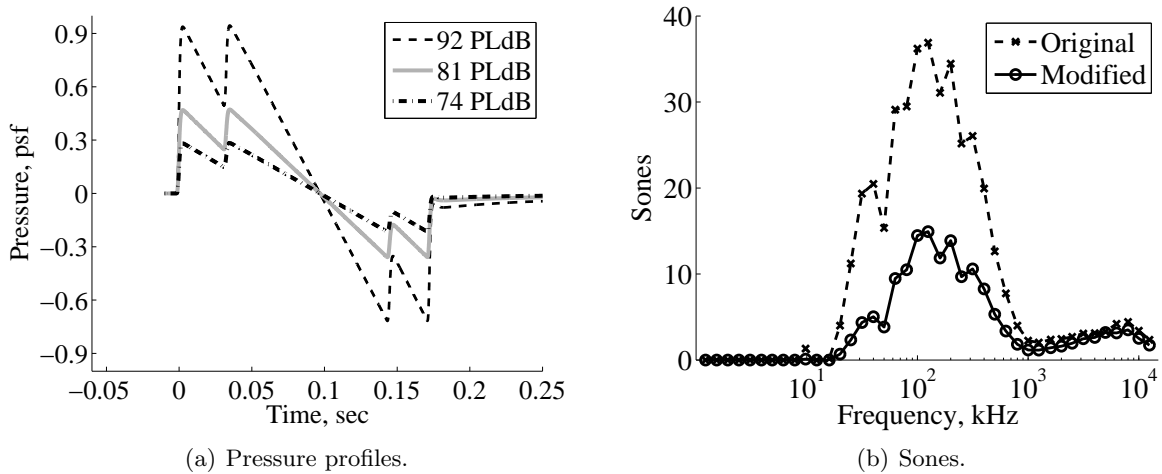
Figure 10.3: Scaling the pressures.

10.3.2   Filtering

Based on the above discussion on PLdB, some insight can be gained about how to reduce the PLdB. The pressure profile, frequency content and sones for the Frozen trim condition were shown in Fig. 10.1. The frequencies below 50 Hz, have high acoustical power, as shown in Fig. 10.1(b), but because of the high threshold in the sone contours, these bands have low sone levels as shown in Fig. 10.1(c). One can also see that the weighting has moderately increased the influence of the frequencies from 3,150 to 8,000 Hz. Despite the weighting, the frequencies from 100 to 300 Hz dominates the PLdB value. Therefore, filtering out these frequencies seems to offer a targeted solution.

Figure 10.4 shows the pressure profile from Fig. 10.1(a) put through a 20-pole Butterworth 100 to 300 Hz band-stop filter. The filtering is effective at reducing the PLdB to 83. The advantage of this method is that it accomplishes the PLdB reduction with minimal effect on the overpressure. In fact, maximum overpressure actually increases. This increase in peak overpressure with a reduction in PLdB is proof of the issues discussed in the opening of this chapter: ISPR and PLdB do not necessarily change proportionally. However, the drop in PLdB from 92 to 83 is not as effective as anticipated, but Eq. (10.2) provides an explanation. For sonic booms in this study the first term, S_{max}, contributed to approximately 30% of S_t. When the associated frequency band is eliminated by the filter, one may expect a 30% reduction in PLdB. However, the next band with the highest sones will become S_{max}; thus, the reduction is less dramatic. This filtering technique although effective, does not meet the 70 PLdB goal and will be difficult to incorporate into an aircraft design.

10.3.3   Smoothing

A similar concept to filtering, smoothing is implemented via averaging. The signal from Fig. 10.1(a) is smoothed by setting the value at a location to the mean for the 20 closest points. This smoothing is continued 80 times, resulting in the pressure profile shown in Fig. 10.5(a). This

smoothing rounds the peaks and lowers the high frequency sones, as shown in Fig. 10.5(b). This method was selected over a low pass filter because the low pass filter causes a series of overshoots around the shock locations. The smoothing combined with the amplitude reduction is also presented in Fig. 10.5. The combination of smoothing and using $c_1 = 0.5$ is able to reduce the loudness to 68 PLdB, meeting the 70 PLdB goal. Molecular relaxation can smooth a pressure profile as it propagates to the ground, but it will be difficult to design an aircraft that generates a smooth pressure profile at the surface.


(a) Pressure profiles.

(b) Sones.
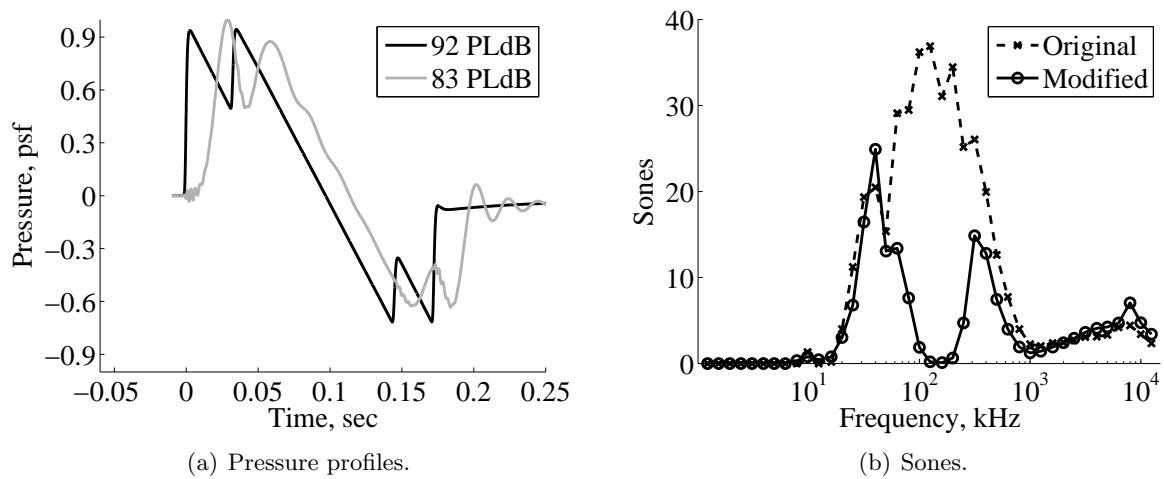
Figure 10.4: Band-stop filtering.

(a) Pressure profiles.

(b) Sones.
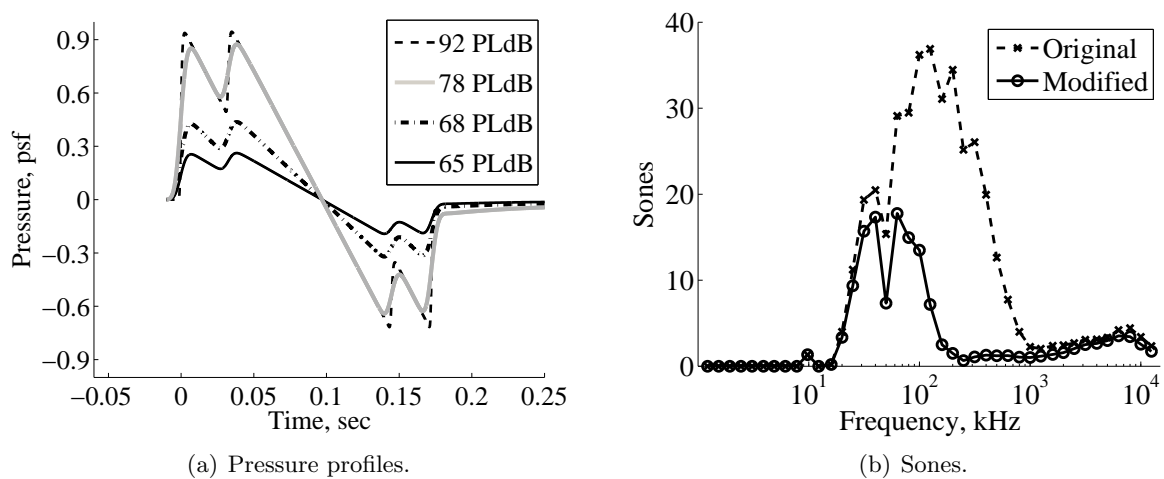
Figure 10.5: Smoothing the signal.

10.3.4   Increasing rise times

Another choice to reduce PLdB is to create a long rise time. This is initially done by adding a 50 msec linear rise to the leading and trailing shocks, as shown in Fig. 10.6(a). This has limited impact on the PLdB, reducing the PLdB from 92 to 88. As shown in Fig. 10.6(b), the rise time caused moderate reduction in sone levels for all frequencies. In fact, slight increases in sones are seen at high frequencies due to the sharp corners. Even when accompanied with $c_1 = 0.5$, the pressure profile still equates to a PLdB above the 70 PLdB goal. The rise time has limit impact on PLdB because the interior shock were not modified.


(a) Pressure profiles.   (b) Sones.
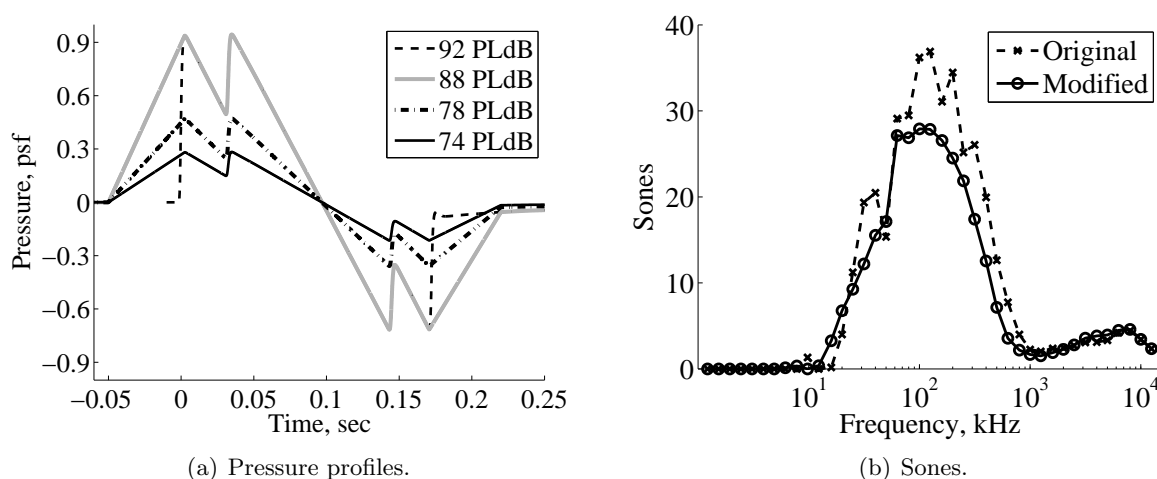
Figure 10.6: Increasing rise times.

10.3.5   Flattening the top

Figure 10.7 examines a pressure profile with the double leading and trailing shocks replaced with a flat top profile. This is effective at reducing the PLdB to 80. However, there are some consequences of this method. The frequency content is shown on Fig. 10.8, which shows an increase of energy below 50 Hz, compared to Fig. 10.1(b). In fact, this signature has an overall energy of 122 dB versus 114 dB for the baseline case. This flat top boom also has a higher impulse. In short, although this signature decreases the PLdB, it has negative impacts on other metrics. In order to

lower the impulse, the flat top is looked at without a nose modification, as shown in Fig. 10.9. This signature is also smooth in as similar manor as was done in Fig. 10.5. The combination of smoothing and flat top in Fig. 10.9 is more effective than the flat top with nose and tail modifications from Fig. 10.6.

(a) Pressure profiles.

(b) Sones.
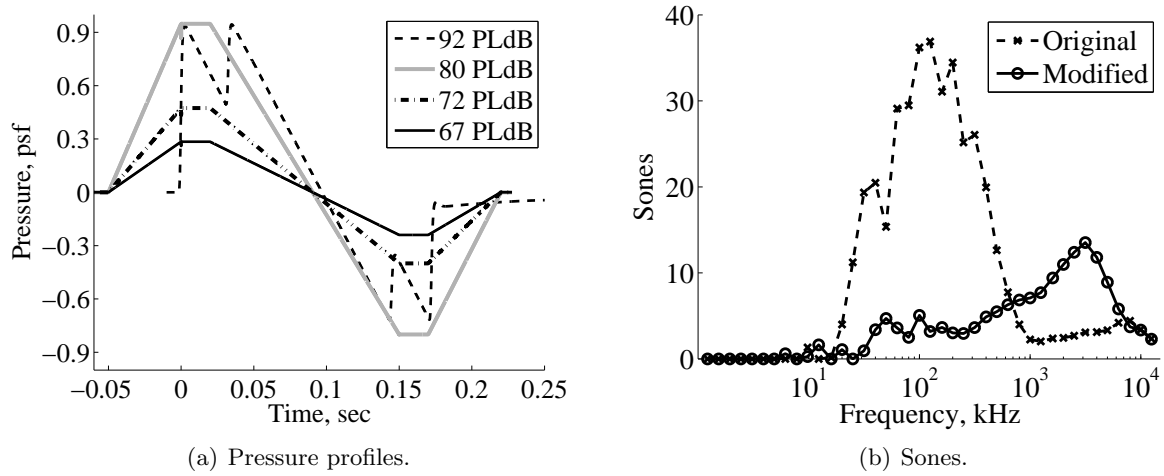
Figure 10.7: Flat-top signature and nose and tail extensions.
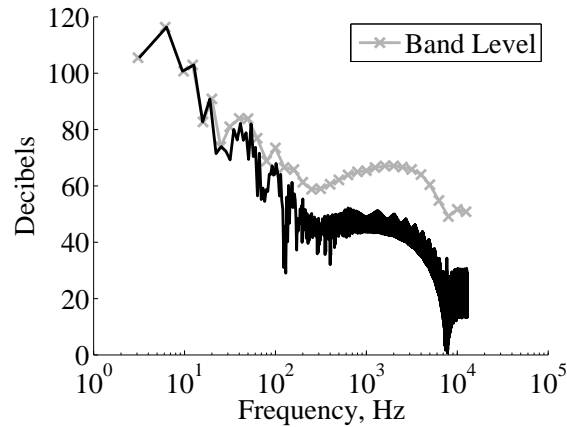
Figure 10.8: Frequency spectrum of flat top signature with nose and tail extensions.

10.3.6 Increasing duration

Finally, the signal duration is increased by a factor of two, as shown in Fig. 10.10. In general, if the duration is doubled, it will double the dB of the signal. However, it will also shift the

(a) Pressure profiles.

(b) Sones.
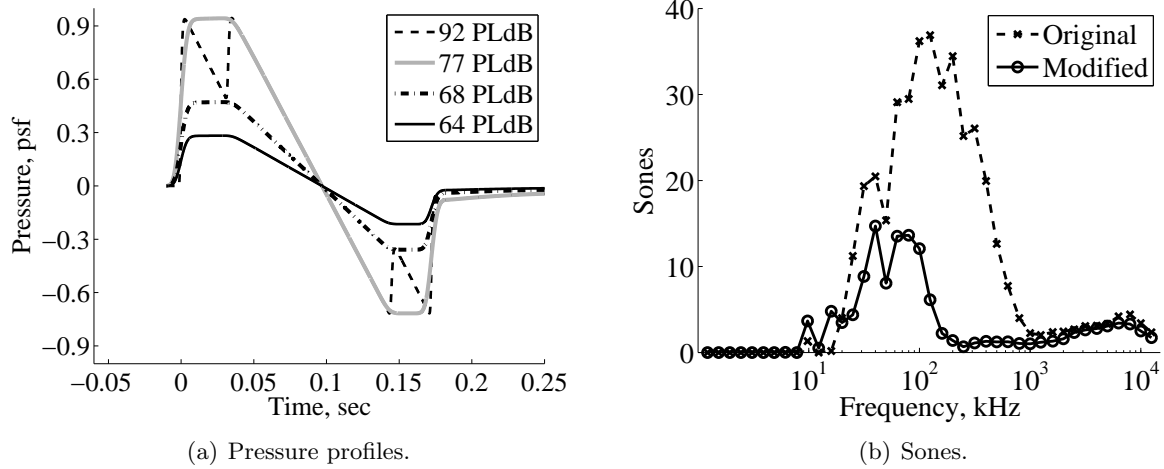
Figure 10.9: Smoothed signature with flat top.

acoustical power to lower frequencies. Since the human is less responsive to lower frequencies, the PLdB will decrease. Furthermore, it is reasonable to assume that if the duration is doubled, then the amplitude will be cut in half (same weight spread over a larger distance). Thus, as shown in Fig. 10.10, increasing duration should be able to reduce the level to 75 PLdB. Although this is still above the 70 PLdB target, it is seen as being practical from the design perspective. The duration can be made longer by increasing the overall length of the aircraft. In addition, the effective length can be increased by dihedral and locating the vertical tail above the aircraft centerline. When the length is increased the peak overpressure should drop because the aircraft's weight is spread over a longer distance. Based on the analysis of all of the techniques, increasing duration offers a reasonable method to lower the PLdB.

As a side note, Fig. 10.10 shows an issue with PLdB calculations. For the case where $c_1 = 0.5$, the PLdB is 75, but when $c_1 = 0.3$, the PLdB increases to 77. This is not logical since the amplitude has been reduced by 40%. As shown in Fig. 10.10(b), this is because the band at 8,000 Hz is dominate due to over sampling the signal. If the sone level for this band is eliminated, then the PLdB is 72 for $c_1 = 0.3$.

(a) Pressure profiles.

(b) Sones.
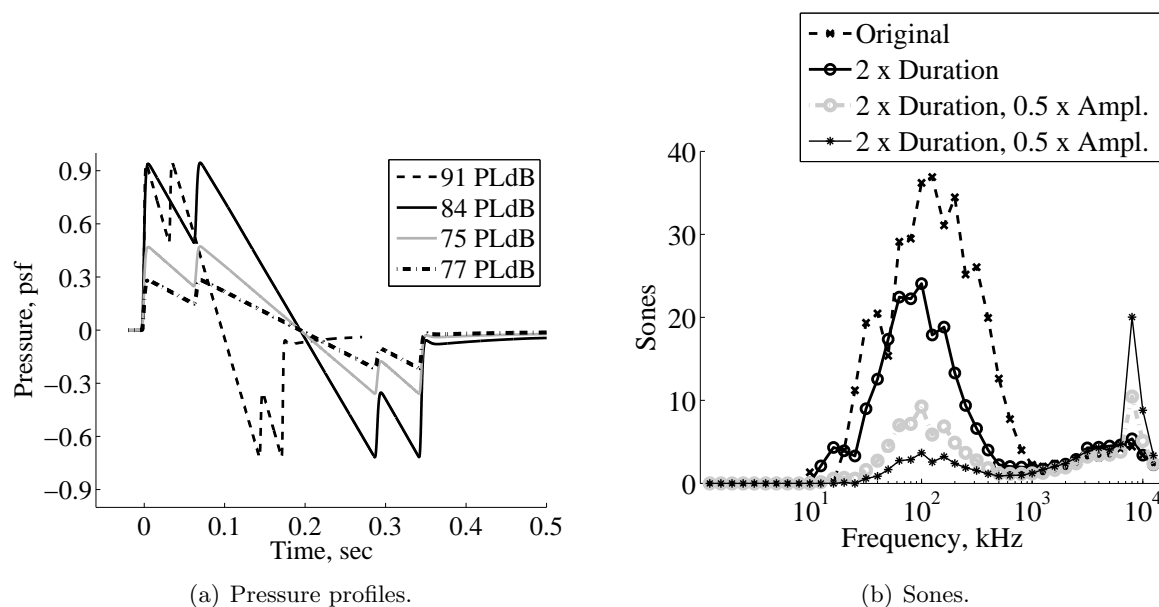
Figure 10.10: Increasing duration.

10.4   Analysis of Quiet Spike [TM]

Analysis of Gulfstream's supersonic business aircraft with a Quiet Spike [TM] nose is presented to determine if its design strategy can be incorporated into the lobe-balance design. Quiet Spike [TM] is a patented [75] method to reduce the annoyance of the sonic boom. An isometric view of the aircraft is shown in Fig. 10.11(a) [82]. The nose has a series of cone-shaped radius increases, followed by straight sections. The overall visual effect is a stair-step increase in fuselage area, which creates a corresponding step increase in the sonic boom pressures, as shown in Fig. 10.11(b). This pressure profile was created using RapidF with no molecular relaxation effects. Figure 10.11(c) shows Gulfstream's prediction of the sonic boom with molecular relaxation, which smooths the steps into one gradual pressure increase. The sone levels are shown in Fig. 10.11(d), revealing that the Quiet Spike [TM] has sone levels nearly constant for all frequencies, resulting in PLdB values of 68. In an attempt to obtain comparable PLdB values with the lobe-balanced aircraft, the pressure profile from Fig. 10.11(c) are put on the lobe balanced aircraft's pressure profile as shown in Fig. 10.12. The results are disappointing: 86 PLdB. Based on this case, it is concluded that the

Quiet Spike ^{TM} nose is not sufficient in lowering the PLdB value to an acceptable level.

(a) Aircraft, reproduced from Ref. [4]).

(b) Profile without relaxation.

(c) Profile with relaxation [80].
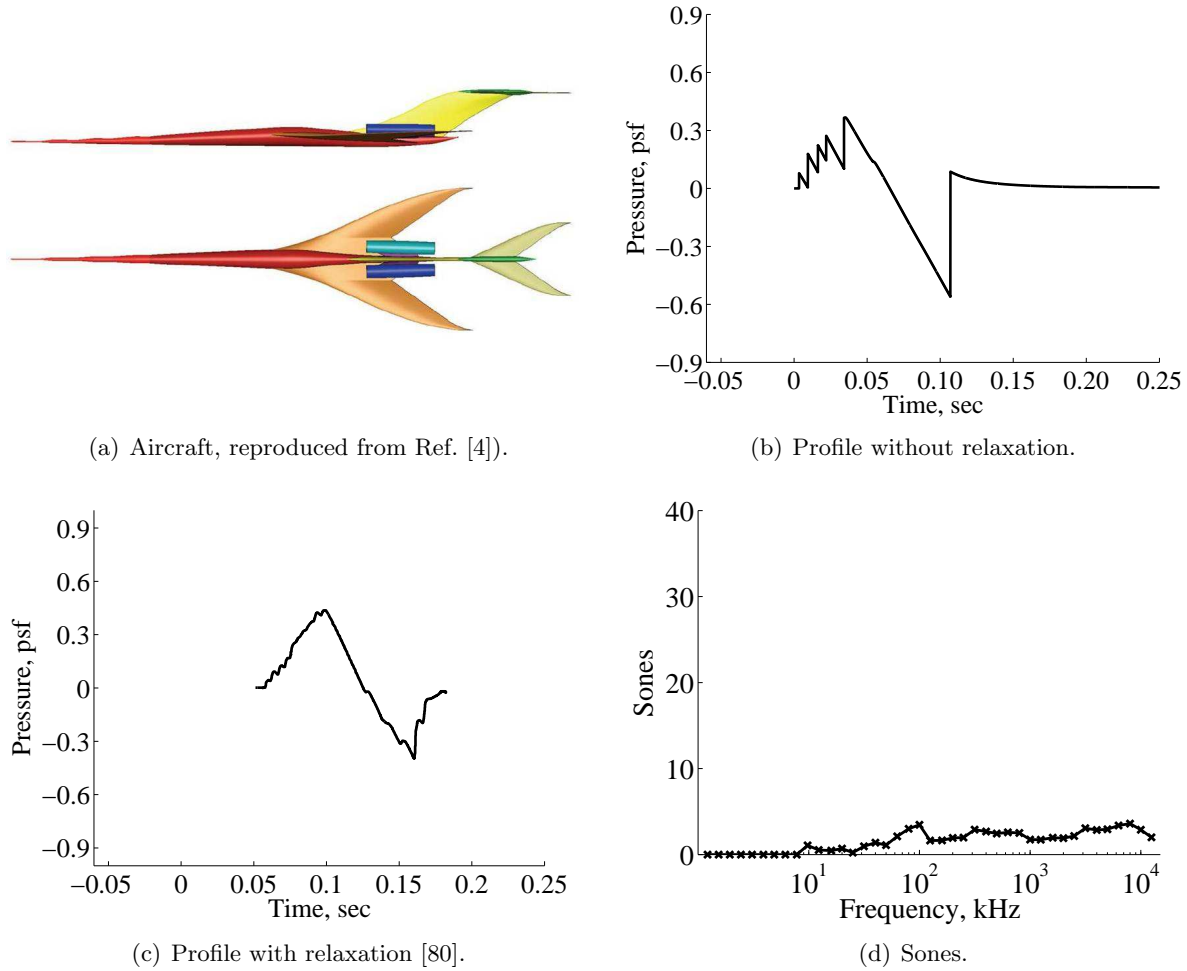
(d) Sones.

Figure 10.11: Gulfstream Quiet Spike.^{TM}

10.5   Chapter Conclusions and Recommendations

- Low boom designers need to start to think in sones and PLdB, not psf overpressures.

- In general, to lower the PLdB, one needs to "push" the acoustical power to the lower frequencies or to the frequencies above 12,500 Hz, as suggested by Howe [79]. For example, if the aircraft had a sonic boom shaped like a sine wave with a one second duration. All the energy would be at 1 Hz. The signal could be up to 160 dB and still not reach the cutoff from Fig. 10.2.

(a) Pressure profile. (b) Profile without relaxation.
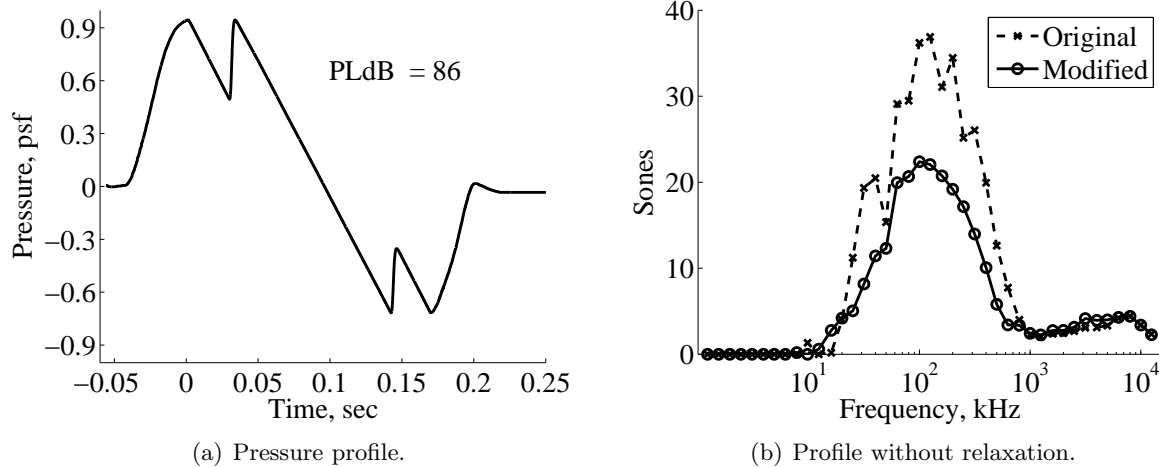
Figure 10.12: Lobe-balanced aircraft with Quiet Spike$^{\text{TM}}$ nose and tail.

- Based on the above analysis, a new lobe-balanced design is recommended. Both the original and modified aircraft are shown in Fig. 10.13. The changes are as follows:

  (1) A single stage Quiet Spike$^{\text{TM}}$ nose is added. Gulfstream's design has a nose that is approximately 70 ft long and must be retracted during non-supersonic mission segments. The extension/retraction mechanism adds weight and the storage sacrifices valuable fuselage volume. Therefore, a fixed single stage spike is used. It is 30 ft long with a maximum radius of 1.65 ft, comparable to a large pitot probe. The desired effect is to create a weak initial shock and increase the sonic boom duration. The fixed spike avoids the complications of the larger spike: increased weight, loss of volume and increased complexity of the retraction system.

  (2) The vertical tail is moved up 15 ft and moved aft 9 ft, increasing the effective length from 150 ft to 177 ft, not including the spike. When combined with the nose extension, this will bring the overall effective length to 207 ft. This is an attempt to increase the duration of the sonic boom like Fig. 10.10, increasing the duration 38%.

  (3) By moving the horizontal tail up, space along the aircraft centerline was made available. The wing's chord is extended from 80 to 95 ft and the sweep increased from

49° to 58°. The planform area is increased from 3,610 to 4,380 ft. These changes will allow the aircraft to operate at lower C_L value and decrease the strength of its lobes, decreasing the maximum overpressure. Although this will increase skin friction drag due to increase surface area, increasing the sweep will change the leading edge from supersonic to subsonic and decrease wave drag. Therefore, performance is not expected to suffer.

(4) The engines are positioned above the wing, but below the vertical tail. The wing should shield the cowl shock from propagating downward. The cowl shock will impact the wing, thus it should not contribute to the ground pressure signature. Although the cowl shock will create an area of high pressure on the top of the wing, decreasing lift, it is positioned so that only the trailing portion of the wing is effected to minimize the performance lost. Likewise the shocks from the engines will impact the majority of the horizontal tail creating a significant amount of interference lift.

(5) Thrust vectoring nozzles are added so that the canard and horizontal tail do not have to be used for pitch changes during supersonic cruise. This will eliminate the chance of a pilot commanded pitch change from upsetting the balanced lobes.

(6) Although not visible in Fig. 10.13(b), the fuselage is not symmetric. The bottom is flatter than the top. Thus the radius change on the bottom will be smaller and the shocks propagating downward will be weaker as proposed by Howe [78].

(a) Original design.

(b) Modified design.
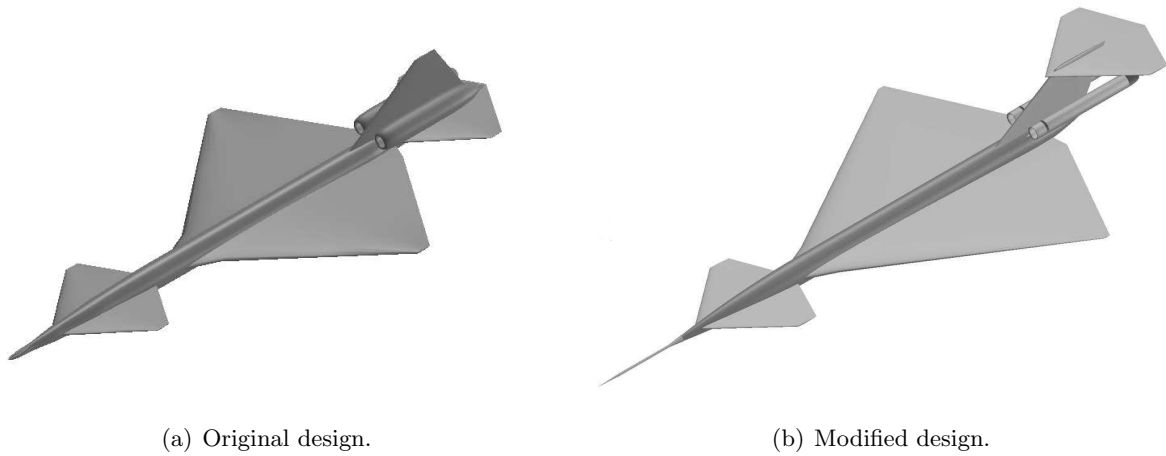
Figure 10.13: Proposed modifications based on PLdB analysis.

Bibliography

[1] Aerion. Specifications. [online], http://www.aerioncorp.com/specifications [retrived 22 Feb 2011].

[2] Aerion, Corp. "Image Downloads". http://www.aerioncorp.com/image-downloads [retrieved 21 Apr 2011].

[3] M. J. Aftosmis, M. J. Berger, and G. Adomavicius. "A Parallel Multilevel Method for Adaptively Refined Cartesian Grids with Embedded Boundaries". AIAA Paper 2000-0808, January 2000.

[4] M. J. Aftosmis, M. Nemec, and S. E. Cliff. "Adjoint-Based Low-Boom Design with Cart3D". AIAA Paper 2011-3500, January 2010.

[5] Anderson, J. D. Jr. Modern Compressible Flow: with Historical Perspectives, chapter 3. McGraw-Hill, New York, 3rd edition, 2003.

[6] Anderson, J. D. Jr. Modern Compressible Flow: with Historical Perspectives, chapter 13. McGraw-Hill, New York, 3rd edition, 2003.

[7] Anderson, J. D. Jr. Modern Compressible Flow: with Historical Perspectives, chapter 8-9. McGraw-Hill, New York, 3rd edition, 2003.

[8] B. Argrow, C. Farhat, K. Maute, and M. Nikbay. Linear-Theory-Based Shape Optimization for Sonic Boom Minimization. In H. Sobieczky, editor, IUTAM Symposium Transsonicum, volume IV, pages 349–354, 2003.

[9] B. Argrow, K. Maute, G. Dickinson, C. Farhat, and M. Nikbay. "F-Function Lobe Balancing for Sonic Boom Minimization". Computational Fluid Dynamics Journal, 17(4):221–234, 2009.

[10] B. Argrow, K. Maute, C. Farhat, and M. Nikbay. "A Shape Optimization Methodology for Reducing the Sonic Boom Initial Pressure Rise. AIAA 2002-145, 2002.

[11] H. H. Arnaiz, J. B. Jr. Peterson, and J. C. Daugherty. "Wind-Tunnel/Flight Correlation Study of Aerodynamic Characteristics of Large Flexible Supersonic Airplane (XB-70-1) Part III". NASA TP 1516, March 1980.

[12] D. C. Aronstein and K. L. Schueler. "Two Supersonic Business Aircraft Conceptual Designs, With and Without Sonic Boom Constraint". Journal of Aircraft, 42:775–786, May 2005.

[13] Aviation Week and Space Technology. "Gas Turbine Engines Specifications". [online], www.aviationweek.com [retrieved 22 Feb. 2011].

[14] R. L. Barger and Jr. F. L. Jordan. "Investigation of a Class of Bodies that Generate Far-Field Sonic-Boom Shock Strength and Impulse Independent of Body Length and Volume". NASA 5148, May 1969.

[15] H. E. Bass and R. Raspet. "Comparison of Sonic Boom Rise Time Prediction Techniques". Journal of the Acoustical Society of America, 91(3):1767–1768, March 1992.

[16] H. E. Bass, R. Raspet, J.P. Chambers, and M. Kelly. "Modification of Sonic Boom Wave Forms During Propagation from the Source to the Ground". The Journal of the Acoustical Society of America, 111:481–486, 2002.

[17] J. J. Bertin. Aerodynamics for Engineers, chapter 8. Prentice Hall, Upper Saddle River, NJ, 4th edition, 2002.

[18] J. J. Bertin. Aerodynamics for Engineers, chapter 4. Prentice Hall, Upper Saddle River, NJ, 4th edition, 2002.

[19] J. J. Bertin. Aerodynamics for Engineers, chapter 8 and 11. Prentice Hall, Upper Saddle River, NJ, 4th edition, 2002.

[20] D. T. Blackstock. Fundamentals of Physical Acoustics. John Wiley & Sons, New York, 2000.

[21] Boeing. The SST: General Description, September 1969.

[22] Boeing. "High-Speed Civil Transport Study". NASA CR-4233, September 1989.

[23] S. A. Brandt, R. J. Stiles, J. J. Bertin, and R. Whitford. Introduction to Aeronautics: A Design Perspective, pages 11–14. AIAA Education Series. AIAA, Inc., Reston, VA, 2nd edition, 2004.

[24] S. A. Brandt, R. J. Stiles, J. J. Bertin, and R. Whitford. Introduction to Aeronautics: A Design Perspective. AIAA Education Series. AIAA, Inc., Reston, VA, 2nd edition, 2004.

[25] T. T. Bui. "CFD Analysis of Nozzle Jet Plume Effects on Sonic Boom Signature". NASA TM-2009-214650, September 2009.

[26] P. G. Buning, D. C. Jespersen, T. H. Pulliam, W. M. Chan, J. P. Slotnick, S. E. Krist, and K. J. Renze. OVERFLOW USER'S MANUAL Version 1.8f. NASA, Hampton, VA, June 1998.

[27] A. Busemann. "Aerodynamischer Auftreib bei Überschallgeswindigkeit", 1935.

[28] A. Busemann. "The Relation Between Minimizing Drag and Noise at Supersonic Speeds". Proceedings in High Speed Aerodynamics, 1955.

[29] H. W. Carlson. "Correlation of Sonic-Boom Theory with Wind-Tunnel and Flight Measurements". NASA-TR-R-213, December 1964.

[30] H. W. Carlson and R. J. Mack. "A Wind-Tunnel Study of the Applicability of the Far-Field Sonic-Boom Theory to the Space Shuttle Orbiter". NASA TP 1186, June 1978.

[31] H. W. Carlson, F. E. McLean, and B. L. Shrout. "A Wind Tunnel Study of Sonic-Boom Characteristics for Basic and Modified Models for a Supersonic Transport Configuration". NASA TM X-1236, May 1966.

[32] H. W. Carlson and D. S. Miller. "Numerical Methods for the Design and Analysis of Wings at Supersonic Speeds". NASA TN D-7713, December 1974.

[33] H. W. Carlson and O. A. Morris. "Wind-Tunnel Investigation of the Sonic-Boom Characteristics of a Large Supersonic Bomber Configuration". NASA TM X-898, January 1963.

[34] J. H. Casper, S. E. Cliff, S. D. Thomas, M. A. Park, M. S. McMullen, J. E. Melton, and D. A. Durston. "Assessment of Near-Field Sonic Boom Simulation Tools". AIAA Paper 2008-6592, August 2008.

[35] T. Cebeci and P. Bradshaw. Momentum Transfer in Boundary Layers. Series in Thermal and Fluids Engineering. Hemisphere Publishing Corporation, 1977.

[36] R. O. Cleveland and D. T. Blackstock. "Waveform Freezing of Sonic Booms Revisited". In D. G. Braize, editor, 1995 NASA High-Speed Research Program Sonic Boom Work Shop, volume 1, pages 20–40, Hampton, VA, September 1996.

[37] R. O. Cleveland, J. P. Chambers, H. E. Bass, R. Raspet, D. T. Blackstock, and M. F. Hamilton. "Comparison of Computer Codes for the Propagation of Sonic Boom Waveforms through Isothermal Atmospheres". Journal of the Acoustical Society of America, 100(5):3017–3027, November 1996.

[38] Committee on Breakthrough Technology for Commercial Supersonic Aircraft. Commercial Supersonic Technology: The Way Ahead, pages 1–6. National Research Council. National Academy Press, Washington D.C., 2001.

[39] Committee on Breakthrough Technology for Commercial Supersonic Aircraft. Commercial Supersonic Technology: The Way Ahead, page 17. National Research Council. National Academy Press, Washington D.C., 2001.

[40] F. Coulouvrat. "The Challenges of Defining an Acceptable Sonic Boom Overland". AIAA Paper 2009-3384, 2009.

[41] R. Cowart and T. Grindle. "An Overview of the Gulfstream / NASA Quiet Spike$^{\text{TM}}$ Flight Test Program". AIAA Paper 2008-123, January 2008.

[42] C. M. Darden. "Sonic Boom Minimization with Nose-Bluntness Relaxation". NASA TN-1348, January 1979.

[43] C. M. Darden. "Charts for Determining Potential Minimum Sonic Boom Overpressures for Supersonic Cruise Aircraft". NASA TP-1820, March 1981.

[44] C. M. Darden. "Limitations of Linear Theory for Sonic Boom Calculations". Journal of Aircraft, 30(3):309–314, May 1993.

[45] DARPA. "Quiet Supersonic Platform Phase II Contractors Selected". DARPA News Release, April 2002.

[46] Desktop Aeronautics, Inc. Quick Start Guide to CART3D (DA v1.2 based on NASA v1.3.6). 2011.

[47] M. Dresher. The Mathematics of Games of Strategy: Theory and Applications. Dover, New York, 1981.

[48] K. R. Elmer and M. C. Joshi. "Variability of Measured Sonic Boom Signatures". NASA CR 191483, II-Data Report, Febuary 1994.

[49] C. Farhat, B. Argrow, M. Nikbay, and K. Maute. "A Shape Optimization Methodology with F-Function Lobe Balancing for Mitigating the Sonic Boom. AIAA Paper 2002-5551, Sept. 2002.

[50] C. Farhat, B. Argrow, M. Nikbay, and K. Maute. "Shape optimization with F-function balancing for reducing the sonic boom initial shock pressure rise". International Journal of Aeroacoustics, 3(4):361–377, 2005.

[51] C. Farhat, B. Argrow, M. Nikbay, and K. Maute. "Shape Optimization Methodology for Reducing the Sonic Boom Initial Pressure Rise". AIAA Journal, 45(5):1007–1018, May 2007.

[52] A. Ferri, H. Wang, and H. Sorensen. "Experimental Verification of Low Sonic Boom Configuration". NASA CR-2070, June 1972.

[53] E. L. Fleeman. Tactical Missile Design. AIAA, Reston, VA, 2001.

[54] W. J. Fredericks, K. R. Antcliff, G. Costa, N. Deshpande, M. D. Moore, E. A. San Miguel, and A. N. Snyder. "Aircraft Conceptual Design Using Vehicle Sketch Pad". AIAA Paper 2010-658, January 2010.

[55] M. P. Friedman. "A Description of a Computer Program for the Study of Atmospheric Effects on Sonic Booms". NASA CR-157, February 1965.

[56] M. P. Friedman, E. J. Kane, and A. Sigalla. "Effects of Atmosphere and Aircraft Motion on the Location and Intensity of a Sonic Boom". AIAA Journal, 1(6):1327–1335, June 1963.

[57] E. L. Friend and W. J. Sefic. "Flight Measurements of Buffet Characteristics of the F-104 Airplane for Selected Wing-Flap Deflections". NASA TN D-6943, August 1972.

[58] T. Furukawa and Y. Makino. "Conceptual Design and Aerodynamic Optimization of Silent Supersonic Aircraft at JAXA". AIAA Paper 2007-4166, June 2007.

[59] B. Garvey. "Supersonic Bizjets Still A Long Way Off". Aviation Week and Space Technology, May 2010.

[60] K. Geiselhart, L. Ozoroski, and J. Shields E. Li W. Fenbert. "Integration of Multifidelity Multidisciplinary Computer Codes for Design and Analysis of Supersonic Aircraft". AIAA Paper 2011-465, 2011.

[61] A. R. George. "Lower Bounds for Sonic Booms in the Midfield". AIAA Journal, 7(8):1542–1545, 1969.

[62] A. R. George and A. R. Seebass. "Sonic Boom Minimization Including Both Front and Rear Shock Waves". <u>AIAA Journal</u>, 10(10):2091–2093, 1969.

[63] J. J. Gottlieb and D. V. Ritzel. "Analytical Study of Sonic Boom From Supersonic Projectiles". <u>Progresses in Aerospace Sciences</u>, 25:131–188, 1988.

[64] A. Haas and I. Kroo. "A Multi-Shock Inverse Design Method for Low-Boom Supersonic Aircraft". <u>AIAA Paper 2010-843</u>, 2010.

[65] Haering, E. A., Jr., J. E. Murray, and D. D. Purifoy. "Airborne Shaped Sonic Boom Demonstration Pressure Measurements with Computational Fluid Dynamics Comparisons". <u>AIAA Paper 2005-9</u>, Jan. 2005.

[66] Hamilton Sundstrand. "Hamilton Sundstrand small engines play powerful role in pioneering UAV programs". http://www.hamiltonsundstrand.com/, Referenced June 12, 2010.

[67] Harris, R. V.,Jr. "An Analysis and Correlation of Aircraft Wave Drag". <u>NASA TM X-947</u>, March 1964.

[68] W. D. Hayes. <u>Linearized Supersonic Flow</u>. PhD thesis, California Institute of Technology, April 1947.

[69] W. D. Hayes. "Brief Review of the Basic Theory". <u>NASA SP-147</u>, June 1967.

[70] W. D. Hayes. "Review of Sonic Boom Theory". <u>AFOSR-UTIAS Symposium on Aerodynamic Noise</u>, 1968.

[71] W. D. Hayes and R. C. Haefeli. "The ARAP Sonic Boom Computer Code". In I. A. Schwartz, editor, <u>NASA SP-180</u>, Second Conference on Sonic Boom Research, pages 151–158, May 1968.

[72] W. D. Hayes, R. C. Haefeli, and H. E. Kulsrud. "Sonic Boom Propagation in a Stratified Atmosphere, with Computer Program". <u>NASA CR-1299</u>, April 1969.

[73] W. D. Hayes and Jr. H. R. Runyan. "Sonic-Boom Propagation through a Stratified Atmosphere". <u>Journal of the Acoustical Society of America</u>, 51(2C):695–701, 1972.

[74] W. D. Hayes and F. B. Weiskopf. "Optimum Configurations for Bangless Sonic Booms". <u>Quarterly of Applied Mathematics</u>, 30:311–328, October 1972.

[75] P. A. Henne, D.C. Howe, R. R. Wolz, and Handcock, J. L., Jr. "Supersonic Aircraft with Spike for Controlling and Reducing Sonic Boom". <u>US Patent 2010 0012777 A1</u>, January 2011.

[76] J. W. Hicks and J. Kania. "Challenges in Modeling the X-29A Flight Test Performance". <u>NASA TM 88282</u>, January 1987.

[77] D. A. Hilton, V. Huckel, R. Steiner, and D. J. Maglieri. "Sonic-Boom Exposures During FAA Community-Response Studies over a 6-Month Period in the Oklahoma City Area". <u>NASA TN D-2539</u>, December 1964.

[78] D.C. Howe. "Sonic Boom Minimization through the use of Non-axisymmetric Configuration Shaping". <u>AIAA Paper 2003-0929</u>, 2003.

[79] D.C. Howe. "Improved Sonic Boom Minimization with Extendable Nose Spike". AIAA Paper 2005-1014, 2005.

[80] D.C. Howe. "Hybrid CART3D/OVERFLOW Near-Field Analysis of a Low Boom Configuration with Wind Tunnel Comparisons". AIAA Paper 2011-3336, June 2011.

[81] D.C. Howe and P. A. Henne. "Improved Sonic Boom Scaling Algorithm". AIAA Paper 2006-0027, January 2006.

[82] D.C. Howe, F. Simmons, and D. Freund. "Development of the Gulfstream Quiet Spike^{TM} for Sonic Boom Minimization". AIAA Paper 2008-124, Jan. 2008.

[83] D.C. Howe, K. A. Waithe, and E. A. Jr. Haering. "Quiet Spike ^{TM}Near Field Flight Test Pressure Measurements with Computational Fluid Dynamics Comparisons". AIAA Paper 2008-128, January 2008.

[84] H. H. Hubbard, editor. Aeroacoustics of Flight Vehicles: Theory and Practice, volume 2: Noise Control. Acoustical Society of America, 1995.

[85] H. H. Hubbard, editor. Aeroacoustics of Flight Vehicles: Theory and Practice, volume 1: Noise Sources. Acoustical Society of America, 1995.

[86] H. H. Hubbard and D. J. Maglieri. "Sonic Boom Signature Data from Cruciform Microphone Array Experiments during the 1966-1967 EAFB National Sonic Boom Evaluation Program". NASA CR-182027, May 1990.

[87] H. H. Hubbard, D. J. Maglieri, V. Huckel, and D. A. Hilton. "Ground Measurements of Sonic-Boom Pressures for the Altitude Range of 10,000 to 75,000 Feet". NASA TR R-198, March 1964.

[88] L. W. Hunton, R. M. Hicks, and J. P. Mendoza. "Some Effects of Wing Planform on Sonic Boom". NASA TN D-7160, January 1973.

[89] D. R. Johnson and D. W. Robinson. "Procedure for Calculating the Loudness of Sonic Bangs". Acustica, 21(6):307–318, 1969.

[90] L. B. Jones. "Lower Bounds for Sonic Bangs". Journal Royal Aeronautical Society, 65:1–4, 1961.

[91] L. B. Jones. "Lower Bounds for Sonic Bang in the Far Field". Aeronautical Quarterly, 18:1–21, Feb. 1967.

[92] L. B. Jones. "Lower Bounds for the Pressure Jump of the Bow Shock of a Supersonic Transport". Aeronautical Quarterly, 21:1–17, Feb. 1967.

[93] R. T. Jones. "Theory of Wing-Body Drag at Supersonic Speeds". NACA Report 1284, Feb. 1976.

[94] T. P. Jung, R. P. Starkey, and B. Argrow. "Design Methods to Create Frozen Sonic Booms via Lobe Balancing using Aircraft Components". AIAA 2011-2857, June 2011.

[95] T. P. Jung, R. P. Starkey, and B. Argrow. "Feasibility Study of using a Small-Scale UAV for Sonic Boom Minimization Research". AIAA 2011-1280, January 2011.

[96] T. P. Jung, R. P. Starkey, and B. Argrow. "Lobe Balancing Design Method to Create Frozen Sonic Booms using Aircraft Components". Journal of Aircraft, In review, 2011.

[97] T. P. Jung, R. P. Starkey, and B. Argrow. "Comparison of Sonic Booms from Modified Linear Theory to Flight Test Data". AIAA 2012-0018, January 2012.

[98] T. P. Jung, R. P. Starkey, and B. Argrow. "Methodology for Conducting Scaled Sonic Boom Flight Tests using Unmanned Aircraft Systems". Journal of Aircraft, IN REVIEW 2012.

[99] O. A. Kandel, I. A. Ozcer, X. Zheng, and P. J. Bobbitt. "Comparison of Full-Potential Propagation-Code Computations with F-5E "Shaped Sonic Boom Experiment" Program". AIAA Paper 2005-0013, 2005.

[100] J. Kang. Nonlinear Acoustic Propagation of Shock Waves through the Atmosphere with Molecular Relaxation. PhD thesis, Department of Mechanical Engineering, Pennsylvania State University, May 1991.

[101] R. K. Koegler. "Sonic Boom Analysis". AIAA Paper 1966-941, December 1966.

[102] R. K. Koegler. "Possible Means of Reducing Sonic Booms and Effects Through Shock Decay Phenomena and Some Comments on Aural Response. NASA SP-147, pages 95–102, 1967.

[103] S. Komadina and A. Drake. "Development of a Quiet Supersonic Aircraft with Technology Applications to Military and Civil Aircraft". AIAA Paper 2002-0519, Jan. 2002.

[104] J. D. Leatherwood and B. M. Sullivan. "Laboratory study of Effects of Sonic Boom Shaping on Subjective Loudness and Acceptability". NASA TP 3269, October 1992.

[105] J. D. Leatherwood and B. M. Sullivan. "A Laboratory Study of Subjective Annoyance Response to Sonic Booms and Aircraft Flyovers". NASA TM-109113, May 1994.

[106] J. D. Leatherwood, B. M. Sullivan, K. P. Shepard, D. A. McCurdy, and S. A. Brown. "Summary of recent NASA studies of human response to sonic booms". Journal of the Acoustical Society of America, 111(1):586–598, January 2002.

[107] W. Li, E. Shields, and K. Geiselhart. "Mixed-Fidelity Approach for Design of Low-Boom Supersonic Aircraft". Journal of Aircraft, 48(4):1131–1135, 2011.

[108] W. Li, E. Shields, and D. Le. "Interactive Inverse Design Optimization of Fuselage Shape for Low-Boom Supersonic Concepts". Journal of Aircraft, 45(4):1381–1397, 2008.

[109] H. W. Liepmann and A. Roshko. Elements of Gasdynamics, pages 178–247. Galcit Aeronautical Series. John Wiley & Sons, New York, 1957.

[110] M. J. Lighthill. "Supersonic Flow Past Slender Bodies of Revolution the Slope of Whose Meridian Section is Discontinuous". The Quarterly Journal of Mechanics and Applied Math, 1(1):90–102, 1948.

[111] L.K. Jr. Loftin. Quest for performance: The evolution of modern aircraft. Number NASA SP-468. NASA, 1985.

[112] H. Lomax, M. A. Heaslet, and F. B. Fuller. "Formulas for Source, Doublet and Vortex Distributions in Supersonic Wing Theory". NACA Report 2252, December 1950.

[113] J. L. Lung. A computer program for the design of supersonic aircraft to minimize their sonic boom. Master's thesis, Cornell University, January 1975.

[114] R. J. Mack. "Numerical Method for Evaluation and Utilization of Supersonic Nacelle-Wing Interference". NASA TN D-5057, March 1969.

[115] R. J. Mack. "Method for Estimating the Sonic-Boom Characteristics of Lifting Canard-Wing Aircraft Concepts". NASA TM-2005-213930, December 2005.

[116] D. J. Maglieri. "Compilation and Review of Supersonic Business Jet Studies from 1963 through 1995". NASA/CR–2011-217144, May 2011.

[117] D. J. Maglieri, H. R. Henderson, and A. F. Tinetti. "Measured Sonic Boom Signatures Above and Below the XB-70 Airplane Flying at Mach 1.5 and 37,000 Feet". NASA CR-2011-217077, April 2011.

[118] D. J. Maglieri, V. Huckel, and H. R. Henderson. "Variability in Sonic-Boom Signatures Measured along an 8000-foot Linear Array". NASA TN D-5040, Febuary 1969.

[119] D. J. Maglieri, V. Huckel, and H. R. Henderson. "Sonic-Boom Measurements for SR-71 Aircraft Operating at Mach Numbers to 3.0 and Altitudes to 24,384 Meters". NASA TN D-6823, September 1972.

[120] D. J. Maglieri and V. E. Sothcott. "Summary of Sonic Boom Rise Times Observed During FAA Community Response Studies Over a 6-Month Period in the Oklahoma City Area". NASA CR-4277, April 1990.

[121] D. J. Maglieri, V. E. Sothcott, and T. N. Jr. Keefer. "A Summary of XB-70 Sonic Boom Signature Data". NASA CR-189630, April 1992.

[122] D. J. Maglieri, V. E. Sothcott, and T. N. Jr. Keefer. "Feasibility Study on Conducting Overflight Measurements of Shaped Sonic Boom Signatures Using the Firebee BQM-34E RPV". NASA CR-189715, February 1993.

[123] Y. Makino. "Low Sonic-Boom Design of a Silent Supersonic Technology Demonstrator – Development of CAPAS and its Application". In JAXA Special Publication, Proceedings of International Workshops on Numerical Simulation Technology for Design of Next Generation Supersonic Civil Transport (SST-CFD Workshop), 2007.

[124] Y. Makino and I. Kroo. "Robust objective functions for sonic-boom minimization". Journal of Aircraft, 43(5):1301–1306, 2006.

[125] P. Marks. "New Supersonic Business Jet Takes Shape". The New Scientist, July 2010.

[126] K. Maute, C. Farhat, B. Argrow, and M. Nikbay. "Sonic Boom Mitigation via Shape Optimization: An Adjoint Method and Application to a Supersonic Fighter Aircraft". European Journal of Computational Mechanics, 17:217–243, 2008.

[127] F. E. McLean. "Some Nonasymptotic Effects on the Sonic Boom of Large Airplanes". NASA TN D-2877, June 1965.

[128] F. E. McLean. "Supersonic Cruise Technology". NASA SP-472, February 1985.

[129] W. D. Middleton and H. W. Carlson. "A Numerical Method for Calculating Near-Field Sonic-Boom Pressure Signatures". NASA TN D-3082, November 1965.

[130] D. S. Miller and H. W. Carlson. "A Study of the Applications of Heat or Force Fields to the Sonic-Boom-Minimization Problem". NASA TN D-5582, December 1969.

[131] J. M. Morgenstern, A. Arslan, V. Lyman, and J. Vadyak. "F-5 Shaped Sonic Boom Demonstrator: Persistence of Boom Shaping Reduction through Turbulence". AIAA Paper 2005-12, Jan. 2005.

[132] NASA. "NASA's High-Speed Research Program", Referenced June 12, 2010.

[133] M. Nemec, M. J. Aftosmis, and M. Wintzer. "Adjoint-Based Adaptive Mesh Refinement for Complex Geometries". AIAA Paper 2008-0725, January 2008.

[134] M. Nikbay. Coupled Sensitivity Analysis by Discrete Analytical Direct and Adjoint Methods with Applications to Aeroelastic Optimization and Sonic Boom Minimization. PhD thesis, University of Colorado, Boulder, October 2002.

[135] NOAA, NASA, and U.S. Air Force. "US Standard Atmosphere 1976". NASA-TM-X-74335, October 1976.

[136] I. Ordaz and S. K. Rallabhandi. "Boom Minimization Framework for Supersonic Aircraft Using CFD Analysis". AIAA Paper 2010-1506, 2010.

[137] A. Parsch. "Directory of U.S. Military Rockets and Missiles: AQM/BQM/MQM/BGM-34". [online], http://www.designation-systems.net/dusrm/m-34.html [retrieved 22 Feb 2011], 2003.

[138] J. W. Pawlowski, D. H. Graham, C. H. Boccadoro, P. G. Coen, and D. J. Maglieri. "Origins and Overview of the Shaped Sonic Boom Demonstration Program". AIAA 2005-5, January 2005.

[139] K. S. Pearsons and R. L. Bennet. "Handbook of Noise Ratings". NASA CR-2376, pages 60–74, April 1974.

[140] J. S. Petty. "Lower Bounds for Sonic Boom Considering the Negative Overpressure Region". Journal of Aircraft, 7(4):375–377, 1970.

[141] A. D. Pierce. Acoustics: An Introduction to Its Physical Principles and Applications. Acoustical Society of America, New York, 1989.

[142] A. D. Pierce. "Rise profiles of initial shocks in sonic boom waveforms". The Journal of the Acoustical Society of America, 104(3):1829–1829, 1998.

[143] K. J. Plotkin. "On the Aging of Sonic Booms". NASA N94-28194, May 1993.

[144] K. J. Plotkin. "State of the art of sonic boom modeling". The Journal of the Acoustical Society of America, 111(1):530–536, 2002.

[145] K. J. Plotkin. "Ground Data Collection of Shaped Sonic Boom Experiment Aircraft Pressure Signatures". AIAA Paper 2005-10, Jan. 2005.

[146] K. J. Plotkin and A. R. George. "Sonic Boom Waveforms and Amplitudes in a Real Atmosphere". AIAA Journal, 7(10):1978–1981, 1969.

[147] K. J. Plotkin and F. Grandi. "Computer Models for Sonic Boom Analysis: CABoom, BooMap, CORBoom". Wyle Report WR 02-11, June 2002.

[148] K. J. Plotkin and D. J. Maglieri. "Sonic Boom Research: History and Future". AIAA Paper 2003-3575, June 2003.

[149] K. J. Plotkin, R. Martin, D. J. Maglieri, E. A. Jr. Haering, and J. E. Murray. "Pushover Focus Booms from the Shaped Sonic Boom Demonstrator". AIAA Paper 2005-0011, January 2005.

[150] J. O. Powers and D. J. Maglieri. "Survey of Sonic Boom Experiments". Aviation and Space Conference, American Society of Mechanical Engineers, June 1968.

[151] S. K. Rallabhandi. Sonic Boom Minimization through Vehicle Shape Optimization and Probabilistic Acoustic Propagation. PhD thesis, Georgia Institute of Technology, April 2005.

[152] S. K. Rallabhandi. "Sonic Boom Adjoint Methodology and its Applications". AIAA Paper 2011-3497, 2011.

[153] S. K. Rallabhandi, W. Li, and K. Geiselhart. "Boom-Constrained Drag Minimization for Design of Supersonic Concepts". AIAA Paper 2010-844, 2010.

[154] D. Raymer. Aircraft Design, A Conceptual Approach. AIAA Education Series. AIAA, Inc., Blacksburg, VA, 4th edition, 2006.

[155] D. Raymer. Aircraft Design, A Conceptual Approach, chapter 5. AIAA Education Series. AIAA, Inc., Blacksburg, VA, 4th edition, 2006.

[156] I. L. Rhyming. "The Supersonic Boom of a Projectile Related to Drag and Volume". Journal of Aerospace Sciences, 28:113–118, 1961.

[157] D. V. Ritzel and J. J. Gottlieb. "The Overpressure Signature from a Supersonic Projectile". Technical Report UTIAS No. 279, Canadian Defense Research Establishment, 1987.

[158] I. A. Schwartz, editor. "Airplane Configurations for Low Sonic Boom", NASA SP-255, Third Conference on Sonic Boom Research, October 1970.

[159] A. R. Seebass. "Minimum Sonic Boom Shock Strengths and Overpressures". Nature, 221:651–653, Feb. 1969.

[160] A. R. Seebass. "Sonic Boom Theory". Journal of Aircraft, 6(3):177–184, 1969.

[161] A. R. Seebass and B. Argrow. "Sonic Boon Minimization Revisited". AIAA Paper 1998-2956, 1998.

[162] A. R. Seebass and A. R. George. "Design and Operation of Aircraft to Minimize Their Sonic Boom". Journal of Aircraft, 11(9):509–517, 1974.

[163] A. R. Seebass and George A. R. "Sonic-Boom Minimization". Journal of the Acoustical Society of America, 51(2, Part 3):686–694, 1972.

[164] K. P. Shepherd and B. M. Sullivan. "A Loudness Calculation Procedure Applied to Shaped Sonic Booms". NASA TP-3134, November 1991.

[165] K. P. Shepherd, B. M. Sullivan, J. D. Leatherwood, and D. A. McCurdy. "Sonic Boom Acceptability Studies". NASA N94-33500, April 1992.

[166] F. III Simmons and D. Freund. "Morphing Concept for Quiet Supersonic Jet Boom Mitigation". AIAA Paper 2005-1015, 2005.

[167] S. S. Stevens. "Perceived level of Noise by Mark VII and Decibels". Journal of the Acoustical Society of America, 51(2):575–601, 1972.

[168] B. Sweetman. "Gulfstream Progresses on Supersonic As Work Advances on Hushing Boom". Aviation Week and Space Technology [online], May 2010.

[169] T. T. Takahashiand, R. j. Spall, D. C. Turner, and M. Birney. "A Multi-Disciplinary Survey of Advanced Subsonic Tactical Cruise Missile Configurations". AIAA Paper 2005-0709, January 2005.

[170] H. Tang. "On the sonic point glitch". Journal of Computational Physics, 202(2):507–532, 2005.

[171] C. L. Thomas. "Extrapolation of Sonic Boom Pressure Signatures by the Waveform Parameter Method". Technical Note TN D-6832, NASA, 1972.

[172] A. F. Tinetti, D. J. Maglieri, and P. J. Bobbitt. "Equivalent Longitudinal Area Distributions of the B-58 and XB-70-1 Airplanes for Use in Wave Drag and Sonic Boom Calculations". NASA CR-2011-217078, March 2011.

[173] U.S. Air Force. "Sonic Booms Produced by United States Air Force and United States Navy Aircraft: Measured Data". AL-TR-191-0099, January 1991.

[174] F. Walkden. "The Shock Pattern of a Wing-Body Combination". Aeronautical Quarterly, 9(2):164–194, May 1958.

[175] S. Walter and R. P. Starkey. "GOJETT: A Supersonic Unmanned Aerial Flight System". AIAA Paper 2012-22, 2012.

[176] H. R. Welge, J. Bonet, T. Magee, D. Tompkins, T. R. Britt, C. Nelson, G. Miller, D. Stenson, J. B. Staubach, N. Bala, R. Duge, O'Brien M., R. Cedoz, A. Barlow, S. Martins, P. Viars, A. Rasheed, M. Kirby, C. Raczynski, K. Roughen, S. Doyle, K. Alston, J. Page, and K. J. Plotkin. "N+3 Advanced Concept Studies for Supersonic Commercial Transport Aircraft Entering Service in the 2030-2035 Period". NASA CR-2011-217084, April 2011.

[177] G. B. Whitham. "The Behavior of Supersonic Flow Past a Body of Revolution, Far from Axis". Proceedings of the Royal Society, Series A, 201:89–109, 1950.

[178] G. B. Whitham. "The Flow Pattern of a Supersonic Projectile". Communications in Pure Applied Math, 5(3):301–348, 1952.

[179] G. B. Whitham. "On the propagation of weak shock waves". Journal of Fluid Mechanics, 1(3):290–318, 1956.

[180] R. Willgoss, V. Rosenfeld, and J. Billingsley. "High precision GPS guidance of mobile robots". In Proceedings of the Australasian Conference in Robotics and Automation, 2003.

[181] J. R. Wilson. "A new Boom in Supersonics". Aerospace America, pages 30–36, February 2011. AIAA.

[182] M. Wintzer, M. Nemec, and M. J. Aftosmis. "Adjoint-Based Adaptive Mesh Refinement for Sonic Boom Prediction". AIAA Paper 2008-6593, August 2008.

[183] R. Wolz. "A Summary of Recent Supersonic Vehicle Studies at Gulfstream Aerospace". AIAA Paper 2003-0558, Jan. 2003.

[184] H. Yamashita and S. Obayashi. "Sonic Boom Variability Due to Homogeneous Atmospheric Turbulence". Journal of Aircraft, 46:1886–1893, Nov. 2009.

[185] M. Yonezawa and S. Obayashi. "Aerodynamic Performance of the Three-Dimensional Lifting Supersonic Biplane". Journal of Aircraft, 47(3):983–981, 2010.

[186] K. Yoshida. "Supersonic Drag Reduction Technology in the Scaled Supersonic Experimental Airplane Project by JAXA". Progress in Aerospace Sciences, 45:124–146, May 2009.

Appendix A

RAPIDF INPUT FILE

```
clear; clc;  close all;

%% Options
% Scaling
options.scaling_ratio = 1.0;  % Scaling ratio (1.0 = full scale)
options.dx    = 0.5;    % Spacing between longitudinal pts (ft)
                                  % Recommend to get 200 pts on body
 options.F_scale = 300; % Ratio used to scale F-function in Fig1

 % File output
 options.write_to_file = 'no';
options.case_id        = 'Lober_Mar12_Buldge'; % name used in files

% Toggles
options.viscous_toggle   = 'yes';   % Adds boundary layer to total area
options.lift_model       = 'homo';  % Choices are: panel, linear or homog
options.wave_drag_toggle = 'no';    % If 'off': only slices for sonic boom
                                        %    If 'on' slicing aircraft
                                        %    at 3 different agles,
                                        %    improves wave drag,
                                        %    but slows down program
options.slicer_toggle    = 'yes';   % If on: Slices aircraft at Mach angle
                                        % Should be on
options.rise_times       = 'yes';   % Adds rise time estimates to shocks
options.Ffunct_choice    = 'Light'; % Choices: 'Light'or 'Whit'
options.interference_lift= 'no';    % If 'on' estimates interference lift
options.refelction_calcs = 'no';    % If 'on' cacls the reflection
                                    %    off of the ground


%% Flight Conditions
aircraft.mach_cruise     = 1.7;
aircraft.altitude_cruise = 51e3;           % (ft)
aircraft.range_nm        = 4500;           % Desired range (nm)
```

```
aircraft.AOA            = 0.0*pi/180;   % (radians)
canard.incedenceAngle = (1.7)*pi/180; % Angle canard is inclined (radians)
wing.incedenceAngle   = (0.81)*pi/180;% Angle wing is inclined   (radians)
canard2.incedenceAngle= (1.55)*pi/180;% Angle H-tail is inclided (radians)

%% Aircraft description
    % Fuselage
fuselage.nose_length    = 50.0;     % Length of nose (ft)
fuselage.nose_power     = 1.0;      % Exponenet used if 'power' nose
fuselage.nose_type       = 'ogive'; % Choices: 'power', 'ogive' or 'cone'

fuselage.length_straight= 70.0;   % Dist after nose to start of boatTail (ft)
fuselage.diameter       = 7.0;   % (ft)
                    % NOTE: RapidF cals this if fus_file_flag ='yes'
fuselage.file_toggle    = 'no';
fuselage.file_name      = 'SGD_fus.txt';
          % 2 column file with dist (ft) and radius (ft)

fuselage.boatTail_length = 40.0;  % (ft)
fuselage.boatTail_power  =  0.75; % Exponenet used if 'power' tail
fuselage.boatTail_type   = 'ogive'; % Choices: 'power', 'ogive' or 'cone'

% Budlges are based on the erf function
fuselage.bulge_location         = 75;
            %  Dist from nose to inflection pt of bulge  (ft)
fuselage.bulge_radius_increase    = 0;
            % increase/decrease in radius (ft),  set to zero for no buldge
fuselage.bulge_distance         = 10;
            % Distance over which change occurs (ft)
fuselage.bulge2_location        = 130;
fuselage.bulge2_radius_increase = 0.0;
fuselage.bulge2_distance        = 7.0;

 % Engine:
engine.number = 2;              % Set to zero for no engines
engine.flowthru_ratio= 0.70;   % Fraction of flow through engine
engine.location = 127.0 ;      % Location of the start of the engine (ft)
engine.Y =7;                   % Distance from centerline toward wingtip(ft)
engine.Z =2;                   % Verticle dist of engine (ft)
engine.radius = 2.0;           % Engine radius (ft)
engine.length = 28;  % (ft)    % Engine length (ft)
weight.engine = 4000;          % lbs per engine,  Aprox:= 1/5 of thrust
engine.thrust_SL = 28000;      % Installed thrust (lbs/engine)
engine.TSFC = 1.0;             % TSFC (1/hr), Approx = TSFC/Mach =0.6 (Book)
engine.type = 'external';      % 'internal' means engine is in fuslage.
                               % In this case only  plume is calcualted
 engine.nozzPressRatio= 4.7;   % Choices: 3.9 = over expanded
```

```
%                       4.7 = perfectly expanded
%                       9.7 = under expanded
%                       25.2 = very under expanded


% Engine        Radius       Length       Weight        Thrust (SL w/ Burner)
% TJ-150        8.5/24         2          25*1.3            300
%   J-85        1.5/2        50/12         421           2840
% F-110         2.0         230/12        4000              28000 (source Wiki)


% Wing
 wing.exists    = 'yes';
wing.location          = 49;       % Centerline dist from nose (ft)
wing.location_sweep2 = 65;         % From nose to LE sweep change (ft)
wing.sweep_LE_1 = 65. *pi/180;     % Leading edge sweep at root (radians)
wing.sweep_LE_2 = 49. *pi/180;     % Leading edge seep at tip (radians)
wing.sweep_TE   = -20*pi/180;      % Traling edge seep at root (radians)
wing.sweep_TE_2 = -20*pi/180;      % Traling edge seep at tip (radians)
wing.location_sweep_TE_2 = 126;    % From nose to change TE edge sweep (ft)
wing.loc_vert   = 0.0;             % Location above centerline (ft)
wing.chord_root = 80;              % (ft)
wing.span       = 90;              % (ft)

wing.alpha_CLzero =0.0;            % (radians)
wing.airfoil_c_L_alpha = 0.11*180/pi; % Lift curv slope (1/radian)
wing.twist    = 0;                 % (radians)
wing.dihedral = 0*pi/180;          % (radians)
wing.file     = 'airfoil_0003_63.txt';
        % Columns: 1 = x/chord, 2 = thickness/chord, 3 = camber, 4 = slope
        % Symmetric aifoil only requires first 2 columns
wing.C_L_max =1.5;                 % Max C_L used in Takeoff calcs

% Canard (see wing for explination of terms)
    canard.exists     = 'yes';
    canard.location   = 14;
    canard.location_sweep2 = 20;
    canard.sweep_LE_1 = 50.0 *pi/180;
    canard.sweep_LE_2 = 50.0 *pi/180;
    canard.sweep_TE = -30.0*pi/180;
    canard.sweep_TE_2 = -20*pi/180;
    canard.location_sweep_TE_2 = canard.location+35-3;
    canard.loc_vert = 0.0;

    canard.chord_root = 35.0;
    canard.span       = 35.0;
    canard.alpha_CLzero =0.0;
    canard.airfoil_c_L_alpha = 0.11*180/pi;
    canard.twist    = 0.0;
```

```
    canard.dihedral = 0.0;
    canard.file     = 'airfoil_0003_63.txt';



%  Horizontal tail  (see wing for explination of terms)
    canard2.exists ='yes';
    canard2.location = 126;
    canard2.location_sweep2= canard2.location+5;
    canard2.sweep_LE_1 = 50.0 *pi/180;
    canard2.sweep_LE_2 = 50.0 *pi/180;
    canard2.sweep_TE = -30.0*pi/180;
    canard2.sweep_TE_2 = -20*pi/180;
    canard2.location_sweep_TE_2 = canard2.location+35-3;
    canard2.loc_vert = 0.0;

    canard2.chord_root = 37.0;
    canard2.span = 37.0;
    canard2.alpha_CLzero =0.0;
    canard2.airfoil_c_L_alpha = 0.11*180/pi;

    canard2.twist =0;
    canard2.dihedral =0;
    canard2.file = 'airfoil_0003_63.txt';



% Vertical tail (see wing for discription of terms)
      vTail.exists ='yes';
      vTail.location = 110.0;
      vTail.location_sweep2= vTail.location+10;
      vTail.sweep_LE_1 = 58.0 *pi/180;
      vTail.sweep_LE_2 = 58.0 *pi/180;
      vTail.sweep_TE = -20*pi/180;
      vTail.sweep_TE_2 = -20*pi/180;
      vTail.location_sweep_TE_2=vTail.location+vTail.chord_root*.99;

      vTail.chord_root = 46.0;
      vTail.span = 19;            % Dist from centerline to tip (ft)
      vTail.airfoilLiftCurveSlope = 0.11*180/pi; %
      vTail.file = 'airfoil_0003_63.txt';
      vTail.number = 2 ;
      vTail.horz_dist =20.0; % Dist toward wingtip if number >1 (ft)
      vTail.type= 'dorsal'; % 'dorsal' or 'ventral'
      vTail.dihedral = 90*pi/180;

% Ventral fin(s) (see wing for discription of terms)
      ventral.exists ='no';
      ventral.location = 100.0;
```

```
        ventral.location_sweep2= ventral.location+10;
        ventral.sweep_LE_1 = 58.0 *pi/180;
        ventral.sweep_LE_2 = 58.0 *pi/180;
        ventral.sweep_TE = -20*pi/180;
        ventral.sweep_TE_2 = -20*pi/180;
        ventral.location_sweep_TE_2=ventral.location+ventral.chord_root*.99;
        ventral.chord_root = 46.0;
        ventral.span = 19;     % Dist from centerline to tip (ft)
        ventral.airfoilLiftCurveSlope = 0.11; % per degree
        ventral.file = 'airfoil_0003_63.txt';
        ventral.number = 1 ;
        ventral.horiz_dist =0.0; % Dist toward wingtip if number >1 (ft)
        ventral.type= 'ventral'; % 'dorsal' or 'ventral'
        ventral.dihedral = 90*pi/180;


% Weight
    % Estimates factors from Raymer Table 15.2
    weight.wt_2_wing_area=  9.0;   % lbs per S_exposed
    weight.wt_2_canard_area= 4.0 ; % lbs per S_exposed
    weight.wt_2_vTail_area= 5.3;   % lbs per S_exposed
    weight.wt_2_fusWetArea  = 4.8; % lbs per wetted area
    weight.wtPara_2_wTO=  0.057;   % lbs of landing gear per takeoff weight
    weight.wtMisc_2_wTO = 0.17;    % lbs of misc. stuff per takeoff weight
    weight.ballast_loc = 50;       % Location of ballast (ft)
    weight.ballast = 20e3;         % Ballast (lbs)
    weight.cruise = 120000;        % Crusie weight estimate (lbs)
    weight.fuel = 20000;           % Fuel weight (lbs)
                                   % Book says weight fraction is 0.5

    % Raymer Table 15.2
    %               Fighter         Transport    Gen. Av.   Mult by
    %   Wing        9.0             10.0         2.5        S_exposed
    %   Canard      4.0             5.5          2.0        "
    %   V-tail      5.3             5.5          2.0        "
    %   Fuselage    4.8             5.0          1.4        S_wet
    %   Land gear   0.033(0.057 NAVY) 0.043      0.057      TOGW
    %   Engine      1.3             1.3          1.4        Eng weight
    %   Misc        0.17            0.17         0.10       TOGW


% Propagation inputs
        acoustics.reflection_factor = 1.9;
                % Ground Refelction coefficient (recommend = 1.9)
                % No reflection, then 1.0
                % Normal range 1.8 to 2.0
```

```
        acoustics.altitude_ground          =0; % Ground elevation (ft MSL)
        acoustics.number_of_grid_pts =10e3;
              % Number of grid pts used to finds shocks (recommend 10e3)
        acoustics.first_step      = 1000;
              % Distance below aircraft to start geoemtric acoustics (ft)
              %    Recommend 10 body lengths or 1,000 ft
        acoustics.step_size       = 25;
              % Step size through the atmosphere (ft),
              % used to calc Acoustic Area and Age, recommend 25
        acoustics.winds = [ 0 ,  0,  0;
              10e3,  0,  0;
              50e3,  0,  0;
              100e3  0,  0;];
              % matrix with each row:
              % alt(ft), direction blowing from (deg),mangitude (ft/sec)
              %        or filename
        acoustics.phi_ray = 0*pi/180 ; % Angle from verticle (radians)
        acoustics.heading_deg =0;       % 0 = North, 90 = East
        acoustics.file_name = 'no'; % 'no; or file name to speed up calcs
            % file format x, y,z, time, area and age
        atm_type ='std';  % Choices: 'homo', 'std', 'iso,' or  'tabulated'
        height_scale =51e3;   % Scale height for iso and homo atm (ft)


% Output requests
    fig.fig1 = 'yes'; %  Planform view with (F-funct vs. y) overlayed
    fig.fig2 = 'yes'; %  Areas vs x-distance
    fig.fig3 = 'no';  %  1st & Second Derivatives and F-funct vs y
    fig.fig4 = 'no';  %  Area Profile (non dimensional)
    fig.fig5 = 'no';  %  F-function vs non-dimensional distance
    fig.fig6 = 'yes'; %  F-Function vs x distance
    fig.fig7 = 'yes'; %  Side view
    fig.fig8 = 'no';  %  Flow angles
                      %  Ground pressure vs time (automatic with CUBoom)
    fig.fig10 ='no';  %  Sonic boom: dBs vs freq
    fig.fig11 = 'no'; %  3-D ray path
    fig.fig12 = 'yes';%  Wing pressure contour
    fig.fig13 = 'no'; %  Sonic boom: Pressure vs distance
```